Universidad de Concepción
Dirección de Postgrado
Facultad de Ciencias Químicas
Programa Doctorado en Ciencias Geológicas

Estructura del sistema magmático alimentador en el Complejo Volcánico Nevados de Chillán: factores de control y los efectos en la evolución magmática

Tesis para optar al grado de Doctor en Ciencias Geológicas

ANDRÉS SEBASTIÁN OYARZÚN SUAZO
CONCEPCIÓN-CHILE
2023

Profesor Guía: Luis Lara Pulgar
Profesor Co-Guía: Andrés Tassara Oddo
Dpto. de Ciencias de la Tierra, Facultad de Ciencias Químicas
Universidad de Concepción

AGRADECIMIENTOS

Quisiera comenzar agradeciendo a los profesores Dr. Luis Lara Pulgar y Dr. Andrés Tassara Oddo, quienes me han apoyado durante toda mi permanencia en el Programa de Doctorado en Ciencias Geológicas y por sus valiosos aportes que me ayudaron a desarrollar esta investigación. Agradezco a los profesores del Departamento de Ciencias de la Tierra, quienes han contribuido en distintas etapas de mi formación científica. También quisiera agradecer especialmente a Marcela Salgado Vargas por su compañía y apoyo moral y a mi querida familia y mis amigos quienes han sido un soporte fundamental durante esta larga etapa doctoral. A María Esperanza Aravena por todo su aliento y amistad. A todos las personas que me acompañaron en las salidas a terreno. Agradecer a la profesora Laura Hernández por su apoyo en los trabajos efectuados con la microsonda del Instituto GEA y a todas las personas que conforma el Taller de Cortes del GEA por su buena disposición y excelente trabajo. Para finalizar, agradezco el financiamento aportado por el proyecto Fondecyt 1151175 “Active Tectonics and Volcanism at the Southern Andes” (A. Tassara PI) y por las becas de estipendio y arancel de Conicyt de Doctorado Nacional 2019 y de la Dirección de Postgrado de la Universidad de Concepción.

RESUMEN

El Complejo Volcánico Nevados de Chillán (NdC), localizado en los Andes del Sur, es un sistema volcánico controlado estructuralmente que presenta un nutrido registro de actividad eruptiva y que inició su más reciente ciclo eruptivo en enero de 2016. De acuerdo a estos antecedentes y a la peligrosidad que representa este volcán, el objetivo principal de esta tesis es ampliar el conocimiento que se tiene actualmente sobre la arquitectura del sistema magmático alimentador del NdC y de su funcionamiento interno, ya que como los volcanes son una expresión de su sistema magmático, la modalidad eruptiva y la geoquímica de sus productos dependen del funcionamiento interno de sus sistemas magmáticos. De esta forma, esta investigación aportaría insumos para tener pronósticos eruptivos más fiables.

Los resultados de este estudio, obtenidos principalmente con herramientas petrológicas, revelan que las profundidades de cristalización de las principales fases minerales presentes en los productos eruptivos del NdC, estimadas para unidades que abarcan edades entre el Pleistoceno Superior y Holoceno Medio, varían entre 2,2 a 16,9 km bajo la superficie, lo cual coincide en gran medida con la configuración del sistema alimentador actual, propuesto mediante estudios geofísicos. Las profundidades de cristalización, inferidas en esta tesis mediante los análisis termobarométricos, también revelan una zonación composicional vertical del sistema magmático alimentador del NdC, la cual coincide con la profundidad de la Discontinuidad Intracortical de Densidad (ICD). En este estudio, esta relación también es reconocida en otros sistemas volcánicos de la Zona Volcánica Sur de los Andes, lo cual destaca el rol de primer orden que cumple esta discontinuidad en controlar la configuración de los sistemas alimentadores, al menos en esta zona volcánica. Sobre esta discontinuidad, los magmas se alojarían en una estructura noroeste (NO) heredada del basamento, la cual presenta un comportamiento compresivo en el largo plazo en relación al régimen de esfuerzo dictado por la convergencia de las placas.

La evolución magmática del NdC estaría controlada por la estructura del basamento de rumbo NO y por la evolución temporal y espacial de su sistema

alimentador magmático durante el Holoceno, la cual es expresada en el establecimiento de un nivel de almacenamiento de magmas evolucionados en la corteza superior y en sus variaciones temporales de volumen. En una primera etapa serían emitidos magmas andesíticos basáltico, alojados bajo la profundidad de la ICD, cuando el nivel de almacenamiento más somero aún no se ha establecido. Los magmas que no alcanzan la superficie, son alojados a lo largo de la estructura NO en la corteza superior, los cuales diferencian por cristalización fraccionada a magmas más evolucionados, favorecidos por el comportamiento compresivo de esta estructura en el largo plazo. Estos magmas evolucionados actúan como filtro de densidad para magmas menos diferenciados provenientes de los niveles de almacenamiento más profundos del sistema magmático alimentador. La mezcla de estos magmas, composicionalmente diferentes, da origen a las composiciones intermedias del NdC, las cuales predominan con el tiempo en el registro eruptivo del NdC, como consecuencia del decrecimiento del volumen de magma riodacítico almacenado en la corteza superior.

Finalmente, los resultados de esta tesis contribuyen en ampliar el conocimiento del sistema magmático alimentador del NdC y de su funcionamiento interno. Adicionalmente, conocer los factores claves que influyen en la evolución magmática, podría dar algunas señales sobre el comportamiento actual de un volcán, una clave para un pronóstico eruptivo fiable.

.

ABSTRACT

The Nevados de Chillán Volcanic Complex (NdC), located in the Southern Andes, is a structurally controlled volcanic system that presents a rich record of eruptive activity and that began its most recent eruptive cycle in January 2016. According to these antecedents and to the hazard that this volcano represents, the main objective of this thesis is to broaden the knowledge that we currently have about the architecture of the magmatic system that feeds the NdC and its inner worked, since as volcanoes are an expression of their magmatic system, the eruptive modality and the geochemistry of its products depend on the inner worked of its magmatic systems. In this way, this research would provide inputs to have more reliable eruptive forecasts.

The results of this study, obtained mainly with petrological tools, reveal that the crystallization depths of the main mineral phases present in the eruptive products of the NdC, estimated for units ranging in age from the Late Pleistocene to the Middle Holocene, vary between 2.2 to 16.9 km below the surface, which largely coincides with the configuration of the current feeder system, proposed by geophysical studies. The crystallization depths, inferred in this thesis through thermobarometric analyses, also reveal a vertical compositional zonation of the NdC magmatic system, which coincides with the depth of the Intracrustal Density Discontinuity (ICD). In this study, this relationship is also recognized in other volcanic systems of the Southern Volcanic Zone of the Andes, which highlights the first-order role played by this discontinuity in controlling the configuration of the magmatic systems, at least in this volcanic zone. On this discontinuity, the magmas would be housed in a northwest (NW) structure inherited from the basement, which presents a compressive behavior in the long term in relation to the stress regime dictated by the convergence of the plates.

The magmatic evolution of the NdC would be controlled by the structure of the NW-trending basement and by the temporal and spatial evolution of its magmatic system during the Holocene, which is expressed in the establishment of a storage level of evolved magmas in the upper crust and in its temporal variations of volume. In a first stage, basaltic andesitic magmas would be emitted, lodged below the depth

of the ICD, when the shallowest storage level has not yet been established. The magmas that do not reach the surface are housed along the NW structure in the upper crust, which differentiate by fractional crystallization to more evolved magmas, favored by the compressive behavior of this structure in the long term. These evolved magmas act as a density filter for less differentiated magmas coming from the deeper storage levels of the magmatic system. The mixture of these magmas, compositionally different, gives rise to the intermediate compositions of the NdC, which predominate over time in the eruptive record of the NdC, as a consequence of the decrease in the volume of rhyodacitic magma stored in the upper crust.

Finally, the results of this thesis contribute to broaden the knowledge of the magmatic system that feeds the NdC and its inner functioning. Additionally, knowing the key factors that influence magmatic evolution could give some clues about the current behavior of a volcano, a key to a reliable eruptive forecast.

ÍNDICE DE CONTENIDOS

ÍNDICE DE FIGURAS

ÍNDICE DE TABLAS

CAPÍTULO I: INTRODUCCIÓN GENERAL

1.1 Estructura de la tesis

El capítulo I de esta tesis corresponde a la introducción general de esta investigación. En este capítulo se formula el problema científico, con una revisión general de los estudios previos y del contexto geológico del caso de estudio, el Complejo Volcánico Nevados de Chillán. A continuación, se formulan las preguntas de investigación que guían esta tesis y los objetivos específicos que se necesitan alcanzar para responder a estas preguntas. Posteriormente se describen los materiales y metodologías empleadas en este estudio para cumplir con cada uno de los objetivos específicos de esta tesis.

El capitulo II, esta conformado integramente por el artículo publicado en Journal of Volcanology and Geothermal Research, titulado “Decoding the plumbing system of Nevados de Chillán Volcanic Complex, Southern Andes”. En este capítulo se aportan nuevos antecedentes sobre la configuración del sistema magmático alimentador del Complejo Volcánico Nevados de Chillán y se discute el rol que desempeñan las discontinuidades corticales en su arquitectura.

El capítulo III, esta compuesto por el artículo enviado para revisión el día 02 de diciembre de 2022 a la revista Journal of Petrology. El artículo se titula ”The effects of the temporal/spatial evolution of the magmatic system in the upper crust on magmatic evolution”. Los resultados destaca el rol que cumple la evolución del sistema magmático del NdC, expresada en el establecimiento de un nivel con magmas diferenciados en la corteza superior y en sus variaciones de volumen con el tiempo, en la evolución magmática del NdC y en controlar el predominio de composiciones intermedias por procesos de mezcla de magma.

En el capítulo IV se discuten los resultados principales de esta investigación y como contribuyen a resolver las preguntas de investigación. En el capítulo V se destacan las conclusiones más relevantes obtenidas durante el proceso de esta investigación.

1.2 Formulación del problema científico

Las erupciones volcánicas representan una amenaza para las comunidades locales y globales y, por lo tanto, se requiere la mitigación de su impacto para un desarrollo sostenible. Los riesgos pueden ser en gran parte mitigados si se conoce el comportamiento de un volcán. Debido a que los volcanes son una expresión de su sistema magmático, la modalidad eruptiva y la geoquímica de sus productos dependen del funcionamiento interno de sus sistemas magmáticos, por lo cual conocer la dinámica interna de un volcán y su evolución, permitiría tener pronósticos eruptivos más fiables de la magnitud de sus erupciones. Sin embargo, muchos volcanes carecen de estudios detallados que proporcionen restricciones geofísicas y/o petrológicas para la arquitectura de sus sistemas alimentadores y de su dinámica interna. Uno de ellos es el Complejo Volcánico Nevados de Chillán (NdC; 36°50' S/ 71°23' W) en los Andes del Sur, un volcán controlado estructuralmente que presenta un nutrido registro de actividad eruptiva y que inició su más reciente ciclo eruptivo en enero de 2016, pasando de explosiones aisladas a la emisión de una lava dacítica que continúa al momento de escribir esta tesis (www.sernageomin.cl). En este contexto, el desconocimiento del sistema magmático alimentador del NdC y de su dinámica interna, junto a su alta peligrosidad, de acuerdo al ranking del Servicio Geológico Chileno (Sernageomin), ha motivado el desarrollo de numerosas investigaciones científicas durante la última década, las cuales se han basado principalmente en herramientas geofísicas.

Con respecto a la configuración del sistema magmático alimentador del NdC, González et al. (2018), mediante tomografía de ruido sísmico ambiental, reconocen un nivel de almacenamiento de magma entre los 10 y 20 km de profundidad bajo el NdC. La investigación abarca una zona comprendida entre las latitudes 33°S y 38°S y considera datos sísmicos obtenidos entre noviembre de 2013 y abril de 2015. Por su parte, Cardona et al. (2020), investigan el ciclo eruptivo actual del NdC, donde han determinado cinco fases de actividad, basados en la sismicidad, cambios morfológicos y algunas características petrológicas. En ese estudio se propone un modelo hipotético del sistema de alimentación magmático del NdC. El modelo

consiste en la presencia de un tapón de magma en la parte somera del conducto (0,5–1,1 km) y en una cámara magmática localizada entre 4 a 6 km de profundidad que sigue la tendencia de la falla Cortaderas de rumbo noroeste. Astort et al. (2022), también estudian el ciclo eruptivo más reciente del NdC, empleando series de tiempo DInSAR. Ellos reconocen una deformación superficial entre octubre de 2019 y noviembre de 2020, la cual sería originada por la intrusión de magma en un reservorio localizado a 5.5 ± 0.5 km de profundidad desde la superficie, lo cual revela información sobre la dinámica y los procesos magmáticos que están operando en el sistema magmático alimentador del NdC. En esta misma línea, Mousallam et al. (2018) identifica un material de composición andesítica basáltica en la tefra asociada con la actividad Vulcaniana del ciclo eruptivo actual, y sugiere que una pequeña intrusión de magma andesítico basáltico en los niveles más someros del sistema magmático alimentador podría haber gatillado la actividad explosiva. Sin embargo, no existen estudios petrológicos detallados que investiguen la petrogénesis de los magmas del NdC.

Otros estudios que se refieren a la dinámica del sistema magmático alimentador del NdC, se centran en la interacción entre el sistema volcánico del NdC y los sismos de subducción. Farias et al. (2014), mediante el análisis de datos sísmicos obtenidos por cuatro sismómetros ubicados en la cima y alrededores del NdC, estudian la respuesta sísmica del sistema volcánico con la llegada de las ondas símicas de dos réplicas del Terremoto del Maule (M 6.1 en enero de 2012 y M 7.1 en abril de 2012, a 200 km de distancia del NdC). En la investigación observan cambios en la dinámica del sistema volcánico del NdC, los cuales dependen del ángulo de incidencia de la energía sísmica entrante. Farías y Galván (2019), usando simulaciones numéricas de propagación de ondas, continúan con el estudio de los cambios físicos en el sistema volcánico del NdC inducidos por las réplicas del Terremoto del Maule (2010). En ese estudio sugieren que la geometría de las estructuras locales en las interacciones sismo-volcánicas puede influir en el comportamiento de los sistemas volcánicos. Conclusiones similares son propuestas por Farías y Basualto (2020), quienes estudian el impacto de las ondas símicas del Terremoto de Illapel de 2015 (M 8.3) en los volcanes Nevados de Chillán

(aproximadamente a 500 km de distancia), Copahue y Villarrica, utilizando datos sísmicos, geodésicos y observaciones geoquímicas, en combinación con simulaciones numéricas de propagación de ondas.

Por otra parte, mientras estos estudios han revelado parcialmente la arquitectura del sistema magmático alimentador del NdC, no se han propuesto los factores que controlan su configuración. Actualmente, los sistemas de alimentación magmática asociados a volcanes activos se consideran divididos en zonas verticales con múltiples niveles de acumulación de magma (Gilbert et al., 2012; Annen et al., 2015; Sparks y Cashman, 2017). Los factores que controlan una estructura tan compleja son los contrastes de densidad entre el magma y las rocas de la corteza y las discontinuidades inherentes de la litosfera (ej., Valentine y Krogh, 2006; Kavanagh et al., 2006; Menand, 2008). Por lo tanto, se cree que las discontinuidades de Moho (límite corteza-manto) y de Conrad (intracorteza) desempeñan un papel fundamental en el almacenamiento de magmas (ej., Annen y Sparks, 2002; Kavanagh et al., 2006). Otro factor relevante que influye en la configuración de los sistemas alimentadores de magma es el enrejado estructural sobre el cual se desarrollan los sistemas volcánicos (Cembrano y Lara, 2009), en el cual los magmas pueden almacenarse en un cruce de estructuras oblicuas al arco (Piquer et al., 2019). En este contexto, para la Zona Volcánica Sur de los Andes (Fig. 1.1) se ha propuesto que existe una relación en el largo plazo entre las estructuras del basamento y la tectónica, la cual se expresa en el grado de diferenciación de los productos volcánicos (Cembrano y Lara, 2009). Cembrano y Lara (2009) establecen en esta zona volcánica dos categorías principales de interacciones volcano-tectónica: asociaciones cinemáticamente acopladas o desacopladas. En la primera categoría, la organización espacial de volcanes o de cluster de volcanes estarían asociadas con estructuras orientadas subparalelas al máximo stress horizontal dictado por la convergencia de placas en dirección noreste (NE), con un comportamiento extensional en el largo plazo y, en general, presentan las composiciones magmáticas más primitivas. Composiciones más evolucionados ocurren generalmente en asociaciones cinemáticamente desacopladas, en la cual volcanes y grupos de volcanes están espacial y temporalmente asociadas con estructuras corticales

ancestrales de rumbo noroeste (NO), transversales al arco volcánico, el cual sería el caso del NdC (Stanton-Yonge et al. , 2016; González-Vidal et al., 2018) . En particular, el NdC es un buen caso de estudio en el contexto de dominios compresivos del arco volcánico (González et al., 2018; Lupi et al., 2020) y permitiría comprender como interactúan el régimen de esfuerzo y la estructura de la litósfera en la producción de magmas evolucionados.

En este contexto, esta investigación se propone identificar, mediante técnicas petrológicas, el sistema magmático alimentador del NdC y comprender los factores geológicos que controlan su configuración. También se evaluarán los procesos que dan origen a las composiciones dacíticas emitidas en tiempos históricos, lo que nos permitirá acercarnos a comprender mejor cómo funcionan estos sistemas volcánicos. Adicionalmente, el NdC presenta cambios temporales en las composiciones emitidas durante el Holoceno, con predominio de composiciones intermedias en los productos más jóvenes. Estas variaciones composicionales permiten evaluar algunos de los factores claves que influyen en la evolución magmática de un volcán. De esta forma, una mejor comprensión de la evolución magmática y de los factores que la controlan podría dar algunas señales sobre el comportamiento actual de un volcán, una clave para un pronóstico eruptivo fiable.

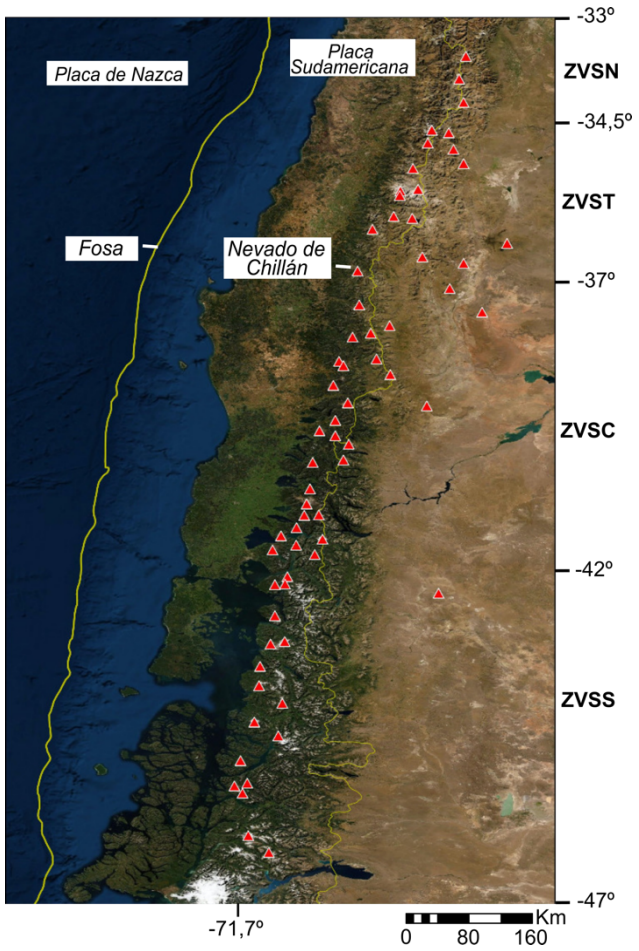

Figura 1.1. Mapa de la Zona Volcánica Sur de los Andes con la ubicación del Complejo Volcánico Nevados de Chillán.

1.3 Antecedentes geológicos del Complejo Volcánico Nevados de Chillán

La Zona Volcánica Sur de los Andes (SVZ), que se extiende desde los 33,5° hasta los 46,5° S, la cual resulta de la subducción de la placa oceánica de Nazca bajo la placa Sudamericana (Fig. 1.1), ha sido dividida en cuatro subsegmentos (López-Escobar et al., 1995) según algunas características geológicas sobresalientes: NSVZ (norte; 33º - 34,5º S); TSVZ (de transición; 34,5º - 37º S); CSVZ (central; 37º - 42º S) y SSVZ (sur; 42º - 46º S). El Complejo Volcánico Nevados de Chillán (NdC; 36°50' S/ 71°23' W) está ubicado en la TSVZ, tiene aprox. 16 km de largo y está compuesto por dos edificios volcánicos principales (Cerro

Blanco y Las Termas) que albergan 13 centros eruptivos que forman una alineación con dirección NO sobre una estructura transversal del basamento andino (Stanton-Yonge et al. , 2016; González-Vidal et al., 2018).

La historia eruptiva del NdC comenzó alrededor de los 640 ka (Dixon et al., 1999; Naranjo et al., 2008) con actividad mayoritariamente efusiva de composiciones andesíticas y andesíticas basálticas e intermitente hasta ca. 40 ka. El desarrollo de ambos edificios actuales comenzó después de los ca. 40 ka.

La actividad eruptiva en el edificio Cerro Blanco (CB) comienza con la emisión de composiciones predominantemente andesíticas basálticas (Dixon et al., 1999; Naranjo et al., 2008). Posteriormente, los productos eruptivos han sido emitidos desde diferentes centros eruptivos dentro de este edificio, con composiciones andesíticas predominantes. La última erupción ocurrió en el flanco NW del edificio, en el período 1861-1865, con composiciones andesíticas basálticas predominantes (Dixon et al., 1999; Naranjo et al., 2008).

Composiciones más evolucionadas (dacitas y riodacitas) predominan en el edificio Las Termas (LT), excepto algunas unidades basálticas andesíticas y andesíticas expuestas en los flancos. La actividad eruptiva en este edificio comienza ca. 40 ka (Dixon et al., 1999) con la emisión de composiciones andesíticas y posteriormente, ca. 30 ± 2.2 ka (Dixon et al., 1999), son emitidos magmas riodacíticos. La actividad holocena comienza con la emisión de lavas andesíticas basálticas (Dixon et al., 1999), las cuales subyacen a lavas riodacíticas, pobres en cristales, que se han emitidos por diferentes centros eruptivos alojados en la estructura principal de este edificio. Este último evento está datado en ca. 5.8 a 5.3 ka (Dixon et al., 1999), en un depósito de tefras asociado a una actividad pliniana, que se han interpretado como las contrapartes efusivas de las lavas riodacíticas, por sus características geoquímicas similares (Dixon et al., 1999). Posteriormente son emitidas lavas andesíticas y dacíticas (7,7 ± 2,8 ka; Naranjo et al., 2008), ricas en cristales, que sobreyacen a las lavas riodacíticas y que contienen enclaves macroscópicamente distinguibles de composición andesítica basáltica (Murphy, 1995; Dixon et al., 1999). Tefras negras de composición andesítica basáltica se superponen a la secuencia de piedra pómez anterior (Dixon et al., 1999) y se

reconocen dos flujos de piroclastos de composición andesítica (ca. 2.2 and 3.5 ka) que son asignadas al volcán Viejo (Dixon et al., 1999).

En el último siglo la actividad eruptiva se ha concentrado en el edificio Las Termas, con la emisión de magmas dacíticos, ricos en cristales, desde diferentes centros eruptivos: Nuevo (1906-1946); Arrau (1973-1986); San Sebastián (2008; Coppola et al., 2016) y Nicanor (2016-presente; Mousallam et al., 2018; Benet et al., 2021; Cardona et al., 2021). Un episodio vulcaniano menor ocurrió en 2003 (Naranjo & Lara, 2004) originado en un área entre los cráteres Nuevo y Arrau. Este último es también el área donde ocurre la erupción actual (cráter y domo de Nicanor) que comenzó en 2016 (Mousallam et al., 2018; Benet et al., 2021; Cardona et al., 2021) como explosiones débiles generando una columna eruptiva de ~2 km de altura que se hizo más fuerte y culminó con la extrusión de lava en enero de 2018, esta última formando una serie de pequeños domos que ahora alimentan un flujo de lava en bloque en la ladera sureste (Benet et al., 2021; Cardona et al., 2021). La actividad volcánica actual evolucionó de una fase con dominancia hidrotermal a una efusiva, aún acompañada de persistentes explosiones vulcanianas de baja y media intensidad (Cardona et al., 2021).

1.4 Preguntas de investigación

- ¿Qué nuevos antecedentes nos proporcionan las herramientas petrológicas sobre la configuración del sistema magmático alimentador del Complejo Volcánico Nevados de Chillán y de los factores que la controlan?
- ¿Cuál es el funcionamiento interno del sistema magmático alimentador del Complejo Volcánico Nevados de Chillán?
- ¿Qué factores explican la evolución magmática del Complejo Volcánico Nevados de Chillán que da origen a un predominio de composiciones intermedias en los productos volcánicos más jóvenes?

1.5 Hipótesis de investigación

El sistema magmático alimentador del Complejo Volcánico Nevados de Chillán presentaría una zonación composicional en la vertical. Los niveles de acumulación de magmas más someros se correlacionarían aproximadamente a las profundidades inferidas por los estudios geofísicos, entre 4 a 6 km y entre 10 a 20 km bajo la superficie, cuya ubicación estaría limitada por la Discontinuidad Intracortical de Densidad. El sistema magmático alimentador del Complejo Volcánico Nevados de Chillán estaría vinculado a la falla Cortaderas de rumbo noroeste, que presentaría un comportamiento compresivo en el largo plazo, favoreciendo la producción de magmas evolucionados. Por otra parte, la evolución del sistema magmático alimentador del Complejo Volcánico Nevados de Chillán también condicionaría su evolución magmática y explicaría el predominio de composiciones intermedias en los productos volcánicos más recientes.

1.6 Objetivos

1.6.1 Objetivo general

Contribuir en el conocimiento de la arquitectura del sistema magmático alimentador del Complejo Volcánico Nevados de Chillán y comprender los factores que controlan su configuración y su evolución magmática.

1.6.2 Objetivos específicos

Objetivo específico 1: Contribuir en el conocimiento de la configuración del sistema magmático alimentador del Complejo Volcánico Nevados de Chillán y los factores geológicos que la controlan.

Objetivo específico 2: Comprender el funcionamiento interno del sistema magmático alimentador del NdC, evaluando los procesos magmáticos que dan origen a sus composiciones.

Objetivo específico 3: Realizar un modelo conceptual que integre la configuración del sistema magmático alimentador del Complejo Volcánico Nevados de Chillán, su evolución temporal y los efectos en la evolución magmática.

1.7 Materiales y metodología

Para esta tesis se efectuaron dos campañas de campo (durante enero y febrero de 2018 y 2019) al Complejo Volcánico Nevados de Chillán (NdC), en las cuales se recolectaron cincuenta muestras representativas de unidades de flujo de lava de edad Pleistoceno-Holoceno, tres diques y una muestra de tefra de un cono piroclástico (Figura 2.1)

Para los análisis petrográficos de estas muestras se realizaron treinta secciones delgadas pulidas, las cuales se describieron con un microscopio óptico en el Departamento de Ciencias de la Tierra de la Universidad de Concepción (Chile) y con imágenes BSE (electrones retrodispersados) obtenidas por microsonda electrónica en la Universidad de Concepción (Chile) y en la Universidad de Rice (EE.UU). Se determinaron los porcentajes modales de fases minerales, masa fundamental y tipos de plagioclasas (según sus texturas) de catorce muestras representativas de lavas y de los tres diques, utilizando un contador (1000 puntos por sección). Los cristales menores de 100 micras se consideraron como parte de la masa fundamental.

Se determinaron las concentraciones de elementos principales y trazas para 22 muestras representativas en ACME Laboratories (Canadá). Los análisis químicos de roca total se realizaron mediante espectrometría de emisión de plasma de acoplamiento inductivo ICP-ES (elementos principales) y espectrometría de masas de plasma de acoplamiento inductivo ICP-MS (elementos traza). Los resultados y los límites de detección del método (MDL) para todos los óxidos y elementos traza

principales se detallados en Anexo 1 (más detalles de las condiciones analíticas son dadas en la sección 2.3).

Las composiciones del centro y borde de piroxenos, plagioclasa, olivino y óxidos de Fe-Ti se obtuvieron mediante espectrometría de dispersión de longitud de onda (WDS) utilizando la microsonda electrónica (JEOLJXA-8600M) en la Universidad de Concepción (Chile) y en la Universidad de Rice (EE. UU; JEOLJXA 8530F). Las condiciones analíticas son detalladas en el Anexo 2 y en las secciones 2.3 y 3.4. Los resultados son listados en el Anexo 3.

Las descripciones petrográficas y los análisis químicos de roca total y mineral nos permiten cumplir los objetivos mediante diferentes herramientas metodológicas y análisis petrológicos. Específicamente, con las ecuaciones de equilibrio fundido/cristal dadas por Putirka (2008), se estimaron las presiones de cristalización de las principales fases minerales, con lo cual, junto a las descripciones petrográficas, se infiere la configuración del sistema magmático alimentador del NdC (Los detalles metodológicos son dados en la sección 2.4.4). Por otra parte, los procesos magmáticos principales que dan origen a los magmas dacíticos del NdC fueron determinados mediante las observaciones petrográficas, el análisis petrológico de la química mineral y con modelamientos geoquímicos de cristalización fraccionada con el algoritmo Rhyolite-MELTS (Gualda et al., 2012; Ghiorso and Gualda, 2015) y de mezcla de magmas con los programas MIXING (Carr and Gazel, 2017) y PETROMODELER (Ersoy, 2013). Los detalles metodológicos son dados en la sección 3.5.3.

CAPÍTULO II: DECODING THE PLUMBING SYSTEM OF NEVADOS DE CHILLÁN VOLCANIC COMPLEX, SOUTHERN ANDES

Artículo publicado en Journal of Volcanology and Geothermal Research.

Oyarzún, A., Lara, L. E. & Tassara, A. (2022). Decoding the plumbing system of Nevados de Chillán Volcanic complex, Southern Andes. *Journal of Volcanology and Geothermal Research*, 422, 107455. https://doi.org/10.1016/j.jvolgeores.2021.107455

Andrés Oyarzún[1*], Luis E. Lara[2, 3], Andrés Tassara[1, 4]

[1]Departamento de Ciencias de la Tierra, Universidad de Concepción, Victor Lamas 1290, Concepción, Chile

[2]Servicio Nacional de Geología y Minería, Avenida Santa María 0104, Santiago, Chile.

[3]Research Center for Integrated Disaster Risk Management (CIGIDEN), Avenida Vicuña Mackenna 4860, Santiago, Chile

[4] Millennium Nucleus The Seismic Cycle along Subduction Zones (CYCLO)

*Corresponding author. E-mail: andresoyarzunsuazo@gmail.com

Abstract

Eruptions pose a threat to local and global communities and hence mitigation of the impact is required for a sustainable development. An extended knowledge of the plumbing system beneath volcanoes is key to assess volcanic hazards through a correct interpretation of the geophysical signals detected by monitoring networks. However, many volcanoes lack detailed studies that provide geophysical and/or petrological constrains for their plumbing systems. One of them is the Nevados de Chillán Volcanic Complex (NdCVC) in Southern Andes, which reawakened in January 2016 escalating from isolated explosions to lava emission that continues at the time of writing (December, 2021). In this context, our aim is to constrain the architecture of the NdCVC plumbing system by means of petrological tools and provide insights for a more comprehensive interpretation of magmatic processes and ultimately the geophysical signals recorded at monitoring stations. In this study, mineral-melt

equilibrium thermobarometry was performed for clinopyroxenes, orthopyroxenes and plagioclases included in volcanic rocks. Our thermobarometric results suggest that the NdCVC plumbing system extends vertically from ca. 2 to 17 km depth. The depth of crystallization for mineral phases included in basaltic andesites/andesites matches the intracrustal Conrad discontinuity in this area, while evolved magmas migrate and store above this level, which in turn suggests a compositionally zoned plumbing system. Our results highlight the first-order role played by crustal geological discontinuities in the configuration of a plumbing system, despite the concomitant role that external forcings as crustal tectonics may play.

2.1 Introduction

Eruptions pose a threat to local and global communities and hence mitigation of their impact is required for a sustainable development. In coping with volcanic hazards and risks, early warning systems and instrumental monitoring networks are essential. However, the analysis of geophysical data requires an extended knowledge of the plumbing systems allowing for a correct interpretation of the signals and time series (e.g., Aiuppa et al., 2010; Kahl et al., 2011). In fact, conceptual models of plumbing systems constrained by petrology are useful to better understand patterns of seismicity and deformation observed in volcanoes under unrest, which usually show different patterns depending on the geological context (e.g., Sigmundsson et al., 2018). However, many volcanoes lack detailed studies that provide geophysical and/or petrological constrains for the architecture of their plumbing systems. One of them is Nevados de Chillán Volcanic Complex in Southern Andes, which reawakened in January 2016 (Mousallam et al., 2018; Benet et al., 2021; Cardona et al., 2021), escalating from isolated explosions to lava emission that continues at the time of writing (www.sernageomin.cl).

Currently, plumbing systems are imagined as vertically-zoned with multiple levels of magma ponding and subsequent differentiation (Gilbert et al., 2012; Annen et al., 2015; Sparks and Cashman, 2017). Factors controlling such a complex structure are density contrasts between magma and crustal rocks and the inherent

discontinuities of the lithosphere, which express themselves in temperature and elastic properties changing over the crustal column (e.g., Valentine and Krogh, 2006; Kavanagh et al., 2006; Menand, 2008). The well-known Moho (crust-mantle boundary) and the Conrad (intracrustal) discontinuity, are hence thought to be playing a role in the transit and storage of magmas (e.g., Annen and Sparks, 2002; Kavanagh et al., 2006).

In this context, interpretation of the seismic signals carries some ambiguity and affect the quality of hazards assessment. We select Nevados de Chillán Volcanic Complex as a case-study because of both the present activity that deserves attention and the availability of a large number of samples from different geological units, which provide an opportunity to test petrological tools and assess the stability of the plumbing system over time. Our aim is to constrain the geometry of the plumbing system and provide insights for a more comprehensive interpretation of magmatic processes and ultimately the geophysical signals recorded by the monitoring networks

2.2 Geological setting

Nevados de Chillán Volcanic Complex (NdCVC) is located in the Southern Andean Volcanic Zone (SVZ), right on the transition from a thick (>50 km) subarc continental crust in the north to a thin (<40 km) crust southward (López-Escobar et al., 1993; Stern, 2004; Tassara and Echaurren, 2012). The NdCVC is ranked fourth by the Chilean Geological Survey (Sernageomin) in terms of hazards and exposure (www.sernageomin.cl) and also scored high in other hazards classification schemes (e.g., Lara et al., 2021).

The NdCVC has an elevation that exceeds 3100 m.a.s.l with a height of 1000-1250 m (Naranjo et al., 2008) and overlies a ca. 1000 m thick basement (Folguera et al., 2006) formed by a subhorizontal sequence of Pliocene to Early Pleistocene volcanic rocks (Cola de Zorro Formation; González and Vergara, 1962; Vergara and Muñoz, 1982). The Cola de Zorro Formation overlies folded Cenozoic volcano–sedimentary rocks (Cura-Mallin Formation) that form a cover at least 2500 m thick

(Radic, 2010) above the crystalline basement. The continental crust is ca. 40 km thick at this latitude and is vertically segmented with the intracrustal density discontinuity (ICD) at a depth of ca. 8 km b.s.l (Tassara and Echaurren, 2012).

NdCVC is composed of two main volcanic edifices (Cerro Blanco and Las Termas; Dixon et al., 1999) that host 13 eruptive centers forming a NW-striking alignment ca. 16 km long (Fig. 2.1). The volcanic edifices are separated by a saddle region with three eruptive centers (Pichicalfú, Baños and Shangri-La units; Dixon et al., 1999; Naranjo et al., 2008). Two Holocene scoria cones, Las Lagunillas y Parador, are located on the eastern and western flanks respectively, ca. 5 km away from the main edifices.

The NdCVC eruptive history started around 640 ka with the eruption of thick and extensive sub-glacial andesitic lava flows (Naranjo et al., 2008). From ca. 640-50 ka, sub-glacial andesitic lavas predominate including Pincheira, Atacalco, Diguillín and Lanalhue units (Naranjo et al., 2008), which form the basement for the composite modern edifice (Dixon et al., 1999; Naranjo et al., 2008). Around 40 ka, deposits of non-welded pyroclastic density currents and ash, pumice and scoria layers fall deposits were emplaced from eruptions that possibly correlate with a caldera formation event (Dixon et al., 1999), although evidence for that is still scarce. These deposits form a succession named as El Castillo ignimbrites (Naranjo et al., 2008), which have been correlated with the extensive ignimbrites recognized up to 100 km west-northwest of the NdCVC (Varela and Moreno, 1982; Naranjo et al., 1994;). After this major explosive event, the development of the present edifices began.

In the Cerro Blanco edifice (CB) the andesitic compositions predominate and the eruptive activity began at ca. 24 ka (Orientales unit; Dixon et al., 1999; Naranjo et al., 2008). During the Holocene the eruptive products have been emitted from different eruptive centers (Colcura, Gato, Blanco, Calfú units; Dixon et al., 1999; Naranjo et al., 2008) and the last eruption occurred in the 1861-1865 period (Santa Gertrudis unit; Dixon et al., 1999; Naranjo et al., 2008). More evolved compositions dominate the edifice of Las Termas (LT), except for some andesitic lavas (Sur, Democrático and upper Chillán units; Dixon et al., 1999; Naranjo et al., 2008). Its eruptive activity also began at ca. 40 ka with an andesitic lava sequence (Sur unit)

followed by dacitic lavas (Aguas Calientes unit; ca. 30 ka), all of them with ice-contact features (Dixon et al., 1999; Naranjo et al., 2008). In the post-glacial period, the eruptive products were also emitted from different eruptive centers (Democrático, Viejo, Chillán, Pata de Perro, Nuevo, Arrau, Chudcún, San Sebastián and Nicanor). Holocene tephra fall deposits crop-out to the east and south of NdCVC being geochemically correlated with Viejo and Calfú eruptive centers (Dixon et al., 1999).

In the last century, volcanic activity has been concentrated in Las Termas edifice with a relatively uniform dacitic composition of the eruptive products. The largest (and longer) historical eruptions occurred in 1906-1948 (Nuevo unit) and 1973-1986 (Arrau unit) with a minor Vulcanian episode in 2003 (Chudcún crater; Naranjo and Lara., 2004) and a gently effusive eruption in 2008 (San Sebastián unit; Coppola et al., 2016), both sourced from an area between the Nuevo and Arrau craters. The latter is also the vent area for the current eruption (Nicanor crater and dome), which started in 2016 (Mousallam et al., 2018; Benet et al., 2021; Cardona et al., 2021) as weak explosions that became stronger and culminated with magma extrusion in January 2018 forming a series of small domes that feed a lava flow on the southwestern slope.

The NdCVC magmatic evolution has been qualitatively discussed and can be understood by three main processes: fractional crystallization, magma mixing and assimilation of continental crust (Murphy, 1995). Differences in the content of some trace elements of the more evolved and the less differentiated rocks are probably due to different parents and/or fractionation histories (Murphy, 1995). Compositional differences are also observed between volcanic edifices and are thought to result from different residence times of the magmas within the crust (Dixon et al., 1999). The CB system would have been replenished more frequently than LT promoting a higher eruptive frequency, which in turn might be a consequence of the local basement structure (Dixon et al., 1999).

A remarkable feature of NdCVC is the NW-striking alignment of eruptive centers, which is related to the regional-scale basement structure making this a case of basement-controlled volcanic clusters (Cembrano and Lara, 2009). Radic (2006, 2010) proposed that former normal faults connecting depocenters of the extensional

Oligo-Miocene basins were inverted in the Upper Miocene to define the present structure. It has also been proposed that NdCVC developed upon the prolongation of the NW- trending Cortaderas lineament (e.g., Stanton-Yonge et al., 2016; Gonzalez-Vidal et al., 2018), which would be a crustal-scale discontinuity now better exposed in the back-arc region (Hernando et al., 2012; Søager et al., 2013). Despite the nature of the basement anisotropy, the distribution of shear wave velocities beneath the NdCVC (Gonzalez-Vidal et al., 2018) seems to confirm a NW-striking pattern, which is also illuminated by the present seismicity (Cardona et al., 2021).

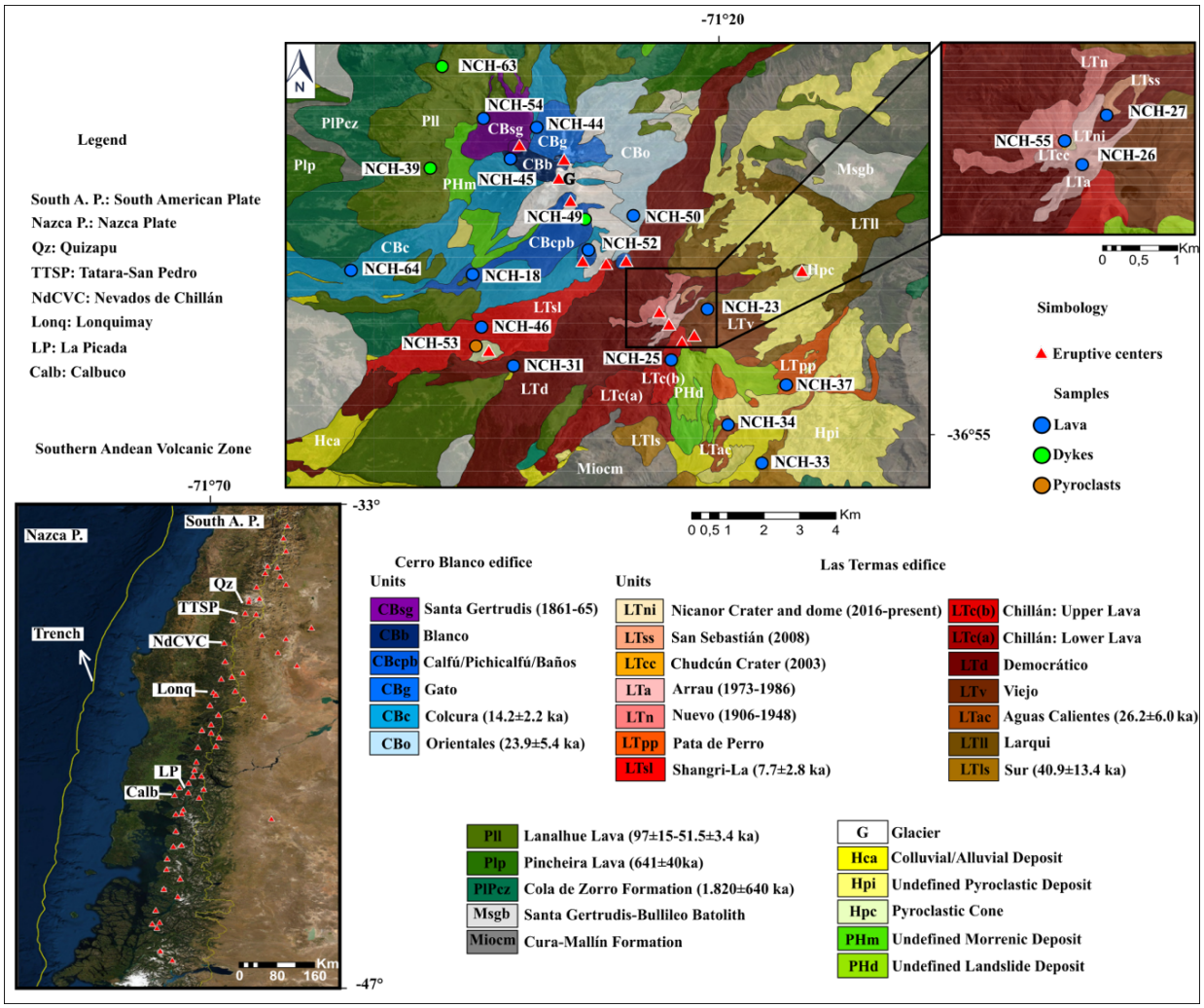

Figure 2.1. Simplified geological Map of Nevados de Chillán Volcanic Complex (NdCVC) from Naranjo et al. (2008). The modern composite NdCVC is formed since the last ca. 40 ka by two volcanic edifices; Cerro Blanco and Las Termas. Cura-Mallín Formation, Cola de Zorro Formation and Santa Gertrudis-Bullileo Batolith are part of the NdCVC basement. The radiometric ages are taken from Dixon et al. (1999), Mee (2004, 2009) and Naranjo et al. (2008). Circles show the location of samples collected for chemical analysis in this study and red triangles show the location of eruptive centers.

2.3 Material and methods

2.3.1 Sampling and petrographic study

Fifty representative samples of post-caldera Pleistocene-Holocene lava flow units, three dykes (NCH-49, NCH-39 and NCH-63) and a tephra sample from a pyroclastic cone (NCH-53), were collected during two field campaigns (2018, 2019). Thirty polished thin sections were described petrographically with an optical microscope and fifteen with BSE (backscattered electron) images obtained by electron microprobe. The modal percentages of mineral phases, groundmass and plagioclase types (according to their textures) of fourteen representative lavas samples and the three dykes were determined using a controlled stage and a counter (1000 points per section). The crystals smaller than 100 microns were considered as part of the groundmass.

2.3.2 Whole-rock and mineral chemistry

Major and trace element concentrations of whole-rock for 22 samples, were acquired at ACME Laboratories (Canada). Whole-rock analyses were performed by inductively coupled plasma-emission spectrometry ICP-ES (major elements) and inductively coupled plasma–mass spectrometry ICP-MS (trace elements). The results and Method Detection Limits (MDLs) for all major oxides and trace elements are listed in Anexo 1. Accuracy of the methods was confirmed by internal reference materials (SO-19 for major and trace elements) and duplicates. In addition, in this study we use as reference the major and trace element concentrations of 85 samples obtained from Murphy (1995), Dixon et al. (1999), Deruelle and Lopez-Escobar (1999) and Mee et al. (2009). Since the FeO total is usually reported as FeO_t or $Fe2O3_t$ in previous contributions, it was necessary to estimate the proportions of both cations for each sample, and to calculate the FeO total accordingly. These ratios were obtained from the concentrations of both oxides for different volcanic rocks as proposed by Middlemost (1989).

Pyroxene, plagioclase, olivine and Fe-Ti oxides core-rim compositions (Anexo 3) were obtained by wavelength-dispersive spectrometry (WDS) using the electron microprobe (JEOLJXA-8600M Superprobe) at Universidad de Concepción (Chile) and

Rice University (USA; JEOLJXA 8530F Hyperprobe). Analyses were carried out using standard operating conditions of 15 kV accelerating voltage and 20 nA beam current and a spot size of 3 μm was used for the all analyses with exception of plagioclase, for which the beam size was set to 10 μm beam diameter to avoid Na and K loss during sample-beam interaction.

2.4 Results

2.4.1 Geochemistry

Based on the entire geochemical dataset (this study and previous data) the NdCVC lavas range from basaltic andesite to rhyolite, between 53.1 and 70.6 wt% SiO_2 (volatile-free normalization; Fig. 2.2). The mineral phases present are plagioclase (Pl), clinopyroxene (Cpx), orthopyroxene (Opx), olivine (Ol), Fe-Ti oxides (Ox), apatite and trace amounts of sulfides. Hydrated minerals such as amphiboles and biotites are absent (Table 2.1).

The SiO_2 content shows a negative correlation with Al_2O_3, FeOt, CaO, MgO, Sr, Sc, V, Co and Ni, and a positive correlation with K_2O, Na_2O, Rb, Ba, Y, Zr, Hf, Nb, Th and REE. For TiO_2 and P_2O_5, SiO_2 shows a positive correlation up to ca. 60 wt% SiO_2, and then the correlation become negative. The observed variation in major oxides and trace element (Fig. 2.3 and 2.4) is consistent with fractionation of calcic plagioclase, pyroxene, olivine at an early crystallization stage and dominantly sodic plagioclase, pyroxene, titanomagnetite/ilmenite and apatite in later stages. The TiO_2 and FeOt/MgO vs SiO_2 (wt%) diagrams (Fig. 2.3) show significant differences in samples with the same degree of differentiation. In general, samples that plot in the lower trend in TiO_2 and FeOt/MgO are those from Las Termas edifice that contain macroscopically distinguishable mafic enclaves. Hypothetical fractionation and mixing trends (Fig. 2.3) in TiO_2 and FeOt/MgO vs SiO_2 (wt%) were obtained from Murphy (1995) and Dixon et al. (1999). Other chemical differences in rocks with same SiO_2 content is probably due to different parents and/or fractionation

history.

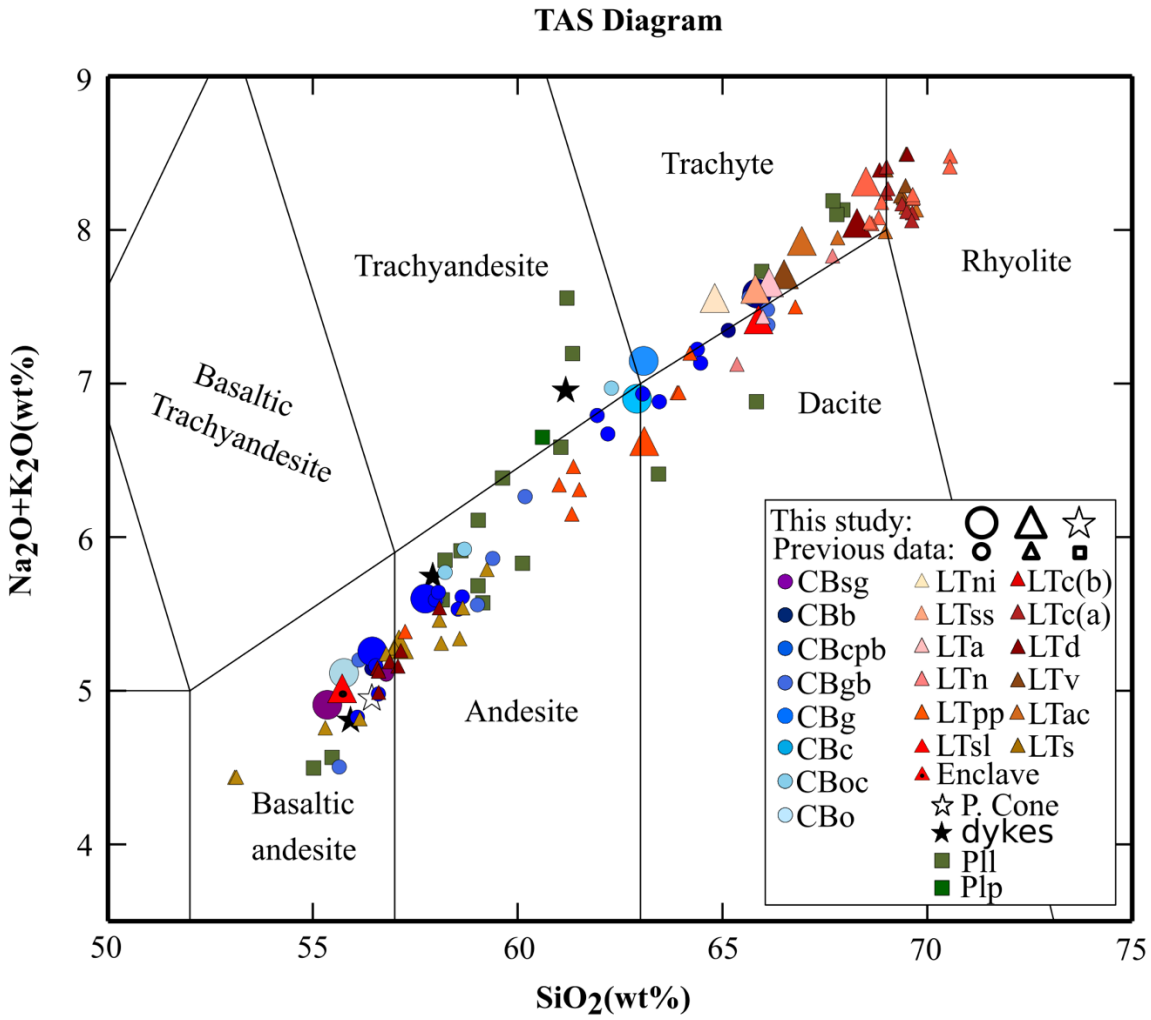

Figure 2.2. Total alkali versus silica diagram. (TAS; Bas et al., 1986) for NdCVC samples. The compositions span from basaltic andesite to rhyolite for all samples. Largest circles, triangles and stars show the data from this study (mafic enclave in LTsl is represented by a black circle within a red triangle). Previous data (smaller symbols) were obtained from Murphy (1995), Dixon et al. (1999), Deruelle and Lopez-Escobar (1999) and Mee et al. (2009). Data were normalized on a volatile-free basis. CB: Cerro Blanco edifice; LT: Las Termas edifice; P.cone: Pyroclastic cone. Pincheira, and Lanalhue lavas were emitted prior to the development of the two volcanic edifices.

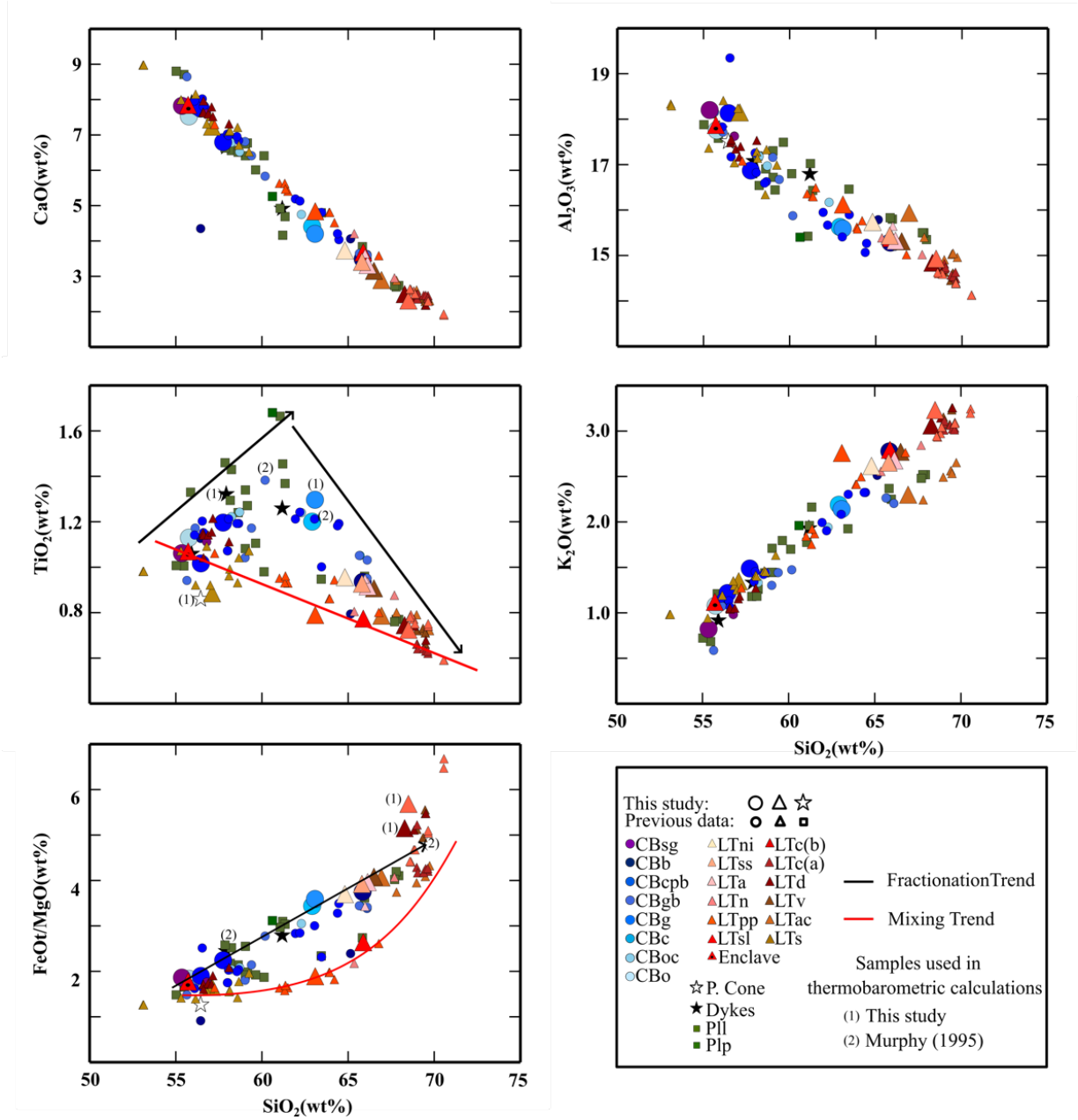

Figure 2.3. Harker diagrams of CaO, $A_{l2}O_3$, TiO_2, K_2O and FeOt/MgO vs SiO_2 (wt%). The observed variation in these major element oxides is consistent with fractionation of calcic plagioclase, pyroxene, olivine and Fe-Ti oxides. Symbols as in figure 2.2. Hypothetical fractionation and mixing trend were obtained from Murphy (1995) and Dixon et al. (1999). Numbers in parentheses indicate the samples used in thermobarometric estimates: (1) samples from this study and (2) samples from Murphy (1995).

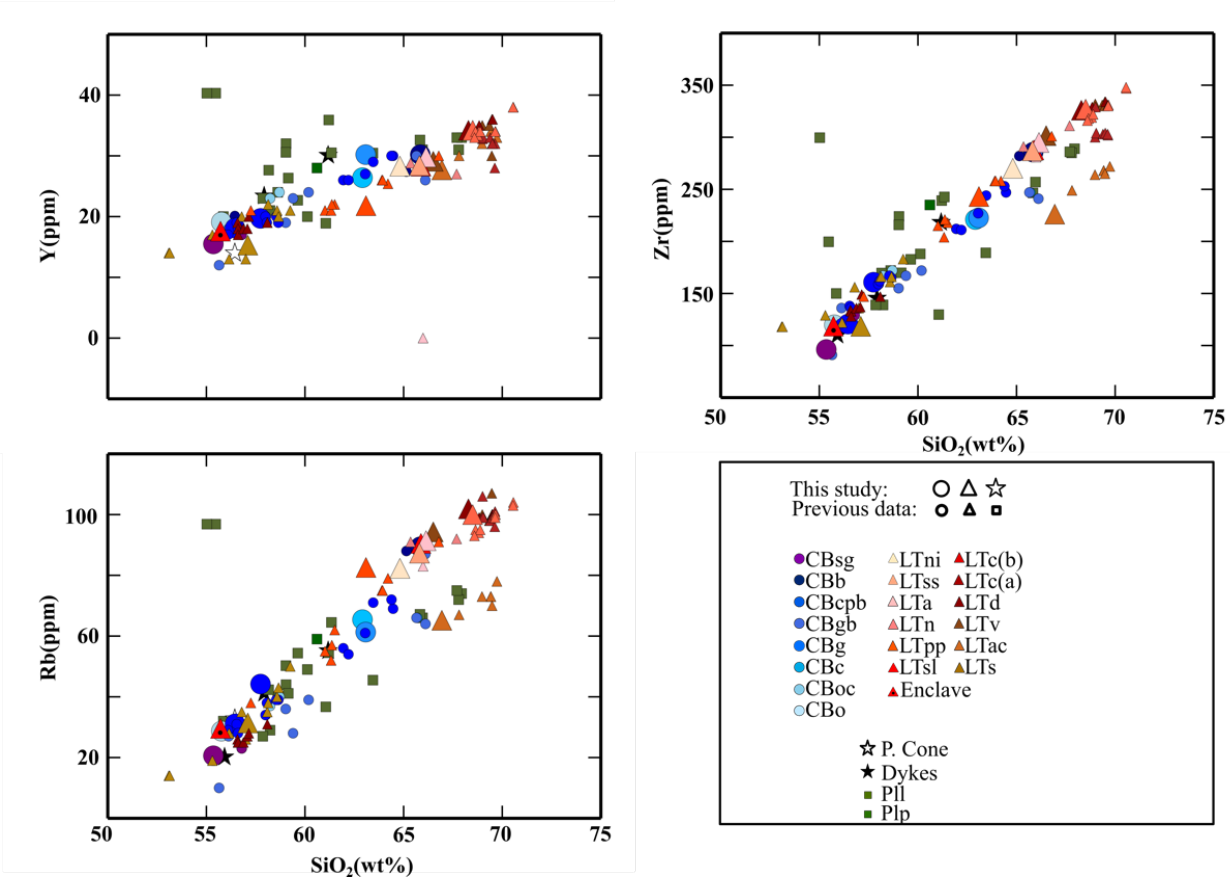

Figure 2.4. Harker diagrams for some trace elements. Y, Zr and Rb (ppm) vs SiO_2 (wt%). Symbols as in figure2.2.

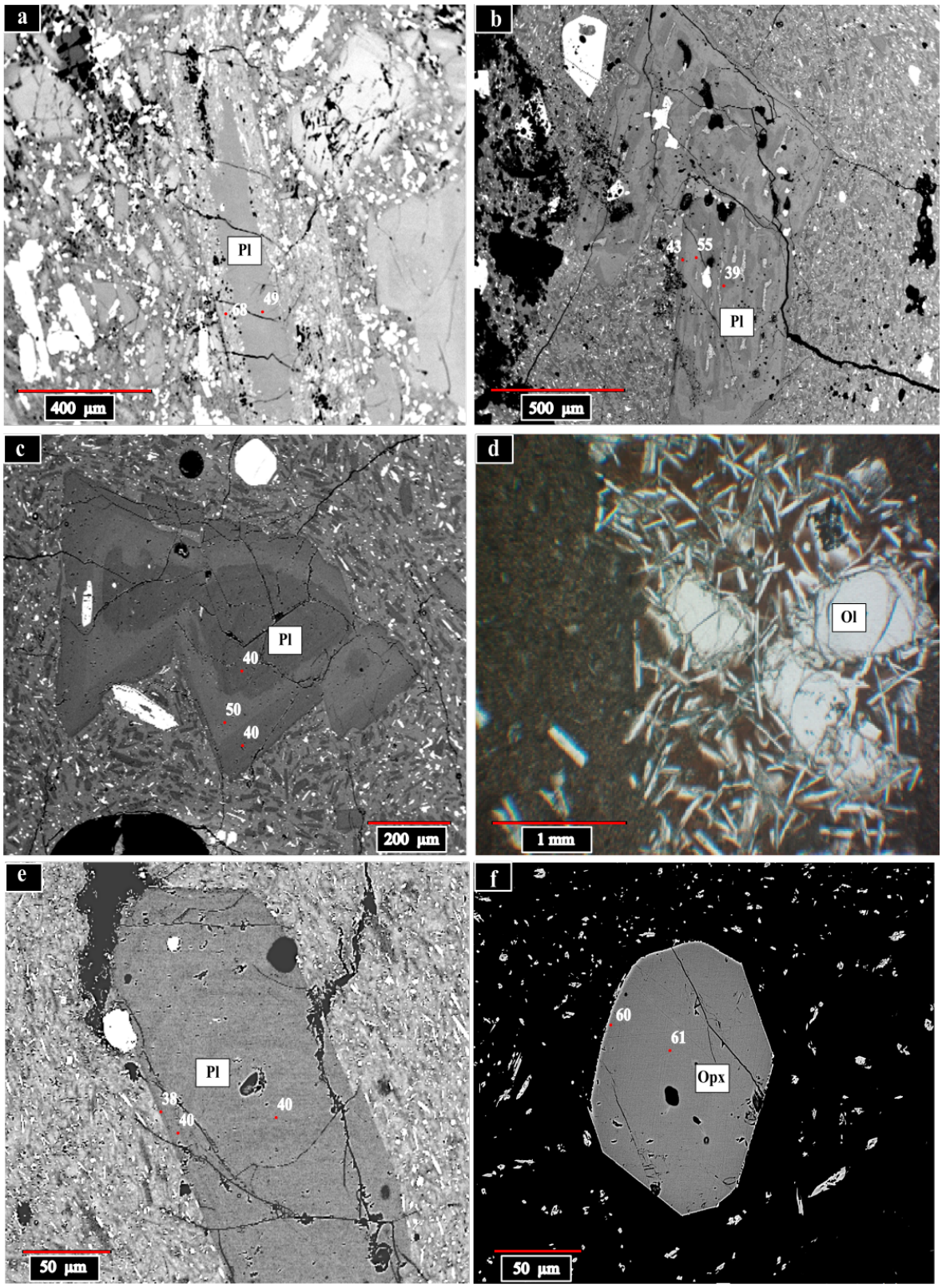

Figure 2.5. BSE images and from an optical microscope. (a) Type 1 plagioclase (Pl) with fine sieve texture in the rim; (b) Type 2 plagioclase (Pl) with coarse sieve texture

in the core; (c) Type 3 plagioclase (Pl) with a partially anhedral resorbed anorthite-poor core; (d) Basaltic andesite enclave with phenocrysts of plagioclase and olivine (Ol) set in a glassy, diktytaxitic groundmass; (e) Type 3 plagioclase with weakly oscillatory zoning in NCH-31 and; (f) Orthopyroxene in NCH-37. (a), (b), (c), (e) and (f), BSE images taken with an electronic probe and (d) images from an optical microscope. Red circle: Anorthite and Mg# contents for plagioclase and orthopyroxene, respectively.

2.4.2 Petrography and mineral chemistry

Modal analyses for selected samples, many of which have been analyzed with microprobe, are given in Table 2.1. Mineral compositions are listed in Anexo 3. For the plagioclase, the anorthite content was calculated as the molar ratio Ca/(Ca+Na+K) and is reported as mol %. For the pyroxene and olivine, the Mg-number (Mg#) and the forsterite content (Fo), were calculated as the molar ratio Mg/(Mg+Fe) both being reported as a percentage.

Table 2.1. Mass fractions for representative NdCVC samples analyzed in this study. Abbreviations: Pl, Plagioclase; Cpx, Clinopyroxene; Opx, Orthopyroxene; Ol, Olivine; Ox: Fe-Ti oxides; Gms, Groundmass. The types of plagioclases are explained in the text.

Samples	SiO_2%**	Mass fraction (%)*						Plagioclase texture%		
		Pl	Cpx	Opx	Ol	Ox	Gms	Type 1	Type 2	Type 3
NCH-18	57.4	21.7	2.9	0.3	0.2	0.1	74.8	0	42	58
NCH-25	61.5	11.2	2.0	0.0	0.2	0.4	86.2	10	16	74
NCH-26	65.7	13.1	2.2	0.6	0.0	1.1	83.0	0	0	100
NCH-27	65.2	19.6	2.2	1.0	0.0	1.6	75.5	0	4	96
NCH-31	67.8	4.2	0.2	0.2	0.0	0.2	95.2	0	0	100
NCH-33	56.8	19.6	4.0	1.0	0.0	0.0	75.4	28	29	43
NCH-34	66.3	7.6	0.9	0.1	0.0	0.9	90.5	0	0	100
NCH-37	68.0	8.0	0.2	0.1	0.0	0.4	91.3	0	0	100
NCH-39	60.3	2.1	0.4	0.2	0.0	0.0	97.3	0	0	100
NCH-44	62.8	5.2	0.9	0.6	0.0	0.8	92.5	0	8	92
NCH-45	65.5	13.7	1.7	0.6	0.0	1.4	82.6	0	5	95
NCH-46	65.6	11.8	2.5	0.1	0.9	0.6	84.1	14	12	74
NCH-49	54.9	20.2	2.4	0.0	0.0	0.0	77.4	28	40	33
NCH-50	55.3	23.0	1.7	0.0	3.7	0.0	71.5	0	88	12
NCH-54	55.3	28.8	5.9	0.0	0.0	0.1	65.2	4	0	96
NCH-55	64.4	16.1	0.7	0.4	0.0	1.2	81.5	0	2	98
NCH-63	57.0	3.4	0.6	0.0	0.0	0.0	96.0	0	65	35

*Estimated from point counting data (1000 points per sample). Apatite was not considered, but their occurrence increases with differentiation. Trace amounts of sulfides are also observed

**Whole rock analyses.

Lavas and dykes analyzed have a phenocrysts content between 3 and 35 vol% (normalized to vesicle-free, Table 2.1). Often the phenocrysts are present as individual grains, but clusters of plagioclases and clots of plagioclases, pyroxenes and/or Fe-Ti oxides and/or apatite also are observed. The biggest crystals are usually included in crystal clots. The groundmass is commonly hypocrystalline and trachytic, to a lesser extent intersertal, and is generally composed of glass and crystals of plagioclases, pyroxenes and Fe-Ti oxides.

Plagioclase is the most abundant mineral phase in all samples (Table 2.1), either as individual grains or forming clots with other minerals. They are commonly euhedral to subhedral, presenting three main types of textures and in some cases all three types are observed in the same sample (Table 2.1): Type 1 with fine sieve or dusty texture, given by the intergrowth of plagioclase and glass mainly confined in the rims of the plagioclases (Fig. 2.5a); Type 2 usually larger crystals with coarse sieve texture given by large melts inclusions mainly in the core (Fig. 2.5b) and, usually accompanied of patchy and; Type 3 without melts inclusions. The latter is the most abundant, with no zoning or showing normal or reverse oscillatory zoning and, in some cases, dissolution/reabsorption textures (Fig. 2.5c). Type 1 textures reflect major dissolution boundaries of the resorbed plagioclase and are commonly attributed to episodes of magma mixing (e.g., Tsuchiyama, 1985; Tepley et al., 1999). Type 2 textures may occur by rapid decompression when the P (H_2O) of the system increases reducing the stability of plagioclase and causing dissolution (Nelson and Montana, 1992, Blundy and Cashman, 2001, Humphreys et al, 2006). In basaltic andesites and andesites the sizes of the phenocrysts of plagioclases range between 0.15 and 2.0 mm and have a compositional range in the core between An_{51-80} and in the rim of An_{43-67}. In dacites and rhyodacites the sizes range between 0.15-1.5 mm and the composition in the core ranges from An_{39-73} and the rim between An_{32-57}.

Pyroxenes are euhedral to subhedral and occur usually without zoning or with reverse and normal zoning, but some pyroxenes present patchy zoning texture in the whole crystal. Clinopyroxenes are the second most abundant mineral phase and are present in all samples analyzed (Table 2.1). The orthopyroxenes increase their proportion with the differentiation. In basaltic andesites and andesites the sizes of the

phenocrysts of pyroxenes range between 0.1 and 0.7 mm and have a compositional range in the core between $Mg\#_{72-81}$ and in the rim of $Mg\#_{68-76.}$ Orthopyroxenes (0.05-0.6 mm in size) are unzoned or with a magnesium-rich rim and the core composition ranges between $Mg\#_{68-73}$ and the rim between $Mg\#_{66-75}$. In dacites and rhyodacites the clinopyroxenes the sizes range between 0.1-0.6 mm and the core ranges between $Mg\#_{65-81}$ and the rim between $Mg\#_{62-78}$ and the orthopyroxenes (0.1-0.7 mm in sizes) range between $Mg\#_{58-70}$ in the core and between $Mg\#_{56-74}$ in the rim.

Olivines are usually found in the less differentiated rocks and mafic enclaves. Olivine phenocrystals (2-3 mm in size) occur as individual and rounded grains, unzoned and in some cases, with a rim of low Ca-pyroxenes. In NCH-18 two grains have Fo_{67-71} in the rim. In mafic enclaves (e.g., NCH-60), individual olivines grains are accompanied of phenocrysts of plagioclases, clinopyroxenes and orthopyroxenes set in a glassy, diktytaxitic groundmass (Fig. 2.5d). An individual olivine grain analyzed in a mafic enclave is zoned with Mg-rich core (Fo_{84}) and more iron-rich rim (Fo_{77}). Some lavas (e.g., NCH-46, NCH-25, NCH-34) contain mafic enclaves reaching 30 cm in diameter and rounded grains of olivine crystals are also observed in the dacitic part of these lavas, possibly due to disaggregation (e.g., Zellmer and Turner, 2007; Ruprecht et al., 2020).

Fe-Ti oxides occur as small individual grains mainly in the groundmass or as inclusions within pyroxene and some plagioclase phenocrysts and increase their proportions with the differentiation. In NCH-31 small euhedral crystals of titanomagnetite range from Ulv_{50-54} and ilmenite from $Ilm_{89-91.}$ Euhedral apatite occurs as small individual grains or as inclusions in plagioclases and pyroxenes and their proportion increase with the differentiation. Some small crystals of sulfides are found as inclusions in pyroxenes.

The mineral-melt equilibrium equations used for estimations of pressure and temperature of crystallization, consider the whole-rock composition as representative of the melt, only when the content of crystals is ca. <10 vol%. Samples that show clear textural or compositional evidence of magma mixing (e.g., Type 1 plagioclase, presence of mafic enclaves or that fall into the hypothetical mixing trend; Fig. 2.3)

were also discarded, because the composition of the whole-rock might not be representative of the melt in which the crystal grew.

Along with the general features described above, we use selected samples to show in detail textures and mineral compositions that support the extensive use of thermobarometers. Those samples were selected because they represent dominant lithologies recognized in the most conspicuous eruptive units, they are crystal-poor, without clear textural or compositional evidence of magma mixing and they have unzoned or weakly zoned crystals.

NCH-31 (LTd, 67.8 wt% SiO_2)

This sample has a phenocryst content of 4.8 vol% (normalized to vesicle-free, Table 2.1). Phenocrysts of plagioclase and orthopyroxene predominate as individual grains, but clots of plagioclase, pyroxene, Fe-Ti oxide and apatite also are observed. Fe-Ti oxides (titanomagnetite > ilmenite) and apatite also occur as small individual grains mainly in the groundmass and as inclusions within pyroxene and plagioclase phenocrysts. The predominant texture of the groundmass is intersertal trachytic with plagioclase microlites, pyroxenes and Fe-Ti oxides. Only Type 3 plagioclases are present and eight individual grains were analyzed. The sizes of the euhedral to subhedral plagioclases range between 0.2 and 0.4 mm and they are relatively homogeneous in composition from core to rim with weakly oscillatory zoning (Fig. 2.5e). The oscillatory zoning in Type 3 plagioclases, without reabsorption and with fine banding, may be largely kinetically controlled (e.g., Ginibre et al., 2002a; Humphreys et al, 2006). Plagioclase composition core ranges between An_{39-44}, except for a grain with core An_{50}, and the rim ranges between An_{39-43}. Two euhedral to subhedral clinopyroxenes analyzed have sizes of 0.1 mm and they are unzoned and weakly zoned. The composition in the core is $Mg\#_{66}$ and the rim ranges between $Mg\#_{65-66}$. Ten euhedral to subhedral orthopyroxenes analyzed have sizes between 0.05-0.2 mm and show subtle normal zoning. The core ranges between $Mg\#_{60-65}$, except for a grain with core $Mg\#_{70}$ and, the rim between $Mg\#_{58-62}$. Small euhedral crystals of titanomagnetite and ilmenite range from Ulv_{50-54} and from $Ilm_{89-91,}$ respectively.

NCH-37 (LTpp, 68.0 wt% SiO_2)

This sample has a phenocryst content of 8.7 vol% (normalized to vesicle-free, Table 2.1). The mineral phases and their occurrence are the same as in NCH-31 (Table 2.1), but with a higher proportion of plagioclase and Fe-Ti oxides (titanomagnetite > ilmenite). Clinopyroxenes usually occur in clots with plagioclases, orthopyroxenes, Fe-Ti oxides and apatite. The predominant texture of the groundmass is intersertal trachityc with plagioclase microlites, pyroxenes and Fe-Ti oxides. As in NCH-31, Only Type 3 plagioclases are present and six individual grains were analyzed. The plagioclases are euhedral to subhedral and their sizes range between 0.2 and 0.4 mm and they are relatively homogeneous in composition from core to rim con weakly oscillatory zoning. Plagioclase composition core ranges between An_{39-42}, except for a grain with core An_{51}, and the rim between An_{37-40}. One subhedral clinopyroxene analyzed has size of 0.3 mm and it is weakly zoned. The core ranges between $Mg\#_{66-67}$, and the rim has $Mg\#_{65}$. Six euhedral to subhedral orthopyroxenes analyzed have sizes between 0.1-0.3 mm and show subtle normal zoning (Fig. 2.5f). The core composition ranges between $Mg\#_{58-61}$ and the rim between $Mg\#_{56-60}$.

NCH-44 (CBg, 62.8 wt% SiO_2)

This sample has a phenocryst content of 7.5 vol% (normalized to vesicle-free, Table 2.1). Pyroxenes and plagioclases are usually euhedral to subhedral and occur as individual grains or in clots, often with titanomagnetite. Titanomagnetite also occurs as small individual grains mainly in the groundmass and as inclusions within pyroxene and plagioclase phenocrysts and in clots with those minerals. The predominant textures of the groundmass are hypocrystalline to trachytic with plagioclase microlites, pyroxenes and titanomagnetite. Type 3 plagioclases predominate (0.15-0.8 mm in size) with weakly oscillatory zoning in the whole crystal with a decrease of anorthite from core to rim. The composition of the plagioclases range in the core between An_{49-51} and the rim between An_{42-50}. The lowest values of anorthite were measured in the outermost part of the crystal and in some cases coincides with an increase in Fe/Al, which suggests oxidation as a result of degassing

of H_2O during decompression (Humphreys et al., 2006). Nine clinopyroxenes analyzed have sizes between 0.2-0.4 mm and they are generally unzoned or with subtle normal zoning, without major textural and compositional differences between phenocryst as individual grains or in the clots. The core ranges between $Mg\#_{73-74}$, and the rim between $Mg\#_{70-73}$. Nine orthopyroxenes analyzed have sizes between 0.1-0.4 mm and they are unzoned. The core and rim range between $Mg\#_{70-73}$.

2.4.3 Water content

To constrain the water content on select samples for thermobarometric calculations, we used the plagioclase-melt hygrometer of Waters and Lange (2015), with a standard error of estimate (SEE) ± 0.35 wt% H_2O. This hygrometer requires an estimate of the crystallization pressure but is relatively insensitive to this parameter. Over the range of 100–900 MPa, the calculated water content varies by only 0.15 wt%. Therefore, calculations were made at a constant pressure of 3 kbar. This hygrometer also requires as input a value of the melt temperature. The temperature used in these calculations correspond to the lowest estimated temperature for clinopyroxenes with a thermobarometer independent of the water content (Putirka, 2003 in Putirka, 2008) for each sample (Table 2.2). In the case of the NCH-31 sample this temperature estimate is in agreement with the temperature calculated with Fe-Ti oxides (three pairs). Compositions of Fe–Ti oxide pairs that passed the Mg-Mn equilibrium test by Bacon and Hirschmann (1988) were used to estimate temperatures according to the method outlined in Ghiorso and Evans (2008). With these temperature values the estimated water content for NCH-31 is 3.0 wt%, NCH-37 of 3.1 wt% and 2.2 wt% for NCH-44, respectively. These water contents are lower than the values estimated with experimental and petrological studies in dacitic lavas of volcanic centers near the NdCVC. In Quizapu volcano these values are in the range 4-6 wt% (Ruprecht et al., 2012) and between 4.5-5.5 wt% at the San Pedro volcano (Costa et al., 2004), in which hydrated minerals such as amphibole are part of the mineral assemblage of these lavas. The absence of amphibole in NdCVC lavas would support lower water content estimates (e.g., Andújar et al., 2015; Sisson & Grove, 1993).

2.4.4 Thermobarometry

In order to understand the configuration of the NdCVC plumbing system, we use selected samples to estimate the pressure and temperature of crystallization for the main mineral phases following Putirka (2008), which uses mineral-melt equilibrium equations. We consider in this study the whole-rock composition as representative of the melt assemblages for whole-rock–phenocryst rims (we only consider individual grains) when the content of crystals is <10 vol%.

Assessment of the mineral-melt equilibrium was carried out using the spreadsheet provided by Putirka (2008). In the case of clinopyroxenes and orthopyroxenes, the equilibrium was tested on the basis of the Fe/Mg partitioning between the melt (whole-rock) and mineral. To visualize this equilibrium test, the Rhodes diagram (Rhodes et al., 1979; Putirka, 2008) was used, where the Mg# of clinopyroxene is plotted versus the Mg# of whole-rock (Fig. 2.6a; Kd [Fe-Mg] = 0.27 ± 0.8). For orthopyroxenes (Fig. 2.6b; Kd [Fe-Mg] = 0.29 ± 0.6), we estimated the ratio Fe^{2+}/Fe_t in the melt. To obtain this value, we used the ratios between both oxides, for different volcanic rocks, proposed by Middlemost (1989). For plagioclase, the Kd [Ab-An] equilibrium test was used, based on the exchange of An-Ab between the melt/whole-rock and the mineral (Fig. 2.6c). To validate the equilibrium, this value of Kd [Ab-An] must be between 0.11 ± 0.5 for Tº <1050°C and between 0.27 ± 0.11 for Tº >1050°C (Putirka, 2008).

Thermobarometric equations were only applied to the mineral phases that passed the equilibrium test. For clinopyroxenes the temperature was estimated as in Purtirka (2003, in Putirka, 2008), with a standard error of estimate (SEE) ± 59°C and the pressure with clinopyroxene barometer for hydrous compositions (equation-30; Putirka, 2008). This model is based on the jadeite-diopside/hedenbergite exchange between clinopyroxene and the associated melt and allows the determination of pressure with SEE ± 1.6 kbar. This would produce the most accurate result of all clinopyroxene barometers available (Mollo et al., 2010). For orthopyroxenes we used the thermometer of equation-28a (Putirka, 2008), with SEE ± 28°C and the orthopyroxene barometer for hydrous compositions (equation-29b; Putirka, 2008) with

SEE ± 2.1 kbar for hydrous systems. For plagioclases we used the model calibrated for hydrous systems that estimates pressure with SEE ± 2.47 kbar (equation-25a; Putirka, 2008) and temperature with SEE ± 36°C (equation 24a; Putirka, 2008). All these P-T estimates were made fixing the water content through iterative calculations.

In order to increase the dataset, we applied the thermobarometers to additional mineral phases of four crystal-poor NdCVC lavas (ca. <10 vol% in phenocrystal content; Table 2.2) with geochemical data available from the literature (Murphy, 1995). These samples have textural information showing absence or no compositional evidence of magma mixing with relatively homogeneous composition of the phenocrysts in the core and rims. The results show P-T undistinguishable from those yielded by the selected ones. In addition, we include P-T estimates for mineral phases included in a crystal-poor dike (NCH-63; Table 2.2) and also for clinopyroxene-glass in equilibrium included in a pyroclastic sample (NCH-53). Samples used in the thermobarometric calculations are listed in Table 2.2, together with the SiO_2 wt%, crystal content and the temperature used for water content estimations for each one. Our analysis encompasses from basaltic andesitic to rhyodacitic compositions, Late Pleistocene to Holocene in age and thus we extrapolate the results to entire lifespan of this volcanic complex.

For clinopyroxenes, calculated P-T range from 918 to 1130ºC and 0.6 to 4.6 kbar. For orthopyroxene the calculated P-T range from 934 to 1069ºC and 3.0 to 5.4 kbar and for plagioclase these values are between 913 and 1088ºC and from 1.2 to 3.9 kbar. In figure 2.7, the calculated P-T values for orthopyroxene, plagioclase and clinopyroxene are plotted together. In addition, with the pressure values and using a density of 2.7 g / cm³ for the upper crust in this area (Tassara et al., 2006), we estimated the crystallization depth of different mineral phases. In general, the lower crystallization pressures are obtained in mineral phases included in dacites and rhyodacites.

Crystallization pressures of the orthopyroxenes included in dacites and rhyodacites could be overrated. We assume this because plagioclase/orthopyroxene pairs coexist across a wide range of natural melts and should continuously evolve under similar pressure-temperature conditions (Almeev et al., 2013). This is not

observed in these samples despite the fact that clinopyroxene, orthopyroxene and plagioclase form crystal clots suggesting that these minerals probably formed simultaneously. On the other hand, the crystallization temperatures calculated for orthopyroxenes, plagioclases and clinopyroxenes are close, since the orthopyroxene-melt thermometer (equation-28a; Putirka, 2008) has a range of applicability that includes these compositions of the melt. Instead, the differences between the pressures of orthopyroxene with the other mineral phases in the dacites and rhyodacites could be due to the fact that, for certain compositions, the orthopyroxene geobarometers presented in Putirka (2008) might not work well, because they have been calibrated using mainly mafic to ultramafic compositions. Histograms for all data and separated by host rock compositions are presented in figure 2.8, in which the crystallization pressures of orthopyroxenes in dacites and rhyolites and the SEE of thermobarometric calculations are not consider. For all data the depth spans from 2.2 to 16.9 km, with basaltic andesites/andesites from 7.7 to 16.9 km and, dacites/rhyodacites from 2.2 to 9.7 km. These results suggest a vertical compositional zoning in the NdCVC plumbing system.

Table 2.2. Samples used in thermobarometric calculations

Samples*	**Unit**	**SiO2 wt%**	**Crystal content (%)****	**Temperature (ºC)*****	Average (SEE ± 0.35 wt% H_2O)******
NCH-31	LTd	67.8	5	930 -931	3.0
NCH-37	LTpp	68.0	9	920	3.1
NCH-44	CBg	62.8	7	1012	2.2
NCH-53	P. Cone	56.1	-	-	-
NCH-63	Dyke	57.9	4	1075	2.2
C11	CBcpb	63.0	11	1033	1.9
C29	CBgb	60.2	3	1065	1.7
C44	Pll	58.2	5	1077	1.9
C52	LTv	69.5	11	905	3.3

*Samples identified with the prefix C data taken from Murphy (1995)

** Normalized to vesicle-free

*** The temperature corresponds to the lowest temperature for clinopyroxenes estimated with a thermobarometer independent of the water content (Putirka, 2003 in Putirka, 2008). In NCH-31 the estimated temperature according to the method outlined in Ghiorso and Evans, 2008 with pairs of Fe-Ti oxides in equilibrium is also shown.

**** Calculated H_2O (wt%) contents using the plagioclase-melt hygrometer proposed by Waters and Lange (2015). Average of the estimates in rim-whole rock pairs. For NCH-53 we used 2.2 H_2O wt%, because plagioclase analysis was not performed in this sample

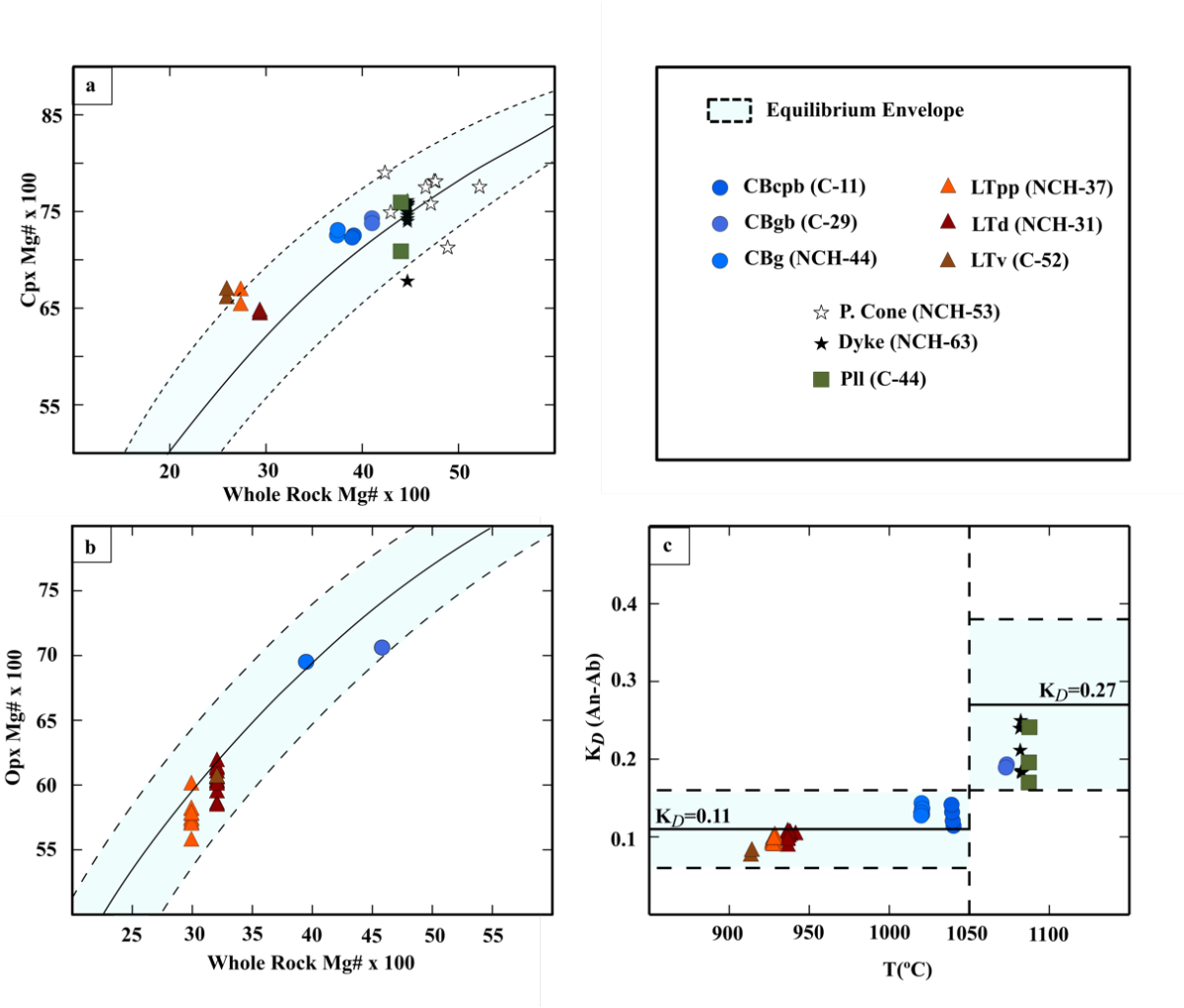

Figure 2.6. Mineral-melt equilibrium. Light blue zone shows the equilibrium area for the different minerals. (a) Rhodes diagram to evaluate the equilibrium of clinopyroxenes, Mg# of whole-rock vs Mg# of clinopyroxene. The equilibrium envelope is given by Kd [Fe-Mg] = 0.28±0.8; (b) Rhodes diagram to evaluate the equilibrium of orthopyroxenes, Mg# of whole-rock vs Mg# of orthopyroxenes. The equilibrium envelope is given by Kd [Fe-Mg] = 0.29±0.6; (c) Plagioclase equilibrium test. For Tº <1050°C the equilibrium area is given by Kd [An-Ab] = 0.11±0.5 and for Tº >1050ºC the equilibrium envelope is given by Kd [An-Ab] = 0.27±0.11. The Kd ranges between minerals and melt (in this case the whole-rock) are taken from Putirka, 2008.

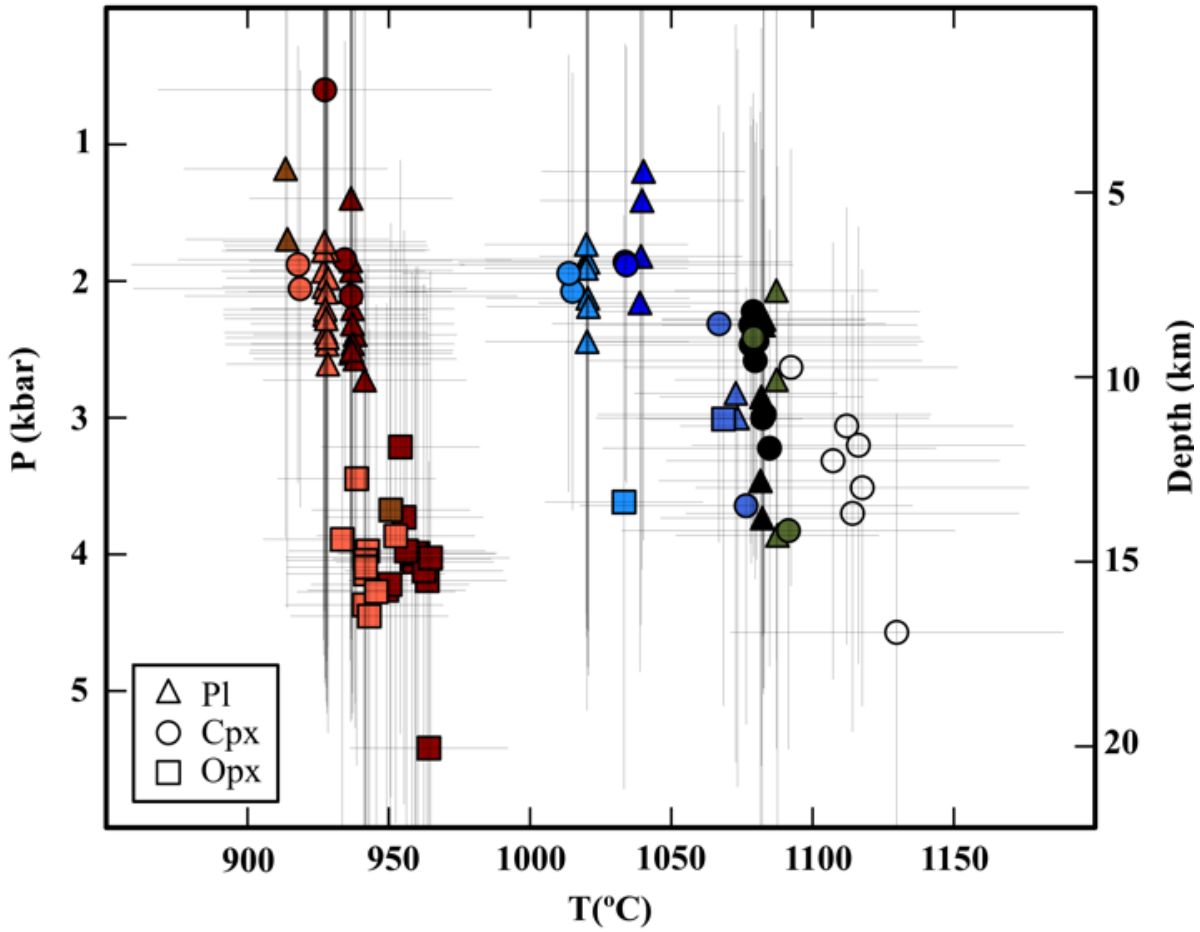

Figure 2.7. P-T-Depth diagram. Results for clinopyroxene thermobarometer (Putirka, 2008) with the temperature estimated from Putirka (2003, in Putirka, 2008) and standard error of estimate (SEE) ± 59°C and pressure (Cpx Eq.30; Putirka, 2008) with SEE ± 1.6 kbar; for plagioclase thermobarometer (Pl Eq.25a SEE ± 2.47 kbar, equation 24a SEE ± 36ºC; Putirka, 2008), and orthopyroxene thermobarometer (Opx Eq.29b SEE ± 2.1 kbar, equation 28a SEE ± 28ºC; Putirka, 2008). The depth was estimated with a crustal density of 2.7 g/cm³. Symbols as in figure 2.6.

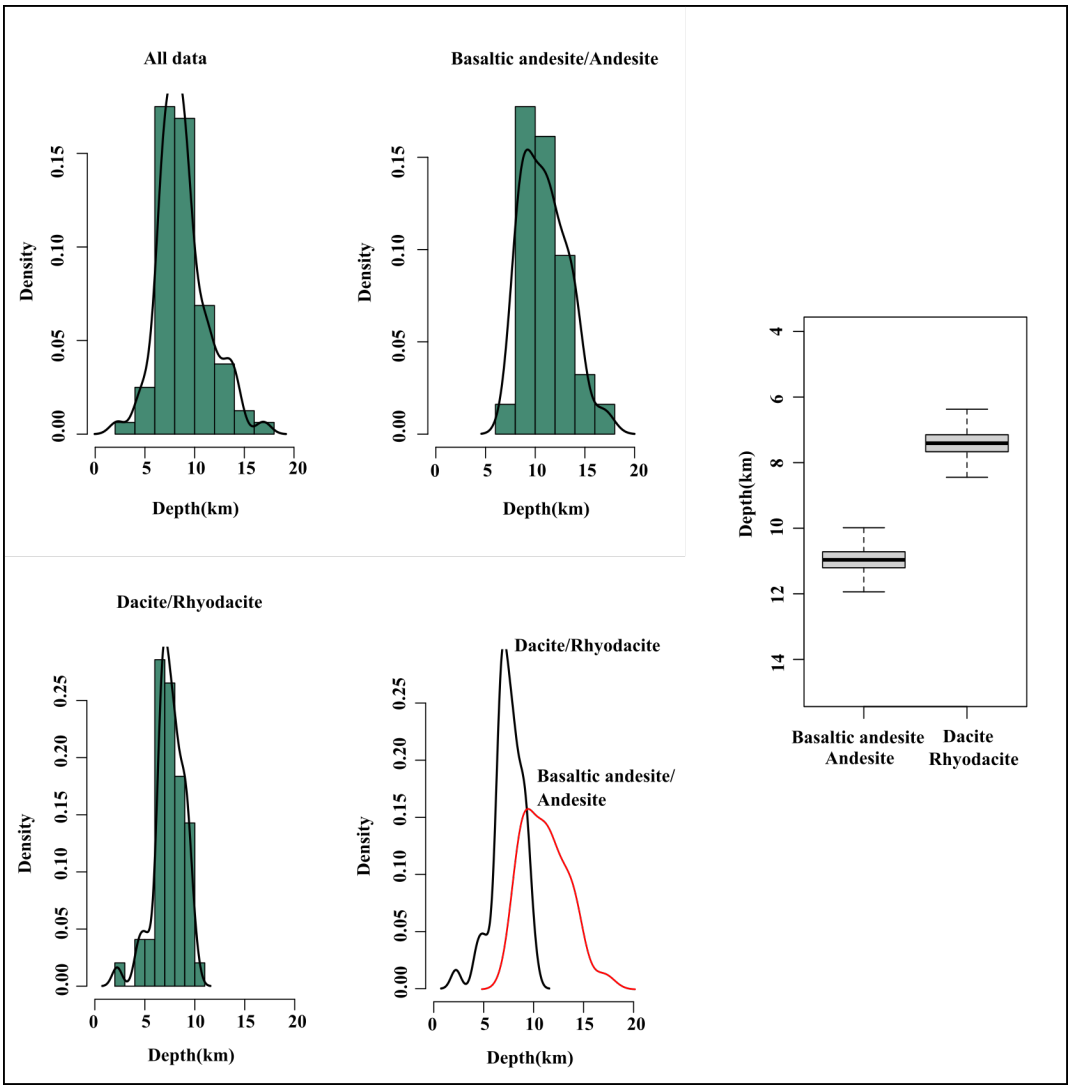

Figure 2.8. Histograms and boxplot. Histograms with the depth of crystallization for different host rock compositions (density curve with black line) and Boxplot (Confidence Interval: 95%; center line, median; box limits, upper and lower quartiles; whiskers, 1.5 times interquartile range) with the mean of the most probable crystallization depths according to host rock composition.

In order to consider the SEE of the different geobarometers, the data obtained from crystallization pressures (Fig. 2.8) were treated by means of a Bayesian bootstrap analysis (details in Rubin, 1981). This analysis yielded the most probable value of the mean pressure/depth within a 95% confidence interval. Bayesian bootstraps used the RStudio (Rstudio Team, 2020) and the bayesboot package

(v0.2.2; Bååth, 2018). Before applying this analysis and due to the limited number of samples, we simulate 50 samples of 1000 data each, with a normal distribution, with the arithmetic mean of our depth and with the SEE from the used geobarometers. After that, the Bayesian bootstrap analysis was performed, where a resampling with 4000 points was carried out for each of the 50 simulated samples. Results for the most probable mean crystallization depth within the 95% confidence for mineral phases included in dacites/rhyodacites ranges from 6.2 to 8.5 km below the Earth surface, and for basaltic andesites/andesites between 9.9 and 11.9 km (Boxplot in Fig. 2.8).

This statistical analysis would confirm a compositional zonation of the plumbing system, at least in the Cerro Blanco edifice. In Las Termas edifice, field-based evidence as to the presence of basaltic andesitic enclaves in some dacites and rhyodacites, suggest a similar configuration of the plumbing system. On the other hand, P-T estimates of pre-caldera lavas (C-44, PII) and a dyke that cuts this unit (NCH-63) suggests that at least the deepest determined level of the plumbing system has been stable since Late Pleistocene.

2.5 Discussion

2.5.1 Vertical zonation of the plumbing system

Within uncertainties, pressure estimations unravel a plumbing system that extends vertically from 2.2 to 16.9 km below the Nevados de Chillán Volcanic Complex. However, as the crystallization depth of 2.2 km is obtained from a single crystal, this could indicate crystallization during the ascent of the magma towards the surface. This plumbing system seems to be compositionally zoned in the vertical dimension, as also observed for other volcanic systems of the SVZ (e.g., Gilbert et al., 2012; Ruprecht et al., 2012) and elsewhere (e.g., Samaniego et al., 2020; Giacomoni et al., 2016). This zonation is consistent with the most accepted view that more evolved magmas, when structurally trapped at upper crustal levels, would act as density filters for less evolved magmas reaching from deeper levels of the crust (e.g., Eichelberger, 2010).

2.5.2 Relating the plumbing system with crustal discontinuities

Factors controlling magma storage at depth are multiple and their interplay is still controversial (e.g., Valentine and Krogh, 2006; Kavanagh et al., 2006; Menand, 2008). Density contrast between the uprising magmas and continental crust is an important factor producing large scale filters (Eichelberger, 2010), which is in turn modulated by the local stress regime (e.g., Gudmunsson, 2011; Sparks and Cashman, 2017) and the internal stratification of the plumbing system. We use the figure 2.9 to show the possible role played by the crustal architecture underneath NdCVC in controlling the observed vertical zonation of the plumbing system. We explore in figure 2.9 the relationship between our estimated crystallization depths and the geophysically-constrained structure of the subduction zone at the latitude of NdCVC. Particularly, figure 2.9a is an EW cross-section at 36.85ºS showing the geometries of four major discontinuities (slab upper surface, lithosphere-astenosphere boundary (LAB), Moho and intracrustal density discontinuity (ICD)) extracted from the 3D model of Tassara and Echaurren (2012). This is a continental-scale representation of the mass distribution underneath the Andean margin that was created performing a forward modeling of gravity anomalies and using different sources of seismic data as constraint (Tassara et al., 2006; Tassara and Echaurren, 2012). Also shown are contours of the Vs seismic noise model of Gonzalez-Vidal et al. (2018) that are expressed as the variation of Vs with respect to its absolute mean value at a given depth (dVs/Vs x 100%).

Outside the volcanic arc region, we note a general coincidence between the contour line for dVs/Vs=-3% and the depth of the ICD, which separates the light (density r=2.7 g/cm^3) upper crust from a dense (r=3.1 g/cm^3) lower crust. This demonstrates that both independently obtained geophysical images are tied to the underlying crustal structure, with the ICD reflecting the structural contact between crustal layers. The mid-lower crust beneath the volcanic arc is characterized by an anomalously low Vs region, pointing to high temperatures probably related to a vertical transport of magma from a MASH zone (melting, assimilation, storage and homogenization). Figure 2.9b represents the plumbing system below NdCVC over a lithosphere marked by four discontinuities modeled by Tassara and Echaurren (2012)

and the crystallization depths that we estimated for the two different compositional ranges in figure 2.8. Unlike rhyodacites, basaltic andesites are not emitted from the main edifice, therefore, for these compositions, the height of the volcanic edifice is not considered in the crystallization depth estimates. The most important feature of this scheme is that magmas transported from the MASH zone throughout the mid-lower crust are accumulated underneath the ICD, where they partially differentiated to produce a basaltic andesitic and andesitic magmas. The further differentiation of this magma by fractional crystallization generates a lighter melt that ascend above the ICD and then produces the more evolved dacitic/rhyodacitic magma characterizing the upper level of the system. Thus, the ICD seems to represent a fundamental discontinuity of the plumbing system, separating a deep intermediate-to-basic reservoir from an evolved zone.

Figure 2.9c compares the NdCVC lithospheric column and magmatic plumbing system with the structure and crystallization depths proposed for other volcanic systems of the SVZ that have been studied with similar petrological techniques (e.g., Costa et al., 2004; Gilbert et al., 2012; Ruprecht et al., 2012; Castro et al., 2013; Morgado et al., 2019; Vander Auwera et al., 2019). Latitudinal variations in the depth to the LAB and Moho reflects first-order differences in the deep crustal and lithospheric structure along the SVZ, which has been shown as an influence in the nature of primitive magmas reaching the MASH zone (e.g., Hildreth and Moorbath, 1988; Voelker et al., 2011). Despite the differences and spatial variations of the ICD that are likely related to differences in the geologically-controlled upper crustal structure (Tassara et al., 2006), we note that all the compared volcanic systems developed a vertical zonation that is similar to NdCVC in that evolved and mafic compositions seem to be separated by the ICD. Indeed, all the estimated depths for the crystallization of intermediate-to-evolved magmas lies above the local ICD, whereas the roof of the depth ranges where intermediate-to-mafic magmas crystallize approach this intracrustal discontinuity.

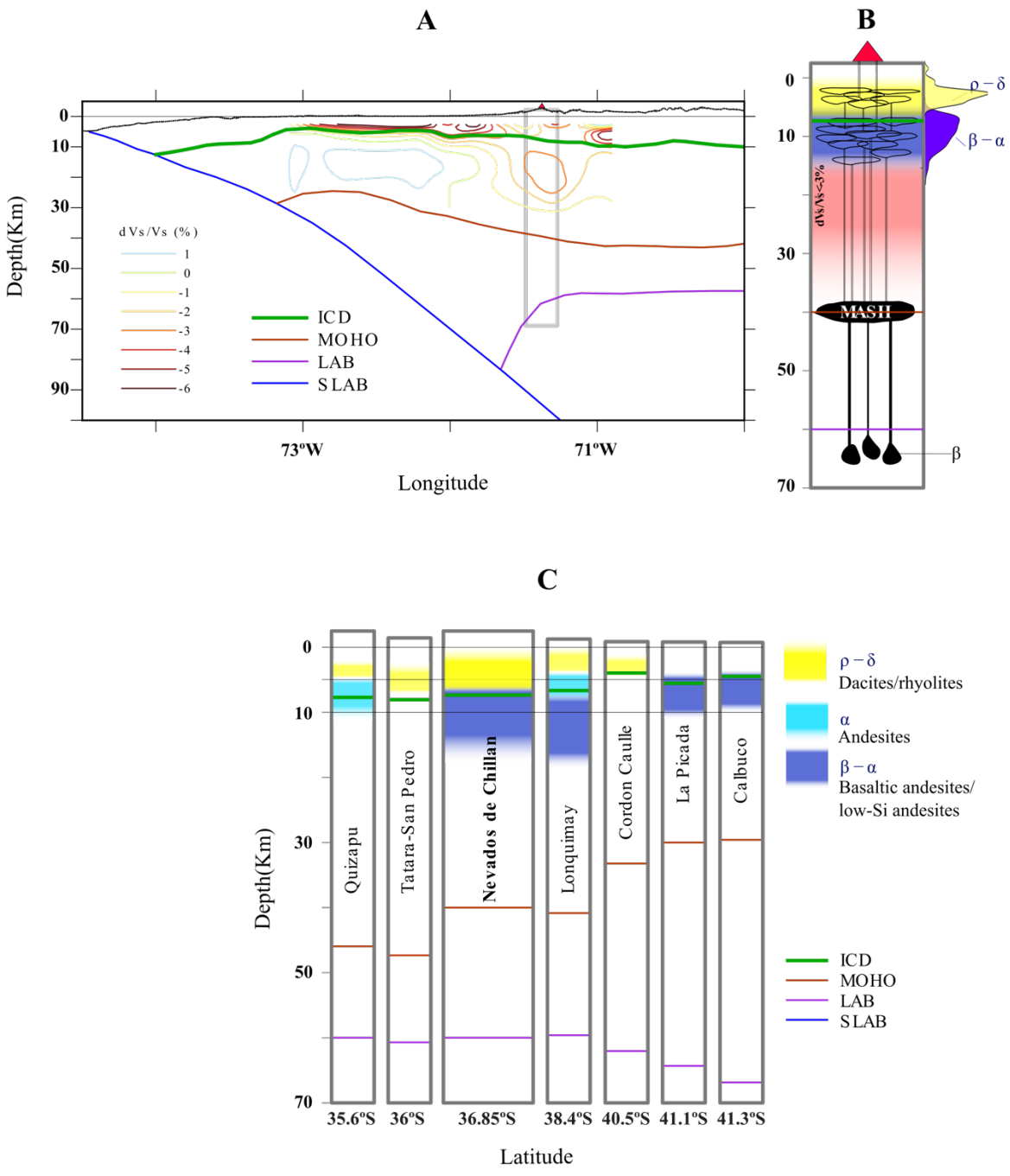

Figure 2.9. A) Lithospheric-scale structure of the Andean subduction zone at the latitude of NdCVC (36.85ºS) as derived from the model of Tassara and Echaurren (2012). This model defines the geometries (depth w/r to sea level) of the subducted slab upper surface (SLAB), lithosphere-asthenosphere boundary (LAB), crust-mantle boundary (MOHO) and intracrustal Conrad discontinuity (ICD). Colored contours are

extracted from the ambient seismic noise model of González-Vidal et al. (2018) and show lines of equal Vs anomaly (dVs) as expressed in percentage with respect to the average value of Vs at a given depth range. The position of NdCVC is marked with a red triangle on top of the topographic profile. B) Representative lithospheric column below NdCVC highlighting the main structural features extracted from A and our estimated ranges of crystallization depths for dacites/rhyodacites (r-d) and basaltic andesites-andesites (b-a), as informed in figure 2.8 (depth w/r to Earth surface, right-hand side of the column). We draw here a schematic representation of the magmatic plumbing system that includes a region of asthenospheric partial melting below the LAB where primitive basalts (b) are created; a MASH zone at the MOHO where these basalts are trapped; dikes transporting basalts homogenized in this zone to a mid-crust reservoir formed by coalescent sills below the ICD where basaltic-andesitic magmas crystalize and differentiates forming more evolved magmas that ascent by dikes to an upper crustal reservoir located above the ICD C) Comparison between the lithospheric structure (Tassara and Echaurren, 2012) and compositional zonation of magmatic plumbing systems underneath several volcanoes of the Southern Volcanic Zone where petrological studies similar to our approach have been published.

2.6 Conclusions

Our thermobarometric results suggest that the NdCVC plumbing system extends vertically from 2.2 to 16.9 km. This architecture would have persisted over time without significant variations in the crystallization depth range throughout the Late Pleistocene-Holocene evolution of NdCVC, at least in terms of the lowest boundary. The depth of crystallization for mineral phases included in basaltic andesites/andesites extends beneath the intracrustal Conrad discontinuity in this area while evolved magmas migrate and store above this level, which depicts a compositionally zoned plumbing system. Our results highlight the first-order role that crustal geological discontinuities may play in the long-term configuration of a plumbing system.

2.7 Acknowledgements

The authors grateful to Laura Hernández (GEA, Universidad de Concepción, Chile) who provided effective assistance in EPMA. The use of the EPMA facility at the Department of Earth Science, Rice University, Houston, TX is kindly acknowledged. We thank Francisco Ríos for assisting with the statistical analysis and to Nicolás Luengo for providing us with the sample NCH-55. We also thank Dr. Heidi Wehrmann for the use of chemical data (clinopyroxene and glass included in tephra samples) obtained at the Universidad de Concepción summer school (2017). We thank to both anonymous reviewers for their criticism that certainly improved the manuscript.

CAPÍTULO III: THE EFFECTS OF THE TEMPORAL/SPATIAL EVOLUTION OF THE MAGMATIC SYSTEM IN THE UPPER CRUST ON MAGMATIC EVOLUTION

Artículo sometido a revision a Journal of Petrology el día 02 de diciembre de 2022.

Andrés Oyarzún[1,*], Luis E. Lara[2, 3], Andrés Tassara[1, 4]

[1]Departamento de Ciencias de la Tierra, Universidad de Concepción, Victor Lamas 1290, Concepción, Chile

[2]Servicio Nacional de Geología y Minería, Avenida Santa María 0104, Santiago, Chile.

[3]Research Center for Integrated Disaster Risk Management (CIGIDEN), Avenida Vicuña Mackenna 4860, Santiago, Chile

[4] Millennium Nucleus The Seismic Cycle along Subduction Zones (CYCLO)

*Corresponding author. E-mail: aoyarzun@udec.cl

Abstract

Understanding the behavior of volcanoes is one of the great challenges of volcanology, since it would allow more reliable forecasts and estimates of the magnitude of their eruptions, mitigating the risk. Volcanoes are an expression of their underlying magmatic system; therefore, the eruptive modalities of volcanoes and the geochemistry of their products will depend on the inner workings of their magmatic system, which undergoes changes over the long-life span of volcanoes. This seems to be the case of the Nevados de Chillán volcanic complex (NdC), because a change in the compositional trend occurred during the post-LGM (Last Glacial Maximum), focused on the area where historical activity is concentrated, with a shift from bimodal compositions at the beginning to a predominance of intermediate compositions in the most recent events. In this way, the NdC is presented as a good case study to identify the main factors that control its magmatic evolution, key to having more reliable eruptive forecasts.

We determined, based on new textural and mineral chemistry data, that the dacites emitted in the historical eruptions of the NdC were generated by magma mixing. Based on the analyzes carried out in this study and with the information available in the literature, a mechanism is proposed to explain the magmatic evolution of the NdC during the Holocene, which gives rise to a predominance of intermediate compositions in the youngest eruptive products. Crustal anisotropies enhanced by locally compressive tectonic regime hinder the ascent of poorly evolved magmas, building a storage zone under the Intracrustal Density Discontinuity (ICD). Some of these magmas are emitted on the surface when they manage to overcome these crustal barriers, while another portion of these magmas are stored in the upper crust, where they are differentiated by fractional crystallization. The resulting more differentiated magmas, stored in the upper crust, would act as a density filter for less evolved magmas generating intermediate compositions by magma mixing processes. The less evolved magmas would be emitted only when they do not intercept the more differentiated magmas stored in the upper level. The latter was possible in the early post-LGM stage, when this storage level with evolved magmas has not yet been established, or after that when they do not intersect with them during their rise, due to a decrease of its lateral extent.

We propose that the temporal/spatial evolution of the upper part of the NdC magmatic system, expressed in the establishment of a storage level with differentiated magmas and in its variations in volume, conditions the NdC magmatic evolution. This type of temporal/spatial evolution of the magmatic system may be playing a relevant role in the predominance of intermediate compositions in continental arc systems. Finally, a better understanding of the temporal evolution of magmatic systems could shed light on the present behavior of volcanoes, a key for reliable eruptive forecast.

3.1 Introduction

Volcanic eruptions can generate serious socioeconomic damage in communities, which can be mitigated to a large extent if the behavior and evolution of the volcano is known, key to having reliable eruptive forecasts and estimates of their magnitudes. Because volcanoes are an expression of their underlying magmatic system (Cashman et al., 2017), the eruptive modalities of volcanoes and the geochemistry of their products will depend on the inner workings of their magmatic system (Caricchi & Blundy, 2015; Burchardt, 2018). These magmatic systems undergo changes over the long-life span of polygenetic volcanoes and magmatic provinces (Bouvet de Maisonneuve et al. 2021). These can be, variations of the chemical and physical properties of magma as it rises through the crust, in the flow of magma between the different portions of this plumbing system (Caricchi & Blundy, 2015) or in other cases, an alternation between the absence or presence of the shallowest portions of a plumbing system (Weber et al., 2019), which represents a density barrier to the ascent of deeply sourced magma (Lucci et al., 2020). In this way, this temporal and spatial evolution of the magmatic system affects the behavior of a volcano and the geochemistry of their products (e.g, Gilbert et al., 2014). This seems to be the case of the Nevados de Chillán volcanic complex (NdC), because a change in the compositional trend occurred during the post-LGM (Last Glacial Maximum) focused on the area where historical activity is concentrated, with a shift from bimodal compositions at the beginning to a predominance of intermediate compositions in the most recent events (Oyarzún et al., 2022). In this way, the NdC is presented as a good case study to identify the main factors that control its magmatic evolution.

To carry out this research, this study presents new textural and mineral chemistry data of the most recent dacites emitted by the NdC, which includes the ongoing eruption that lasted between January 2016 (Mousallam et al., 2018; Benet et al. al., 2021; Cardona et al., 2021) and January 2023 (www.sernageomin.cl). These new antecedents, together with the data published in the literature, evaluate the petrogenesis of these dacites and the eruptive products previously emitted by the NdC, which allows us to discuss the Holocene magmatic evolution of the NdC.

Finally, with the estimation of the volumes of lavas emitted during the Holocene presented in this study, together with the configuration of its magmatic system proposed in previous studies, we discuss the effects that temporal/spatial changes of the NdC magmatic system have on its magmatic evolution.

3.2 Geological background

The Southern Andean Volcanic Zone (SVZ), which extends from 33.5° to 46.5° S and results from subduction of the oceanic Nazca plate under the South American plate, it has been divided into four subsegments (López-Escobar et al., 1995) according to some salient geological features: NSVZ (northern; 33º - 34.5º S); TSVZ (transitional; 34.5º - 37º S); CSVZ (central; 37º - 42º S) and SSVZ (southern; 42º - 46º S). Nevados de Chillán Volcanic Complex (NdC; 36°50' S/ 71°23' W) is located in the TSVZ, is ca. 16 km long and is composed of two main volcanic edifices (Cerro Blanco and Las Termas edifices; Fig. 3.1) that host 13 eruptive centers forming a NW-striking alignment atop of a transversal Andean basement structure (e.g., Stanton-Yonge et al., 2016; Gonzalez-Vidal et al., 2018).

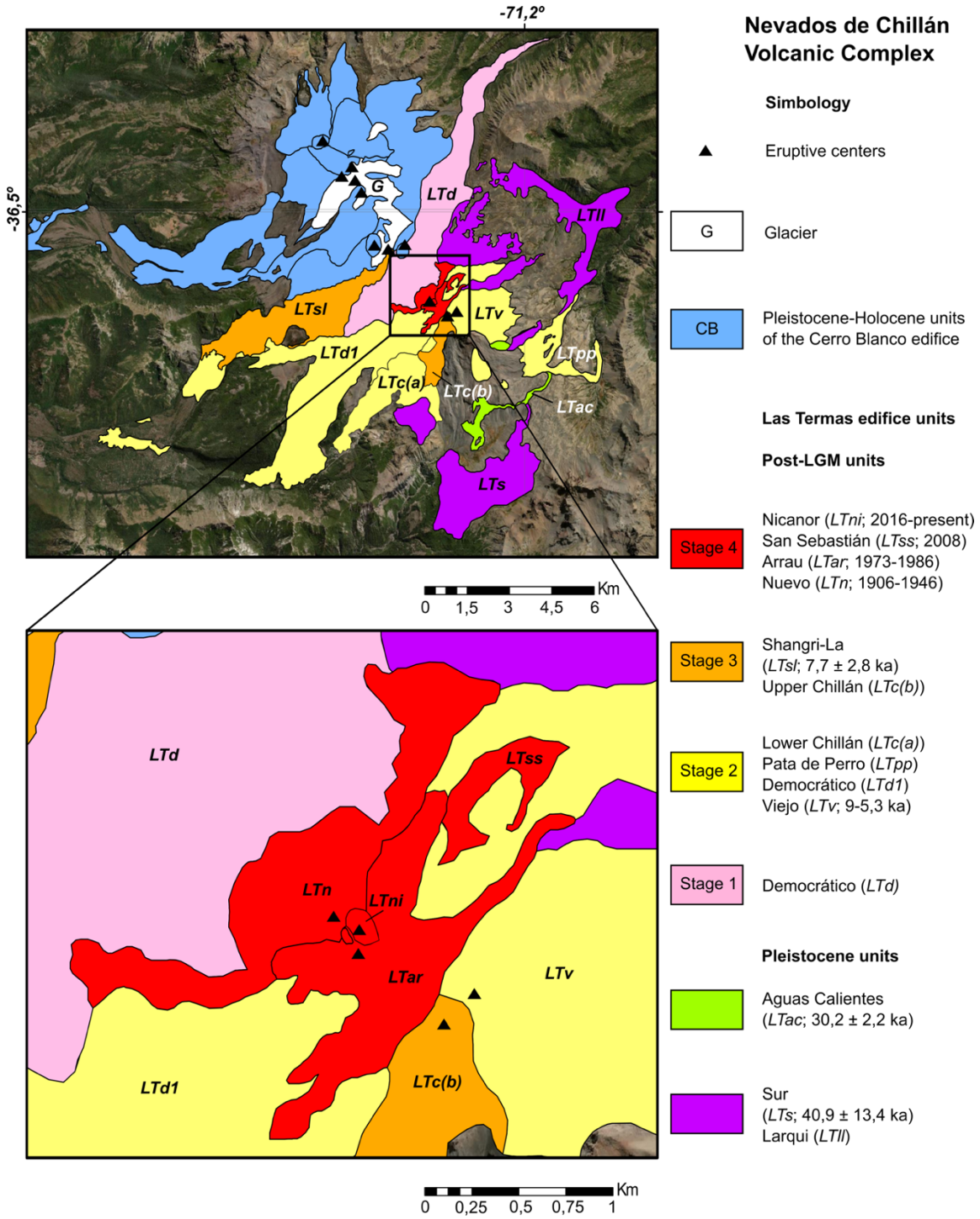

Figure 3.1. Simplified geological Map of Nevados de Chillán Volcanic Complex from Naranjo et al. (2008). The modern composite is formed by two volcanic edifices; Cerro Blanco and Las Termas. The units are grouped into stages according to their geochronological sequence and geochemical similarities to facilitate discussion.

3.2.1 Petro-volcanological background of the Nevados de Chillán volcanic complex

The NdC eruptive history started around ca. 640 ka (Dixon et al., 1999; Naranjo et al., 2008) with mostly effusive activity intermittently up to 40 ka and predominance of andesitic and basaltic andesitic compositions (Fig 3.2). The development of the present edifices began after 40 ka.

Eruptive activity at Cerro Blanco edifice (CB) began at ca. 24 ka (Orientales unit; Dixon et al., 1999; Naranjo et al., 2008) with predominant basaltic andesitic and low-Si andesitic compositions (Fig. 3.2). Subsequently, the eruptive products have been emitted from different flank eruptive centers with predominant andesitic compositions. The last eruption occurred on the NW flank of the CB edifice in the 1861-1865 period (Santa Gertrudis unit; Naranjo et al., 2008), with predominant basaltic andesitic compositions (Oyarzún et al., 2022).

More evolved compositions (dacites and rhyodacites; Fig. 3.2) dominate in Las Termas edifice (LT), except for some basaltic andesitic and andesitic units exposed on the flanks (LTs: Lavas Sur; LTll: Lavas Larqui and LTd: Democrático). The eruptive activity in this edifice begins ca. 40 ka (Dixon et al., 1999) with the emission of andesitic compositions (LTs and LTll). Subsequently, the rhyodacitic magmas of the Aguas Calientes unit (LTac; ca. 30 ± 2.2 ka; Dixon et al., 1999) were evacuated. The differences in the content of some elements (mainly K and Rb; Fig. 3.2) between the rhyodacites of the Aguas Calientes unit (Pleistocene) and the younger rhyodacites (Holocene) are probably due to different parent magmas and/or fractionation histories (Murphy, 1995). The holocene activity began with the emission of basaltic andesitic lavas (LTd; Dixon et al., 1999). Subsequently, possibly Plinian fallout pumice tephra was sourced from Viejo volcano (LTv; ca. 5.8 to 5.3 ka; Dixon et al., 1999), with geochemical features similar to the lava flows of the Democrático (LTd1) and Pata de Perro (LTpp) units, which have been interpreted as the effusive counterparts of the tephra (Dixon et al., 1999). The Chillán (LTc(a) and LTc(b)) and Shangri-La lavas (LTsl; 7.7 ± 2.8 ka; Naranjo et al., 2008) overlie the Democrático lavas (LTd1) and the Viejo crater is partially destroyed by the Chillán crater (Dixon et al., 1999). The Shangri-La and Chillán lavas (LTc(b)) have similar field appearances and occur in the same stratigraphic position (Dixon et al., 1999), and although were

erupted from geographically separate sources (Fig. 3.1), they have been interpreted as the same eruptive event (Dixon et al., 1999). Black tephra of basaltic andesitic composition emitted from the Viejo volcano overlie the older pumice sequence and the Viejo crater (Dixon et al., 1999). Additionally, two andesitic pyroclastic flows (ca 2.2 and 3.5 ka) are recognized that are assigned to the Viejo volcano (Dixon et al., 1999).

In the last century, only dacitic magmas have been emitted from different vents as Nuevo (1906-1946), Arrau (1973-1986), San Sebastián (2008; Coppola et al., 2016) and Nicanor units (2016-present; Mousallam et al., 2018; Benet et al., 2021; Cardona et al., 2021). A minor Vulcanian episode occurred in 2003 (Naranjo & Lara, 2004) sourced from an area between the Nuevo and Arrau craters (Fig. 3.1). The latter is also the vent area for the current eruption (Nicanor crater and dome) that started in 2016 (Mousallam et al., 2018; Benet et al., 2021; Cardona et al., 2021) as weak explosions generating an eruptive column of ~2 km height that became stronger and culminated with lava extrusion in January 2018, the latter forming a series of small domes that now feed a blocky lava flow on the southeastern slope (Benet et al., 2021; Cardona et al., 2021). The current volcanic activity evolved from a phase with hydrothermal dominance to an effusive one, still accompanied by persistent Vulcanian explosions of low and middle intensity (Cardona et al., 2021). Despite the dacitic composition of the lava, Mousallam et al. (2018) identified a fresh, sparsely vesicular material of basaltic andesite composition in the tephra associated with the Vulcanian activity and suggested that a small intrusion of basaltic to andesitic magma at shallow level would have led to the explosive activity.

The NdC Pleistocene-Holocene magmatic evolution has been not discussed in detail. A hypothetical mixing trend (Fig. 3.2) was proposed by Dixon et al., 1999 mainly considering some andesitic and dacitic lavas from the Shangri-la (LTsl) and Chillán units (LTc(b)), which carry macroscopically distinguishable enclaves of basaltic andesitic composition (Murphy, 1995; Dixon et al., 1999). In this study, in order to facilitate the discussion of the magmatic evolution of the NdC, the Postglacial units sourced from Las Termas edifice have been grouped into four stages, according to stratigraphic criteria and compositional and/or textural similarities (Fig. 3.1) The first

stage (stage 1) includes the basaltic andesitic and andesitic rocks of the Democrático unit (LTd). The crystal-poor rhyodacites of the Democrático (LTd1), Viejo (LTv), Pata de Perro (LTpp) and Chillán (LTc(a)) units are grouped in stage 2. The latest emitted rhyodacites ((LTc(a)) contain little mafic enclaves that have only a minor effect on the whole rock chemistry (Murphy, 1995). Stage 3 includes the crystal-rich dacites and andesites of Chillán and Shangri-La units and stage 4 the crystal-rich dacites emitted in the last century.

Regarding the configuration of the NdC plumbing system, thermobarometric studies on pyroxene and plagioclase crystals from Late Pleistocene to pre-historic Holocene lavas have revealed a compositionally zoned plumbing system that extends vertically from 2.2 km to 16.9 km (Oyarzún et al., 2022). This configuration is similar to the one proposed by Singh (2019) by means of thermobarometric studies in different minerals of the mixed lavas of the Shangri-La unit. According to Singh (2019), the Mg-rich clinopyroxenes would have crystallized between 16.5 and 24 km and the plagioclases and Mg-poor clinopyroxene between 6 and 9 km. The shallowest magma storage level has also been recognized using other methodological techniques. Through multiparametric data acquired by the monitoring network from 2012 to 2020, Cardona et al. (2021) suggests a depth of the magma chamber between 4 to 6 km following the NW-SE trend of a major fault structure.

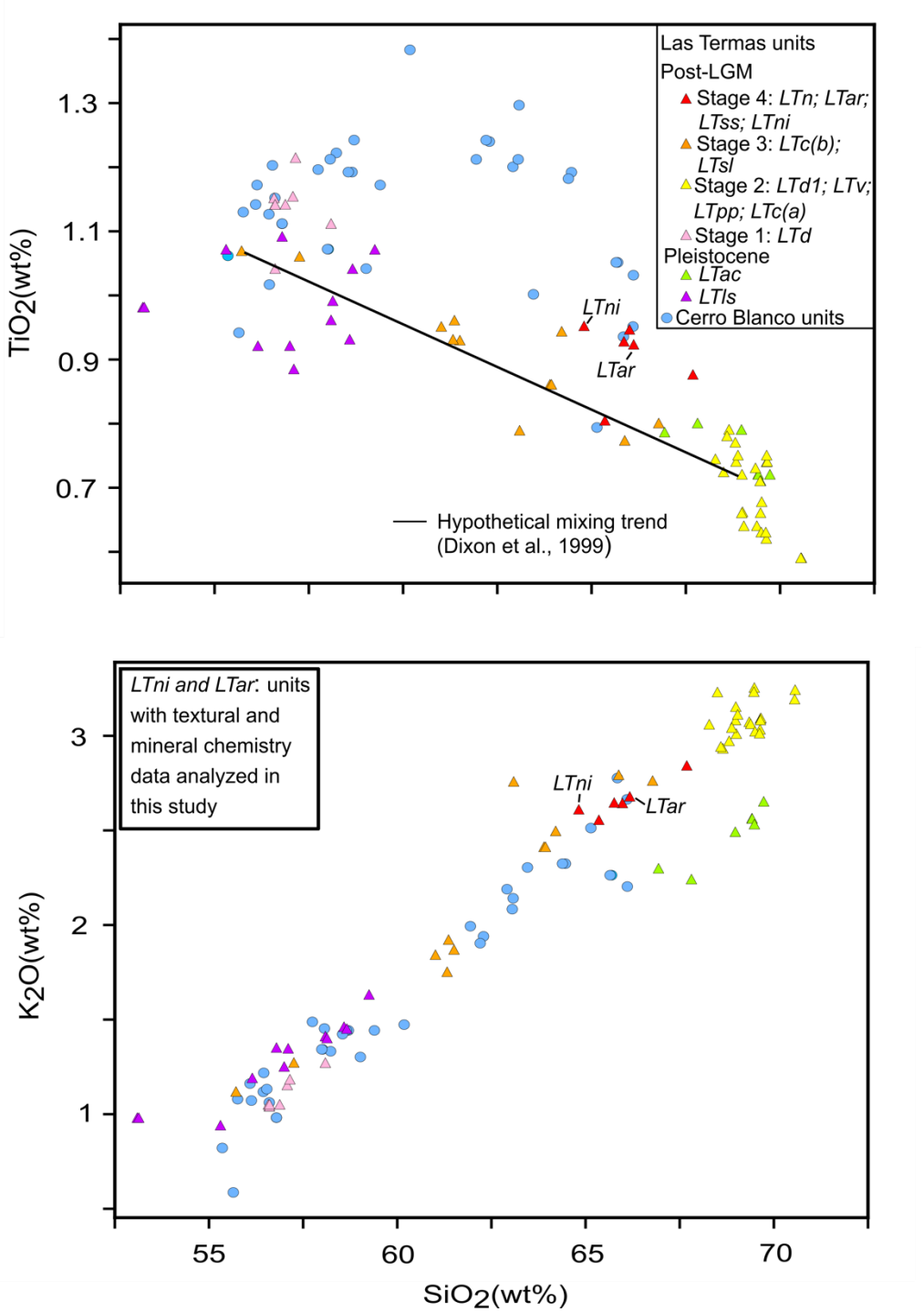

Figure 3.2. Harker diagrams of TiO_2 and K_2O vs SiO_2 (wt%). Data were obtained from Murphy (1995), Dixon et al. (1999), Deruelle & Lopez-Escobar (1999), Mee et al. (2009) and Oyarzún et al. (2022). Data were normalized on a volatile-free basis. Hypothetical mixing trend is obtained from Dixon et al. (1999).

3.3 Analytical techniques

3.3.1 Phenocryst major and trace element analyses

Pyroxenes and plagioclases core-rim compositions and core-to-rim compositional profiles in representative plagioclase from two samples lava emitted in the most important recent eruptive processes (1973-1986 and 2016-present) were obtained by wavelength-dispersive spectrometry (WDS) using the electron microprobe at Rice University (USA; JEOLJXA 8530F Hyperprobe). Analyses were carried out using standard operating conditions of 15 kV accelerating voltage and 20 nA beam current and a spot size of 3 μm was used for the all analyses with exception of plagioclase, which the beam size was set to 10 μm beam diameter to avoid Na and K loss during sample-beam interaction. Natural and synthetic minerals and simple oxides were used as reference samples, and the set of these samples varied depending on the object of analysis. The reference samples were as follows: plagioclase-SPI (Si, Na, Ca and Al), orthoclase-SPI (K in plagioclase), biotite-SPI (K in pyroxenes), rutile-SPI (Ti), olivine-SPI (Fe and Mg), chromite (Cr in pyroxenes), rhodonite (Mn) and jadeite-SPI (Na in pyroxenes),. The counting times were of 10 s on peaks and the high and low background count times were half the peak times for all elements, except for Fe and Mg in plagioclase with counting times of 50 s and 80 s, respectively, and background count times for Fe of 40 s and Mg of 60 s. Corrections for the matrix effect were calculated by the ZAF method.

3.3.2 Lava volume estimation

The calculation of the lava volumes of the different units was carried out with the Cut/Fill tool (3D Analyst) of the Arcgis software and using an Alos Palsar DEM. A map based on two input surfaces (before and after) was created showing the areas and volumes of surface materials that were changed by removing or adding surface material. The elevation of the floor of each lava unit was estimated in contact with the unit that overlies it.

3.4 Results

3.4.1 Petrography and mineral chemistry

In this section, textural observations and mineral chemistry data are analyzed in detail for two samples obtained from lavas emitted in the most recent large eruptive processes (1973-1986 and 2016-present). The analysis considers 396 mineral chemistry data, which includes 113 data in the same samples obtained from Oyarzún et al. (2022). For the plagioclase, the anorthite content was calculated as the molar ratio Ca/(Ca+Na+K) and is reported as mol %. For the pyroxene and olivine, the Mg-number (Mg#) and the forsterite content (Fo), were calculated as the molar ratio Mg/(Mg+Fe) both being reported as a percentage. The analyzed samples were obtained from the Arrau lava (LTar; 65.7 wt% SiO_2; NCH-26 in Oyarzún et al., 2022) and the Nicanor dome (LTni; 64.4 wt% SiO_2; NCH-55 in Oyarzún et al., 2022) and their mineral compositions are presented in the Figure 3.3 and listed in the appendix (Anexo 2).

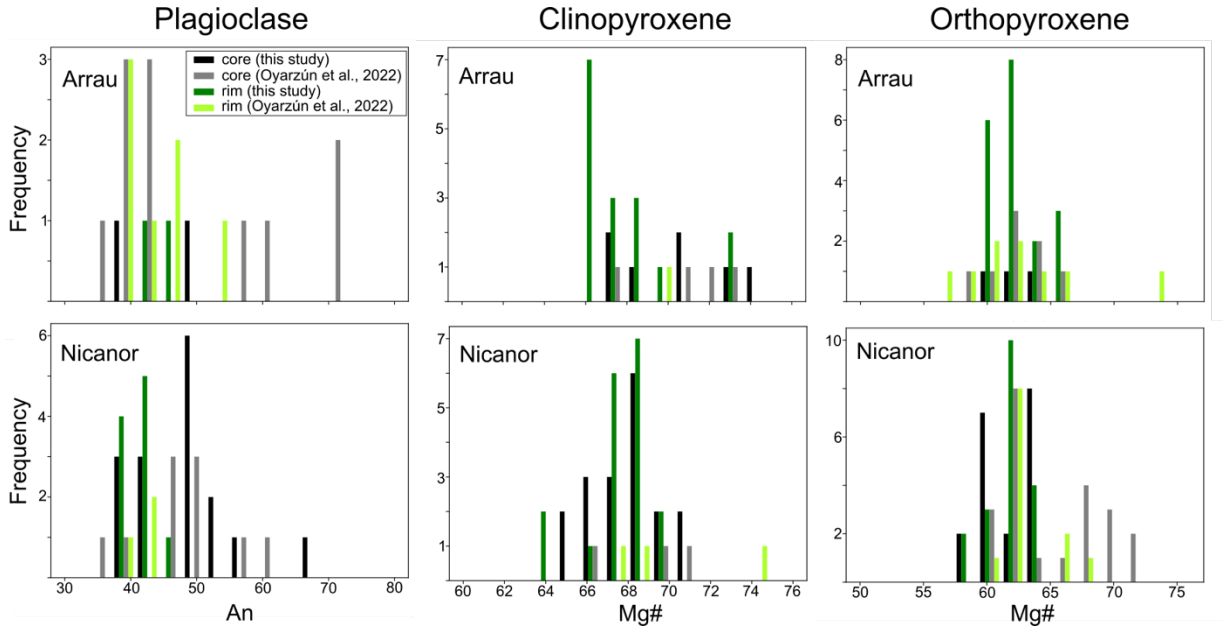

Figure 3.3. Frequency histograms showing core and rim compositions of plagioclase, clinopyroxene and orthopyroxene for Arrau lava and Nicanor dome. Data from Oyarzún et al (2022) and from this study. Abbreviations: An: anorthite content [100 * Ca/(Ca+Na+K)]; Mg#: magnesian number [100 * Mg/(Mg+Fe)].

Both samples have a phenocryst content of ca. 17.0 vol% (Oyarzún et al., 2022), but only 30 vol% of them occur as individual grains, since crystal agglomerates predominate. Phenocrysts of plagioclase and pyroxene occur as individual grains, but they are usually observed in clots with Fe-Ti oxide and apatite. The biggest crystals are usually included in crystal clots. Fe-Ti oxides (titanomagnetite > ilmenite) and apatite also occur as small individual grains mainly in the groundmass and as inclusions within pyroxene and plagioclase phenocrysts. Some small crystals of sulfides are found as inclusions in pyroxenes mainly. The predominant texture of the groundmass is intersertal trachytic with plagioclase microlites, pyroxenes, Fe-Ti oxides, and glass. The main difference between both samples is the occurrence of microscopic mafic enclaves (Fig 3.4a) and olivine phenocrysts (Fig. 3.4b) in the sample of the Nicanor dome.

Plagioclase is the most abundant mineral phase in both samples. Euhedral to subhedral plagioclase crystals predominate with sizes between 0.2 mm and 1.0 mm. Plagioclase with oscillatory zoning is frequent, either in the whole crystal or only in the rim. In the last case, dissolution/reabsorption horizons with partially resorbed anorthite-poor cores are observed (Fig. 3.4c). Plagioclase with large melt inclusions in the core and, usually accompanied of patchy texture, are also present (Fig. 3.4d). In Arrau lava, plagioclase composition in the core ranges from An_{36-71} and the rim between $An_{38-53.}$ In the Nicanor dome, the composition in the core ranges between An_{37-67} and in the rim from $An_{39-44.}$

High-contrast BSE Images coupled with compositional profiles of major and some minor elements (Fe and Mg) of a representative selection of plagioclases from both samples are presented (Fig. 3.5). Dissolution/resorption events are recorded in the cores and near to rims and the plagioclase that crystallizes subsequent to resorption horizons is always more calcic. Simple resorption is indicated by subtle resorption interfaces or rounded boundaries with only minor changes in An content (<5 An mol%; Fig. 3.5). Plagioclase growth after major rough and irregular resorption/dissolution interfaces shows a major increase in An content (> 5 An mol%; Fig. 3.5), which is usually coupled with an increase in FeO (e.g., from 4500 to 5500

ppm in sample from LTni; Fig. 3.5a) and MgO (e.g., from 300 to 500 ppm in sample from LTar; Fig. 3.5d).

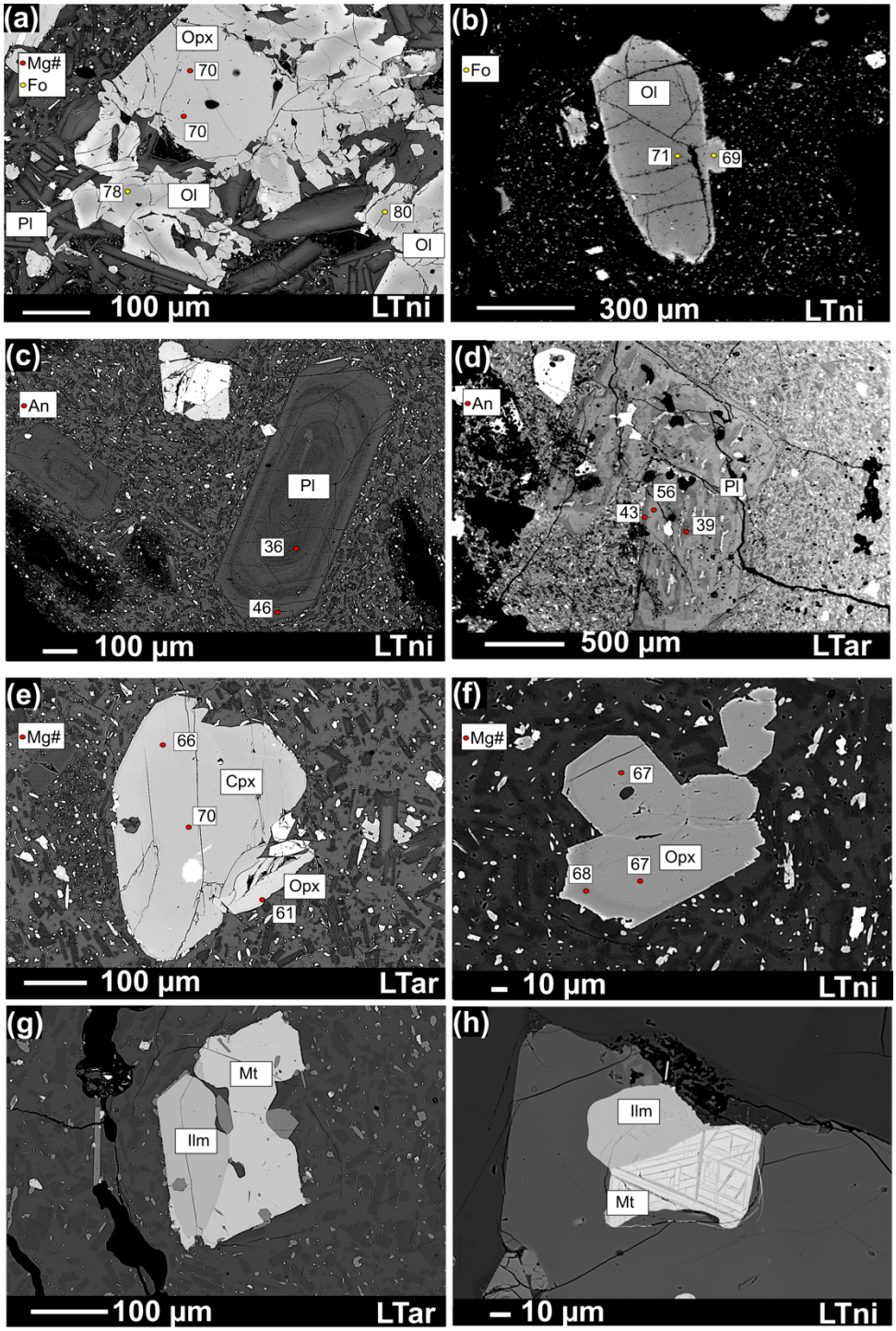

Figure 3.4. BSE Images. (a) Mafic enclave with phenocrysts of plagioclase (Pl), orthopyroxene (Opx) and olivine (Ol) set in a glassy, diktytaxitic groundmass; (b)

Olivine phenocryst; (c) Plagioclase with oscillatory and reverse zonation; (d)Plagioclase with melt inclusions; (e) Clinopyroxene (Cpx) with Mg-rich rim and orthopyroxene (Opx); (f) Orthopyroxene with Mg-rich rim; (g) Titanomagnetite (Mt) and ilmenite (Ilm) pair and (H) Titanomagnetite with dissolution texture. BSE images taken with an electronic probe. Red circle: Anorthite, Mg# and Fo contents for plagioclase, pyroxene and olivine, respectively.

Clinopyroxenes are euhedral to subhedral and either unzoned or with normal/oscillatory zoning. Some of the crystals, have magnesium-rich rims (Fig. 3.4e). The phenocrysts have sizes between 0.05 mm to 0.6 mm and a compositional range in the core between $Mg\#_{67-74}$ and in the rim of $Mg\#_{66-73}$ in Arrau lava and between $Mg\#_{65-71}$ and $Mg\#_{64-74}$ for core and rim respectively in the Nicanor dome. Orthopyroxenes are euhedral to subhedral (0.1-0.7 mm in size) and they are unzoned or with normal and reverse zoning (Fig. 3.4f). In Arrau lava, the core composition ranges between $Mg\#_{58-66}$ and the rim between $Mg\#_{57-74}$. For the Nicanor dome, the core composition ranges between $Mg\#_{58-72}$ and the rim between $Mg\#_{57-68}$. An orthopyroxene within of a mafic enclave have a composition in the core of $Mg\#_{70}$

Fe-Ti oxides (titanomagnetite > ilmenite) are small euhedral to subhedral crystals. In Arrau lava, titanomagnetite (Fig. 3.4g) range from Ulv_{52-58} and ilmenite from $Ilm_{87-92.}$ For the Nicanor dome, titanomagnetite range from Ulv_{56-58} and ilmenite from $Ilm_{85-92,}$ and some titanomagnetite crystals with exsolution textures are observed (Fig. 3.4h). Olivine phenocrysts in the Nicanor dome appear both in the dacitic part (Fig. 3.4b) and within microscopic mafic enclaves (Fig. 3.4a) accompanied by phenocrysts of pyroxenes and plagioclases set in a glassy, diktytaxitic groundmass. Olivines phenocrysts (0.3 – 0.6 mm in size) are with normal zoning. The core composition range between Fo_{71-80} and a rim analyzed have Fo_{69}.

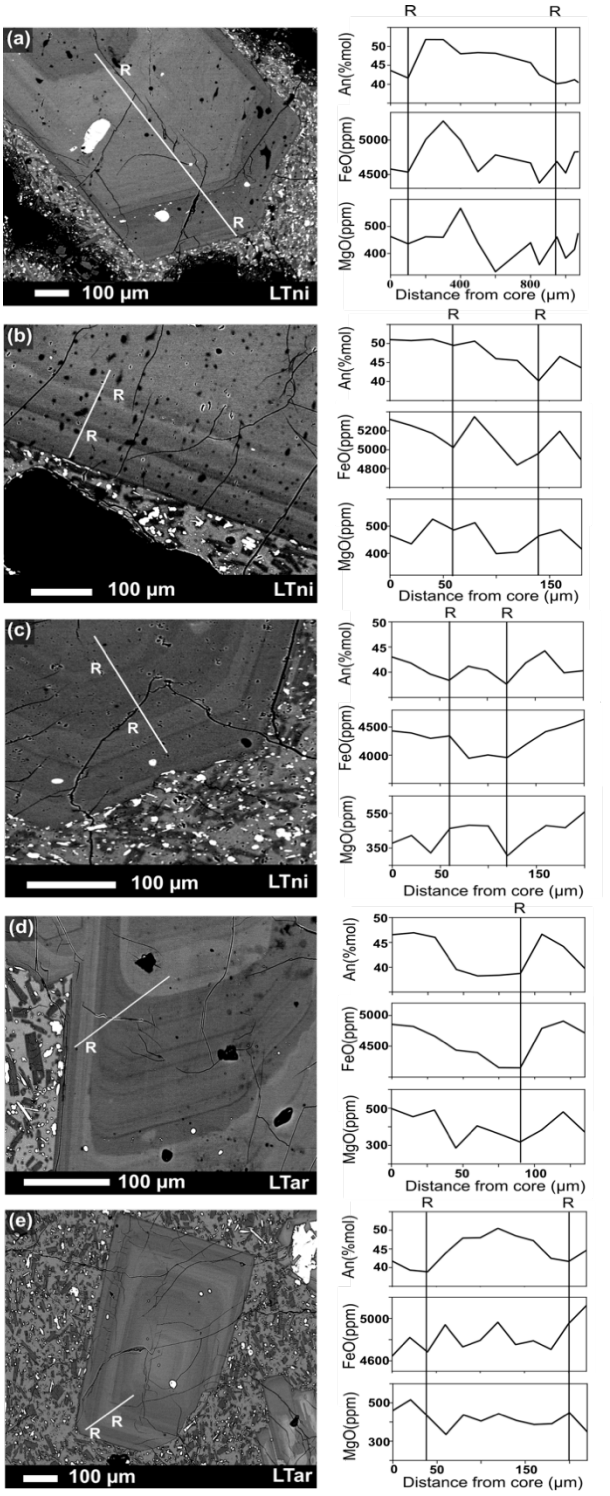

Figure 3.5. BSE images and measured EMPA compositional profiles for representative plagioclase crystals from Nicanor dome (a, b and c) and Arrau lava (d and e). R: resorption horizons.

3.4.2 Lava volume estimations

The results show a decrease in the volumes of lava emitted in the last century from the Las Termas edifice (Table 3.1). Additionally, a decrease in the volumes of lavas emitted from stage 2 to stage 4 is also observed.

Table 3.1. Lava volume estimations for Holocene Las Termas units

Stage	**Units**	**Lava volume (km^3)**	**Total stage (km^3)**
Stage 1	LTd	0.23339	0.23339
Stage 2	LTd1	0.45494	0.75415
	LTv	0.10648	
	LTpp	0.04713	
	LTc(a)	0.14560	
Stage 3	LTc(b)	0.04423	0.19277
	LTsl	0.14854	
Stage 4	LTn	0.01688	0.02227
	LTar	0.00466	
	LTss	0.00043	
	LTni*	0.00030	

* Data from Cardona et al. (2021)

3.5 Discussion

The first part of this chapter discusses the petrogenesis of the dacites analyzed in this study (LTar and LTni; stage 4), using geochemical modeling and new textural and geochemical data. Additionally, in order to understand the magmatic evolution of the Las Termas del NdC edifice, the petrogenesis of the oldest units is evaluated with the information available in the literature. Finally, the main factors that explain the magmatic evolution during the Holocene of the Las Termas del NdC edifice and that lead to a predominance of intermediate compositions of the youngest eruptive products are discussed.

3.5.1 Dacites petrogenesis

In general, the mixing processes of compositionally distinct magmas are typically inferred by the presence of enclaves (e.g., Davidson et al., 2001), geochemical zonation in phenocrysts (e.g., Eichelberger, 1980; Singer et al., 1995; Davidson et al., 2001), different populations of crystals with disequilibrium textures (Streck, 2008), and by a continuous linear trend in variation diagrams of major oxides in a suite of igneous rocks (e.g., Blundy & Cashman, 2008). All these characteristics are observed in the andesites and dacites of stage 3 (LTsl and LTc(b); Murphy, 1995; Dixon et al., 1999), which supports the origin by mixing of magmas for these units proposed by Murphy (1995) and Dixon et al. (1999). On the other hand, Murphy (1995) suggests that the rocks that move away from the mixing trend that these units form (Fig. 3.6), which would be the case for the youngest NdC dacites (stage 4), would have originated by fractional crystallization. This hypothesis is then tested by geochemical simulations.

3.5.1.1 Fractionation crystallization

We have tested the hypothesis of fractionation crystallization from a basaltic andesite (an enclave in Shangri-La lava; NCH-60 in Oyarzún et al., 2022) with the Rhyolite-MELTS algorithm (Gualda et al., 2012; Ghiorso & Gualda, 2015). The MELTS-modelled liquid-line-of-descent has been calculated for pressures (between

0.5 and 8 kbar) covering the entire thickness of the crust at this latitude (Tassara et al., 2006; Tassara & Echaurren, 2012), with water content between 0.5 and 3 wt% H_2O, an oxygen fugacity (fO_2) between QFM-2 and QFM+2 and with temperature just above the liquidus in the starting composition.

The MELTS model that best fit the major element variations is given with initial pressure conditions of 4.5 kbar, 1 wt% H_2O and fO_2 of QFM+2 (Fig. 3.7). However, this simulation only predicts well the compositions of some rocks with less than 63 wt% SiO_2. The fractionated mineral phases, the values of An mol% in plagioclase, and the water content and melt temperature given by the simulation are consistent with the values obtained by Oyarzún et al. (2022) for a crystal-poor NdC lavas with 63 wt% SiO_2 (CBg; NHC-44 in Oyarzún et al., 2022)

In addition, we tested the hypothesis of fractional crystallization of an andesite (CBg; NHC-44 in Oyarzún et al., 2022) that fits relatively well in the simulation carried out in the previous stage. The simulations were carried out with the same ranges of pressures, water content and oxygen fugacity as the other. However, none of them predicted the compositions of the dacites and rhyodacites lavas. The largest mismatches are in P_2O_5, CaO and Al_2O_3, probably because MELTS software underestimates the fractionation amounts of accessory minerals such as apatite. In conclusion, fractional crystallization simulations suggest that at least some andesites are generated by this process, but not all of them. On the other hand, the lack of significant Eu anomalies (Eu_n/Eu^*_n= 0.95) in the basaltic andesite enclave (LTsl(me); Fig. 3.8a), indicates that plagioclase crystallization occurred under high fO_2 conditions where $Eu3^+$ is prevalent. This is consistent with the initial conditions in the MELTS model that best fit with the major element variations for compositions of rocks with less than 63 wt% SiO_2 (Fig. 3.7).

Although with the MELTS software simulations it is not possible to evaluate the generation of dacitic and rhyodacitic compositions by fractional crystallization, the similar pattern of incompatible elements between the less differentiated compositions (LTsl(me)) and the rhyodacites (LTpp) and younger dacites (stage 4) suggests that they had a similar parental magma (Fig. 3.8a). The residual magma becomes poorer in P, Ti and Sr with differentiation due to increased crystallization of apatite, Fe-Ti

oxides and plagioclase, respectively. Along with these antecedents, the absence of disequilibrium textures in the mineral phases present in the rhyodacitic lavas from stage 2 and their geochemical homogeneity (Oyarzún et al., 2022), suggests that these compositions have been generated by fractional crystallization. On the other hand, the textural and geochemical variability of the mineral phases of the youngest dacites could be a consequence of magma mixing, which is evaluated below.

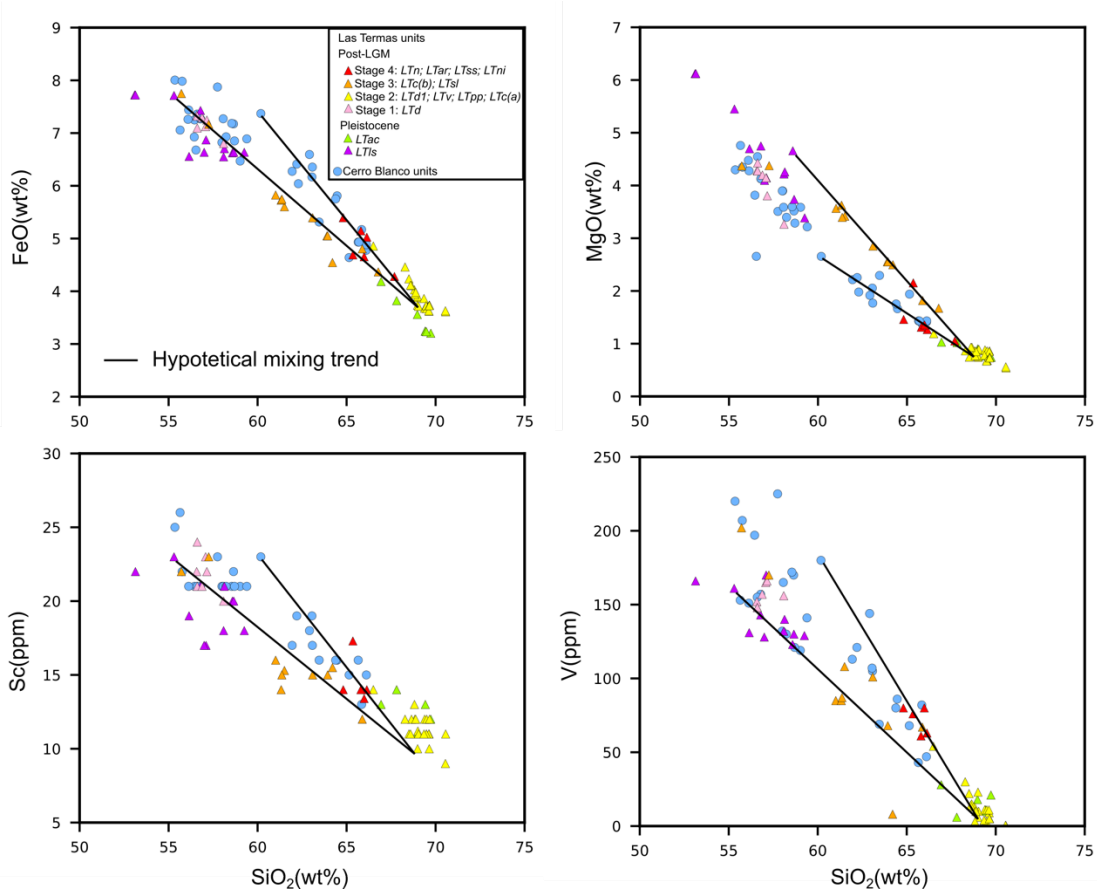

Figure 3.6. Harker diagrams of FeO, MgO, Sc, V vs SiO2 (wt%). Data were obtained from Murphy (1995), Dixon et al. (1999), Deruelle & Lopez-Escobar (1999), Mee et al. (2009) and Oyarzún et al. (2022).

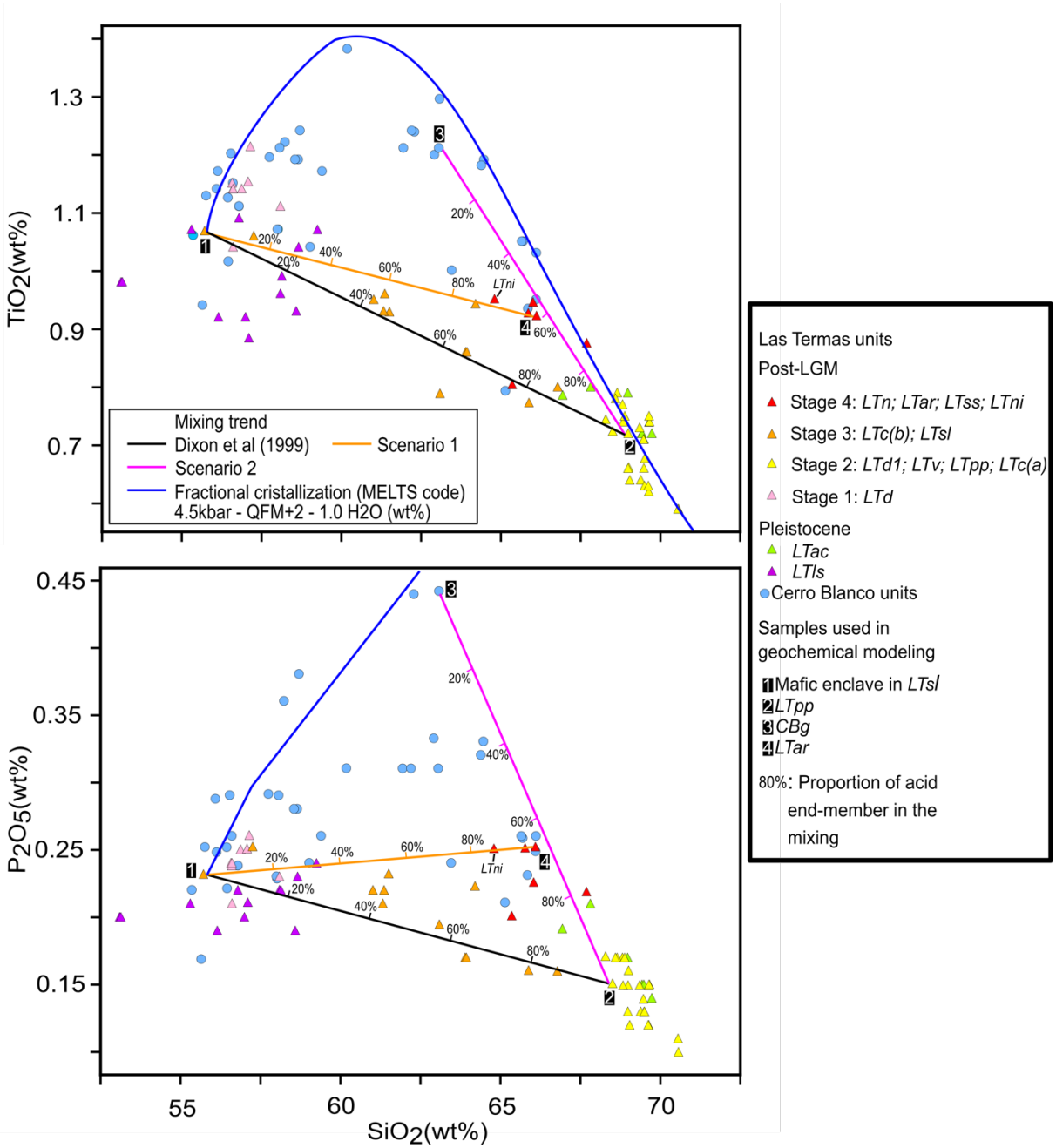

Figure 3.7. TiO_2 and P_2O_5 vs SiO_2 (wt%) diagram showing the simulated evolution of the residual melt compositions by rhyolite-MELTS and three different mixing trends.

3.5.1.2 Magma Mixing

Dacites analyzed in this study (LTar and LTni) bear different populations of crystals (textural and/or compositional) with disequilibrium textures. This can be the result of different processes such as: convection in a zoned chamber (e.g., Singer et al., 1995), mineral/melt segregation (e.g., Holness et al., 2007), degassing-induced crystallization (e.g., Frey & Lange, 2011), crystallization by decompression (Blundy et al., 2006), thermal convection (Couch et al., 2001), and magma mixing processes in an open-system (e.g., Davidson et al., 2001). For the latter, intrusions of mafic magma into magmatic mushes can lead to mush disaggregation and eruption (e.g., Kahl et al., 2011). The predominance of crystal agglomerates in Arrau and Nicanor dacites suggests a disruption of the mush by intrusions of magma (e.g, Edmonds et al., 2019).

Along with the predominance of crystal agglomerates, in the Nicanor dacites there is other evidence that supports their origin by magma mixing, such as: **1)** the presence of juvenile-looking enclaves (diktytaxitic groundmass and vesicular texture) with olivine (Fig. 3.4a). This is consistent with a fresh, sparsely vesicular material of basaltic andesite composition identified by Mousallam et al. (2018) in the tephra of the current eruptive process; **2)** olivine phenocrysts in the dacitic part (Fig. 3.4f); **3)** disequilibrium textures in plagioclase, magnetite, pyroxenes (Fig. 3.4) and; **4)** reverse zonation in some plagioclase and pyroxene phenocrysts (Fig. 3.4). Additionally, other evidence supporting magma mixing in the generation of Nicanor dacites arises from the interpretation of compositional profiles in plagioclase.

Major, minor and trace element concentration combined with textural images in plagioclase have been widely used to identify the causes of zoning patterns (e.g., Ginibre et al., 2002). A plagioclase growth zone with an An-rich spike accompanied by higher Mg and Fe contents compared to the adjacent older zone would be linked to a less differentiated magma recharge (open-system; e.g., Ruprecht & Worner, 2007; Ginibre & Worner, 2007). This process can generate rounded resorption surfaces or highly complex resorption and growth morphologies (e.g., Ginibre & Worner, 2007). On the contrary, an An-rich spike with the Fe and Mg contents remaining constant, might be implying the resorption event indicate thermal changes

(closed-system; e.g., Ruprecht & Worner, 2007; Ginibre & Worner, 2007). In the profiles carried out on plagioclase from Nicanor sample (Fig. 3.5), some growth zones with an An-rich spike, after of resorption surfaces are observed. Some of these zones are accompanied by higher Mg and Fe contents compared to the adjacent zone, both in the core (Fig. 3.5a) and near the rim (Fig. 3.5b and 3.5c), which may be attributable to recharge events with less differentiated magmas.

The genesis of the Nicanor dacites by magma mixing processes is evaluated using mass-balance method with major elements with MIXING software (Carr & Gazel, 2017) and mixing model for incompatible elements with PETROMODELER software (Ersoy, 2013). In this evaluation, a basaltic andesite (enclave in Shangri-La sample; LTsl(me); NCH-60 in Oyarzún et al., 2022) is considered as mafic end-members, since the enclaves observed in the Nicanor sample are similar to those found in LTsl and LTc(b). The other considered end-member is the Arrau dacite (LTar), evacuated around three decades before the Nicanor dacites. With the proportion obtained from the mass-balance method for this analysis (scenario 1; Table 3.2) a good fit is obtained in the mixing model for incompatible elements (Fig 3.7a, b).

Table 3.2. Mass-balance method for scenario 1

	Sample[1] enclave LTsl(me)	Sample LTar	Calculated with LTsl(me) and LTar (1:9)[2]	Measured (LTni)	Diff * wt %
Major element (wt %)					
SiO_2	55.71	66.07	65.05	64.81	0.10
TiO_2	1.07	0.93	0.94	0.96	0.02
Al_2O_3	17.87	15.29	15.54	15.74	0.10
FeOt	7.75	5.05	5.31	5.40	0.08
MnO	0.13	0.10	0.10	0.10	0.00
MgO	4.37	1.28	1.58	1.46	0.12
CaO	7.85	3.34	3.78	3.73	0.05
Na_2O	3.90	5.01	4.90	4.94	0.04
K_2O	1.12	2.70	2.54	2.62	0.08
P_2O_5	0.23	0.25	0.25	0.25	0.00
Total	100.0	100.0	100.0	100.0	

[1] WR data is obtained from Oyarzún et al. (2022). [2] End-members proportion

On the other hand, in the Arrau dacites no mafic enclaves are observed, however, as in the Nicanor dacites, crystal agglomerates predominate and some phenocrysts present disequilibrium textures and reverse zonation. In the plagioclase compositional profiles of the Arrau sample, only one zone presented An-rich spike accompanied by higher Mg and Fe contents (Fig. 3.5d), which affected the outer growth zone near the rim. These new plagioclase growth zone may be attributable to recharge events with less differentiated magmas. On the other hand, an An-rich spike in the core of the plagioclase in the Arrau sample is not accompanied by an increase in the Fe and Mg contents (Fig. 3.5e), which would correspond to a thermal change. On the other hand, in addition to the mixing trend proposed in previous works (Fig 3.2; Dixon et al., 1999), represented by andesitic and dacitic lavas (stage 3) from the Shangri-La (LTsl) and Chillan units (LTc(b)), in the harker diagrams (Fig.3.6) another linear trend is observed that contains the youngest dacites (stage 4), which suggests that these compositions could be generated by mixing magmas, although in this case the mafic end-member would be an andesitic magma. In this scenario 2 (Table 3.3), the considered end-members are an andesite (CBg) and a rhyodacite (LTpp). Whole-rock compositions of these samples were obtained from Oyarzún et al. (2022), where they are described as crystal-poor without clear evidence of magma mixing. With the proportion obtained from the mass-balance method a good fit is obtained in the mixing model for incompatible elements (Fig 3.8c, d).

Table 3.3. Mass-balance method for scenario 2

	Sample[1] CBg	Sample LTpp	Calculated (4:6)	Measured (LTar)	Diff * wt %
Major element (wt %)					
SiO_2	63.03	68.44	66.00	66.07	0.03
TiO_2	1.30	0.72	0.99	0.93	0.06
Al_2O_3	15.56	14.90	15.19	15.29	0.05
FeOt	6.37	4.26	5.21	5.05	0.16
MnO	0.12	0.09	0.10	0.10	0.00
MgO	1.78	0.74	1.21	1.28	0.07
CaO	4.22	2.33	3.18	3.34	0.16
Na_2O	5.03	5.11	5.07	5.01	0.07
K_2O	2.15	3.25	2.75	2.70	0.06
P_2O_5	0.44	0.15	0.28	0.25	0.03
Total	100.0	100.0	100.0	100.0	

[1] WR data is obtained from Oyarzún et al. (2022). [2] End-members proportion

However, the textural and geochemical variability of the mineral phases present in these dacites could also be due to the incorporation of xenocrysts into the magma. In this case, it is inferred that the percentage of xenocrystals incorporated into the magma would be lower than that of the phenocrysts originating from it (e.g., Zhang et al., 2020). This hypothesis is evaluated in the Figure 3.9, which shows the compositional range of the plagioclase contained in the rhyodacites and the andesite, which fit well in the fractional crystallization models and do not present clear evidence of magma mixing, together with the composition of the core of the plagioclase present in the dacites emitted in the last decades and which are not part of glomerocrysts. Accordingly, these dacites are dominated by plagioclase that would have originated from andesitic and rhyodacitic magmas, which supports the idea that these compositions would have been generated by a magma mixing, generating a new plagioclase growth zone after of the mixing (Fig. 3.9).

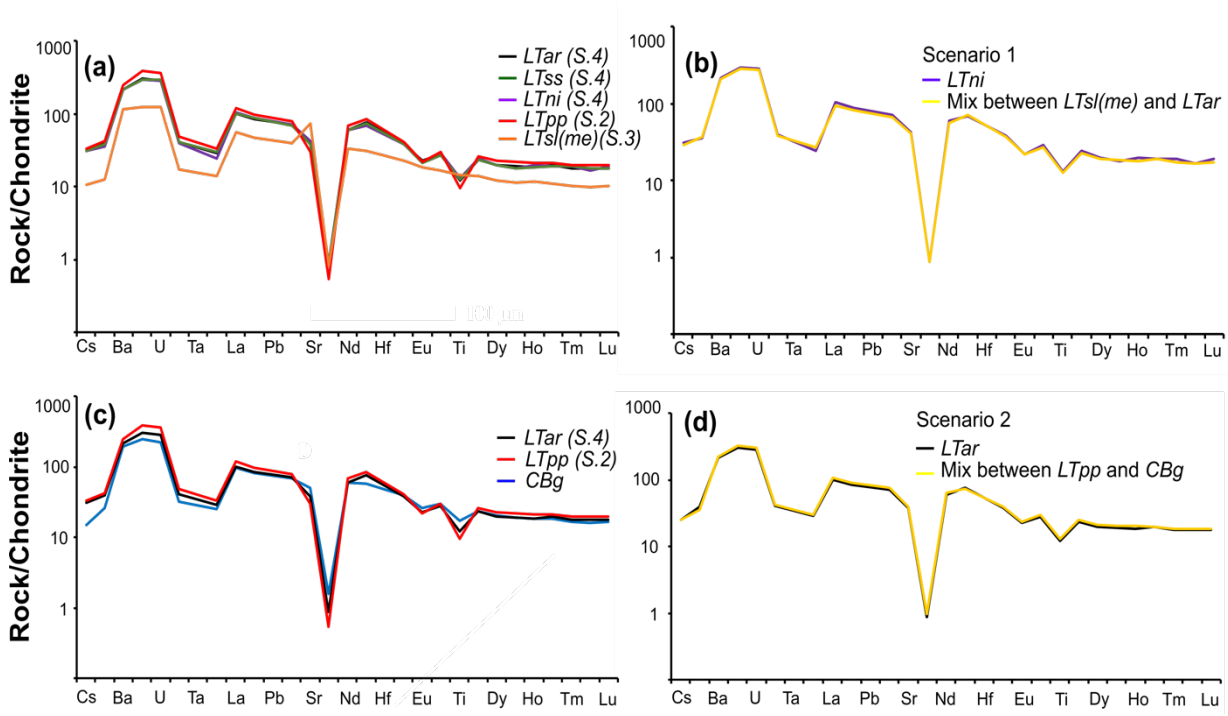

Figure 3.8. Chondrite-normalized multi-element diagrams and mixing model for incompatible elements. (a) show Arrau dacite (LTar); Pata de Perro rhyodacite (LTpp), and Gato andesite (CBg) incompatible elements concentration; (b) mixing model for Arrau dacite generation; (c) show Arrau dacite (LTar); San Sebastián dacite (LTss); Pata de Perro rhyodacite (LTpp); Nicanor dacites (LTni), and enclave (within Shangri-La; LTsl(me)) incompatible elements concentration, and (d) mixing model for Nicanor dacite generation (LTni). Normalizing factors from Sun & McDonough (1989). Incompatible elements data are obtained from Oyarzún et al. (2022).

In summary, the textural and chemical evidence and the geochemical models support the hypothesis that mixing processes occurred in the origin of the younger dacites. The dacites are generated by the injection of andesitic magma in the rhyodacitic reservoir and subsequently, a minor injection of basaltic andesitic magmas into the dacitic magma explain the composition of the Nicanor dacites.

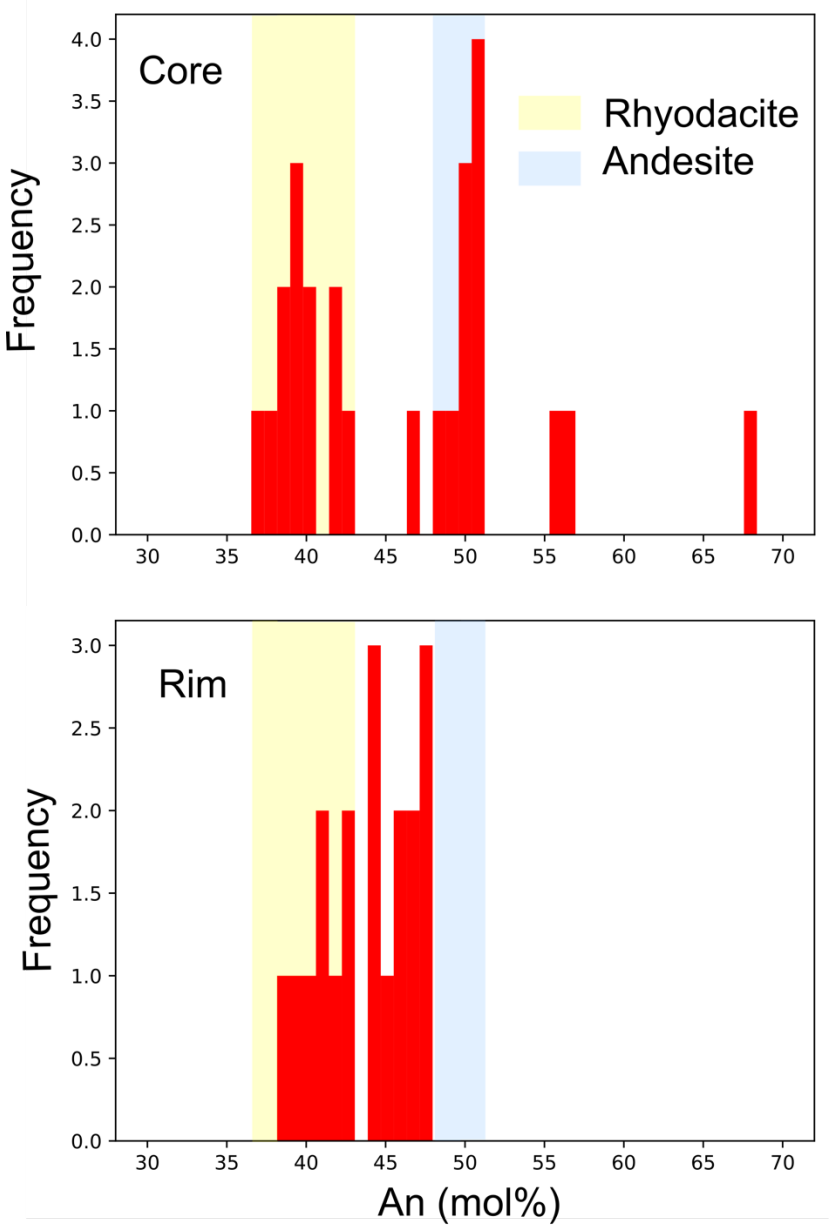

Figure 3.9. Histogram with the composition of the plagioclase present in the dacites emitted in the last century in the NdC and that are not part of crystal clots. The colored areas show the compositional range of the plagioclase present in the riodactitic and andesitic lavas (Oyarzún et al., 2022) that do not show clear evidence of magma mixing.

3.5.2 The effects of the temporal/spatial evolution of the magmatic system in the upper crust on magmatic evolution

The results discussed previously, together with the geochronological information available in the literature allow us to reconstruct the post-LGM magmatic evolution of the Las Termas edifice. Additionally, the effects of the temporal/spatial changes in the NdC magmatic system on magmatic evolution are discussed.

The eruptive products emitted post-LGM from the Las Termas edifice ranged from 56.6 to 70.6 wt% SiO_2 (Fig 3.2), with a predominance of compositions in an intermediate range of silica in the youngest eruptive products (Fig 3.10). The postglacial eruptive history begins (stage 1: LTd; Fig 3.10) with the evacuation of basaltic andesitic lavas (Dixon et al., 1999). In this study, the genesis of these lavas is not evaluated, since there are no less evolved compositions in the NdC that can be used as parent magma, however, the crystallization pressures of the mineral phases of these compositions in the NdC reveal that these magmas would be stored below ICD (Intracrustal Density Discontinuity; ca. 10 km depth in this area) in the long term (Oyarzún et al., 2022).

Subsequently, rhyodacite lavas and tephra were emitted (stage 2: LTd1, LTv, LTpp and LTc(a); Fig 3.10) between ca. 5.8 to 5.3 ka before present (Dixon et al., 1999; Naranjo et al., 2008). As previously discussed, these rhyodacitic magmas are generated by fractional crystallization, and because the crystallization depths of the mineral phases of these lavas are above the ICD (Oyarzún et al., 2022), we infer that they originate in the upper crust. Annen et al. (2006) point out that it is unlikely that in subduction-related magmatism, more evolved compositions are generated from basaltic magmas in the upper crust, due to the volume of mafic parent magma required, however they point out that these silica-rich magmas can be generated by fractional crystallization from andesitic magmas that are stored in the upper crust. Based on these antecedents, it is likely that stage 2 rhyodacitic magmas are generated by the differentiation of andesitic magmas that moved from the ICD and were not evacuated to the surface. On the other hand, the presence of small mafic enclaves in the last rhyodacitic lavas emitted in stage 2 (LTc(a); Murphy, 1995)

evidence mafic magma injection processes, in which rhyodacitic magmas would act as a density filter for less evolved magmas coming from deeper levels of the crust (e.g., Kent et al., 2010). The lavas of stage 2 are partially covered by lavas of intermediate compositions (stage 3: LTc(b) and LTsl; Fig. 3.10), which contain macroscopically distinguishable basaltic andesitic enclaves (Dixon et al., 1999; Oyarzún et al., 2022). Although stage 3 lavas have been emitted from different eruptive centers, they have been interpreted as the same magma batch that was erupted from different craters, due to their geochemical, textural, and stratigraphic position similarities (Dixon et al., 1999). The $^{40}Ar/^{39}Ar$ radiometric age of this event is 7.7 ± 2.8 (Naranjo et al., 2008), but since they overlie the rhyodacites, we bracket their age to between 5.3 and 4.9 ka. After andesitic pyroclastic flows (ca 2.2 and 3.5 ka; Dixon et al., 1999) and basaltic andesitic tephras with a minimum age of 500 BP (historical time), all sourced at the Viejo crater, are emitted, which suggests the absence of rhyodacitic magmas in the upper crust in that sector, since the density filter would not operate. The absence of rhyodacitic magmas stored in the upper crust in this sector is due to a lateral decrease in its extension, which would also explain the areal concentration of stage 4 volcanism (LTn, LTar, LTss, LTni). In addition, the absence of eruptive products of andesitic or basaltic andesitic compositions, after stage 1, in the sector where the youngest dacites have been evacuated, suggests that rhyodacitic magmas have been present throughout this period of time in the upper crust, acting as a density filter. These rhyodacitic magmas mix with less differentiated magmas, originating the dacitic compositions of the units emitted in stage 4.

On the other hand, the decrease in the lateral extension of the rhyodacitic magmas stored in the upper crust is also supported by the decrease in the volumes of lavas emitted from stages 2 to 4 (Table 3.1; Fig. 3.10), although the time scales are different. However, if we consider only the units of stage 4, this process is also observed (Table 3.1). This decrease in lava volumes may be due to a decrease in the volume of rhyodacitic magma in the upper crust over time, although it may also respond to other factors, such as the viscosity of the magmas, the stress imposed by the charge of the volcanic edifice or the depth from which the magmas would come.

With respect to viscosity, it is expected that a more viscous magma has less mobility in relation to a less viscous magma, therefore a greater difficulty in reaching the surface. However, as the viscosity is mainly controlled by the silica content of the magmas, lower volumes of rhyodacitic magmas would be expected compared to intermediate magmas, which is contrary to the estimated lava volumes in this study. This comparison of the volumes of rhyodacitic and intermediate lavas is easier to observe in the LTc(a) and LTc(b) units, which are emitted from the same crater and with a similar height to the dacites emitted in stage 4, which also rules out the influence of the stress imposed by the charge of the volcanic edifice. In the same way, the depths from which these magmas would come would be similar, according to the estimates proposed by Cardona et al. (2021) and Benet et al. (2021) for the depth of the current reservoir and those inferred by thermobarometric studies for stage 2 rhyodacitic magmas (Oyarzún et al., 2022). Finally, the decrease in the volume of lavas emitted could respond to a lower flow of magma recharge, however this would not explain the predominance of intermediate compositions in the youngest rocks of the NdC. Along with crustal filters, it has been suggested that the occurrence of intermediate compositions would depend on the volume of the involved end-members (e.g., Gilbert et al., 2014). In periods where there is a higher flux of less evolved magma from depth that intercepts the shallow and more mature storage level, the evacuation of intermediate products generated by mixing would be favored (e.g., Lonquimay Volcano; Gilbert et al., 2014). According to this assumption, a decrease in the volume of the more differentiated host magma would favor a similar result, which seems to be the case for the NdC, which is consistent with the decrease in lava volume over time.

In summary, the changes that the NdC magmatic system has undergone during the Holocene have conditioned its magmatic evolution. The basaltic andesites emitted in stage 1 (LTd; Fig. 3.11a), which would rise from middle levels of the crust linked to the Intracrustal Density Discontinuity (Oyarzún et al., 2022), manage to be erupted when the shallowest storage level with differentiated magmas not yet formed. Subsequently, the shallowest storage level is established and differentiation of the magmas by fractional crystallization continues to give rise the rhyodacitic magma

evacuated in stage 2 (Fig. 3.11b). This new level of storage with evolved magmas would act as a density filter for the next batches of denser magmas coming from depth. The greater volume of host magma in stage 2 in comparison to stage 3 and 4, would explain the absence of intermediate eruptive products generated by mixing processes in this stage (Fig. 3.11b). As volcanic eruptions are commonly triggered by recharge events (Morgavi et al., 2017), the mixing compositional affected a limited volume of the host magma, probably restricted to the basal portion of the magma body. This limited interaction explains the low content of glomerocrysts, coming from the disruption of the mush caused by magmatic recharge in these lavas (Oyarzún et al., 2022) compared to the lavas emitted later, where the glomerocrysts would be distributed throughout the reservoir (Fig.3.11c and d). On the other hand, the smallest volume of host magma in stage 3 and 4, possibility that the mixing compositional affects all of the host magma. This depletion of rhyodacitic magma explains the absence of lavas from these compositions in the last stage, although another possibility is that the rhyodacitic magmas in these last stages are more viscous than those of stage 2 and fail to reach the surface, which could be due to to a higher content of glomerocrysts and/or to presenting a higher content of silica.

Other volcanoes, such as Nevados de Longaví (36°20' S/ 71°16' W) and San Pedro (35°99' S/ 70°86' W), which belong to the same subsegment of the NdC (TSVZ), display a post-LGM eruptive sequence and compositional features comparable to those of the NdC (Fig. 3.12), which suggests that what is proposed is not a peculiarity of the case study.

We propose that the temporal/spatial evolution of the upper part of the NdC magmatic system, expressed in the establishment of a storage level with differentiated magmas and in its variations in volume, conditions the magmatic evolution of the NdC. In addition, this type of temporal/spatial evolution of the magmatic system may be playing a relevant role in the predominance of intermediate compositions in continental arc systems.

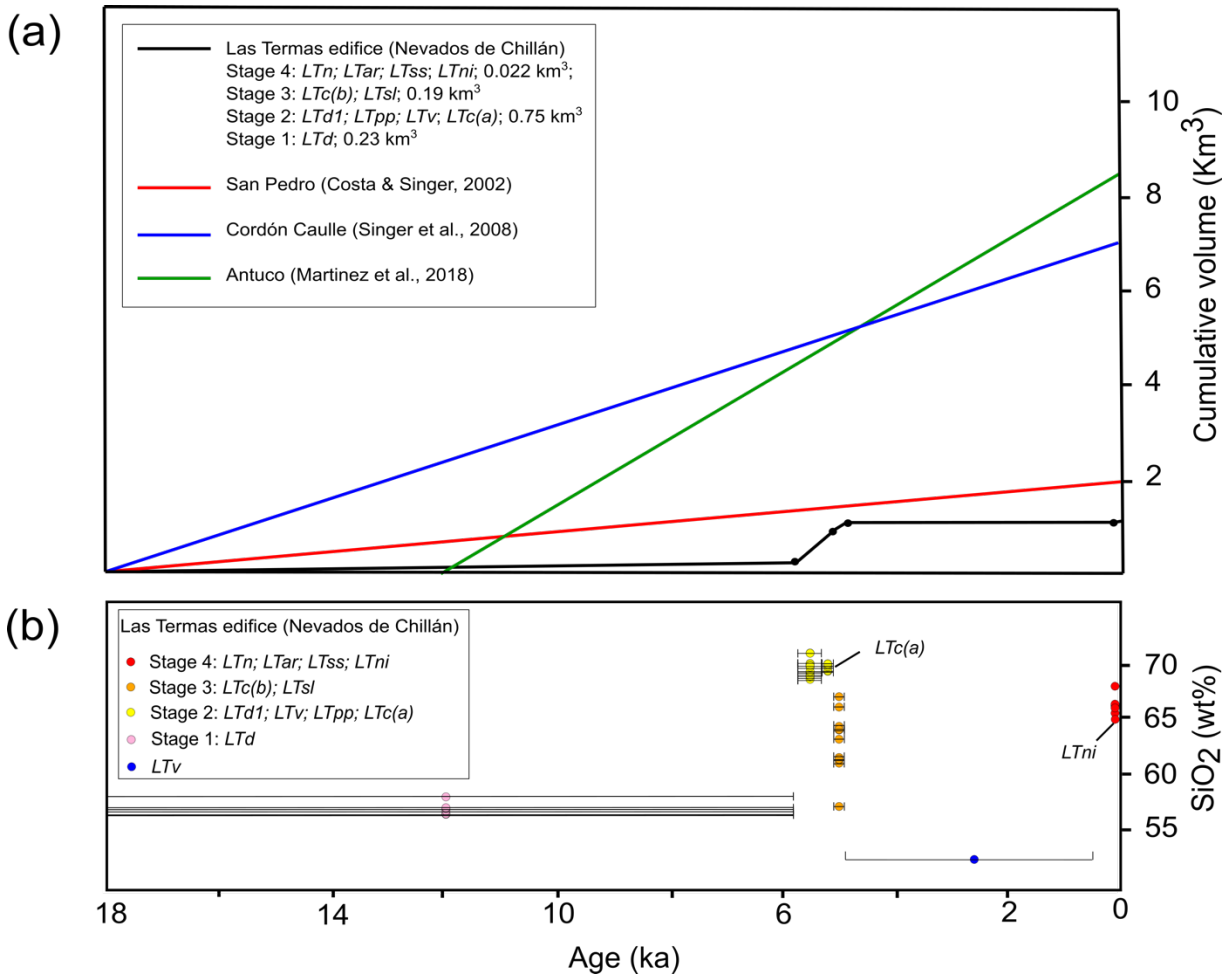

Figure 3.10. (a) Age (ka) vs cumulative volume (km^3) diagram for units emitted post-LGM from Las Termas edifice; San Pedro, Cordón Caulle and Antuco; (b) Age vs silica content diagram for Las Termas edifice. LTc(a) unit overlie LTc(b) unit.

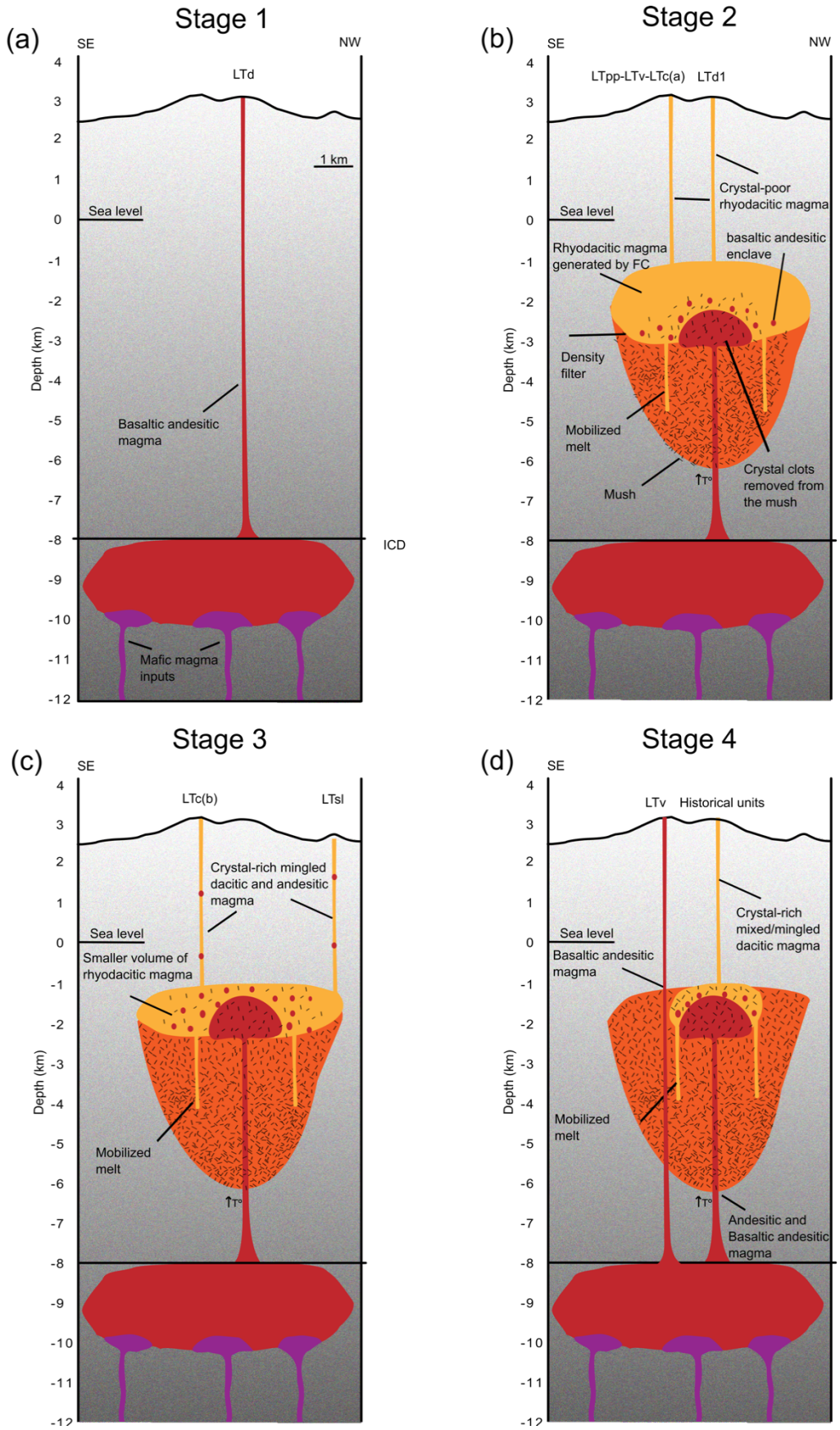
Stage 1
(a)
SE
NW
LTd
1 km
Sea level
Depth (km)
Basaltic andesitic magma
ICD
Mafic magma inputs
Stage 2
(b)
SE
NW
LTpp-LTv-LTc(a)
LTd1
Crystal-poor rhyodacitic magma
Sea level
basaltic andesitic enclave
Rhyodacitic magma generated by FC
Density filter
Mobilized melt
Mush
↑T°
Crystal clots removed from the mush
Depth (km)
Stage 3
(c)
SE
LTc(b)
LTsl
Crystal-rich mingled dacitic and andesitic magma
Sea level
Smaller volume of rhyodacitic magma
Mobilized melt
↑T°
Depth (km)
Stage 4
(d)
SE
LTv
Historical units
Crystal-rich mixed/mingled dacitic magma
Sea level
Basaltic andesitic magma
Mobilized melt
↑T°
Andesitic and Basaltic andesitic magma
Depth (km)

Figure 3.11. Simplified and interpretive scheme to explain the post-LGM magmatic evolution of the Las Termas edifice (NdC) conditioned by temporal/spatial evolution of the magmatic system. **(a)** In stage 1, basaltic andesitic compositions (LTd) are emitted from a magma storage level located at the depth of the ICD (Intracrustal Density Discontinuity). This storage level is fed by batches of less differentiated magmas from deeper levels of the crust. **(b)** Basaltic andesitic magmas, which are not evacuated in stage 1, are stored on the ICD where evolve by fractional crystallization giving rise to silica-rich magmas over time. These evolved magmas act as a density filter for less differentiated magmas that intercept it. The intrusion of higher temperature magmas contributes to lowering the viscosity of the host magmas and the overpressure on the top of the reservoir increases allowing their ascent. In this stage, the magmas of intermediate compositions, generated by the interaction of the magmas of both storage levels, are not transported to the surface because the interaction is restricted to the base of the shallowest storage level. **(c)** in stage 3, because the volume of evolved magma has decreased, a new intrusion of less evolved magmas would affect a larger proportion of the host magma **(d)** Less evolved magmas reach the surface when they do not intersect the shallowest storage level, as a consequence of its decrease in volume over time, which is also evidenced by the focusing of volcanism in historical times.

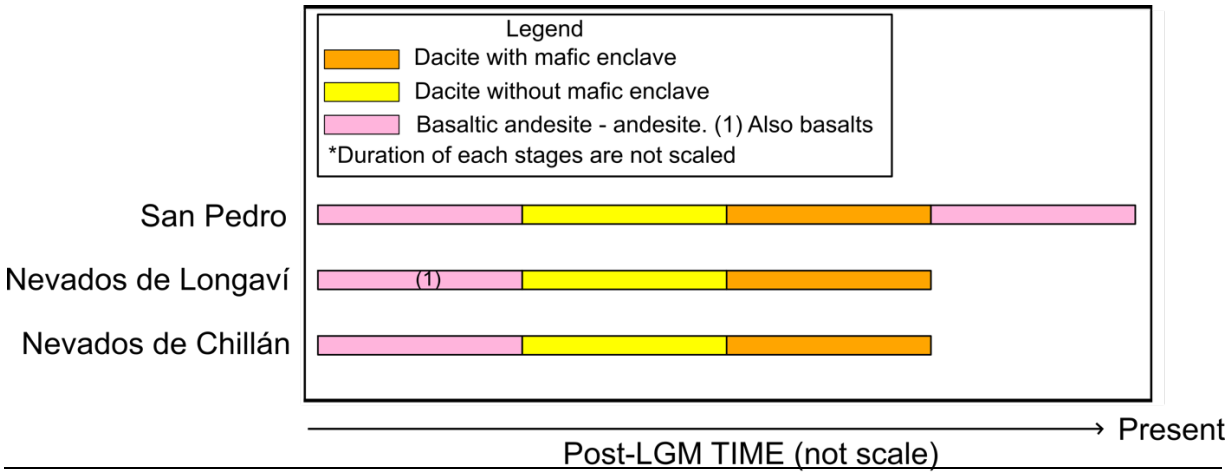

Figure 3.12. Comparison of the eruptive sequence and compositional characteristics during the post-LGM of the NdC with other volcanoes located in the same volcanic segment (TSVZ). Data obtained from Costa & Singer (2002) for San Pedro volcano and Sellés et al. (2004) and Rodríguez et al. (2007) for Nevados de Longaví volcano.

3.6 Conclusions

Based on textural evidence, mineral chemistry and geochemical modelling, we determined that the dacites emitted in the historical eruptions of the NdC were generated by magma mixing. A mechanism is proposed to explain the magmatic evolution of the LoC during the Holocene and that gives rise to a predominance of intermediate compositions in the youngest eruptive products. Crustal anisotropies enhanced by locally compressive tectonic regime hinder the ascent of basaltic andesitic magmas building a storage zone under the Intracrustal Density Discontinuity. The magmas that manage to overcome these crustal barriers are stored in the upper crust, where they are differentiated by fractional crystallization. The more differentiated magmas would act as a density filter for less evolved magmas from depth generating intermediate compositions by magma mixing processes. The less evolved magmas would be emitted only when they do not intercept the more differentiated magmas stored in the upper level. The latter was possible in the early post-LGM stage, when this storage level with evolved magmas

has not yet been established, or after that when they do not intersect with them during their rise, due to a decrease of its lateral extent.

We propose that the temporal/spatial evolution of the upper part of the NdC magmatic system, expressed in the establishment of a storage level with differentiated magmas and in its variations in volume, conditions the magmatic evolution of the NdC. This type of temporal/spatial evolution of the magmatic system may be playing a relevant role in the predominance of intermediate compositions in continental arc systems. Finally, a better understanding of the temporal evolution of magmatic systems could shed light on the present behavior of volcanoes, a key for reliable eruptive forecast.

3.7 Acknowledgements

The use of the EPMA facility at the Department of Earth Science, Rice University, Houston, TX is kindly acknowledged. We thank to Nicolás Luengo for providing us with the sample NCH-55 (Nicanor dome).

CAPÍTULO IV: DISCUSIÓN

Los resultados termobarométricos obtenidos en esta investigación revelan que las profundidades de cristalización de las fases minerales, incluidas en unidades de edad Pleistoceno Superior a Holoceno Medio, se extienden desde los 2.2 a 16.9 km de profundidad bajo la superficie. Por otra parte, el análisis de estos datos también revelan una zonación composicional vertical del sistema magmático alimentador del NdC, lo cual concuerda con lo sugerido por Mousallam et al. (2018), que identifican un material de composición andesítica basáltica, de aspecto juvenil, en la tefra asociada con la actividad Vulcaniana del ciclo eruptivo actual. Por otro lado, si sustraemos desde los resultados el valor de 2.2 km, obtenido a partir de sólo un cristal, lo que sugiere que pudo deberse a un crecimiento cristalino en su tránsito a superficie, los datos de profundidad de cristalización de las fases minerales en equilibrio con el fundido riodacítico abarcan desde ca. 4.4 a 10 km. Esta profundidad de cristalización coincide en parte con el nivel de almacenamiento de magma dacítico que estaría activo en tiempos recientes y que son inferidos en trabajos previos mediante el análisis de datos geofísicos (entre 4 a 6 km en Cardona et al. 2020 y 5.5 ± 0.5 km en Astort et al., 2022). Por otra parte, el nivel de almacenamiento más profundo y con magmas menos diferenciados, inferido en este estudio, concuerda con el nivel detectado por Gonzáles et al. (2018), el cual abarca profundidades entre 10 a 20 km bajo la superficie, lo que sugiere una estabilidad de los niveles de almacenamiento de magma del sistema alimentador del NdC durante el Holoceno. De esta forma, la información obtenida en esta investigación, mediante el uso de herramientas petrológicas, contribuye en ampliar el conocimiento acerca de la configuración del sistema magmático alimentador del NdC.

Sobre los factores que controlan la configuración del sistema magmático alimentador del NdC, los resultados termobarométricos muestran que la profundidad de cristalización de las fases minerales incluidas en las andesitas (<60 %wt SiO_2)/andesitas basálticas se extiende, en su mayoría, por debajo de la Discontinuidad Intracortical de Densidad (ICD) en esta área. Por su parte, las profundidades calculadas para las fases minerales en las lavas más evolucionadas

(>60 %wt SiO_2) estarían sobre este nivel. Adicionalmente, en este estudio se muestra que esta relación entre la ICD con los niveles de acumulación y composición de los magmas, también ocurre en otros sistemas volcánicos de la Zona Volcánica Sur de los Andes (ZVS), como por ejemplo en el Volcán Lonquimay. De esta forma, se destaca el rol que cumple la ICD en la acumulación de magmas en niveles intermedios de la corteza. Por otra parte, para los niveles de acumulación de magmas más someros, se ha propuesto, en algunos sistemas volcánicos de la ZVS (Piquer et al., 2019), que los magmas son almacenado en la intersección de estructuras oblicuas al arco (NO y NE). Aunque en esta tesis no se efectuaron estudios estructurales, los antecedentes geofísicos (González et al., 2018; Cardona et al., 2020) y el alineamiento de los centros eruptivos, sugieren que el sistema magmático del NdC estaría controlado por una estructura heredada del basamento de rumbo noroeste (Falla Cortaderas). De esta forma, se puede especular que los magmas más evolucionados del NdC se almacenan en la intersección de esta falla (NO) con otras estructuras de rumbo noreste (NE) que se han reconocidos en la zona del NdC (Meulle-Stef. 2016). El techo del reservorio podría estar limitado por los rellenos volcano-clásticos oligo-miocenos de la subcuenca Chillán, los cuales tienen un espesor aproximado de 2.5 km en un área cercana al Complejo Volcánico Nevados de Chillán (Radic, 2010), ya que las diferencias de rigidez entre distintas capas del basamento favorecen la acumulación de magmas (Gudmundsson, 2006). En forma análoga, la ICD también representa un cambio en las propiedades mecánicas entre distintas capas de la corteza, lo que favorece el estancamiento de magmas. Este cambió en las propiedades mecánicas entre las capas de la corteza limitadas por la ICD es consistente con el patrón NO de los datos geofísicos bajo el NdC (Lupi et al., 2020), aproximadamente sobre la profundidad de la ICD en esta zona. Estos antecedentes destacan el papel de primer orden que desempeñan las discontinuidades corticales y las estructuras del basamento en la arquitectura de un sistema magmático alimentador.

Por otra parte, la evaluación de los procesos magmáticos, que dan origen a los magmas dacíticos evacuados en tiempos históricos en el NdC, nos entrega información sobre la dinámica actual del sistema magmático alimentador. Los

resultados, basados en herramientas petrológicas, revelan un origen por procesos de mezcla de magma en la corteza superior para estas dacitas. Los magmas más evolucionados almacenados en los niveles superiores del sistema magmático alimentador del NdC son recargados con magmas más densos y menos evolucionados provenientes de niveles más profundos de la corteza, generando las composiciones intermedias. Estos proceso de intrusión de magma hacia el reservorio más somero también es propuesto por Astort et al. (2022) y Mousallam et al. (2018) para el ciclo eruptivo más reciente del NdC. La ocurrencia de estos procesos de intrusión de magmas pudo ser favorecida por una reactivación de la estructura heredada del basamento de rumbo noroeste (NO). Lupi et al. (2020) sugiere, mediante estudios de deformación inter y post-sísmica y de datos sísmicos en el área del NdC, que el Terremoto del Maule de 2010 (M 8.8) generó variaciones transitorias de tensión en el arco volcánico, que posiblemente reactivó las estructura noroeste sobre la cual se desarrollan los edificios volcánicos.

La petrogénesis de algunas unidades más antiguas del NdC también fueron evaluadas, lo cual junto con la información cronoestratigráfica disponible en la literatura (Dixon et al., 1999; Naranjo et al., 2008), permiten discutir la evolución magmática del edificio Las Termas del NdC y los factores principales que la controlan. En las primeras etapas Post-LGM (último máximo glacial), son emitidos magmas de composiciones andesíticas basálticas desde el edificio Las Termas del NdC. Se infiere que los magmas andesíticos basálticos, provenientes de profundidades bajo la ICD y que no alcanzan la superficie, son almacenados a lo largo de la estructura mayor de rumbo noroeste (NO), donde evolucionan por cristalización fraccionada hasta composiciones magmáticas riodacíticas, desarrollando un reservorio tipo mush. En este contexto, el NdC forma parte de una asociación volcano-tectónica cinemáticamente desacoplada con el régimen tectónico dictado por la convergencia de placas en el largo plazo (Cembrano y Lara, 2009). En este tipo de interacción volcano-tectónica y para la ZVS, Cembrano y Lara (2009) sugieren que los tiempo de residencia de los magmas en la corteza son más largos en un sistema magmático alimentador dominado por estructuras de rumbo NO, en comparación a sistemas dominados por estructuras de rumbo diferente, ya que

presentarían un comportamiento transpresional/compresivo en el largo plazo. Este mayor tiempo de residencia de los magmas promueve la diferenciación por cristalización fraccionada de los magmas en la corteza superior, en períodos con bajas presiones de fluidos, y por lo tanto la erupción de magmas evolucionados (Cembrano y Lara., 2009). De esta forma, el control tectónico del NdC explica las composiciones más evolucionadas del edificio Las Termas del NdC y su diferenciación por cristalización fraccionada. Estos magmas evolucionados actúan como filtro de densidad para los magmas más densos provenientes desde niveles más profundos de la corteza, generando las composiciones intermedias del NdC mediante temporal/espacial del sistema alimentador magmático del NdC, expresada en el establecimiento de un nivel de almacenamiento en la corteza superior con magma evolucionados, y el control tectónico juegan un rol clave en su evolución magmática.

Adicionalmente, se discute en esta tesis que la evolución magmática del NdC, que da origen a un predominio de composiciones intermedias en las lavas más jóvenes del NdC, es también influenciado por la disminución en el tiempo del volumen de magma riodacítico almacenado en la corteza superior. La erupción de los magmas riodacíticos del NdC emitidos en etapas previas a las composiciones intermedias fueron probablemente gatilladas por eventos de recarga de magmas máficos, ya que se ha propuesto que es el mecanismo más común en generar las erupciones volcánicas (Morgavi et al., 2017) y esto es consistente con la presencia de pequeños enclaves máficos en las últimas lavas riodacíticas emitidas en esa etapa. En esta etapa la mezcla composicional afectaría un volumen limitado del magma hospedante, probablemente restringido a su porción basal, lo cual explica la ausencia de composiciones intermedias en las lavas emitidas durante ese periodo en el NdC. Posteriormente, la emisión de composiciones intermedias sería favorecida por una disminución en el volumen de magma riodacítico almacenado en la corteza superior. Esta disminución del volumen de los magmas riodacíticos es respaldada por la disminución del volumen de las lavas con el tiempo y por una disminución de la extensión lateral de este reservorio, que es sugerida por la concentración acotada espacialmente del volcanismo en tiempos históricos y la emisión de composiciones

andesitícas basálticas, por un sector donde previamente fueron emitidas lavas riodacíticas. Como consecuencia, un menor volumen del end-member más evolucionado y hospedante, permite una proporción de magma mezclado mayor que en etapas previas, lo cual explicaría el predominio de composiciones intermedias en las unidades más jóvenes del NdC. Si bien, en otros sistemas volcánicos se ha propuesto que el predominio de composiciones intermedias, está relacionado a un mayor flujo de magma racargante (end-member menos evolucionado), en este estudio se propone que con un menor volumen del end-member más evolucionado se obtendrían los mismos resultados, siendo otro factor que se debería tener en cuenta al evaluar la evolución magmática de un volcán, lo que también es consistente con la disminución en el volumen de las lavas con el tiempo. En comparación a la erupción de los magmas riodacíticos del NdC, asociados a potentes depósitos de pómez, las erupciones históricas presentan un estilo eruptivo diferente (Figura 4.1), con menores contenidos de piroclastos, lo cual estaría principalmente asociado a una menor viscosidad de los magmas, que es controlado en gran medida por el contenido de sílice de los magmas. De esta forma, conocer la evolución magmática de un sistema volcánico y los factores principales que la controlan, ayudarían a tener pronósticos de las magnitudes de las erupciones más fiables.

Por último, las diferencias composicionales del edificio Cerro Blanco en comparación al edificio Las Termas, sugieren una evolución geológica diferente, cuyas causas deben ser analizadas en estudios más detallados en un futuro, lo cual ayudaría a tener una comprensión más completa del funcionamiento interno de los volcanes.

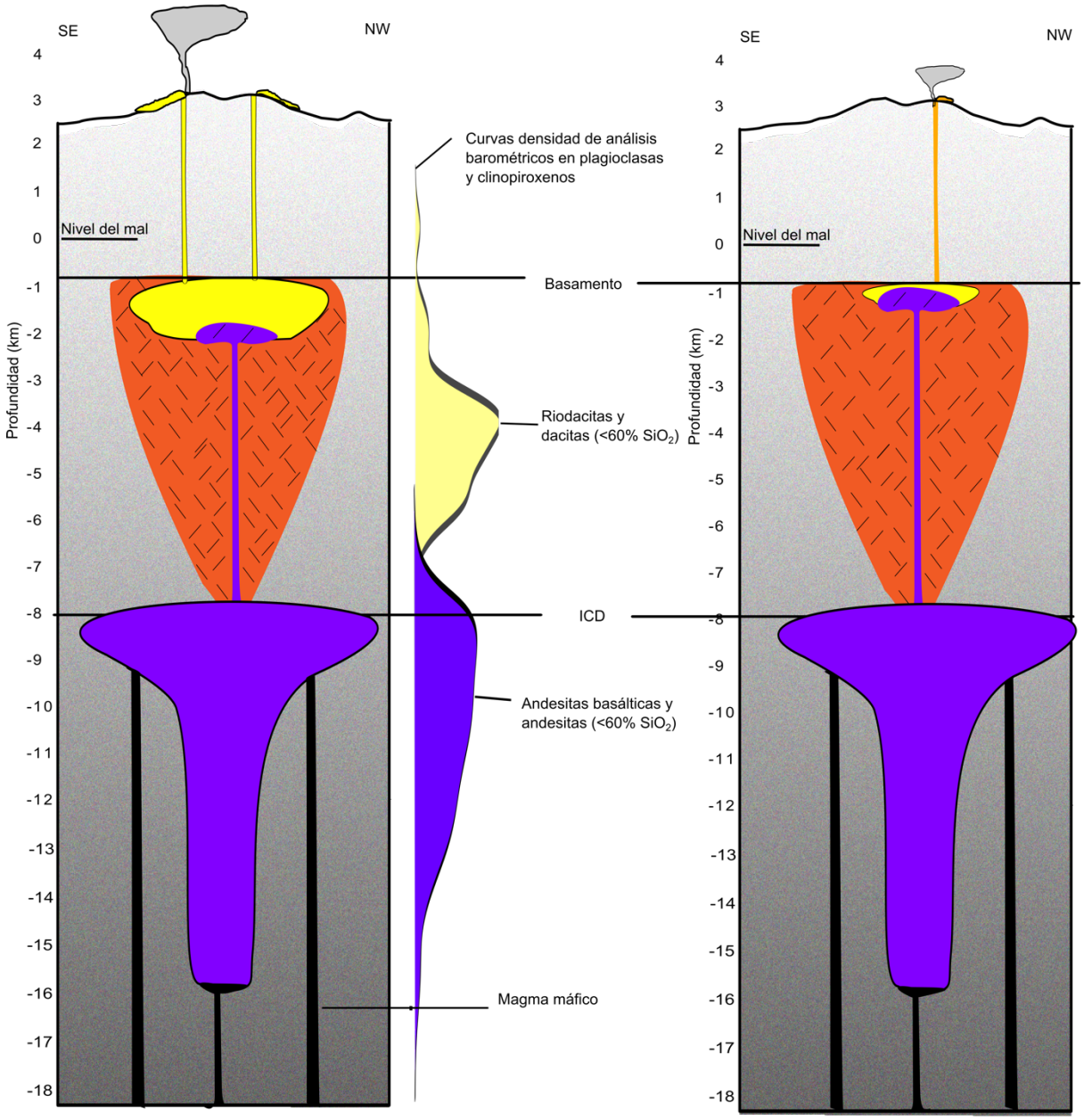

Figura 4.1. Modelo esquemático que integra las resultados de este tesis y los diferentes estilos eruptivos.

CAPÍTULO V: CONCLUSIONES

Las profundidades de cristalización, de las principales fases minerales de los productos eruptivos del Complejo Volcánico Nevados de Chillán (NdC), emitidos entre el Pleistoceno Superior y Holoceno Medio, abarcan profundidades entre 2.2 y 16.9 km bajo la superficie, lo cual coincide en gran medida con la configuración del sistema alimentador actual, propuesto mediante estudios geofísicos. La profundidades de cristalización, inferidas en esta tesis mediante los análisis termobarométricos, también revelan una zonación composicional vertical del sistema magmático alimentador del NdC, la cual coincide con la profundidad de la Discontinuidad Intracortical de Densidad (ICD). En este estudio, esta relación también es reconocida en otros sistemas volcánicos de la Zona Volcánica Sur de los Andes, lo cual destaca el rol de primer orden que cumple esta discontinuidad en controlar la configuración de los sistemas alimentadores, al menos en esta zona volcánica. Sobre esta discontinuidad, los magmas se alojarían en una estructura noroeste (NO) heredada del basamento, la cual presenta un comportamiento compresivo en el largo plazo en relación al régimen de esfuerzo dictado por la convergencia de las placas.

La evolución magmática del NdC estaría controlada por la estructura del basamento de rumbo NO y por la evolución temporal y espacial de su sistema alimentador magmático durante el Holoceno, la cual es expresada en el establecimiento de un nivel de almacenamiento de magmas evolucionados en la corteza superior y en sus variaciones temporales de volumen. En una primera etapa serían emitidos magmas andesíticos basáltico, alojados bajo la profundidad de la ICD, cuando el nivel de almacenamiento más somero aún no se ha establecido. Los magmas que no alcanzan la superficie, son alojados a lo largo de la estructura NO en la corteza superior, los cuales diferencian por cristalización fraccionada a magmas más evolucionados, favorecidos por el comportamiento compresivo de esta estructura en el largo plazo. Estos magmas evolucionados actúan como filtro de densidad para magmas menos diferenciados provenientes de los niveles de almacenamiento más profundos del sistema magmático alimentador. La mezcla de

estos magmas, composicionalmente diferentes, da origen a las composiciones intermedias del NdC, las cuales predominan con el tiempo en el registro eruptivo del NdC, como consecuencia del decrecimiento del volumen de magma riodacítico almacenado en la corteza superior.

Los resultados de esta tesis contribuyen en ampliar el conocimiento del sistema magmático alimentador del NdC y de su funcionamiento interno. Adicionalmente, conocer los factores claves que influyen en la evolución magmática, podría dar algunas señales sobre el comportamiento actual de un volcán, una clave para un pronóstico eruptivo fiable.

REFERENCIAS

Aiuppa, A., Cannata, A., Cannavò, F., Di Grazia, G., Ferrari, F., Giudice, G., Gurrieri, S., Liuzzo, M., Mattia, M., Montalto, P., Patanè, D., Puglisi, G., 2010. Patterns in the recent 2007–2008 activity of Mount Etna volcano investigated by integrated geophysical and geochemical observations. Geochemistry, Geophysics, Geosystems. 11(9). https://doi.org/10.1029/2010GC003168

Almeev, R. R., Kimura, J. I., Ariskin, A. A., Ozerov, A. Y., 2013. Decoding crystal fractionation in calc-alkaline magmas from the Bezymianny Volcano (Kamchatka, Russia) using mineral and bulk rock compositions. Journal of Volcanology and Geothermal Research. *263*, 141-171. https://doi.org/10.1016/j.jvolgeores.2013.01.003

Andújar, J., Scaillet, B., Pichavant, M., Druitt, T. H., 2015. Differentiation conditions of a basaltic magma from Santorini, and its bearing on the production of andesite in arc settings. Journal of Petrology. *56*(4), 765-794. https://doi.org/10.1093/petrology/egv016

Annen, C., Sparks, R. S. J., 2002. Effects of repetitive emplacement of basaltic intrusions on thermal evolution and melt generation in the crust. Earth and Planetary Science Letters. 203(3-4), 937-955. https://doi.org/10.1016/S0012-821X(02)00929-9

Annen, C., Blundy, J. D., & Sparks, R. S. J., 2006. The genesis of intermediate and silicic magmas in deep crustal hot zones. *Journal of Petrology*, *47*(3), 505-539.

Annen, C., Blundy, J. D., Leuthold, J., Sparks, R. S. J., 2015. Construction and evolution of igneous bodies: Towards an integrated perspective of crustal magmatism. Lithos. 230, 206-221. https://doi.org/10.1016/j.lithos.2015.05.008

Astort, A., Boixart, G., Folguera, A., & Battaglia, M., 2022. Volcanic unrest at Nevados de Chillán (Southern Andean Volcanic Zone) from January 2019 to November 2020, imaged by DInSAR. *Journal of Volcanology and Geothermal Research*, *427*, 107568.

Bååth, R., 2018. Bayesboot: An Implementation of Rubin's (1981) Bayesian Bootstrap. R package version 0.2.2. https://CRAN.R-project.org/package=bayesboot

Bacon, C. R., Hirschmann, M. M., 1988. Mg/Mn partitioning as a test for equilibrium between coexisting Fe-Ti oxides. American Mineralogist. *73*(1-2), 57-61.

Bas, M. L., Maitre, R. L., Streckeisen, A., Zanettin, B., IUGS Subcommission on the Systematics of Igneous Rocks., 1986. A chemical classification of volcanic rocks based on the total alkali-silica diagram. Journal of Petrology. *27*(3), 745-750.

Benet, D., Costa, F., Pedreros, G., & Cardona, C., 2021. The volcanic ash record of shallow magma intrusion and dome emplacement at Nevados de Chillán Volcanic complex, Chile. *Journal of Volcanology and Geothermal Research*, 417, 107308. https://doi.org/10.1016/j.jvolgeores.2021.107308

Blundy, J., Cashman, K., 2001. Ascent-driven crystallisation of dacite magmas at Mount St Helens, 1980–1986. Contributions to Mineralogy and Petrology. *140*(6), 631-650.

Blundy, J., & Cashman, K., 2008. Petrologic reconstruction of magmatic system variables and processes. *Reviews in Mineralogy and Geochemistry*, 69(1), 179-239. https://doi.org/10.2138/rmg.2008.69.6

Blundy, J., Cashman, K., & Humphreys, M., 2006. Magma heating by decompression-driven crystallization beneath andesite volcanoes. *Nature*, 443(7107), 76-80. https://doi.org/10.1038/nature05100

Bouvet de Maisonneuve, C. B., Forni, F., & Bachmann, O., 2021. Magma reservoir evolution during the build up to and recovery from caldera-forming eruptions–A generalizable model?. *Earth-Science Reviews*, *218*, 103684.

Burchardt, S., 2018. Introduction to volcanic and igneous plumbing systems—Developing a discipline and common concepts. In *Volcanic and igneous plumbing systems* (pp. 1-12). Elsevier.

Cardona, C., Gil-Cruz, F., Franco-Marín, L., San Martín, J., Valderrama, O., Lazo, J., Cartes, C., Morales, S., Hernández, E., Quijada, J., Pinto, C., Vidal, M., Bravo, C., Pedreros, G., Contreras, M., Figueroa, M., Córdova, L., Mardones, C., Alarcón, A., Velásquez, G. & Bucarey, C., 2021. Volcanic activity accompanying the emplacement of dacitic lava domes and effusion of lava flows at Nevados de Chillán Volcanic Complex–Chilean Andes (2012 to 2020). *Journal of Volcanology and Geothermal Research*, 107409. https://doi.org/10.1016/j.jvolgeores.2021.107409

Caricchi, L., & Blundy, J., 2015. The temporal evolution of chemical and physical properties of magmatic systems. *Geological Society, London, Special Publications*, *422*(1), 1-15.

Carr, M. J. & Gazel, E., 2017. Igpet software for modeling igneous processes: examples of application using the open educational version. *Mineralogy and Petrology*, 111(2), 283-289. https://doi.org/10.1007/s00710-016-0473-z

Cashman, K. V., Sparks, R. S. J., & Blundy, J. D., 2017. Vertically extensive and unstable magmatic systems: a unified view of igneous processes. *Science*, *355*(6331), eaag3055.

Castro, J.M., Schipper, C.I., Mueller, S. P., Militzer, A, S., Amigo, A., Parejas, C. S., Jacob, D., 2013. Storage and eruption of near-liquidus rhyolite magma at Cordón

Caulle, Chile. Bulletin of Volcanology. 75(4), 1-17. https://doi.org/10.1007/s00445-013-0702-9

Cembrano, J., Lara, L., 2009. The link between volcanism and tectonics in the southern volcanic zone of the Chilean Andes: a review. Tectonophysics. 471(1-2), 96-113. https://doi.org/10.1016/j.tecto.2009.02.038

Costa, F. & Singer, B., 2002. Evolution of Holocene dacite and compositionally zoned magma, Volcán San Pedro, southern volcanic zone, Chile. *Journal of Petrology*, 43(8), 1571-1593. https://doi.org/10.1093/petrology/43.8.1571

Costa, F., Scaillet, B. & Pichavant, M., 2004. Petrological and experimental constraints on the pre-eruption conditions of Holocene dacite from Volcán San Pedro (36 S, Chilean Andes) and the importance of sulphur in silicic subduction-related magmas. *Journal of Petrology*, 45(4), 855-881. https://doi.org/10.1093/petrology/egg114

Coppola, D., Laiolo, M., Lara, L. E., Cigolini, C. & Orozco, G., 2016. The 2008 “silent” eruption of Nevados de Chillán (Chile) detected from space: Effusive rates and trends from the MIROVA system. *Journal of Volcanology and Geothermal Research*, 327, 322-329. https://doi.org/10.1016/j.jvolgeores.2016.08.016

Couch, S., Sparks, R. S. J. & Carroll, M. R., 2001. Mineral disequilibrium in lavas explained by convective self-mixing in open magma chambers. *Nature*, 411(6841), 1037-1039. https://doi.org/10.1038/35082540

Davidson, J., Tepley III, F., Palacz, Z. & Meffan-Main, S., 2001. Magma recharge, contamination and residence times revealed by in situ laser ablation isotopic analysis of feldspar in volcanic rocks. *Earth and Planetary Science Letters*, 184(2), 427-442. https://doi.org/10.1016/S0012-821X(00)00333-2

Deruelle B. & López-Escobar L., 1999. Basalts, andesites, dacites and rhyolites from Nevados de Chillán and Antuco stratovolcanoes (Southern Andes): A remarkable example of magmatic differentiation through crystal fractionation. *Comp. Rend. Acad. Sci. Paris,* Ser. 2A.329, 337-344.

Dixon, H. J., Murphy, M. D., Sparks, R. S. J., Chaves, R., Naranjo, J. A., Dunkley, P. N., Young, S., Gilbert, J. & Pringle, M. R., 1999. The evolution of Volcan Nevados de Chillan, Chile. *Revista Geologica de Chile*, 26(2), 227-253. http://dx.doi.org/10.4067/S0716-02081999000200006

Edmonds, M., Cashman, K. V., Holness, M. & Jackson, M., 2019. Architecture and dynamics of magma reservoirs. *Philosophical Transactions of the Royal Society A*, 377(2139), 20180298. https://doi.org/10-1098/rsta.2018.0298

Ersoy, E. Y., 2013. PETROMODELER (Petrological Modeler): a Microsoft® Excel© spreadsheet program for modelling melting, mixing, crystallization and assimilation processes in magmatic systems. *Turkish Journal of Earth Sciences*, 22(1), 115-125. https://doi.org/10.3906/yer-1104-6

Eichelberger, J. C., 1980. Vesiculation of mafic magma during replenishment of silicic magma reservoirs. *Nature*, 288(5790), 446-450. https://doi.org/10.1038/288446a0

Eichelberger, J., 2010. Messy magma mixtures. *Nature Geoscience*, 3(9), 593-594. https://doi.org/10.1038/ngeo951

Farías, C., Lupi, M., Fuchs, F., & Miller, S. A., 2014. Seismic activity of the Nevados de Chillán volcanic complex after the 2010 Mw8. 8 Maule, Chile, earthquake. *Journal of volcanology and geothermal research*, *283*, 116-126.

Farías, C., & Basualto, D., 2020. Reactivating and calming volcanoes: the 2015 MW 8.3 Illapel megathrust strike. *Geophysical Research Letters*, *47*(16), e2020GL087738.

Farias, C., & Galvan, B., 2020. Numerical wave propagation study of the unusual response of Nevados de Chillán volcano to two aftershocks of the 2010 MW= 8.8 Maule earthquake. *Journal of Volcanology and Geothermal Research*, *389*, 106735.

Frey, H. M. & Lange, R. A., 2011. Phenocryst complexity in andesites and dacites from the Tequila volcanic field, Mexico: resolving the effects of degassing vs. magma mixing. *Contributions to Mineralogy and Petrology*, 162(2), 415-445. https://doi.org/10.1007/s00410-010-0604-1

Folguera, A., Zapata, T., Ramos, V. A., 2006. Late Cenozoic extension and the evolution of the Neuquén Andes. Special Papers-Geological Society of America. 407, 267.

Giacomoni, P. P., Coltorti, M., Bryce, J. G., Fahnestock, M. F., Guitreau, M., 2016. Mt. Etna plumbing system revealed by combined textural, compositional, and thermobarometric studies in clinopyroxenes. Contributions to Mineralogy and Petrology. 171(4), 34.

Ghiorso, M. S., Evans, B. W., 2008. Thermodynamics of rhombohedral oxide solid solutions and a revision of the Fe-Ti two-oxide geothermometer and oxygen-barometer. American Journal of Science. 308(9), 957-1039. https://doi.org/10.2475/09.2008.01

Ghiorso, M. S. & Gualda, G. A., 2015. An H2O–CO2 mixed fluid saturation model compatible with rhyolite-MELTS. *Contributions to Mineralogy and Petrology*, 169(6), 1-30. https://doi.org/10.1007/s00410-015-1141-8

Gilbert, D., Freundt, A., Kutterolf, S. & Burkert, C., 2014. Post-glacial time series of explosive eruptions and associated changes in the magma plumbing system of

Lonquimay volcano, south central Chile. *International Journal of Earth Sciences*, 103(7), 2043-2062. https://doi.org/10.1007/s00531-012-0796-x

Gill, J. B., 1981. What is “Typical Calcalkaline Andesite”?. *Orogenic Andesites and Plate Tectonics*, 16, 1-12. https://doi.org/10.1007/978-3-642-68012-0_1

Ginibre, C. & Wörner, G., 2007. Variable parent magmas and recharge regimes of the Parinacota magma system (N. Chile) revealed by Fe, Mg and Sr zoning in plagioclase. *Lithos*, 98(1-4), 118-140. https://doi.org/10.1016/j.lithos.2007.03.004

Ginibre, C., Wörner, G. & Kronz, A., 2002. Minor-and trace-element zoning in plagioclase: implications for magma chamber processes at Parinacota volcano, northern Chile. *Contributions to Mineralogy and Petrology*, 143(3), 300-315. https://doi.org/10.1007/s00410-002-0351-z

Ginibre, C., Kronz, A., WoÈrner, G., 2002. High-resolution quantitative imaging of plagioclase composition using accumulated backscattered electron images: new constraints on oscillatory zoning. Contributions to Mineralogy and Petrology. 142(4), 436-448. https://doi.org/10.1007/s004100100298

Gualda, G. A., Ghiorso, M. S., Lemons, R. V. & Carley, T. L., 2012. Rhyolite-MELTS: a modified calibration of MELTS optimized for silica-rich, fluid-bearing magmatic systems. *Journal of Petrology*, 53(5), 875-890. https://doi.org/10.1093/petrology/egr080

Gudmundsson, A., 2006. How local stresses control magma-chamber ruptures, dyke injections, and eruptions in composite volcanoes. *Earth-science reviews*, *79*(1-2), 1-31.

González, O., Vergara, M., 1962. Reconocimiento Geológico de la cordillera de los Andes entre los paralelos 35º y 38ºS. Universidad de Chile, Instituto de Geología Publicacion. 24,121.

González-Vidal, D., Obermann, A., Tassara, A., Bataille, K. & Lupi, M., 2018. Crustal model of the Southern Central Andes derived from ambient seismic noise Rayleigh-wave tomography. *Tectonophysics*, 744, 215-226. https://doi.org/10.1016/j.tecto.2018.07.004

Gudmundsson, A., 2011. Deflection of dykes into sills at discontinuities and magma-chamber formation. Tectonophysics. 500(1-4), 50-64. https://doi.org/10.1016/j.tecto.2009.10.015

Hernando, I. R., Llambías, E. J., González, P. D., Sato, K., 2012. Estratigrafía volcánica y evidencia de mezcla de magmas en el volcán Payún Matrú del Cuaternario, en el retroarco andino de Argentina occidental. Andean Geology. 39(1), 158-179.

Hildreth, W., Moorbath, S., 1988. Crustal contributions to arc magmatism in the Andes of central Chile. Contributions to Mineralogy and Petrology. 98(4), 455-489. https://doi.org/10.1007/BF00372365

Holness, M. B., Hallworth, M. A., Woods, A. & Sides, R. E., 2007. Infiltration metasomatism of cumulates by intrusive magma replenishment: the Wavy Horizon, Isle of Rum, Scotland. *Journal of Petrology*, 48(3), 563-587. https://doi.org/10.1093/petrology/egl072

Humphreys, M. C., Blundy, J. D., Sparks, R. S. J., 2006. Magma evolution and open-system processes at Shiveluch Volcano: Insights from phenocryst zoning. Journal of Petrology. 47(12), 2303-2334. https://doi.org/10.1093/petrology/egl045

Kahl, M., Chakraborty, S., Costa, F. & Pompilio, M., 2011. Dynamic plumbing system beneath volcanoes revealed by kinetic modeling, and the connection to monitoring data: An example from Mt. Etna. *Earth and Planetary Science Letters*, 308(1-2), 11-22. https://doi.org/10.1016/j.epsl.2011.05.008

Kavanagh, J. L., Menand, T., Sparks, R. S. J., 2006. An experimental investigation of sill formation and propagation in layered elastic media. Earth and Planetary Science Letters. 245(3-4), 799-813. https://doi.org/10.1016/j.epsl.2006.03.025

Kent, A. J., Darr, C., Koleszar, A. M., Salisbury, M. J. & Cooper, K. M., 2010. Preferential eruption of andesitic magmas through recharge filtering. *Nature geoscience*, 3(9), 631-636. https://doi.org/10.1038/ngeo924

Lara, L. E., Flores, F., Calderón, R. & Cardona, C., 2021. Volcano hazards and risks in Chile. In Forecasting and Planning for Volcanic Hazards, Risks, and Disasters. *Elsevier*, 617-633. https://doi.org/10.1016/B978-0-12-818082-2.00017-2

López-Escobar, L., Kilian, R., Kempton, P. D., Tagiri, M., 1993. Petrography and geochemistry of Quaternary rocks from the Southern Volcanic Zone of the Andes between 41 30' and 46 00'S, Chile. Andean Geology. 20(1), 33-55. http://dx.doi.org/10.5027/andgeoV20n1-a04

López-Escobar, L., Cembrano, J. & Moreno, H., 1995. Geochemistry and tectonics of the Chilean Southern Andes basaltic Quaternary volcanism (37-46 S). *Andean geology*, 22(2), 219-234.

Lucci F, Carrasco-Núñez G, Rossetti F, Theye T, White JC., 2020. Anatomy of the magmatic plumbing system of Los Humeros Caldera (Mexico): implications for geothermal systems. Solid Earth 11:125–59

Lupi, M., Trippanera, D., Gonzalez, D., D'amico, S., Acocella, V., Cabello, C., Muelle, M. & Tassara, A., 2020. Transient tectonic regimes imposed by megathrust earthquakes and the growth of NW-trending volcanic systems in the Southern Andes. *Tectonophysics*, *774*, 228204.

Martínez, P., Singer, B. S., Roa, H. M. & Jicha, B. R., 2018. Volcanologic and petrologic evolution of Antuco-Sierra Velluda, Southern Andes, Chile. *Journal of Volcanology and Geothermal Research*, 349, 392-408. https://doi.org/10.1016/j.jvolgeores.2017.11.026

Mee, K., 2004. The use of volcanic facies as tools for reconstructing former erupting environments at Nevados de Chillán volcano, Chile. Ph.D. Thesis, Lancaster University. Lancaster, United Kingdom.

Mee, K., Gilbert, J. S., McGarvie, D. W., Naranjo, J. A. & Pringle, M. S., 2009. Palaeoenvironment reconstruction, volcanic evolution and geochronology of the Cerro Blanco subcomplex, Nevados de Chillán volcanic complex, central Chile. *Bulletin of Volcanology*, 71(8), 933-952. https://doi.org/10.1007/s00445-009-0277-7

Menand, T., 2008. The mechanics and dynamics of sills in layered elastic rocks and their implications for the growth of laccoliths and other igneous complexes. Earth and Planetary Science Letters. 267(1-2), 93-99. https://doi.org/10.1016/j.epsl.2007.11.043

Middlemost, E. A., 1989. Iron oxidation ratios, norms and the classification of volcanic rocks. Chemical Geology. 77(1), 19-26. https://doi.org/10.1016/0009-2541(89)90011-9

Mollo, S., Del Gaudio, P., Ventura, G., Iezzi, G., Scarlato, P., 2010. Dependence of clinopyroxene composition on cooling rate in basaltic magmas: Implications for thermobarometry. Lithos. 118(3-4), 302-312. https://doi.org/10.1016/j.lithos.2010.05.006

Morgavi, D., Arienzo, I., Montagna, C., Perugini, D. & Dingwell, D. B., 2017. Magma mixing: History and dynamics of an eruption trigger. *Volcanic Unrest*, 123-137.

Morgado, E., Morgan, D. J., Harvey, J., Parada, M. Á., Castruccio, A., Brahm, R., Gutiérrez, F., Georgiev, B., Hammond, S. J., 2019. Localised heating and intensive magmatic conditions prior to the 22–23 April 2015 Calbuco volcano eruption (Southern Chile). Bulletin of Volcanology. 81(4), 1-21. https://doi.org/10.1007/s00445-019-1280-2

Morimoto, N., Fabries, J., Ferguson, A. K. 1988. Pyroxene nomenclature. Mineralogy and Petrology. 39, 55-76. https://doi.org/10.1007/BF01226262

Moussallam, Y., Bani, P., Schipper, C. I., Cardona, C., Franco, L., Barnie, T., Amigo, A., Curtis, A., Peters, N., Aiuppa, A., Giudice, G. & Oppenheimer, C., 2018. Unrest at the Nevados de Chillán volcanic complex: a failed or yet to unfold magmatic eruption?. *Volcanica*. https://doi.org/10.30909/vol.01.01.1932

Meulle-Stef, M., 2016. Modelo estructural y régimen de esfuerzos para el Complejo Volcánico Nevados de Chillán, Región del Biobío, Chile. Memoria de título. Universidad de Concepción, Chile.

Murphy, M. D., 1995. The geology and geochemistry of Nevados de Chillán volcano. *ChileBritish Geological Survey*. Keyworth, Nottingham, U.K.

Naranjo, J. A. & Lara, L. E., 2004. August-September 2003 small vulcanian eruption at the Nevados de Chillán Volcanic Complex (36° 50'S), Southern Andes (Chile). Revista Geológica de Chile. 31(2), 359-366. http://dx.doi.org/10.4067/S0716-02082004000200011

Naranjo, J.A., Gilbert, J. & Sparks, R.S., 2008. Geología del complejo volcánico Nevados de Chillán, Región del Biobío. *Servicio Nacional de Geología y Minería, Carta Geológica de Chile, Serie Geología Básica,* 114: 28. 1 mapa escala 1:50.000.

Naranjo, J. A., Singer, B. S., Jicha, B. R., Moreno, H. & Lara, L. E., 2017. Holocene tephra succession of Puyehue-Cordón Caulle and Antillanca/Casablanca volcanic complexes, southern Andes (40–41 S). *Journal of Volcanology and Geothermal Research*, 332, 109-128. https://doi.org/10.1016/j.jvolgeores.2016.11.017

Nelson, S. T., Montana, A., 1992. Sieve-textured plagioclase in volcanic rocks produced by rapid decompression. American Mineralogist. 77(11-12), 1242-1249.

Oyarzún, A., Lara, L. E. & Tassara, A., 2022. Decoding the plumbing system of Nevados de Chillán Volcanic complex, Southern Andes. *Journal of Volcanology and Geothermal Research*, 422, 107455. https://doi.org/10.1016/j.jvolgeores.2021.107455

Piquer, J., Yáñez, G., Rivera, O., & Cooke, D. R., 2019. Zonas de daño cortical de larga vida, asociadas con intersecciones estructurales en los altos Andes de Chile central. *Andean geology*, *46*(2), 223-239.

Putirka, K. D., 2008. Thermometers and barometers for volcanic systems. Reviews in Mineralogy and Geochemistry. 69(1), 61-120. https://doi.org/10.2138/rmg.2008.69.3

Radic, J. P., 2010. Las cuencas cenozoicas y su control en el volcanismo de los Complejos Nevados de Chillán y Copahue-Callaqui (Andes del Sur, 36-39 S). Andean Geology. 37(1), 220-246.

Radic, J. P., Sipetrol, S. A., 2006. Anisotropías de basamento como control estructural del volcanismo en el Complejo volcánico Chillán (Andes del Sur, 36 S). In XI Congreso Geológico Chileno, Antofagasta. p. Actas (Vol. 2).

Reubi, O. & Blundy, J., 2009. A dearth of intermediate melts at subduction zone volcanoes and the petrogenesis of arc andesites. *Nature*, 461(7268), 1269-1273. https://doi.org/10.1038/nature08510

Rhodes, J. M., Dungan, M. A., Blanchard, D. P., Long, P. E., 1979. Magma mixing at mid-ocean ridges: evidence from basalts drilled near 22 N on the Mid-Atlantic Ridge. Tectonophysics. 55(1-2), 35-61. https://doi.org/10.1016/0040-1951(79)90334-2

RodrÍguez, C., Sellés, D., Dungan, M., Langmuir, C. & Leeman, W., 2007. Adakitic dacites formed by intracrustal crystal fractionation of water-rich parent magmas at Nevado de Longaví volcano (36· 2 S; Andean Southern Volcanic Zone, Central Chile). *Journal of Petrology*, 48(11), 2033-2061. https://doi.org/10.1093/petrology/egm049

RStudio Team., 2020. RStudio: Integrated Development for R. RStudio, PBC, Boston, MA URL http://www.rstudio.com/.

Rubin, D. B., 1981. The bayesian bootstrap. The annals of statistics, 130-134.

Ruprecht, P. & Wörner, G., 2007. Variable regimes in magma systems documented in plagioclase zoning patterns: El Misti stratovolcano and Andahua monogenetic cones. *Journal of Volcanology and Geothermal Research*, 165(3-4), 142-162. https://doi.org/10.1016/j.jvolgeores.2007.06.002

Ruprecht, P., Bergantz, G. W., Cooper, K. M., Hildreth, W., 2012. The crustal magma storage system of Volcán Quizapu, Chile, and the effects of magma mixing on magma diversity. Journal of Petrology. 53(4), 801-840. https://doi.org/10.1093/petrology/egs002

Ruprecht, P., Simon, A. C., Fiege, A., 2020. The survival of mafic enclaves and the timing of magma recharge. Geophysical Research Letters. 47(14), e2020GL087186. https://doi.org/10.1029/2020GL087186

Samaniego, P., Rivera, M., Manrique, N., Schiavi, F., Nauret, F., Liorzou, C., Ancellin, M. A., 2020. Linking magmatic processes and magma chemistry during the post-glacial to recent explosive eruptions of Ubinas volcano (southern Peru). Journal of Volcanology and Geothermal Research. 407, 107095. https://doi.org/10.1016/j.jvolgeores.2020.107095

Sellés, D., Rodríguez, A., Dungan, M. A., Naranjo, J. A. & Gardeweg, M., 2004. Geochemistry of Nevado de Longaví Volcano (36.2 S): a compositionally atypical arc volcano in the Southern Volcanic Zone of the Andes. *Revista geológica de Chile*, 31(2), 293-315. http://dx.doi.org/10.4067/S0716-02082004000200008

Sigmundsson, F., Parks, M., Pedersen, R., Jónsdóttir, K., Ófeigsson, B. G., Grapenthin, R., Dumont, S., Einarsson, P., Drouin, V., Heimisson, E., Hjasrtardóttir, A., Gudmunsson, M., Geirsson, H., Hreinsdóttir., Sturkell, E., Hooper, A., Högnadóttir., Vogfjörd, K., Barnie, T., Roberts, M. J., 2018. Magma movements in volcanic plumbing systems and their associated ground deformation and seismic patterns. In Volcanic and igneous plumbing systems (pp. 285-322). Elsevier. https://doi.org/10.1016/B978-0-12-809749-6.00011-X

Silva, C., Lara, L. E., Amigo, A., Bertin, D. & Orozco, G., 2012. Caracterización de los principales productos emitidos durante la erupción del Complejo Volcánico Puyehue-Cordón Caulle 2011-2012. In *XIII Congreso Geológico Chileno, Antofagasta*, 539-541.

Singer, B. S., Dungan, M. A. & Layne, G. D., 1995. Textures and Sr, Ba, Mg, Fe, K, and Ti compositional profiles in volcanic plagioclase: clues to the dynamics of calc-

alkaline magma chambers. *American Mineralogist*, 80(7-8), 776-798. https://doi.org/10.2138/am-1995-7-819

Singer, B. S., Jicha, B. R., Harper, M. A., Naranjo, J. A., Lara, L. E. & Moreno-Roa, H., 2008. Eruptive history, geochronology, and magmatic evolution of the Puyehue-Cordón Caulle volcanic complex, Chile. *Geological Society of America Bulletin*, 120(5-6), 599-618. https://doi.org/10.1130/B26276.1

Singh Arjona, D. I., 2019. Condiciones pre-eruptivas asociadas a la erupción del volcán Shangri-Lan, Complejo Volcánico Nevados de Chillán, Región del Ñuble, Chile mediante estudios en inclusiones vítreas. Universidad de Chile.

Sisson, T. W., Grove, T. L., 1993. Temperatures and H 2 O contents of low-MgO high-alumina basalts. Contributions to Mineralogy and Petrology. 113(2), 167-184. https://doi.org/10.1007/BF00283225

Sparks, R. S. J., Cashman, K. V., 2017. Dynamic magma systems: implications for forecasting volcanic activity. Elements. 13(1), 35-40. https://doi.org/10.2113/gselements.13.1.35

Stanton-Yonge, A., Griffith, W. A., Cembrano, J., St. Julien, R. & Iturrieta, P., 2016. Tectonic role of margin-parallel and margin-transverse faults during oblique subduction in the southern volcanic zone of the Andes: Insights from boundary element modeling. *Tectonics*, 35(9), 1990-2013. https://doi.org/10.1002/2016TC004226

Stern, C. R., 2004. Active Andean volcanism: its geologic and tectonic setting. Revista Geológica de Chile. 31(2), 161-206. http://dx.doi.org/10.4067/S0716-02082004000200001

Streck, M. J., 2008. Mineral textures and zoning as evidence for open system processes. *Reviews in Mineralogy and Geochemistry*, 69(1), 595-622. https://doi.org/10.2138/rmg.2008.69.15

Søager, N., Holm, P. M., Llambías, E. J., 2013. Payenia volcanic province, southern Mendoza, Argentina: OIB mantle upwelling in a backarc environment. Chemical Geology. 349, 36-53. https://doi.org/10.1016/j.chemgeo.2013.04.007

Sun, S. S., & McDonough, W. F., 1989. Chemical and isotopic systematics of oceanic basalts: implications for mantle composition and processes. *Geological Society, London, Special Publications*, *42*(1), 313-345.

Tassara, A. & Echaurren, A., 2012. Anatomy of the Andean subduction zone: three-dimensional density model upgraded and compared against global-scale models. *Geophysical Journal International*, 189(1), 161-168. https://doi.org/10.1111/j.1365-246X.2012.05397.x

Tassara, A., Götze, H. J., Schmidt, S. & Hackney, R., 2006. Three-dimensional density model of the Nazca plate and the Andean continental margin. *Journal of Geophysical Research: Solid Earth*, 111(B9). https://doi.org/10.1029/2005JB003976

Tepley III, F. J., Davidson, J. P., Clynne, M. A., 1999. Magmatic interactions as recorded in plagioclase phenocrysts of Chaos Crags, Lassen Volcanic Center, California. Journal of Petrology. 40(5), 787-806. https://doi.org/10.1093/petroj/40.5.787

Tsuchiyama, A., 1985. Dissolution kinetics of plagioclase in the melt of the system diopside-albite-anorthite, and origin of dusty plagioclase in andesites. Contributions to Mineralogy and Petrology. 89(1), 1-16. https://doi.org/10.1007/BF01177585

Valentine, G. A., Krogh, K. E., 2006. Emplacement of shallow dikes and sills beneath a small basaltic volcanic center–The role of pre-existing structure (Paiute Ridge, southern Nevada, USA). Earth and Planetary Science Letters. 246(3-4), 217-230. https://doi.org/10.1016/j.epsl.2006.04.031

Vander Auwera, J., Namur, O., Dutrieux, A., Wilkinson, C. M., Ganerod, M., Coumont, V., Bolle, O., 2019. Mantle melting and magmatic processes under La Picada stratovolcane (CSVZ, Chile). Journal of Petrology. 60(5), 907-944. https://doi.org/10.1093/petrology/egz020

Varela, J., Moreno, H., 1982. Los Depósitos de Relleno de la Depresión Central de Chile entre los ríos Lontué y Bío-Bío. In III Congreso Geológico Chileno, Actas, Vol. 2, p. F280-F306.

Vergara, M., Muñoz, J. 1982. La Formación Cola de Zorro en la alta cordillera Andina Chilena (36–39 Lat. S), sus características petrográficas y petrológicas: Una revisión. Revista Geológica de Chile. 17(1), 31-46.

Völker, D., Kutterolf, S., Wehrmann, H., 2011. Comparative mass balance of volcanic edifices at the southern volcanic zone of the Andes between 33 S and 46 S. Journal of Volcanology and Geothermal Research. 205(3-4), 114-129. https://doi.org/10.1016/j.jvolgeores.2011.03.011

Waters, L. E., Lange, R. A., 2015. An updated calibration of the plagioclase-liquid hygrometer-thermometer applicable to basalts through rhyolites. American Mineralogist. 100(10), 2172-2184. https://doi.org/10.2138/am-2015-5232

Weber, G., Arce, J. L., Ulianov, A., & Caricchi, L., 2019. A recurrent magmatic pattern on observable timescales prior to plinian eruptions from Nevado de Toluca (Mexico). *Journal of Geophysical Research: Solid Earth*, *124*(11), 10999-11021.

Wörner, G., Mamani, M. & Blum-Oeste, M., 2018. Magmatism in the central Andes. *Elements: An International Magazine of Mineralogy, Geochemistry, and Petrology*, *14*(4), 237-244. https://doi.org/10.2138/gselements.14.4.237

Zellmer, G. F., Turenr, S. P., 2007. Arc dacite genesis pathways: evidence from mafic enclaves and their hosts in Aegean lavas. Lithos. 95(3-4), 346-362. https://doi.org/10.1016/j.lithos.2006.08.002

Zhang, Y. X., Zeng, Z. G., Gaetani, G., Zhang, L., & Lai, Z. Q., 2020. Mineralogical constraints on the magma mixing beneath the Iheya Graben, an active back-arc spreading centre of the Okinawa trough. *Journal of Petrology*, *61*(9), egaa098.

ANEXOS

Anexo I: Análisis químicos de roca total

Óxidos (wt%)

Samples*	Unit	SiO_2	Al_2O_3	Fe_2O_3	MgO	CaO	Na_2O	K_2O	TiO_2	P_2O_5	MnO	Total
MDL(%)		0.01	0.01	0.04	0.01	0.01	0.01	0.01	0.01	0.01	0.01	
NCH-18	CBcpb	57.4	16.8	8	3.5	6.8	4.1	1.5	1.2	0.3	0.1	99.7
NCH-23	LTv	66	15.2	5	1.2	3.1	4.9	2.7	0.9	0.3	0.1	99.3
NCH-25	LTc(b)	61.5	15.7	5.4	2.8	4.7	3.8	2.7	0.8	0.3	0.1	97.7
NCH-26	LTa	65.7	15.2	5.1	1.3	3.3	4.9	2.7	0.9	0.2	0.1	99.5
NCH-27	LTss	65.2	15.3	5.3	1.3	3.4	4.9	2.6	0.9	0.2	0.1	99.3
NCH-31	LTd	67.8	14.7	4.5	0.9	2.5	4.9	3	0.7	0.2	0.1	99.5
NCH-33	LTs	56.8	18	7	4.1	7.2	3.9	1.3	0.9	0.2	0.1	99.6
NCH-34	LTac	66.3	15.8	4.3	1	2.9	5.6	2.3	0.8	0.2	0.1	99.3
NCH-37	LTpp	68	14.8	4.3	0.7	2.3	5.1	3.2	0.7	0.1	0.1	99.5
NCH-39	Dyke	60.3	16.5	6.7	2.1	4.8	4.9	1.9	1.2	0.2	0.1	99.2
NCH-44	CBg	62.8	15.5	6.5	1.8	4.2	5	2.1	1.3	0.4	0.1	99.7
NCH-45	CBb	65.5	15.2	5.3	1.4	3.5	4.8	2.8	0.9	0.2	0.1	99.6
NCH-46	LTsl	65.6	15.3	4.9	1.8	3.7	4.6	2.8	0.8	0.2	0.1	99.7
NCH-49	Dyke	54.9	17.5	7.9	4.3	7.8	3.8	0.9	1	0.2	0.1	98.4
NCH-50	CBo	55.3	17.6	8.1	4.3	7.5	4	1	1.1	0.2	0.1	99.3
NCH-52	CBcpb	56.1	18	7.4	3.8	7.7	4	1.2	1	0.2	0.1	99.5
NCH-53	P.cone	56.1	17.4	7	5.4	7.6	3.7	1.2	0.8	0.2	0.1	99.6
NCH-54	CBsg	55.3	18.2	8.2	4.3	7.8	4.1	0.8	1.1	0.2	0.1	100
NCH-55	LTni	64.4	15.6	5.5	1.4	3.7	4.9	2.6	0.9	0.2	0.1	99.5
NCH-60**	LTsl	55.2	17.7	7.9	4.3	7.8	3.9	1.1	1	0.2	0.1	99.3
NCH-63	Dyke	57	16.8	8.4	3.1	6.5	4.3	1.3	1.3	0.3	0.1	99.2
NCH-64	CBc	62.4	15.5	6.7	1.9	4.4	4.7	2.2	1.2	0.3	0.1	99.3

Elementos trazas (ppm)

Samples*	Ba	Ni	Sc	Be	Co	Cs	Ga	Hf	Nb	Rb	Sn
MDL(ppm)	**1**	**20**	**1**	**1**	**0.2**	**0.1**	**0.5**	**0.1**	**0.1**	**0.1**	**1**
NCH-18	378	<20	23	1	35.5	1.4	19.2	4.2	6.7	44.2	1
NCH-23	573	<20	14	6	22	5.8	18.1	8.3	8.3	94.3	2
NCH-25	458	33	15	1	42.1	4.7	17.8	6.2	6.6	82.6	1
NCH-26	528	<20	14	<1	19.9	5.8	17.7	8.2	7.1	91.4	3
NCH-27	525	<20	14	2	30.6	5.9	17.5	7.9	7.3	87.3	2
NCH-31	606	<20	12	1	17.8	6.4	17.4	8.7	7.4	101.9	2
NCH-33	340	30	17	0.5	37.2	1.2	17.6	3	3.7	31.4	0.5
NCH-34	498	<20	13	2	22.7	4.1	17.5	6.2	6.4	65.2	1
NCH-37	592	<20	11	<1	18.1	6.3	16.8	8.9	8.2	100	2
NCH-39	437	<20	17	<1	27.5	3.9	18.4	5.6	6.1	55.2	2
NCH-44	475	<20	17	1	26.9	2.8	18.5	5.9	6.3	61.3	2
NCH-45	531	<20	13	2	21.2	5.4	17.2	7.7	7.4	89.4	2
NCH-46	523	<20	12	2	23.6	5.8	16.6	7.9	7.2	90.5	2
NCH-49	258	27	22	2	37.8	1.3	17.7	3	3.4	20.2	<1
NCH-50	273	25	22	1	40.3	2	17.6	3.5	3.5	28.7	<1
NCH-52	289	26	21	2	44.8	2	18.4	3.4	3.5	31.1	<1
NCH-53	115	<20	2	<1	55.8	1.2	11.1	3.1	3	21.6	<1
NCH-54	248	27	25	2	31.9	1.4	20.4	2.6	4.7	20.6	<1
NCH-55	522	<20	14	<1	17.7	5.9	17.3	7.1	6	82.3	2
NCH-60**	275	30	22	1	52.5	2	18.4	3.1	3.4	29.6	<1
NCH-63	318	<20	24	<1	33.4	2.7	18.4	4.1	3.6	41.2	1
NCH-64	447	<20	18	1	23	2	17.6	6.3	5.1	65.4	2

Elementos trazas (ppm)

Samples*	Sr	Ta	Th	U	V	W	Zr	Y	La	Ce	Pr	Nd	Sm
MDL(ppm)	**0.5**	**0.1**	**0.2**	**0.1**	**8**	**0.5**	**0.1**	**0.1**	**0.1**	**0.1**	**0.02**	**0.3**	**0.05**
NCH-18	446.4	0.4	4.6	1.1	225	329.5	160.8	19.7	18.1	38.1	4.76	19.5	4.19
NCH-23	273.6	0.7	9.4	2.2	54	383.2	301.6	29.1	25.4	55.8	7.09	29.1	6.03
NCH-25	377.9	0.5	7	2	101	567	243.1	21.8	21.2	44.8	5.75	22.8	4.7
NCH-26	274.8	0.6	8.8	2.3	63	223.9	295	29.8	23.5	51.4	6.66	27.6	5.85
NCH-27	275.8	0.6	8.6	2.4	61	497.6	287	28.4	23.6	53.1	6.65	28.2	5.88
NCH-31	242.7	0.6	10.3	2.8	30	310	326	34.2	29	63.2	7.82	32.2	6.76
NCH-33	794.2	0.3	4.6	1.5	170	340.5	118.5	15.3	15.6	32.4	4.15	18.2	3.72
NCH-34	282	0.5	6.9	1.9	28	659.9	226.2	27.7	21.7	46.6	6.08	25	5.38
NCH-37	217.7	0.5	11.1	2.9	22	314.1	327	34.2	28	59.2	7.63	31.8	6.26
NCH-39	387.6	0.5	6.1	1.5	104	402	218.3	30.1	22.1	48.9	6.54	28.2	6.26
NCH-44	368.2	0.5	7.1	1.8	105	340.7	222.6	30.2	23.2	49.9	6.54	27.8	6.03
NCH-45	284.2	0.5	9.7	2.5	82	273.2	285.7	30.2	25.9	54.9	6.98	27.9	5.93
NCH-46	290.6	0.6	9.8	2.3	67	329.4	287.8	28.3	25.9	53.3	6.72	26.9	5.66
NCH-49	501.4	0.3	2.7	0.6	213	238.9	110	18	11.9	25.1	3.44	15.1	3.61
NCH-50	483.1	0.2	2.9	0.8	207	355.2	119.9	19.1	12.3	27.3	3.69	16.3	3.66
NCH-52	585.5	0.3	3.7	1.1	197	434.2	120.6	18.1	13.5	29.3	3.85	16.1	3.67
NCH-53	294.4	0.5	19.3	3.5	18	575.6	95.5	2.2	5.1	7.9	0.82	2.8	0.4
NCH-54	515	0.3	1.7	0.5	220	185	96.2	15.5	9.5	21.8	2.96	13.3	3.15
NCH-55	304.6	0.4	8.7	2.3	80	333.5	270.2	28.3	24.8	54.3	6.83	28.4	5.87
NCH-60**	535.5	0.3	3.6	1	202	600.9	118.6	17.6	13.4	28.8	3.7	15.8	3.54
NCH-63	472.2	0.4	3.7	1	231	289.5	145.5	23.4	16.2	36	4.83	21.7	4.89
NCH-64	353.6	0.4	7.3	1.8	144	425	221	26.4	21.7	46.7	6.14	25.9	5.68

Elementos trazas (ppm)

Samples*	Eu	Gd	Tb	Dy	Ho	Er	Tm	Yb	Lu
MDL(ppm)	**0.02**	**0.05**	**0.01**	**0.05**	**0.02**	**0.03**	**0.01**	**0.05**	**0.01**
NCH-18	1.17	4	0.61	3.61	0.69	2.08	0.3	1.95	0.28
NCH-23	1.3	5.66	0.87	5.23	1.09	3.37	0.48	3.13	0.46
NCH-25	1.13	4.42	0.7	4.21	0.81	2.44	0.38	2.34	0.35
NCH-26	1.3	5.68	0.89	5.1	1.05	3.27	0.45	3	0.46
NCH-27	1.25	5.49	0.89	5.11	1.06	3.18	0.48	3.07	0.45
NCH-31	1.39	6.52	1.03	5.7	1.21	3.79	0.53	3.57	0.51
NCH-33	1.01	3.28	0.47	2.71	0.54	1.53	0.22	1.46	0.22
NCH-34	1.29	5.31	0.81	4.94	1.03	2.98	0.43	2.68	0.43
NCH-37	1.28	6.09	0.99	5.7	1.21	3.5	0.51	3.35	0.51
NCH-39	1.48	6.16	0.92	5.28	1.1	3.05	0.43	2.75	0.44
NCH-44	1.51	6.1	0.89	5.14	1.06	3.07	0.43	2.76	0.43
NCH-45	1.24	5.74	0.87	5.2	1.08	3.17	0.46	2.94	0.45
NCH-46	1.1	5.34	0.83	4.84	1.02	2.95	0.43	2.65	0.43
NCH-49	1.01	3.63	0.54	3.19	0.65	1.9	0.28	1.73	0.28
NCH-50	1.14	3.88	0.58	3.37	0.68	2.01	0.28	1.88	0.28
NCH-52	1.09	3.65	0.56	3.27	0.61	1.92	0.26	1.61	0.27
NCH-53	0.33	0.36	0.05	0.32	0.07	0.28	0.04	0.36	0.08
NCH-54	0.98	3.11	0.52	2.96	0.57	1.69	0.24	1.58	0.31
NCH-55	1.28	5.92	0.9	5.03	1.12	3.21	0.49	2.88	0.49
NCH-60**	1.09	3.41	0.53	3.15	0.66	1.83	0.26	1.68	0.26
NCH-63	1.37	4.62	0.73	4.16	0.87	2.51	0.37	2.22	0.34
NCH-64	1.39	5.64	0.83	5.1	1.02	2.91	0.45	2.6	0.43

Anexo II: Condiciones analíticas en la obtención de la química mineral

Las composiciones del centro y borde de piroxenos, plagioclasas, olivinos y óxidos de Fe-Ti se obtuvieron mediante espectrometría de dispersión de longitud de onda (WDS) utilizando la microsonda electrónica (JEOLJXA-8600M Superprobe) en la Universidad de Concepción (Chile) y la Universidad de Rice (EE. UU.; JEOLJXA 8530F Hyperprobe). Los análisis se llevaron a cabo utilizando condiciones operativas estándar de aceleración de voltaje de 15 kV y haz de corriente de 20 nA y se utilizó un tamaño de punto de 3 μm para todos los análisis con la excepción de la plagioclasa, cuyo tamaño de haz se fijó en 10 μm de diámetro para evitar pérdidas de Na y K durante la interacción muestra-haz. Se utilizaron como muestras de referencia minerales naturales y sintéticos y óxidos simples, y el conjunto de estas muestras varió según el objeto de análisis. Para los análisis realizados en la Universidad de Concepción, las muestras de referencia fueron las siguientes: aquellas con código USNM fueron donadas por la Institución Smithsonian, USA (Jarosewich et al., 1980): diópsido USNM 117733 (Si, en olivino y piroxeno) , anortita USNM 137041 (Al), fayalita USNM 85276 (Fe), microclina USNM 143966 (K), cromita USNM 117075 (Cr), MnTiO3 (Ti y Mn), forsterita (Mg), jadeíta (Na), wollastonita (Ca) , sanidina (Si en plagioclasa). Para los análisis realizados en la Universidad de Rice, las muestras de referencia fueron las siguientes: plagioclasa-SPI (Si, Na, Ca y Al), ortoclasa-SPI (K en plagioclasa), biotita-SPI (K en piroxenos), rutilo-SPI (Ti), olivino-SPI (Fe y Mg), Cr-diópsido-SPI (Si en óxidos de Fe-Ti), cromita (Cr en piroxenos y Fe, Al, Mg, Cr en óxidos de Fe-Ti), rodonita (Mn), jadeíta-SPI (Na en piroxenos), diópsido-SPI (Ca en óxidos de Fe-Ti), pentlandita-SPI (Ni), V-SPI (V) y Willemita-SPI (Zn). En todos los casos, los tiempos de conteo de background alto y bajo fueron la mitad de los tiempos pick para todos los elementos y las correcciones por el efecto matriz se calcularon por el método ZAF. Las condiciones analíticas específicas aplicadas para diferentes minerales se describen a continuación.

En la Universidad de Concepción los tiempos de conteo para las plagioclasas fueron de 20 s en pick para Si, Al, Na y Ca, y de 60 s para K, Fe y Mg. La desviación estándar analítica (1σ) para los elementos mayoritarios (Si, Al, Ca y Na) es ≤1%;

para K varía de 1.5% a 17%, con un promedio de ~3%; para Fe varía de 3% a 6%, con un promedio de ~4% y para Mg varía de 9% a 76%, con un promedio de ~23%. El límite de detección promedio para MgO es de 250 ppm. En la Universidad de Rice los tiempos de conteo fueron de 10 s en pick para Si, Al, Na, Ca y K, y de 30 s para Fe y Mg. La desviación estándar analítica 1σ para los elementos mayoritarios (Si, Al, Ca y Na) es ≤1,5%; para K varía de 3% a 14% con un promedio de ~5.5%; para Fe varía de 2% a 4% con un promedio de ~3.5% y para Mg varía de 3% a 62%, con un promedio de ~19%. El límite de detección promedio para MgO es de 110 ppm. Para los perfiles composicionales el tiempo de conteo en el pick fue de 50 s y 80 s para Fe y Mg, respectivamente y los tiempos de conteo en el background fue de 40 s para Fe y 60 s para Mg. La desviación estándar analítica (1σ) para el Fe varía entre 2% a 4% con un promedio de ~2.8% y para Mg varía de 2% a 30%, con un promedio de ~13% Para los clinopiroxeno analizados en la Universidad de Concepción los tiempos de conteo fueron de 20 s en pick para Si, Mg y Ca, 40 s para Fe, Al, Cr, Ti, Mn, Na y K. La desviación estándar analítica (1σ) para Si, Mg, Ca , Fe y Al es ≤1.2%; para Na <5%; para Mn y Ti varía de 4 a 16%, con un promedio de ~7%. Los resultados de cromo y K están por debajo del límite de detección (547 ppm Cr_2O_3 y 120 ppm K_2O). En la Universidad de Rice los tiempos de conteo fueron de 10 s para todos los elementos. La desviación estándar analítica (1σ) para Si, Mg, Ca y Fe es <1%; para Al <3%; para Na <11,5% con una media de ~9%; para Mn varía de 5 a 13%, con un promedio de ~ 8,5%. Los resultados de cromo y K están por debajo del límite de detección (170 ppm Cr_2O_3 y 115 ppm K_2O).

Para los ortopiroxenos analizados en la Universidad de Concepción los tiempos de conteo fueron 20 s en pick para Si, Mg y Fe, 40 s para Ca, Al, Cr, Ti, Mn, Na y K. La desviación estándar analítica (1σ) para elementos mayoritarios (Si, Mg, Fe) es ≤1%; para Ca y Al <2%; para Mn <7%; para Ti varía de 3 a 19%, con un promedio de ~ 10%; para Na varía de 12 a 41%, con un promedio de ~ 24%. El cromo y el K están por debajo del límite de detección (548 y 120 ppm Cr_2O_3 y K_2O, respectivamente). En la Universidad de Rice los tiempos de conteo fueron de 10 s para todos los elementos. La desviación estándar analítica (1σ) para los elementos principales (Si, Mg, Fe) es ≤1%; para Ca <2,5%; para Al y Mn <6%. Los resultados

de datos de cromo, K (170 y 115 ppm Cr_2O_3 y K_2O, respectivamente) y 25 % para Na están por debajo del límite de detección (165 ppm Na_2O).

Los olivinos fueron analizados en la Universidad de Concepción. Los tiempos de conteo en pick fueron de 20 s para Si, Mg y Fe, 30 s para Ca, 40 s para Al y 60 s para Ti y Mn. La desviación estándar analítica (1σ) para los elementos principales (Si, Mg, Fe) es ≤1%; para Mn varía de 5% a 11%, con un promedio de ~7%; para Ca varía de 5% a 7%, con un promedio de ~6%. El titanio (750 ppm TiO_2) y el Al están por debajo del límite de detección (132 ppm Al_2O_3).

Los óxidos de Fe-Ti se analizaron en la Universidad de Rice. Los tiempos de conteo fueron de 10 s en picos para todos los elementos. La desviación estándar analítica (1σ) para Fe y Ti es ≤1%; Para V, Mg y Mn >6% y para Al >10%. Algunos resultados para Si, Ca y Zn están por debajo del límite de detección

Anexo III: Análisis de química mineral

Análisis de plagioclasas en Universidad de Concepción

Sample	Crystal	SiO2	Al2O3	Fe2O3	MgO	CaO	Na2O	K2O	Total	Si	Al	Fe	Mg	Ca	Na	K	O	CatTot
NCH-18	Pl1C	47.940	33.040	0.795	0.064	15.970	2.412	0.086	100.307	2.1942	1.7822	0.0274	0.00439	0.7832	0.2141	0.005	8	5.006
NCH-18	Pl1R	54.510	28.180	0.885	0.112	10.710	5.250	0.290	99.937	2.4674	1.503	0.0301	0.00752	0.5193	0.4607	0.0168	8	4.997
NCH-18	Pl3C	54.810	27.640	0.625	0.049	10.290	5.310	0.232	98.955	2.4973	1.4841	0.0214	0.00331	0.5024	0.4694	0.0135	8	4.988
NCH-18	Pl3R	54.800	28.780	0.615	0.067	11.100	5.120	0.210	100.692	2.4594	1.5221	0.0208	0.00447	0.5336	0.4457	0.012	8	4.994
NCH-18	Pl5C	48.050	31.900	0.824	0.072	15.580	2.569	0.088	99.083	2.2249	1.7409	0.0287	0.00497	0.7728	0.2306	0.0052	8	5.003
NCH-18	Pl5R	53.710	28.690	0.886	0.097	11.530	4.870	0.237	100.020	2.4341	1.5326	0.0302	0.00654	0.5599	0.4282	0.0137	8	4.999
NCH-18	Pl6C	48.200	33.140	0.737	0.056	16.040	2.360	0.078	100.611	2.1981	1.7812	0.0253	0.00379	0.7837	0.2087	0.0046	8	5.001
NCH-18	Pl6R	54.460	28.450	0.903	0.106	11.190	5.120	0.244	100.473	2.4545	1.5112	0.0306	0.00709	0.5406	0.4474	0.014	8	4.998
NCH-18	Pl7C	54.830	27.890	0.760	0.066	10.960	5.190	0.263	99.959	2.48	1.4869	0.0259	0.00443	0.5311	0.4554	0.0152	8	4.994
NCH-18	Pl7R	56.850	26.610	1.043	0.099	8.970	6.400	0.402	100.374	2.553	1.4086	0.0353	0.00659	0.4315	0.557	0.023	8	5.008
NCH-18	Pl8C	49.330	31.940	0.765	0.100	15.140	2.814	0.093	100.182	2.2533	1.7193	0.0263	0.0068	0.7407	0.2492	0.0054	8	4.994
NCH-18	Pl8C1	50.050	31.180	0.720	0.082	14.500	3.260	0.113	99.905	2.289	1.6807	0.0248	0.0066	0.7105	0.2887	0.0066	8	5
NCH-18	Pl8C2	48.360	32.260	0.753	0.090	15.260	2.687	0.079	99.489	2.227	1.7505	0.0261	0.0062	0.7527	0.2399	0.0047	8	5.001
NCH-18	Pl8C3	48.220	32.100	0.792	0.081	15.400	2.585	0.079	99.256	2.2265	1.747	0.0275	0.0056	0.7617	0.2314	0.0046	8	4.999
NCH-18	Pl8C4	47.260	32.840	0.784	0.086	16.340	2.210	0.058	99.578	2.1819	1.787	0.0272	0.00594	0.8082	0.1978	0.0034	8	5.006
NCH-18	Pl8C5	48.740	31.930	0.815	0.070	15.570	2.628	0.088	99.841	2.238	1.7278	0.0281	0.00489	0.7658	0.2339	0.0052	8	4.999
NCH-18	Pl8R	53.420	28.720	0.831	0.126	11.760	4.800	0.219	99.876	2.4265	1.5372	0.0284	0.00853	0.5723	0.4228	0.0127	8	5
NCH-18	Pl8R1	53.620	28.790	0.836	0.115	11.440	4.830	0.228	99.859	2.4327	1.5395	0.0285	0.00775	0.5559	0.4245	0.0132	8	4.994
NCH-18	Pl8R2	53.340	28.930	0.867	0.108	11.750	4.760	0.207	99.961	2.4204	1.5473	0.0296	0.00727	0.5711	0.419	0.012	8	4.999
NCH-18	Pl11C	53.510	28.990	0.690	0.087	11.570	4.740	0.218	99.806	2.428	1.5502	0.0236	0.0059	0.5624	0.4173	0.0126	8	4.994
NCH-18	Pl11R	55.060	27.460	0.810	0.082	10.210	5.030	0.315	98.968	2.5066	1.4734	0.0277	0.0056	0.4982	0.4442	0.0183	8	4.969
NCH-33	Pl1C	52.650	28.420	0.872	0.094	11.900	4.460	0.256	98.652	2.422	1.5409	0.0302	0.0065	0.5865	0.3978	0.015	8	4.999
NCH-33	Pl4C	51.030	30.380	0.875	0.067	13.060	3.800	0.171	99.383	2.3376	1.6403	0.0302	0.0046	0.6408	0.3375	0.01	8	5.001
NCH-33	Pl4R	53.070	28.930	1.081	0.077	11.650	4.780	0.254	99.842	2.4136	1.5507	0.037	0.0052	0.5678	0.4218	0.0147	8	5.011
NCH-33	Pl5C	51.920	29.440	0.755	0.082	12.370	4.210	0.200	98.977	2.3828	1.5921	0.0261	0.0056	0.6082	0.3748	0.0117	8	5.001

Sample	Crystal	SiO2	Al2O3	Fe2O3	MgO	CaO	Na2O	K2O	Total	Si	Al	Fe	Mg	Ca	Na	K	O	CatTot
NCH-33	Pl5C1	55.520	27.080	0.864	0.132	10.000	5.640	0.353	99.589	2.5166	1.4467	0.0295	0.0089	0.4856	0.4954	0.0204	8	5.003
NCH-33	Pl5R	54.010	27.990	0.907	0.087	11.010	5.180	0.278	99.462	2.46	1.5026	0.0311	0.0059	0.537	0.4571	0.0161	8	5.01
NCH-33	Pl6C	56.070	26.930	0.889	0.097	9.260	5.990	0.404	99.641	2.5361	1.4353	0.0303	0.0066	0.4485	0.5256	0.0233	8	5.006
NCH-33	Pl7C1	48.710	32.140	0.701	0.082	14.980	2.828	0.080	99.521	2.2395	1.7418	0.0242	0.0056	0.7378	0.2521	0.0047	8	5.006
NCH-33	Pl7R	53.880	27.970	1.101	0.058	10.480	5.390	0.309	99.188	2.4602	1.5056	0.0378	0.004	0.5127	0.4775	0.018	8	5.016
NCH-33	Pl8C	52.170	29.680	0.733	0.064	12.350	4.300	0.235	99.532	2.3812	1.5964	0.0252	0.0044	0.6038	0.3805	0.0137	8	5.005
NCH-33	Pl8C1	51.950	29.610	0.813	0.075	12.600	4.310	0.221	99.580	2.3736	1.5946	0.0279	0.0051	0.6168	0.3814	0.0129	8	5.012
NCH-33	Pl8C2	53.640	28.530	0.751	0.086	11.240	4.980	0.293	99.520	2.4416	1.5305	0.0257	0.0058	0.5484	0.4392	0.017	8	5.008
NCH-33	Pl8C3	55.070	27.830	0.792	0.084	10.300	5.510	0.358	99.944	2.4897	1.4827	0.0269	0.0057	0.4988	0.4826	0.0207	8	5.007
NCH-33	Pl8C4	55.410	27.230	0.785	0.110	9.650	5.720	0.391	99.296	2.5167	1.4574	0.0268	0.0074	0.4697	0.5033	0.0227	8	5.004
NCH-33	Pl8C5	51.360	29.980	0.892	0.098	12.820	4.120	0.208	99.478	2.3512	1.6179	0.0307	0.0067	0.6289	0.366	0.0121	8	5.014
NCH-33	Pl8R	56.020	27.100	0.851	0.047	9.840	5.880	0.365	100.103	2.5256	1.4399	0.0289	0.0032	0.4751	0.5139	0.021	8	5.008
NCH-33	Pl8R1	54.250	28.420	0.994	0.089	10.690	5.220	0.299	99.962	2.4561	1.5163	0.0339	0.006	0.5187	0.4585	0.0173	8	5.007
NCH-33	Pl11C	54.470	27.580	0.831	0.086	10.280	5.510	0.333	99.090	2.4852	1.4831	0.0285	0.0058	0.5028	0.4877	0.0194	8	5.013
NCH-33	Pl11C1	53.730	28.600	0.763	0.096	11.520	4.780	0.248	99.737	2.4402	1.5307	0.0261	0.0065	0.5604	0.4209	0.0144	8	4.999
NCH-33	Pl11C2	56.630	26.380	0.871	0.120	9.050	6.070	0.411	99.532	2.561	1.4061	0.0296	0.0081	0.4384	0.5323	0.0237	8	4.999
NCH-33	Pl11R	54.400	27.380	0.858	0.097	10.370	5.570	0.330	99.006	2.4864	1.4747	0.0295	0.0066	0.5077	0.4938	0.0193	8	5.018
NCH-33	Pl15C	54.750	28.070	0.377	0.029	10.030	5.520	0.316	99.092	2.4902	1.5047	0.0129	0.0019	0.4888	0.4868	0.0183	8	5.004
NCH-33	Pl15R	50.430	30.800	0.910	0.059	13.560	3.500	0.155	99.414	2.3125	1.6648	0.0314	0.004	0.6664	0.3116	0.0091	8	5
NCH-33	Pl18C	47.330	32.630	0.802	0.067	15.740	2.347	0.060	98.977	2.1946	1.7834	0.028	0.0046	0.7819	0.211	0.0035	8	5.007
NCH-33	Pl18R	47.690	32.910	0.815	0.070	15.640	2.358	0.055	99.537	2.197	1.7868	0.0283	0.0048	0.7719	0.2106	0.0032	8	5.002
NCH-49	Pl1C	48.560	32.770	0.654	0.087	15.530	2.613	0.078	100.292	2.2183	1.764	0.0225	0.00589	0.7599	0.2314	0.0045	8	5.001
NCH-49	Pl1R	53.620	28.910	0.980	0.112	11.380	4.890	0.198	100.091	2.4278	1.5426	0.0334	0.00758	0.5523	0.4295	0.0115	8	4.997
NCH-49	Pl3C	52.290	29.990	0.817	0.126	12.930	4.190	0.127	100.469	2.3675	1.6001	0.0278	0.00847	0.6271	0.3677	0.0073	8	4.998
NCH-49	Pl3R	52.980	29.000	0.942	0.085	12.140	4.590	0.178	99.915	2.4084	1.5536	0.0322	0.00578	0.5915	0.4042	0.0103	8	5
NCH-49	Pl5C	53.170	29.230	0.792	0.115	11.830	4.580	0.174	99.892	2.4127	1.5631	0.027	0.00779	0.5753	0.4025	0.0101	8	4.991
NCH-49	Pl5R	54.130	28.570	0.814	0.117	11.160	4.990	0.196	99.976	2.4496	1.5237	0.0277	0.00787	0.5411	0.4381	0.0113	8	4.992
NCH-49	Pl6C	48.600	32.270	0.712	0.073	15.770	2.658	0.068	100.151	2.2257	1.7418	0.0245	0.00499	0.7741	0.236	0.004	8	5.006
NCH-49	Pl6R	55.530	26.960	0.771	0.077	9.880	5.740	0.276	99.233	2.5235	1.444	0.0263	0.00521	0.4812	0.5062	0.016	8	4.997

Sample	Crystal	SiO2	Al2O3	Fe2O3	MgO	CaO	Na2O	K2O	Total	Si	Al	Fe	Mg	Ca	Na	K	O	CatTot
NCH-49	Pl7C	49.720	31.550	0.883	0.075	14.480	3.160	0.095	99.963	2.2735	1.7001	0.0304	0.00512	0.7094	0.2798	0.0055	8	4.999
NCH-49	Pl10C	53.770	28.840	0.672	0.098	11.140	4.930	0.198	99.647	2.4404	1.5425	0.0229	0.0066	0.5418	0.434	0.0115	8	4.993
NCH-49	Pl10C1	53.800	28.390	1.184	0.102	11.200	5.050	0.230	99.956	2.4409	1.5183	0.0404	0.00692	0.5444	0.4443	0.0133	8	5.002
NCH-49	Pl10C2	53.770	29.350	0.749	0.073	11.760	4.740	0.202	100.643	2.4207	1.5571	0.0254	0.00488	0.5673	0.414	0.0116	8	4.996
NCH-54	Pl1C	54.780	28.180	0.803	0.074	11.040	5.180	0.286	100.343	2.4699	1.4976	0.0272	0.005	0.5335	0.4525	0.0165	8	5.002
NCH-54	Pl1R	56.340	27.450	0.847	0.105	10.050	5.670	0.318	100.780	2.5208	1.4479	0.0285	0.007	0.4817	0.4918	0.0181	8	4.996
NCH-54	Pl2C	53.680	29.180	0.794	0.089	11.590	4.670	0.228	100.230	2.4252	1.5539	0.027	0.006	0.5611	0.4092	0.0131	8	4.995
NCH-54	Pl2R	55.980	27.450	0.853	0.106	10.080	5.520	0.340	100.330	2.5163	1.4541	0.0289	0.0071	0.4852	0.4814	0.0195	8	4.993
NCH-54	Pl4C	56.540	26.710	0.785	0.095	9.570	5.940	0.346	99.987	2.5474	1.4183	0.0266	0.0064	0.4619	0.5191	0.0199	8	5
NCH-54	Pl4R	52.130	30.210	0.733	0.086	13.090	4.130	0.180	100.558	2.3592	1.6113	0.0249	0.0058	0.6349	0.3626	0.0104	8	5.009
NCH-54	Pl6C	54.490	29.020	0.796	0.093	11.630	4.790	0.242	101.061	2.441	1.5324	0.0268	0.0062	0.558	0.4159	0.0138	8	4.994
NCH-54	Pl6C1	54.260	28.860	0.722	0.073	11.670	4.800	0.240	100.624	2.4417	1.5306	0.0245	0.0049	0.5628	0.4191	0.0137	8	4.997
NCH-54	Pl6C2	55.340	27.620	0.801	0.100	10.440	5.260	0.304	99.865	2.5007	1.4711	0.0272	0.0067	0.5052	0.4609	0.0175	8	4.989
NCH-54	Pl6C3	54.260	28.860	0.722	0.073	11.670	4.800	0.240	100.624	2.4417	1.5306	0.0245	0.0049	0.5628	0.4191	0.0137	8	4.997
NCH-54	Pl6C4	53.160	29.300	0.778	0.093	12.090	4.580	0.221	100.222	2.4071	1.5639	0.0265	0.0063	0.5864	0.4022	0.0128	8	5.005
NCH-54	Pl6C5	53.990	28.950	0.772	0.110	11.760	4.820	0.244	100.646	2.4317	1.5368	0.0262	0.0074	0.5673	0.4211	0.014	8	5.004
NCH-54	Pl6C6	53.880	28.970	0.762	0.076	11.740	4.610	0.221	100.260	2.4333	1.5423	0.0259	0.0051	0.568	0.4033	0.0128	8	4.991
NCH-54	Pl6R	56.310	27.700	0.810	0.094	9.960	5.590	0.327	100.791	2.5175	1.4595	0.0272	0.0063	0.4771	0.4843	0.0187	8	4.991
NCH-54	Pl6R1	55.170	27.620	0.853	0.113	10.190	5.400	0.300	99.647	2.4985	1.4744	0.0291	0.0076	0.4944	0.4742	0.0173	8	4.996
NCH-54	Pl6R2	53.280	29.230	0.833	0.109	12.010	4.570	0.169	100.201	2.4117	1.5592	0.0284	0.0074	0.5823	0.4014	0.0098	8	5
NCH-54	Pl8C	50.380	31.590	0.718	0.108	14.610	3.210	0.101	100.717	2.2846	1.6885	0.0245	0.0073	0.71	0.2823	0.0058	8	5.003
NCH-54	Pl8R	54.910	27.830	1.004	0.108	10.990	5.000	0.264	100.107	2.4803	1.4816	0.0341	0.0073	0.5319	0.4381	0.0152	8	4.989
NCH-54	Pl12C	48.950	32.790	0.731	0.074	15.360	2.761	0.085	100.751	2.2251	1.7568	0.025	0.005	0.7479	0.2434	0.0049	8	5.008
NCH-54	Pl12R	54.570	28.120	0.950	0.139	11.060	5.170	0.255	100.263	2.4644	1.4964	0.0323	0.0093	0.5352	0.4528	0.0147	8	5.005
NCH-60	Pl3C	49.900	31.640	0.683	0.081	14.310	3.280	0.107	100.001	2.2785	1.7026	0.0235	0.0055	0.7	0.2904	0.0062	8	5.007
NCH-60	Pl3R	62.120	24.260	0.749	0.037	5.960	7.840	0.760	101.726	2.7229	1.2535	0.0247	0.0024	0.28	0.6666	0.0425	8	4.993
NCH-60	Pl6C	53.780	29.160	0.697	0.081	11.740	4.850	0.211	100.519	2.4247	1.5497	0.0236	0.0054	0.5673	0.4237	0.0121	8	5.007
NCH-39	Pl1R	50.230	31.140	0.789	0.090	13.900	3.490	0.105	99.745	2.2979	1.6787	0.0272	0.0062	0.6814	0.3097	0.0061	8	5.007
NCH-39	Pl2C	50.450	31.270	0.729	0.156	14.540	3.300	0.089	100.534	2.2922	1.6746	0.0249	0.0106	0.7078	0.2908	0.0051	8	5.006

Sample	Crystal	SiO2	Al2O3	Fe2O3	MgO	CaO	Na2O	K2O	Total	Si	Al	Fe	Mg	Ca	Na	K	O	CatTot
NCH-39	Pl4R	53.810	29.180	0.668	0.089	11.680	4.770	0.166	100.364	2.4276	1.5513	0.0227	0.006	0.5645	0.417	0.0095	8	4.999
NCH-39	Pl8C	48.450	32.820	0.719	0.070	15.450	2.627	0.067	100.203	2.2149	1.7686	0.0247	0.0048	0.757	0.2329	0.0039	8	5.007
NCH-63	Pl1C	51.710	31.150	0.694	0.103	13.540	3.610	0.103	100.909	2.3309	1.6549	0.0235	0.0069	0.6539	0.3154	0.0059	8	4.991
NCH-63	Pl1R	53.690	29.710	0.663	0.092	11.960	4.820	0.128	101.062	2.4079	1.5704	0.0224	0.0062	0.5748	0.4193	0.0073	8	5.009
NCH-63	Pl3C	47.870	33.050	0.628	0.088	15.870	2.386	0.057	99.948	2.1965	1.7872	0.0217	0.006	0.7799	0.2123	0.0033	8	5.007
NCH-63	Pl3R	52.700	29.980	0.783	0.097	12.640	4.430	0.110	100.740	2.3774	1.5939	0.0266	0.0065	0.6112	0.3872	0.0063	8	5.009
NCH-63	Pl5C	50.710	31.180	0.719	0.101	13.880	3.610	0.094	100.294	2.306	1.6709	0.0246	0.0069	0.6762	0.318	0.0054	8	5.008
NCH-63	Pl5R	54.370	28.680	0.869	0.087	11.290	5.160	0.158	100.614	2.4471	1.5213	0.0294	0.0058	0.5443	0.4502	0.009	8	5.007
NCH-63	Pl4C	51.280	30.600	0.714	0.100	13.360	3.850	0.108	100.013	2.3345	1.6418	0.0245	0.0068	0.6516	0.3399	0.0063	8	5.005
NCH-63	Pl18C	46.330	34.270	0.682	0.056	17.200	1.626	0.029	100.194	2.1287	1.8555	0.0236	0.0039	0.8468	0.1449	0.0017	8	5.005
NCH-63	Pl18R	54.270	28.210	0.936	0.130	10.950	5.210	0.197	99.903	2.459	1.5062	0.0319	0.0087	0.5314	0.4578	0.0114	8	5.007
NCH-63	Pl6C	51.650	30.140	0.700	0.091	13.420	3.880	0.094	99.975	2.3517	1.6172	0.024	0.0062	0.6547	0.3426	0.0054	8	5.002
NCH-63	Pl6R	52.790	29.870	0.654	0.092	12.460	4.340	0.118	100.323	2.3875	1.592	0.0222	0.0062	0.6036	0.3807	0.0068	8	4.999
NCH-63	Pl7C	51.880	30.440	0.656	0.072	13.200	4.000	0.107	100.356	2.3514	1.6259	0.0224	0.0049	0.6412	0.3514	0.0062	8	5.003
NCH-63	Pl8C	51.910	30.470	0.672	0.080	13.160	4.030	0.096	100.418	2.3512	1.6264	0.0229	0.0054	0.6386	0.3536	0.0056	8	5.004
NCH-63	Pl8R	52.920	29.960	0.590	0.085	12.390	4.380	0.113	100.439	2.3893	1.5941	0.0201	0.0057	0.5995	0.3836	0.0065	8	4.999
NCH-26	Pl1C	58.160	25.930	0.513	0.036	8.080	6.670	0.360	99.749	2.6118	1.3723	0.0173	0.0024	0.3889	0.5805	0.0206	8	4.994
NCH-26	Pl1R1	57.240	26.440	0.578	0.046	8.900	6.360	0.304	99.868	2.5748	1.4018	0.0196	0.0031	0.4291	0.5549	0.0174	8	5.001
NCH-26	Pl2C	46.230	34.660	0.501	0.016	17.160	1.609	0.042	100.218	2.1218	1.875	0.0173	0.0011	0.844	0.1432	0.0025	8	5.005
NCH-26	Pl2C1	55.740	27.360	0.558	0.053	9.700	5.810	0.275	99.495	2.5228	1.4594	0.019	0.0035	0.4705	0.5094	0.0158	8	5.001
NCH-26	Pl2R	57.680	25.730	0.512	0.044	8.230	6.640	0.387	99.223	2.6071	1.3707	0.0174	0.003	0.3984	0.5822	0.0223	8	5.001
NCH-26	Pl3C	56.480	26.980	0.559	0.068	9.200	6.220	0.294	99.801	2.5462	1.4334	0.019	0.0046	0.4442	0.5437	0.0169	8	5.008
NCH-26	Pl3R	58.270	25.340	0.566	0.044	7.890	6.730	0.370	99.210	2.63	1.3478	0.0192	0.003	0.3814	0.5888	0.0213	8	4.992
NCH-26	Pl4C	49.530	31.770	0.664	0.056	14.330	3.200	0.101	99.651	2.2697	1.7158	0.0229	0.0038	0.7037	0.2841	0.0059	8	5.006
NCH-26	Pl5C	59.130	24.990	0.472	0.034	7.200	7.080	0.427	99.333	2.6595	1.3245	0.016	0.0023	0.3471	0.6171	0.0245	8	4.991
NCH-26	Pl5C2	59.130	24.990	0.446	0.057	7.110	7.150	0.437	99.320	2.6597	1.3247	0.0151	0.0038	0.3425	0.624	0.0251	8	4.995
NCH-26	Pl5C3	57.770	26.240	0.513	0.045	8.210	6.700	0.365	99.842	2.595	1.3892	0.0173	0.003	0.3951	0.5834	0.0209	8	5.004
NCH-26	Pl5C4	57.200	26.040	0.489	0.049	8.020	6.510	0.373	98.681	2.597	1.3936	0.0167	0.0033	0.3901	0.5727	0.0216	8	4.995
NCH-26	Pl5R	56.810	26.680	0.487	0.056	8.570	6.240	0.351	99.194	2.5694	1.4222	0.0166	0.0038	0.4155	0.5471	0.0202	8	4.995

Sample	Crystal	SiO2	Al2O3	Fe2O3	MgO	CaO	Na2O	K2O	Total	Si	Al	Fe	Mg	Ca	Na	K	O	CatTot
NCH-26	Pl5R1	57.430	26.060	0.521	0.058	8.310	6.540	0.361	99.280	2.5947	1.3874	0.0177	0.0039	0.4022	0.5729	0.0208	8	5
NCH-26	Pl5R2	56.640	25.950	0.511	0.062	8.330	6.380	0.349	98.221	2.5869	1.3967	0.0175	0.0042	0.4079	0.5652	0.0203	8	4.999
NCH-26	Pl6C1	57.110	26.550	0.521	0.040	8.940	6.400	0.345	99.906	2.5696	1.408	0.0176	0.0027	0.4308	0.5579	0.0198	8	5.006
NCH-26	Pl6R	57.930	26.470	0.540	0.036	8.400	6.590	0.381	100.347	2.5897	1.3946	0.0182	0.0024	0.4025	0.5713	0.0217	8	5
NCH-27	Pl1C	51.630	29.110	0.652	0.063	11.910	4.250	0.175	97.790	2.3939	1.5906	0.0228	0.0043	0.5918	0.3816	0.0104	8	4.995
NCH-27	Pl1C1	51.790	29.630	0.651	0.065	12.100	4.320	0.161	98.717	2.3805	1.605	0.0225	0.0044	0.5958	0.3852	0.0094	8	5.003
NCH-27	Pl1R	55.550	27.140	0.612	0.057	9.700	5.710	0.269	99.039	2.5256	1.4543	0.021	0.0039	0.4726	0.503	0.0156	8	4.996
NCH-27	Pl2C	57.350	25.860	0.497	0.059	8.220	6.620	0.380	98.985	2.599	1.3813	0.0169	0.004	0.399	0.5815	0.0219	8	5.004
NCH-27	Pl2C1	54.820	27.510	0.610	0.062	10.220	5.390	0.246	98.858	2.5006	1.4788	0.0209	0.0042	0.4993	0.477	0.0143	8	4.995
NCH-27	Pl2R	56.500	26.180	0.593	0.035	8.480	6.350	0.356	98.494	2.576	1.4065	0.0203	0.0024	0.4142	0.5614	0.0207	8	5.002
NCH-27	Pl2R1	57.390	25.950	0.538	0.059	8.400	6.600	0.353	99.289	2.5944	1.3823	0.0183	0.004	0.4067	0.5788	0.0203	8	5.005
NCH-27	Pl4C	49.200	31.730	0.696	0.038	14.470	3.150	0.098	99.381	2.2626	1.7199	0.0241	0.0026	0.7131	0.2809	0.0057	8	5.009
NCH-27	Pl4C1	52.250	29.560	0.616	0.025	12.290	4.370	0.162	99.273	2.3885	1.5926	0.0212	0.0017	0.602	0.3877	0.0094	8	5.003
NCH-27	Pl4R	52.680	29.560	0.564	0.053	11.880	4.560	0.169	99.466	2.4002	1.5873	0.0193	0.0036	0.5798	0.4029	0.0098	8	5.003
NCH-27	Pl4R1	55.280	27.700	0.610	0.049	9.970	5.510	0.256	99.375	2.5058	1.48	0.0208	0.0033	0.4843	0.4841	0.0148	8	4.993
NCH-27	Pl5C	55.250	27.720	0.575	0.062	10.150	5.570	0.242	99.569	2.5018	1.4791	0.0196	0.0042	0.4925	0.4894	0.014	8	5
NCH-27	Pl6C	57.190	26.090	0.495	0.059	8.380	6.630	0.344	99.188	2.5879	1.3917	0.0169	0.004	0.4064	0.5821	0.0199	8	5.009
NCH-27	Pl6R	55.500	27.010	0.561	0.045	9.440	5.900	0.291	98.746	2.5306	1.4512	0.0192	0.003	0.4611	0.5212	0.0169	8	5.003
NCH-27	Pl6R1	55.650	27.050	0.579	0.059	9.510	5.910	0.275	99.034	2.5301	1.4496	0.0198	0.004	0.4632	0.521	0.016	8	5.004
NCH-27	Pl9C	54.150	28.340	0.484	0.047	10.650	5.260	0.216	99.147	2.4661	1.521	0.0166	0.0032	0.5195	0.4647	0.0125	8	5.004
NCH-27	Pl9C2	54.700	27.600	0.540	0.061	10.100	5.470	0.235	98.705	2.4982	1.4856	0.0185	0.0041	0.4943	0.4843	0.0137	8	4.999
NCH-27	Pl9R1	54.740	27.920	0.552	0.056	10.410	5.440	0.236	99.355	2.4863	1.4949	0.0189	0.0038	0.5064	0.4794	0.0137	8	5.003
NCH-34	Pl2C	57.240	26.630	0.530	0.045	8.510	6.490	0.268	99.714	2.5753	1.4121	0.018	0.003	0.4103	0.5666	0.0154	8	4.998
NCH-34	Pl2R	58.110	26.070	0.506	0.024	8.240	6.680	0.360	99.990	2.6052	1.3775	0.0171	0.0016	0.3957	0.5806	0.0206	8	4.997
NCH-34	Pl2R1	56.450	27.100	0.604	0.036	9.070	6.110	0.309	99.679	2.5458	1.4405	0.0205	0.0024	0.4383	0.5346	0.0178	8	4.997
NCH-34	Pl5R	56.620	27.220	0.554	0.036	9.440	6.030	0.283	100.183	2.5422	1.4404	0.0187	0.0024	0.454	0.525	0.0162	8	4.996
NCH-34	Pl7C	57.060	27.410	0.443	0.041	9.120	6.250	0.226	100.549	2.5485	1.443	0.0149	0.0027	0.4365	0.5411	0.0129	8	4.997
NCH-34	Pl7R	56.550	27.150	0.474	0.054	9.400	5.990	0.237	99.855	2.545	1.4404	0.016	0.0038	0.4534	0.5226	0.0136	8	4.991
NCH-34	Pl11C	56.560	27.020	0.451	0.058	9.120	6.210	0.224	99.643	2.5504	1.4357	0.0153	0.0039	0.4408	0.5431	0.0129	8	4.998

Sample	Crystal	SiO2	Al2O3	Fe2O3	MgO	CaO	Na2O	K2O	Total	Si	Al	Fe	Mg	Ca	Na	K	O	CatTot
NCH-34	Pl11C1	57.660	26.860	0.472	0.026	8.650	6.460	0.238	100.366	2.5761	1.4145	0.0159	0.0018	0.4138	0.5599	0.0136	8	4.994
NCH-34	Pl11R	58.000	26.330	0.474	0.061	8.460	6.600	0.261	100.185	2.5951	1.3884	0.016	0.004	0.4055	0.5725	0.0149	8	4.992
NCH-34	Pl11R1	57.240	26.890	0.499	0.042	8.990	6.270	0.222	100.153	2.5657	1.4204	0.0168	0.0028	0.4315	0.5445	0.0127	8	4.992
NCH-34	Pl11R2	57.680	26.530	0.518	0.036	8.470	6.670	0.281	100.184	2.5834	1.4005	0.0175	0.0024	0.4063	0.5791	0.016	8	5.003
NCH-34	Pl16C	56.160	27.000	0.454	0.036	9.190	6.180	0.219	99.239	2.5442	1.4414	0.0155	0.0025	0.446	0.543	0.0127	8	5.003
NCH-34	Pl16R	56.390	27.110	0.543	0.021	9.230	6.040	0.261	99.595	2.5449	1.442	0.0184	0.0014	0.4463	0.5289	0.015	8	4.995
NCH-45	Pl1C	52.940	29.300	0.444	0.039	11.990	4.720	0.195	99.628	2.4096	1.5714	0.0152	0.0027	0.5846	0.4161	0.0113	8	5.008
NCH-45	Pl1R	58.120	26.210	0.521	0.048	8.120	6.700	0.408	100.127	2.602	1.3831	0.0176	0.0032	0.3895	0.5813	0.0233	8	4.997
NCH-45	Pl1R1	56.910	26.770	0.504	0.057	9.030	6.190	0.335	99.796	2.5623	1.4206	0.0171	0.0038	0.4354	0.5404	0.0192	8	4.995
NCH-45	Pl5C	57.870	26.190	0.470	0.050	8.450	6.580	0.377	99.986	2.5963	1.385	0.0159	0.0033	0.406	0.5722	0.0216	8	4.997
NCH-45	Pl5R	56.710	26.590	0.647	0.041	9.370	6.000	0.345	99.703	2.5589	1.4139	0.022	0.0028	0.453	0.5253	0.0199	8	4.993
NCH-45	Pl7C	58.030	25.790	0.446	0.043	8.180	6.730	0.435	99.655	2.6113	1.3677	0.0151	0.0029	0.3943	0.5868	0.025	8	5
NCH-45	Pl7R	57.090	27.070	0.662	0.065	9.010	6.140	0.361	100.398	2.5556	1.428	0.0223	0.0044	0.4322	0.5331	0.0206	8	4.992
NCH-45	Pl8C	54.460	28.380	0.668	0.058	10.790	5.170	0.241	99.767	2.4663	1.5148	0.0228	0.0039	0.5235	0.4535	0.0139	8	4.995
NCH-45	Pl8R	57.140	26.590	0.679	0.061	9.330	6.060	0.351	100.211	2.5646	1.4067	0.0229	0.0041	0.4487	0.5272	0.0201	8	4.99
NCH-45	Pl10C	55.510	28.150	0.475	0.020	10.320	5.500	0.253	100.228	2.4961	1.492	0.0161	0.0014	0.4973	0.4799	0.0145	8	4.996
NCH-45	Pl10C2	55.320	27.730	0.473	0.032	10.490	5.480	0.257	99.781	2.5008	1.4775	0.0161	0.0021	0.5083	0.4802	0.0148	8	4.998
NCH-45	Pl10C3	55.610	27.400	0.469	0.040	10.040	5.760	0.315	99.634	2.5166	1.4612	0.016	0.0027	0.4868	0.5051	0.0182	8	5.004
NCH-45	Pl10C4	58.790	25.810	0.485	0.047	8.150	6.890	0.424	100.596	2.6199	1.3558	0.0162	0.0031	0.3891	0.5956	0.0241	8	5.001
NCH-45	Pl10C5	57.180	25.930	0.446	0.029	8.580	6.480	0.387	99.032	2.5923	1.3853	0.0152	0.0019	0.4166	0.5696	0.0224	8	5.002
NCH-45	Pl10C6	58.830	25.810	0.513	0.049	7.780	7.000	0.449	100.431	2.6242	1.3569	0.0172	0.0032	0.3717	0.6054	0.0256	8	5.001
NCH-45	Pl10R	56.460	27.320	0.549	0.039	9.550	5.920	0.320	100.158	2.5365	1.4466	0.0185	0.0027	0.4596	0.516	0.0184	8	4.996
NCH-45	Pl10R1	57.650	26.540	0.529	0.031	8.640	6.460	0.365	100.215	2.582	1.4009	0.0178	0.0021	0.4147	0.5613	0.0208	8	4.998
NCH-45	Pl10R2	58.000	26.280	0.516	0.045	8.370	6.620	0.405	100.235	2.5959	1.3861	0.0174	0.003	0.4013	0.5743	0.0231	8	4.998
NCH-45	Pl12C	49.520	32.050	0.670	0.048	14.840	2.989	0.102	100.219	2.2588	1.7227	0.023	0.0033	0.7254	0.2643	0.0059	8	5
NCH-45	Pl12R	53.540	28.920	0.815	0.082	11.430	4.910	0.220	99.917	2.428	1.546	0.0278	0.0055	0.5556	0.4316	0.0127	8	5.002
NCH-45	Pl12R1	55.960	26.840	0.665	0.064	9.370	5.910	0.336	99.145	2.5408	1.4361	0.0227	0.0043	0.4559	0.5204	0.0194	8	4.995
NCH-45	Pl18C	52.130	30.450	0.484	0.021	12.930	4.080	0.156	100.252	2.3619	1.626	0.0165	0.0014	0.6274	0.3582	0.009	8	4.999
NCH-45	Pl18R	57.590	26.600	0.597	0.054	9.000	6.410	0.410	100.661	2.5726	1.4007	0.0201	0.0036	0.4307	0.5555	0.0234	8	5.003

Sample	Crystal	SiO2	Al2O3	Fe2O3	MgO	CaO	Na2O	K2O	Total	Si	Al	Fe	Mg	Ca	Na	K	O	CatTot
NCH-46	Pl2R	57.850	26.200	0.508	0.041	8.740	6.560	0.391	100.289	2.591	1.3827	0.0171	0.0027	0.4193	0.57	0.0223	8	5.005
NCH-46	Pl7R	58.760	26.060	0.510	0.020	7.920	6.770	0.559	100.599	2.6172	1.3682	0.0171	0.0013	0.3781	0.5848	0.0318	8	4.998
NCH-46	Pl11C	58.180	26.170	0.475	0.036	8.120	6.670	0.436	100.087	2.6051	1.381	0.016	0.0024	0.3897	0.5795	0.0249	8	4.999
NCH-46	Pl11C1	58.430	25.870	0.474	0.036	8.340	6.630	0.435	100.215	2.614	1.3641	0.016	0.0024	0.3996	0.5752	0.0248	8	4.996
NCH-46	Pl11C2	60.130	25.120	0.438	0.033	7.270	7.270	0.532	100.793	2.6666	1.3132	0.0146	0.0022	0.3453	0.6251	0.0301	8	4.997
NCH-46	Pl11C3	58.480	25.660	0.437	0.041	7.780	6.990	0.466	99.853	2.6241	1.3571	0.0147	0.0027	0.3743	0.6077	0.0267	8	5.007
NCH-46	Pl11R	58.400	26.020	0.470	0.030	8.080	6.840	0.437	100.277	2.6108	1.371	0.0158	0.002	0.3872	0.593	0.0249	8	5.005
NCH-46	Pl11R1	59.750	24.810	0.410	0.034	6.950	7.470	0.537	99.961	2.6718	1.3075	0.0138	0.0023	0.3328	0.6479	0.0306	8	5.007
NCH-46	Pl12C	57.750	26.880	0.503	0.056	8.770	6.420	0.405	100.784	2.5731	1.4116	0.0169	0.0037	0.4185	0.5548	0.023	8	5.002
NCH-46	Pl13C	55.760	28.140	0.623	0.049	10.390	5.660	0.277	100.899	2.4942	1.4836	0.021	0.0033	0.4981	0.4909	0.0158	8	5.007
NCH-46	Pl13R	59.480	25.460	0.498	0.035	7.240	7.010	0.536	100.259	2.6511	1.3376	0.0167	0.0023	0.3458	0.6062	0.0305	8	4.99
NCH-55	Pl1C	53.600	28.490	0.646	0.057	11.480	4.840	0.189	99.302	2.4433	1.5307	0.0221	0.0039	0.5609	0.4277	0.011	8	5
NCH-55	Pl1C1	52.410	29.440	0.663	0.058	12.250	4.430	0.164	99.415	2.393	1.5841	0.0228	0.004	0.599	0.392	0.0095	8	5.004
NCH-55	Pl1C2	54.870	28.130	0.609	0.056	10.470	5.490	0.228	99.852	2.481	1.4992	0.0207	0.0037	0.507	0.4817	0.0132	8	5.006
NCH-55	Pl1R1	59.660	24.550	0.634	0.019	6.710	7.490	0.530	99.593	2.6775	1.2986	0.0214	0.0013	0.3227	0.6516	0.0304	8	5.003
NCH-55	Pl2R	57.270	25.910	0.542	0.042	8.380	6.590	0.348	99.082	2.5942	1.3831	0.0185	0.0028	0.4069	0.5787	0.0201	8	5.004
NCH-55	Pl3C	59.240	25.910	0.409	0.038	7.640	7.010	0.413	100.660	2.6321	1.3569	0.0137	0.0025	0.3638	0.6037	0.0234	8	4.996
NCH-55	Pl3C1	58.350	26.200	0.458	0.053	7.940	6.880	0.393	100.274	2.607	1.3798	0.0154	0.0036	0.3803	0.5962	0.0224	8	5.005
NCH-55	Pl3C2	58.900	25.410	0.468	0.038	7.400	7.020	0.419	99.655	2.6426	1.3436	0.0158	0.0025	0.3555	0.611	0.024	8	4.995
NCH-55	Pl3C3	59.150	25.890	0.501	0.051	7.650	6.930	0.412	100.583	2.6304	1.3571	0.0168	0.0033	0.3647	0.5973	0.0234	8	4.993
NCH-55	Pl3R	56.060	26.940	0.474	0.034	9.240	6.110	0.324	99.182	2.5431	1.4403	0.0162	0.0023	0.4489	0.5371	0.0188	8	5.007
NCH-55	Pl3R1	59.270	25.370	0.529	0.040	7.260	7.200	0.439	100.107	2.6476	1.3356	0.0178	0.0026	0.3476	0.624	0.025	8	5
NCH-55	Pl3R2	57.220	26.880	0.567	0.040	8.730	6.330	0.325	100.093	2.5663	1.4212	0.0191	0.0027	0.4197	0.5504	0.0186	8	4.998
NCH-55	Pl4C	56.330	27.090	0.572	0.065	9.440	6.040	0.291	99.828	2.5396	1.4392	0.0194	0.0044	0.456	0.5283	0.0167	8	5.004
NCH-55	Pl4R	57.790	26.180	0.533	0.051	8.200	6.700	0.378	99.832	2.5962	1.3863	0.018	0.0034	0.3948	0.584	0.0216	8	5.004
NCH-55	Pl6C	57.530	26.010	0.536	0.055	8.200	6.690	0.339	99.360	2.5972	1.3836	0.0182	0.0037	0.3967	0.5853	0.0195	8	5.004
NCH-55	Pl6C2	55.540	28.250	0.595	0.048	10.310	5.540	0.239	100.522	2.4914	1.4936	0.0201	0.0032	0.4957	0.4817	0.0137	8	4.999
NCH-55	Pl7C	56.500	27.110	0.719	0.064	9.610	5.850	0.277	100.130	2.5397	1.4363	0.0243	0.0043	0.4627	0.5094	0.0159	8	4.993
NCH-55	Pl7C1	55.940	27.590	0.539	0.045	9.810	5.730	0.253	99.908	2.5204	1.4651	0.0183	0.003	0.4734	0.5006	0.0146	8	4.995

Sample	Crystal	SiO2	Al2O3	Fe2O3	MgO	CaO	Na2O	K2O	Total	Si	Al	Fe	Mg	Ca	Na	K	O	CatTot
NCH-55	Pl9C1	53.210	28.830	0.615	0.051	11.710	4.830	0.200	99.446	2.4252	1.5488	0.0211	0.0035	0.5719	0.4273	0.0116	8	5.009
NCH-55	Pl9R	56.870	27.040	0.560	0.051	8.700	6.290	0.390	99.901	2.557	1.4329	0.0189	0.0034	0.4193	0.5487	0.0224	8	5.003

Análisis de clinopiroxenos en Universidad de Concepción

Sample	Crystal	SiO2	TiO2	Al2O3	FeOt	MnO	MgO	CaO	Na2O	Total	Si	Ti	Al	Fe	Mn	Mg	Ca	Na	O	CatTot
NCH-18	CPX3C	51.120	0.527	1.919	9.160	0.269	15.710	20.010	0.291	99.006	1.923	0.015	0.085	0.288	0.009	0.881	0.806	0.021	6	4.028
NCH-18	CPX3C1	51.290	0.563	1.867	9.200	0.322	15.560	20.450	0.304	99.555	1.922	0.016	0.082	0.288	0.010	0.869	0.821	0.022	6	4.032
NCH-18	CPX5C	52.110	0.490	2.150	7.210	0.205	17.100	20.130	0.252	99.648	1.926	0.014	0.094	0.223	0.006	0.942	0.797	0.018	6	4.022
NCH-18	CPX5R	51.360	0.608	1.959	9.750	0.247	16.400	18.830	0.308	99.462	1.920	0.017	0.086	0.305	0.008	0.914	0.754	0.022	6	4.029
NCH-18	CPX6R	51.550	0.645	1.837	10.700	0.271	15.670	18.760	0.322	99.754	1.930	0.018	0.081	0.335	0.009	0.875	0.753	0.023	6	4.023
NCH-18	CPX7C	50.760	0.660	2.582	8.140	0.215	15.620	20.460	0.322	98.759	1.907	0.019	0.114	0.256	0.007	0.875	0.823	0.023	6	4.027
NCH-18	CPX7R	50.940	0.795	2.585	8.790	0.244	16.200	19.510	0.333	99.398	1.903	0.022	0.114	0.275	0.008	0.902	0.781	0.024	6	4.029
NCH-18	CPX9C	51.100	0.793	2.555	8.640	0.249	15.470	20.500	0.316	99.622	1.908	0.022	0.112	0.270	0.008	0.861	0.820	0.023	6	4.025
NCH-18	CPX9R	51.720	0.621	2.033	9.610	0.261	16.180	19.080	0.343	99.847	1.924	0.017	0.089	0.299	0.008	0.897	0.761	0.025	6	4.025
NCH-18	CPX10C	52.000	0.524	2.445	6.930	0.197	16.020	21.200	0.266	99.582	1.922	0.015	0.107	0.214	0.006	0.883	0.839	0.019	6	4.015
NCH-18	CPX10R	51.440	0.696	2.072	9.740	0.213	15.860	19.430	0.361	99.812	1.919	0.020	0.091	0.304	0.007	0.882	0.777	0.026	6	4.028
NCH-18	CPX11C	51.960	0.522	1.991	8.600	0.243	16.790	19.490	0.279	99.875	1.926	0.015	0.087	0.267	0.008	0.928	0.774	0.020	6	4.025
NCH-18	CPX13R	51.790	0.560	1.899	9.970	0.291	16.320	19.120	0.326	100.276	1.923	0.016	0.083	0.310	0.009	0.903	0.761	0.024	6	4.031
NCH-49	CPX1C	50.980	0.637	2.072	8.820	0.272	16.140	20.130	0.303	99.354	1.910	0.018	0.092	0.277	0.009	0.901	0.808	0.022	6	4.037
NCH-49	CPX2R	50.360	0.583	2.141	8.790	0.249	16.090	20.060	0.290	98.563	1.903	0.017	0.095	0.278	0.008	0.906	0.812	0.021	6	4.042
NCH-49	CPX2R1	50.790	0.712	1.663	10.020	0.350	15.680	19.360	0.352	98.927	1.920	0.020	0.074	0.317	0.011	0.883	0.784	0.026	6	4.036
NCH-49	CPX5R	51.690	0.710	1.459	11.430	0.351	15.670	17.700	0.327	99.337	1.944	0.020	0.065	0.360	0.011	0.878	0.713	0.024	6	4.015
NCH-49	CPX6R	51.050	0.803	1.661	11.940	0.344	15.930	17.720	0.353	99.801	1.919	0.023	0.074	0.375	0.011	0.893	0.714	0.026	6	4.034
NCH-49	CPX8R	51.220	0.799	1.343	11.330	0.308	15.560	17.850	0.349	98.759	1.940	0.023	0.060	0.359	0.010	0.878	0.724	0.026	6	4.020
NCH-49	CPX10R	50.860	0.693	1.892	10.530	0.298	14.670	19.350	0.346	98.639	1.930	0.020	0.085	0.334	0.010	0.830	0.787	0.025	6	4.021
NCH-49	CPX10C	51.560	0.642	1.851	10.780	0.316	15.650	19.020	0.360	100.178	1.925	0.018	0.081	0.337	0.010	0.871	0.761	0.026	6	4.029
NCH-49	CPX11R	50.820	0.604	2.546	9.330	0.278	16.450	18.820	0.322	99.170	1.903	0.017	0.112	0.292	0.009	0.918	0.755	0.023	6	4.034

Sample	Crystal	SiO2	TiO2	Al2O3	FeOt	MnO	MgO	CaO	Na2O	Total	Si	Ti	Al	Fe	Mn	Mg	Ca	Na	O	CatTot
NCH-49	CPX11R1	51.200	0.618	2.489	9.200	0.289	16.330	19.040	0.302	99.468	1.911	0.017	0.110	0.287	0.009	0.908	0.761	0.022	6	4.027
NCH-49	CPX14R	51.060	0.631	1.837	10.700	0.296	14.920	19.110	0.364	98.917	1.931	0.018	0.082	0.339	0.010	0.841	0.774	0.027	6	4.023
NCH-49	CPX16R	51.080	0.625	1.621	11.260	0.343	15.140	18.610	0.346	99.025	1.933	0.018	0.072	0.356	0.011	0.854	0.755	0.025	6	4.025
NCH-54	CPX1R	50.940	0.731	1.920	11.210	0.328	15.020	18.630	0.382	99.161	1.925	0.021	0.086	0.354	0.011	0.846	0.755	0.028	6	4.025
NCH-54	CPX1R1	51.130	0.770	1.835	11.100	0.276	15.860	18.270	0.369	99.609	1.920	0.022	0.081	0.349	0.009	0.888	0.735	0.027	6	4.031
NCH-54	CPX2R	51.390	0.820	1.766	10.950	0.319	15.660	18.500	0.352	99.757	1.926	0.023	0.078	0.343	0.010	0.875	0.743	0.026	6	4.024
NCH-54	CPX3R	51.430	0.642	1.849	11.370	0.325	15.730	18.970	0.371	100.686	1.916	0.018	0.081	0.354	0.010	0.873	0.757	0.027	6	4.038
NCH-54	CPX3R1	51.170	0.738	1.864	10.880	0.311	15.480	18.650	0.368	99.461	1.924	0.021	0.083	0.342	0.010	0.868	0.752	0.027	6	4.027
NCH-54	CPX4C	51.720	0.656	2.008	9.670	0.243	15.610	19.090	0.347	99.344	1.935	0.018	0.089	0.303	0.008	0.870	0.765	0.025	6	4.014
NCH-54	CPX5R	51.300	0.806	1.886	10.590	0.333	15.260	18.490	0.343	99.008	1.933	0.023	0.084	0.334	0.011	0.857	0.746	0.025	6	4.014
NCH-54	CPX6R	51.460	0.763	1.948	11.250	0.311	15.450	18.380	0.380	99.943	1.926	0.022	0.086	0.352	0.010	0.862	0.737	0.028	6	4.023
NCH-54	CPX7R	51.100	0.749	1.938	11.140	0.314	15.360	18.050	0.353	99.004	1.929	0.021	0.086	0.352	0.010	0.864	0.730	0.026	6	4.019
NCH-54	CPX7R1	51.370	0.705	1.943	11.280	0.279	15.650	18.420	0.365	100.012	1.922	0.020	0.086	0.353	0.009	0.873	0.738	0.027	6	4.028
NCH-54	CPX8R	51.270	0.817	2.054	10.700	0.300	15.400	19.450	0.354	100.344	1.913	0.023	0.090	0.334	0.010	0.857	0.778	0.026	6	4.031
NCH-54	CPX9R	50.850	0.790	2.401	10.730	0.288	14.720	19.250	0.357	99.385	1.913	0.022	0.106	0.338	0.009	0.825	0.776	0.026	6	4.022
NCH-54	CPX11R	51.260	0.791	1.924	10.620	0.295	16.100	19.120	0.363	100.473	1.910	0.022	0.085	0.331	0.009	0.894	0.763	0.026	6	4.039
NCH-60	CPX4C	49.370	1.305	3.940	10.940	0.302	13.930	19.710	0.355	99.853	1.859	0.037	0.175	0.345	0.010	0.782	0.795	0.026	6	4.029
NCH-60	CPX4R	51.580	0.779	1.762	12.830	0.488	13.870	18.620	0.340	100.270	1.940	0.022	0.078	0.404	0.016	0.778	0.750	0.025	6	4.012
NCH-60	CPX18R	52.350	0.510	2.209	6.460	0.202	17.290	20.840	0.291	100.152	1.919	0.014	0.095	0.198	0.006	0.945	0.818	0.021	6	4.025
NCH-60	CPX18R1	51.840	0.546	2.649	7.190	0.196	16.820	20.380	0.312	99.934	1.909	0.015	0.115	0.221	0.006	0.923	0.804	0.022	6	4.025
NCH-60	CPX18R2	51.790	0.627	2.790	7.320	0.212	16.790	20.100	0.280	99.908	1.905	0.017	0.121	0.225	0.007	0.921	0.792	0.020	6	4.021
NCH-60	CPX19R	51.630	0.650	3.340	6.860	0.202	15.970	20.720	0.319	99.690	1.902	0.018	0.145	0.212	0.006	0.877	0.818	0.023	6	4.013
NCH-60	CPX19R1	47.650	1.709	5.130	11.810	0.249	14.770	17.890	0.331	99.539	1.803	0.049	0.229	0.374	0.008	0.833	0.725	0.024	6	4.046
NCH-60	CPX20R	48.390	1.414	5.340	9.510	0.200	14.970	19.610	0.393	99.827	1.812	0.040	0.236	0.298	0.006	0.835	0.787	0.029	6	4.045
NCH-60	CPX20R1	49.320	1.446	5.100	9.850	0.259	16.160	18.030	0.340	100.505	1.824	0.040	0.222	0.305	0.008	0.891	0.715	0.024	6	4.035
NCH-60	CPX20R2	49.330	1.572	4.090	11.560	0.312	14.600	18.360	0.396	100.220	1.849	0.044	0.181	0.362	0.010	0.816	0.737	0.029	6	4.030
NCH-39	CPX1C	51.950	0.633	1.693	9.320	0.330	15.880	20.250	0.336	100.392	1.929	0.018	0.074	0.289	0.010	0.879	0.806	0.024	6	4.029

Sample	Crystal	SiO2	TiO2	Al2O3	FeOt	MnO	MgO	CaO	Na2O	Total	Si	Ti	Al	Fe	Mn	Mg	Ca	Na	O	CatTot
NCH-39	CPX2C	50.770	0.691	3.330	7.330	0.177	15.670	21.980	0.313	100.262	1.876	0.019	0.145	0.227	0.006	0.863	0.870	0.022	6	4.038
NCH-39	CPX2R	48.650	1.257	5.650	7.650	0.168	14.780	21.630	0.308	100.093	1.808	0.035	0.248	0.238	0.005	0.819	0.861	0.022	6	4.041
NCH-39	CPX3C	51.710	0.697	2.359	8.570	0.254	15.840	20.930	0.339	100.698	1.911	0.019	0.103	0.265	0.008	0.872	0.829	0.024	6	4.031
NCH-39	CPX3R	51.760	0.799	2.437	9.190	0.303	15.520	20.540	0.376	100.926	1.911	0.022	0.106	0.284	0.010	0.854	0.813	0.027	6	4.027
NCH-39	CPX4R	50.210	0.974	4.200	7.670	0.189	15.780	21.040	0.333	100.395	1.853	0.027	0.183	0.237	0.006	0.868	0.832	0.024	6	4.037
NCH-39	CPX5R	50.080	0.893	4.060	7.840	0.191	15.780	21.320	0.346	100.510	1.852	0.025	0.177	0.242	0.006	0.870	0.845	0.025	6	4.045
NCH-39	CPX6R	47.950	1.322	5.120	9.040	0.210	14.630	20.650	0.328	99.250	1.810	0.038	0.228	0.285	0.007	0.823	0.835	0.024	6	4.050
NCH-39	CPX7C	51.140	0.528	2.439	6.740	0.162	16.360	21.730	0.299	99.398	1.901	0.015	0.107	0.210	0.005	0.906	0.865	0.022	6	4.038
NCH-39	CPX7R	50.400	0.801	2.418	8.470	0.278	15.580	20.950	0.350	99.247	1.895	0.023	0.107	0.266	0.009	0.873	0.844	0.026	6	4.042
NCH-44	CPX2C1	51.170	0.594	1.476	9.810	0.349	15.560	19.980	0.317	99.255	1.928	0.017	0.066	0.309	0.011	0.874	0.806	0.023	6	4.034
NCH-44	CPX5C	51.250	0.774	1.924	9.730	0.394	15.370	20.050	0.338	99.831	1.919	0.022	0.085	0.305	0.013	0.858	0.804	0.025	6	4.029
NCH-44	CPX5C1	51.280	0.777	1.959	10.090	0.363	15.340	19.850	0.327	99.986	1.918	0.022	0.086	0.316	0.012	0.855	0.796	0.024	6	4.029
NCH-44	CPX5R	51.050	0.557	1.606	9.890	0.353	15.840	20.290	0.337	99.923	1.914	0.016	0.071	0.310	0.011	0.885	0.815	0.025	6	4.047
NCH-44	CPX5R1	50.960	0.609	1.779	9.850	0.371	15.210	20.160	0.329	99.267	1.921	0.017	0.079	0.311	0.012	0.855	0.814	0.024	6	4.034
NCH-44	CPX8R	51.210	0.590	1.685	9.810	0.351	15.520	20.310	0.360	99.835	1.920	0.017	0.074	0.308	0.011	0.867	0.816	0.026	6	4.039
NCH-44	CPX9C	50.920	0.699	1.748	10.200	0.392	15.320	19.650	0.338	99.266	1.921	0.020	0.078	0.322	0.013	0.861	0.794	0.025	6	4.033
NCH-44	CPX9R	51.320	0.771	1.930	11.320	0.473	15.070	19.100	0.354	100.338	1.920	0.022	0.085	0.354	0.015	0.841	0.766	0.026	6	4.028
NCH-44	CPX10C	51.860	0.583	1.653	9.860	0.364	15.740	20.270	0.365	100.695	1.925	0.016	0.072	0.306	0.011	0.871	0.806	0.026	6	4.035
NCH-44	CPX11C	51.140	0.749	1.992	10.210	0.393	15.690	19.160	0.336	99.669	1.917	0.021	0.088	0.320	0.013	0.877	0.770	0.024	6	4.030
NCH-44	CPX11R	51.230	0.668	1.686	9.920	0.383	15.040	20.070	0.343	99.339	1.929	0.019	0.075	0.313	0.012	0.844	0.810	0.025	6	4.027
NCH-44	CPX12C	52.120	0.715	1.533	9.730	0.359	15.430	20.110	0.325	100.322	1.938	0.020	0.067	0.303	0.011	0.856	0.801	0.024	6	4.020
NCH-44	CPX12R	51.230	0.741	1.745	9.940	0.380	15.320	20.240	0.327	99.923	1.929	0.019	0.075	0.313	0.012	0.844	0.810	0.025	6	4.027
NCH-44	CPX14C	51.810	0.675	1.615	9.510	0.328	15.190	20.070	0.356	99.554	1.940	0.019	0.071	0.298	0.010	0.848	0.805	0.026	6	4.018
NCH-44	CPX14R	51.690	0.629	1.754	9.990	0.418	15.640	19.660	0.355	100.136	1.928	0.018	0.077	0.312	0.013	0.869	0.786	0.026	6	4.029
NCH-63	CPX1C	50.560	0.735	2.346	8.570	0.251	15.850	21.070	0.292	99.674	1.893	0.021	0.104	0.268	0.008	0.885	0.845	0.021	6	4.045
NCH-63	CPX2C	51.290	0.784	2.189	8.110	0.280	15.640	20.350	0.346	98.988	1.922	0.022	0.097	0.254	0.009	0.873	0.817	0.025	6	4.020
NCH-63	CPX3C	51.470	0.674	2.265	7.450	0.218	16.170	21.410	0.335	99.991	1.909	0.019	0.099	0.231	0.007	0.894	0.851	0.024	6	4.034

Sample	Crystal	SiO2	TiO2	Al2O3	FeOt	MnO	MgO	CaO	Na2O	Total	Si	Ti	Al	Fe	Mn	Mg	Ca	Na	O	CatTot
NCH-63	CPX4C	51.950	0.680	2.234	7.860	0.274	16.230	20.980	0.331	100.539	1.916	0.019	0.097	0.243	0.009	0.892	0.829	0.024	6	4.029
NCH-63	CPX4R	51.700	0.708	2.325	7.810	0.254	15.740	21.040	0.331	99.908	1.919	0.020	0.102	0.242	0.008	0.871	0.837	0.024	6	4.022
NCH-63	CPX5C	52.020	0.636	2.029	7.770	0.251	15.760	20.590	0.310	99.367	1.936	0.018	0.089	0.242	0.008	0.874	0.821	0.022	6	4.012
NCH-63	CPX6C	50.840	0.775	2.682	7.620	0.225	15.780	21.120	0.370	99.411	1.899	0.022	0.118	0.238	0.007	0.879	0.845	0.027	6	4.034
NCH-63	CPX6R	51.920	0.552	1.937	8.210	0.213	16.430	20.820	0.278	100.360	1.920	0.015	0.084	0.254	0.007	0.905	0.825	0.020	6	4.032
NCH-63	CPX7C	51.300	0.622	2.033	8.360	0.241	16.270	20.930	0.313	100.069	1.908	0.017	0.089	0.260	0.008	0.902	0.834	0.023	6	4.041
NCH-63	CPX7R	51.270	0.755	2.224	9.130	0.323	15.540	19.900	0.358	99.499	1.919	0.021	0.098	0.286	0.010	0.867	0.798	0.026	6	4.024
NCH-63	CPX6R	50.200	0.871	3.350	8.970	0.247	15.280	20.200	0.340	99.458	1.881	0.025	0.148	0.281	0.008	0.853	0.811	0.025	6	4.032
NCH-26	CPX1C	50.390	0.607	1.480	12.110	0.412	14.220	19.580	0.326	99.126	1.922	0.017	0.067	0.386	0.013	0.808	0.801	0.024	6	4.039
NCH-26	CPX5C	50.890	0.620	1.662	10.400	0.363	14.850	20.150	0.329	99.264	1.924	0.018	0.074	0.329	0.012	0.837	0.816	0.024	6	4.034
NCH-26	CPX9R	51.380	0.436	1.203	11.080	0.407	14.690	20.280	0.317	99.793	1.938	0.012	0.054	0.350	0.013	0.826	0.819	0.023	6	4.035
NCH-26	CPX11C	51.300	0.500	1.338	10.920	0.349	14.680	20.330	0.340	99.757	1.934	0.014	0.060	0.344	0.011	0.825	0.821	0.025	6	4.035
NCH-26	CPX10R	51.030	0.615	1.640	9.980	0.300	15.420	20.480	0.330	99.795	1.917	0.017	0.073	0.313	0.010	0.864	0.824	0.024	6	4.042
NCH-27	CPX3R	51.980	0.509	1.220	11.630	0.409	14.220	20.030	0.327	100.324	1.978	0.008	0.021	0.722	0.023	1.181	0.067	0.004	6	4.005
NCH-27	CPX4C	51.250	0.625	1.697	10.440	0.347	15.000	20.410	0.348	100.116	1.949	0.014	0.054	0.365	0.013	0.795	0.805	0.024	6	4.021
NCH-27	CPX4R	51.480	0.520	1.299	11.470	0.452	14.430	19.740	0.338	99.728	1.921	0.018	0.075	0.327	0.011	0.838	0.820	0.025	6	4.036
NCH-27	CPX5C	51.140	0.520	1.331	11.070	0.392	14.790	20.280	0.318	99.840	1.943	0.015	0.058	0.362	0.014	0.812	0.798	0.025	6	4.026
NCH-27	CPX5R	51.070	0.444	1.171	12.020	0.468	14.300	20.050	0.322	99.845	1.929	0.015	0.059	0.349	0.013	0.832	0.820	0.023	6	4.039
NCH-27	CPX7R	52.010	0.352	0.897	11.840	0.417	14.080	19.980	0.316	99.891	1.934	0.013	0.052	0.381	0.015	0.807	0.813	0.024	6	4.039
NCH-27	CPX11C	50.110	0.775	2.270	12.260	0.423	13.290	20.050	0.348	99.524	1.907	0.022	0.102	0.390	0.014	0.754	0.818	0.026	6	4.033
NCH-27	CPX11R	51.370	0.445	1.209	11.730	0.442	14.430	20.150	0.310	100.086	1.937	0.013	0.054	0.370	0.014	0.811	0.814	0.023	6	4.035
NCH-45	CPX2R	51.530	0.565	1.484	10.610	0.356	14.860	19.700	0.293	99.397	1.941	0.016	0.066	0.334	0.011	0.834	0.795	0.021	6	4.020
NCH-45	CPX2R1	51.550	0.572	1.535	10.640	0.362	14.540	19.730	0.297	99.226	1.946	0.016	0.068	0.336	0.012	0.818	0.798	0.022	6	4.015
NCH-45	CPX3C	51.140	0.653	2.105	10.530	0.355	15.890	18.890	0.334	99.896	1.914	0.018	0.093	0.330	0.011	0.886	0.757	0.024	6	4.034
NCH-45	CPX3R	52.010	0.650	1.704	11.130	0.430	15.320	19.320	0.332	100.896	1.932	0.018	0.075	0.346	0.014	0.848	0.769	0.024	6	4.025
NCH-45	CPX6C	51.610	0.785	2.152	10.200	0.325	14.800	20.060	0.391	100.322	1.924	0.022	0.095	0.318	0.010	0.822	0.801	0.028	6	4.021
NCH-45	CPX6C1	50.950	0.831	2.177	10.350	0.378	15.120	19.760	0.338	99.904	1.911	0.023	0.096	0.324	0.012	0.845	0.794	0.025	6	4.030

Sample	Crystal	SiO2	TiO2	Al2O3	FeOt	MnO	MgO	CaO	Na2O	Total	Si	Ti	Al	Fe	Mn	Mg	Ca	Na	O	CatTot
NCH-45	CPX9C	52.160	0.375	1.002	11.740	0.512	13.370	19.810	0.316	99.285	1.976	0.011	0.045	0.372	0.016	0.755	0.804	0.023	6	4.002
NCH-45	CPX11C	52.420	0.266	1.023	10.910	0.445	14.310	20.520	0.294	100.188	1.964	0.008	0.045	0.342	0.014	0.799	0.824	0.021	6	4.017
NCH-45	CPX11R	51.760	0.660	1.402	10.930	0.414	14.400	19.810	0.377	99.753	1.946	0.019	0.062	0.344	0.013	0.807	0.798	0.028	6	4.019
NCH-45	CPX15C	50.650	0.548	1.435	10.880	0.420	15.350	19.500	0.339	99.122	1.920	0.016	0.064	0.345	0.014	0.867	0.792	0.025	6	4.044
NCH-46	CPX2C	51.110	0.572	1.660	10.590	0.427	14.150	20.200	0.348	99.058	1.937	0.016	0.074	0.336	0.014	0.799	0.820	0.026	6	4.023
NCH-46	CPX2R	52.360	0.418	1.060	12.200	0.460	13.870	19.560	0.315	100.244	1.966	0.012	0.047	0.383	0.015	0.776	0.787	0.023	6	4.010
NCH-46	CPX3R	51.900	0.437	1.120	11.270	0.494	14.190	20.030	0.321	99.762	1.956	0.012	0.050	0.355	0.016	0.797	0.809	0.023	6	4.018
NCH-46	CPX5R	51.510	0.695	2.011	9.960	0.351	14.890	19.780	0.371	99.568	1.932	0.020	0.089	0.312	0.011	0.833	0.795	0.027	6	4.018
NCH-46	CPX7R	52.880	0.357	0.962	12.130	0.522	14.040	19.720	0.310	100.921	1.971	0.010	0.042	0.378	0.017	0.780	0.788	0.022	6	4.009
NCH-46	CPX10C	51.630	0.496	1.279	12.330	0.513	13.850	20.000	0.327	100.425	1.943	0.014	0.057	0.388	0.016	0.777	0.807	0.024	6	4.026
NCH-46	CPX10R	52.370	0.489	1.015	12.410	0.515	13.280	19.820	0.311	100.210	1.971	0.014	0.045	0.391	0.016	0.745	0.799	0.023	6	4.004
NCH-46	CPX11C	51.980	0.517	1.357	10.360	0.432	15.440	19.540	0.310	99.937	1.944	0.015	0.060	0.324	0.014	0.861	0.783	0.023	6	4.023
NCH-46	CPX11R	52.270	0.457	0.993	12.370	0.502	13.850	20.150	0.320	100.911	1.956	0.013	0.044	0.387	0.016	0.773	0.808	0.023	6	4.020
NCH-46	CPX12R	51.560	0.382	1.011	11.740	0.458	13.650	20.020	0.329	99.150	1.960	0.011	0.045	0.373	0.015	0.774	0.816	0.024	6	4.018
NCH-46	CPX15C	52.100	0.482	1.103	11.740	0.474	13.780	19.330	0.297	99.306	1.970	0.014	0.049	0.371	0.015	0.777	0.783	0.022	6	4.002
NCH-46	CPX15R	51.220	0.735	1.954	11.490	0.432	13.890	20.040	0.339	100.100	1.927	0.021	0.087	0.361	0.014	0.779	0.808	0.025	6	4.021
NCH-55	CPX1R1	51.280	0.536	1.239	11.650	0.409	14.200	20.010	0.346	99.670	1.940	0.015	0.055	0.369	0.013	0.801	0.811	0.025	6	4.030
NCH-55	CPX5C	51.790	0.577	1.429	10.900	0.368	14.970	20.480	0.316	100.831	1.930	0.016	0.063	0.340	0.012	0.832	0.818	0.023	6	4.033
NCH-55	CPX 6R	50.090	0.842	2.591	9.670	0.267	15.370	20.270	0.367	99.468	1.886	0.024	0.115	0.305	0.009	0.863	0.818	0.027	6	4.046
NCH-55	CPX7C	51.990	0.483	1.182	11.280	0.408	14.520	20.290	0.324	100.477	1.947	0.014	0.052	0.353	0.013	0.810	0.814	0.024	6	4.026
NCH-55	CPX9R	52.090	0.380	0.984	12.270	0.434	13.820	20.410	0.319	100.707	1.955	0.011	0.044	0.385	0.014	0.773	0.821	0.023	6	4.025
NCH-55	CPX11R	50.430	0.677	1.808	12.040	0.383	14.310	20.090	0.355	100.093	1.907	0.019	0.081	0.381	0.012	0.806	0.814	0.026	6	4.046

Análisis de ortopiroxenos en Universidad de Concepción

Sample	Crystal	SiO2	TiO2	Al2O3	FeOt	MnO	MgO	CaO	Na2O	Total	Si	Ti	Al	Fe	Mn	Mg	Ca	Na	O	CatTot
NCH-18	OPX1C	52.530	0.294	0.915	17.910	0.443	25.330	2.146	0.06	99.567	1.938	0.008	0.040	0.553	0.014	1.393	0.085	0.004	6	4.036
NCH-18	OPX3C	52.120	0.267	0.875	20.350	0.601	23.650	1.570	0.03	99.433	1.946	0.008	0.039	0.635	0.019	1.316	0.063	0.002	6	4.028
NCH-18	OPX3C1	52.620	0.309	1.156	17.940	0.497	24.210	1.702	0.04	98.434	1.960	0.009	0.051	0.559	0.016	1.344	0.068	0.003	6	4.008
NCH-18	OPX4C	52.790	0.331	1.486	16.730	0.371	25.890	1.726	0.05	99.324	1.937	0.009	0.064	0.513	0.012	1.415	0.068	0.003	6	4.023
NCH-18	OPX6R	52.990	0.406	1.438	16.180	0.417	25.130	2.655	0.05	99.216	1.945	0.011	0.062	0.497	0.013	1.375	0.104	0.003	6	4.013
NCH-18	OPX7C	53.520	0.440	1.209	17.130	0.384	25.390	2.419	0.04	100.492	1.947	0.012	0.052	0.521	0.012	1.376	0.094	0.003	6	4.017
NCH-18	OPX10R	53.500	0.322	0.811	16.860	0.427	25.570	2.262	0.06	99.751	1.958	0.009	0.035	0.516	0.013	1.394	0.089	0.005	6	4.018
NCH-18	OPX11R	53.550	0.432	1.126	15.800	0.419	26.230	1.986	0.04	99.542	1.951	0.012	0.048	0.482	0.013	1.425	0.078	0.003	6	4.013
NCH-18	OPX13R	53.320	0.409	1.094	16.800	0.420	25.230	2.232	0.05	99.505	1.955	0.011	0.047	0.515	0.013	1.378	0.088	0.004	6	4.012
NCH-49	OPX2R	53.270	0.386	1.097	16.410	0.423	26.370	1.719	0.01	99.675	1.945	0.011	0.047	0.501	0.013	1.435	0.067	0.001	6	4.021
NCH-49	OPX5C	53.030	0.314	0.925	16.460	0.488	26.280	1.823	0.03	99.321	1.946	0.009	0.040	0.505	0.015	1.438	0.072	0.002	6	4.026
NCH-49	OPX6R	53.440	0.334	1.108	16.410	0.414	26.390	1.749	0.03	99.846	1.947	0.009	0.048	0.500	0.013	1.433	0.068	0.002	6	4.021
NCH-49	OPX8R	53.550	0.355	1.052	15.710	0.365	27.070	1.908	0.05	100.011	1.942	0.010	0.045	0.477	0.011	1.463	0.074	0.003	6	4.027
NCH-49	OPX9C	52.180	0.388	1.155	19.480	0.550	24.300	1.787	0.05	99.840	1.933	0.011	0.050	0.604	0.017	1.342	0.071	0.003	6	4.032
NCH-49	OPX9C1	52.790	0.346	0.830	19.280	0.552	24.390	1.927	0.04	100.115	1.948	0.010	0.036	0.595	0.017	1.341	0.076	0.003	6	4.026
NCH-49	OPX10R	52.240	0.339	0.881	18.900	0.544	24.910	1.930	0.04	99.744	1.934	0.009	0.038	0.585	0.017	1.374	0.077	0.003	6	4.039
NCH-49	OPX14R	52.650	0.365	0.763	17.720	0.471	25.440	1.994	0.05	99.403	1.944	0.010	0.033	0.547	0.015	1.400	0.079	0.004	6	4.031
NCH-49	OPX14R1	53.270	0.368	0.837	17.960	0.432	25.600	1.944	0.04	100.411	1.946	0.010	0.036	0.549	0.013	1.394	0.076	0.003	6	4.027
NCH-49	OPX16R	52.400	0.372	0.776	21.250	0.461	22.930	2.029	0.06	100.218	1.949	0.010	0.034	0.661	0.015	1.271	0.081	0.005	6	4.026
NCH-49	OPX16R1	52.430	0.379	0.961	20.650	0.515	22.290	1.904	0.04	99.128	1.964	0.011	0.042	0.647	0.016	1.245	0.076	0.003	6	4.005
NCH-54	OPX1C	52.600	0.414	0.954	19.490	0.484	24.600	2.027	0.04	100.568	1.935	0.011	0.041	0.600	0.015	1.349	0.080	0.003	6	4.034
NCH-54	OPX1R	53.200	0.408	0.908	19.240	0.459	24.290	2.028	0.05	100.532	1.952	0.011	0.039	0.590	0.014	1.328	0.080	0.004	6	4.019
NCH-54	OPX2C	52.660	0.428	0.941	19.350	0.440	23.960	2.136	0.06	99.914	1.948	0.012	0.041	0.599	0.014	1.321	0.085	0.004	6	4.022
NCH-54	OPX2R	52.730	0.362	0.906	19.270	0.441	23.470	2.075	0.05	99.253	1.961	0.010	0.040	0.599	0.014	1.301	0.083	0.004	6	4.011
NCH-54	OPX4C	52.790	0.394	0.984	18.660	0.448	24.360	2.028	0.05	99.665	1.950	0.011	0.043	0.576	0.014	1.341	0.080	0.004	6	4.019
NCH-54	OPX4R	52.910	0.405	0.958	19.270	0.475	23.700	2.020	0.05	99.738	1.957	0.011	0.042	0.596	0.015	1.307	0.080	0.003	6	4.012

Sample	Crystal	SiO2	TiO2	Al2O3	FeOt	MnO	MgO	CaO	Na2O	Total	Si	Ti	Al	Fe	Mn	Mg	Ca	Na	O	CatTot
NCH-54	OPX5R	52.740	0.488	0.979	18.260	0.424	23.720	2.124	0.06	98.735	1.962	0.014	0.043	0.568	0.013	1.316	0.085	0.004	6	4.005
NCH-54	OPX5R1	53.550	0.337	0.897	19.770	0.467	24.220	2.072	0.05	101.314	1.953	0.009	0.039	0.603	0.014	1.316	0.081	0.004	6	4.020
NCH-54	OPX6R	52.700	0.440	1.013	18.310	0.430	23.980	2.078	0.05	98.951	1.958	0.012	0.044	0.569	0.014	1.327	0.083	0.003	6	4.010
NCH-54	OPX7R	52.950	0.347	0.940	18.840	0.415	24.110	2.016	0.05	99.617	1.957	0.010	0.041	0.582	0.013	1.328	0.080	0.003	6	4.015
NCH-54	OPX7R1	52.540	0.439	0.944	19.260	0.377	24.280	2.043	0.06	99.883	1.942	0.012	0.041	0.596	0.012	1.338	0.081	0.004	6	4.027
NCH-54	OPX8C	53.280	0.496	0.906	19.590	0.438	23.890	2.095	0.04	100.695	1.955	0.014	0.039	0.601	0.014	1.306	0.082	0.003	6	4.014
NCH-54	OPX8C1	52.850	0.451	1.029	19.430	0.403	24.060	1.980	0.05	100.203	1.948	0.013	0.045	0.599	0.013	1.322	0.078	0.004	6	4.019
NCH-54	OPX9C	52.940	0.409	0.937	19.850	0.530	23.300	2.057	0.05	100.024	1.958	0.011	0.041	0.614	0.017	1.285	0.082	0.003	6	4.012
NCH-54	OPX11R	52.940	0.399	0.951	18.870	0.430	24.210	1.978	0.04	99.778	1.954	0.011	0.041	0.582	0.013	1.332	0.078	0.003	6	4.016
NCH-54	OPX14C	53.440	0.376	1.255	16.910	0.397	25.700	1.848	0.03	99.925	1.950	0.010	0.054	0.516	0.012	1.397	0.072	0.002	6	4.014
NCH-60	OPX4R	52.480	0.394	0.899	24.220	0.779	20.260	1.805	0.03	100.837	1.965	0.011	0.040	0.759	0.025	1.131	0.072	0.002	6	4.005
NCH-60	OPX19R	52.290	0.471	0.502	22.320	0.617	20.220	3.030	0.09	99.451	1.975	0.013	0.022	0.705	0.020	1.139	0.123	0.006	6	4.003
NCH-60	OPX13R	52.420	0.455	1.753	18.350	0.512	24.420	1.548	0.04	99.459	1.935	0.013	0.076	0.567	0.016	1.344	0.061	0.003	6	4.015
NCH-39	OPX1R	52.550	0.268	0.797	19.480	0.700	23.550	1.902	0.0299	99.247	1.958	0.008	0.035	0.607	0.022	1.308	0.076	0.0042	6	4.017
NCH-39	OPX2R	52.900	0.386	1.322	17.560	0.516	25.400	1.697	0.0434	99.782	1.940	0.011	0.057	0.539	0.016	1.388	0.067	0.0027	6	4.022
NCH-44	OPX2R	52.600	0.339	0.805	18.720	0.604	24.960	1.707	0.03	99.734	1.944	0.009	0.035	0.579	0.019	1.375	0.068	0.002	6	4.031
NCH-44	OPX5R	52.490	0.314	0.802	18.560	0.600	24.480	1.694	0.03	98.940	1.953	0.009	0.035	0.578	0.019	1.358	0.068	0.002	6	4.021
NCH-44	OPX6R	52.850	0.314	0.724	18.790	0.612	25.240	1.705	0.03	100.236	1.943	0.009	0.031	0.578	0.019	1.383	0.067	0.002	6	4.033
NCH-44	OPX8R	52.140	0.348	0.835	18.450	0.591	24.720	1.694	0.05	98.779	1.944	0.010	0.037	0.575	0.019	1.374	0.068	0.004	6	4.030
NCH-44	OPX8R1	53.210	0.319	0.785	18.970	0.569	24.990	1.715	0.03	100.558	1.950	0.009	0.034	0.581	0.018	1.365	0.067	0.003	6	4.026
NCH-44	OPX9R	52.220	0.436	0.890	18.270	0.629	24.950	1.717	0.04	99.112	1.939	0.012	0.039	0.568	0.020	1.381	0.068	0.003	6	4.030
NCH-44	OPX10R	52.410	0.540	0.940	18.350	0.554	24.780	1.912	0.03	99.485	1.939	0.015	0.041	0.568	0.017	1.367	0.076	0.002	6	4.026
NCH-44	OPX11R	52.950	0.371	0.756	18.400	0.574	25.460	1.772	0.04	100.283	1.943	0.010	0.033	0.565	0.018	1.392	0.070	0.003	6	4.032
NCH-44	OPX12R	52.860	0.453	0.950	18.600	0.581	24.860	1.731	0.04	100.036	1.945	0.013	0.041	0.572	0.018	1.363	0.068	0.003	6	4.023
NCH-44	OPX14R	52.990	0.368	0.921	18.770	0.582	24.680	1.762	0.06	100.072	1.949	0.010	0.040	0.578	0.018	1.353	0.069	0.004	6	4.022
NCH-26	OPX1R	51.340	0.406	0.998	22.790	0.629	21.760	1.751	0.06	99.675	1.937	0.012	0.044	0.719	0.020	1.224	0.071	0.0042	6	4.031
NCH-26	OPX2C	51.550	0.300	0.575	23.810	0.789	20.710	1.634	0.04	99.367	1.960	0.009	0.026	0.757	0.025	1.174	0.067	0.0027	6	4.020
NCH-26	OPX3C	52.490	0.328	0.689	21.480	0.632	22.270	1.720	0.03	99.609	1.965	0.009	0.030	0.672	0.020	1.243	0.069	0.0025	6	4.012

Sample	Crystal	SiO2	TiO2	Al2O3	FeOt	MnO	MgO	CaO	Na2O	Total	Si	Ti	Al	Fe	Mn	Mg	Ca	Na	O	CatTot
NCH-26	OPX5R	51.900	0.362	0.720	21.030	0.603	22.620	1.807	0.04	99.042	1.954	0.010	0.032	0.662	0.019	1.269	0.073	0.0032	6	4.022
NCH-26	OPX6R	51.800	0.289	0.527	24.390	0.800	20.770	1.690	0.05	100.266	1.956	0.008	0.024	0.770	0.026	1.169	0.068	0.0037	6	4.025
NCH-26	OPX7R	53.840	0.240	0.684	16.890	0.440	26.290	1.530	0.04	99.914	1.963	0.007	0.029	0.515	0.014	1.428	0.060	0.003	6	4.018
NCH-26	OPX8C	52.020	0.288	0.594	23.760	0.744	21.110	1.670	0.06	100.186	1.959	0.008	0.026	0.748	0.024	1.185	0.067	0.0047	6	4.022
NCH-26	OPX9C	50.730	0.352	0.965	23.270	0.666	21.260	1.686	0.04	98.929	1.936	0.010	0.043	0.743	0.022	1.209	0.069	0.003	6	4.034
NCH-26	OPX10R	51.690	0.311	0.630	23.210	0.722	21.370	1.684	0.04	99.617	1.955	0.009	0.028	0.734	0.023	1.204	0.068	0.0027	6	4.024
NCH-26	OPX11R	52.430	0.284	0.642	22.470	0.617	22.040	1.671	0.04	100.154	1.961	0.008	0.028	0.703	0.020	1.228	0.067	0.0026	6	4.018
NCH-26	OPX12C	52.220	0.315	0.620	21.990	0.681	22.450	1.639	0.04	99.914	1.955	0.009	0.027	0.688	0.022	1.253	0.066	0.0029	6	4.023
NCH-27	OPX1C	52.210	0.297	0.570	22.960	0.766	21.340	1.655	0.04	99.798	1.966	0.008	0.025	0.723	0.024	1.197	0.067	0.0028	6	4.014
NCH-27	OPX2C	52.000	0.335	1.213	20.830	0.527	23.710	1.601	0.02	100.215	1.931	0.009	0.053	0.647	0.017	1.312	0.064	0.0015	6	4.034
NCH-27	OPX3R	52.380	0.279	0.471	22.850	0.732	20.990	1.646	0.05	99.348	1.978	0.008	0.021	0.722	0.023	1.181	0.067	0.0037	6	4.005
NCH-27	OPX6C	51.910	0.313	0.543	23.720	0.747	20.790	1.743	0.05	99.766	1.964	0.009	0.024	0.750	0.024	1.172	0.071	0.0035	6	4.017
NCH-27	OPX7R	51.850	0.275	0.638	23.600	0.794	20.470	1.674	0.04	99.301	1.969	0.008	0.029	0.749	0.026	1.159	0.068	0.0028	6	4.010
NCH-27	OPX8C	52.590	0.299	0.643	20.840	0.590	23.250	1.683	0.03	99.895	1.958	0.008	0.028	0.649	0.019	1.290	0.067	0.0024	6	4.021
NCH-27	OPX9R	52.860	0.323	0.640	20.590	0.629	23.490	1.770	0.02	100.302	1.957	0.009	0.028	0.638	0.020	1.297	0.070	0.0012	6	4.020
NCH-27	OPX10C	52.840	0.243	0.503	21.420	0.745	22.930	1.670	0.04	100.350	1.963	0.007	0.022	0.666	0.023	1.270	0.067	0.0027	6	4.020
NCH-27	OPX11C	51.610	0.306	0.659	22.970	0.717	21.230	1.585	0.02	99.077	1.959	0.009	0.030	0.729	0.023	1.201	0.065	0.0012	6	4.018
NCH-27	OPX11R	51.370	0.314	0.537	23.640	0.821	20.670	1.756	0.04	99.107	1.937	0.013	0.054	0.370	0.014	0.811	0.814	0.0227	6	4.035
NCH-27	OPX12C	52.000	0.297	0.673	22.430	0.702	21.640	1.661	0.03	99.402	1.962	0.008	0.030	0.708	0.022	1.217	0.067	0.0019	6	4.016
NCH-45	OPX1C	52.470	0.278	0.506	22.620	0.767	21.280	1.741	0.05	99.662	1.975	0.008	0.022	0.712	0.024	1.194	0.070	0.003	6	4.008
NCH-45	OPX1C1	52.450	0.229	0.555	22.710	0.743	20.530	1.902	0.05	99.118	1.985	0.007	0.025	0.719	0.024	1.158	0.077	0.003	6	3.998
NCH-45	OPX2R	52.210	0.303	0.628	21.120	0.723	22.280	1.683	0.01	98.947	1.967	0.009	0.028	0.665	0.023	1.251	0.068	0.001	6	4.011
NCH-45	OPX6C	53.450	0.199	0.619	18.370	0.531	24.720	1.678	0.03	99.567	1.970	0.006	0.027	0.566	0.017	1.358	0.066	0.002	6	4.012
NCH-45	OPX6R	52.970	0.314	1.074	19.240	0.572	24.620	1.720	0.04	100.510	1.944	0.009	0.047	0.591	0.018	1.347	0.068	0.003	6	4.025
NCH-45	OPX8C	52.420	0.293	0.633	20.090	0.662	22.870	1.677	0.02	98.645	1.970	0.008	0.028	0.631	0.021	1.281	0.068	0.002	6	4.009
NCH-45	OPX9C	52.270	0.253	0.500	22.400	0.803	21.980	1.676	0.04	99.881	1.962	0.007	0.022	0.703	0.026	1.230	0.067	0.003	6	4.021
NCH-45	OPX11R	53.500	0.236	0.535	20.190	0.762	22.930	1.672	0.04	99.825	1.983	0.007	0.023	0.626	0.024	1.267	0.066	0.003	6	4.000
NCH-45	OPX15C	51.630	0.262	0.524	22.370	0.866	21.680	1.860	0.04	99.192	1.956	0.008	0.023	0.709	0.028	1.224	0.076	0.003	6	4.026

Sample	Crystal	SiO2	TiO2	Al2O3	FeOt	MnO	MgO	CaO	Na2O	Total	Si	Ti	Al	Fe	Mn	Mg	Ca	Na	O	CatTot
NCH-45	OPX15C1	52.120	0.197	0.463	23.210	0.845	22.040	1.658	0.02	100.533	1.952	0.006	0.021	0.727	0.027	1.231	0.067	0.002	6	4.032
NCH-45	OPX15C2	51.370	0.313	0.613	22.740	0.805	21.190	1.621	0.03	98.653	1.959	0.009	0.028	0.725	0.026	1.205	0.066	0.002	6	4.020
NCH-46	OPX7R	52.380	0.257	0.440	24.150	0.874	19.930	1.564	0.07	99.595	1.985	0.007	0.020	0.765	0.028	1.126	0.064	0.005	6	4.000
NCH-46	OPX3R	52.410	0.214	0.907	23.400	0.674	21.460	1.617	0.04	100.683	1.958	0.006	0.040	0.731	0.021	1.195	0.065	0.003	6	4.018
NCH-46	OPX5R	54.380	0.303	0.710	17.550	0.512	25.230	1.723	0.04	100.409	1.977	0.008	0.030	0.534	0.016	1.367	0.067	0.003	6	4.002
NCH-46	OPX11R	52.290	0.259	0.553	24.430	0.854	20.810	1.663	0.06	100.859	1.961	0.007	0.025	0.766	0.027	1.164	0.067	0.004	6	4.021
NCH-46	OPX15R	52.040	0.285	0.766	24.160	0.777	20.490	1.628	0.05	100.146	1.963	0.008	0.034	0.762	0.025	1.152	0.066	0.003	6	4.014
NCH-55	OPX1R	51.960	0.275	0.535	23.010	0.726	21.290	1.759	0.04	99.555	1.963	0.008	0.024	0.727	0.023	1.199	0.071	0.003	6	4.019
NCH-55	OPX2C	51.720	0.381	0.932	23.000	0.612	21.380	1.689	0.04	99.715	1.950	0.011	0.041	0.725	0.020	1.201	0.068	0.0032	6	4.020
NCH-55	OPX3C	52.720	0.373	1.129	18.540	0.413	24.800	1.872	0.07	99.848	1.942	0.010	0.049	0.571	0.013	1.362	0.074	0.0049	6	4.026
NCH-55	OPX6C	52.560	0.292	0.616	21.220	0.635	23.500	1.709	0.04	100.533	1.949	0.008	0.027	0.658	0.020	1.299	0.068	0.003	6	4.031
NCH-55	OPX7C	52.050	0.328	0.688	23.190	0.703	21.500	1.578	0.05	100.037	1.957	0.009	0.031	0.729	0.022	1.205	0.064	0.0034	6	4.020
NCH-55	OPX9C	52.420	0.284	0.488	23.480	0.803	21.370	1.654	0.05	100.499	1.964	0.008	0.022	0.736	0.026	1.194	0.066	0.0034	6	4.019
NCH-55	OPX10C	52.870	0.270	0.600	21.680	0.672	22.200	1.622	0.04	99.914	1.973	0.008	0.026	0.677	0.021	1.235	0.065	0.003	6	4.008
NCH-55	OPX11C	51.680	0.311	0.578	23.000	0.740	21.750	1.722	0.03	99.782	1.950	0.009	0.026	0.726	0.024	1.223	0.070	0.002	6	4.029
NCH-55	OPX11R	51.650	0.273	0.504	23.960	0.794	20.890	1.636	0.05	99.707	1.958	0.008	0.023	0.760	0.026	1.181	0.067	0.0033	6	4.024

Análisis de olivinos en Universidad de Concepción

Samples	Crystal	SiO2	FeO	MnO	MgO	CaO	Total	Si	Fe	Mn	Mg	Ca	O	CatTot
NCH-18	Ol1C	36.56	28.47	0.42	33.56	0.22	99.23	0.99088	0.64521	0.00964	1.35600	0.00639	4	3.008
NCH-18	Ol1R	36.72	28.95	0.39	33.29	0.25	99.60	0.99270	0.65444	0.00904	1.34170	0.00724	4	3.005
NCH-18	Ol4R	37.20	25.80	0.39	36.17	0.16	99.72	0.98367	0.57046	0.00872	1.42587	0.00452	4	2.993
NCH-46	Ol21C	39.54	15.56	0.22	45.02	0.14	100.48	0.99088	0.32606	0.00466	1.68195	0.00371	4	3.007
NCH-46	Ol21R1	38.66	21.27	0.36	40.24	0.14	100.68	0.99364	0.45713	0.00794	1.54188	0.00398	4	3.005
NCH-55	Ol3C1	39.20	18.51	0.24	42.78	0.19	100.92	0.99188	0.39164	0.00523	1.61377	0.00506	4	3.008
NCH-55	Ol4R	37.31	27.60	0.38	35.17	0.17	100.63	0.99061	0.61276	0.00853	1.39212	0.00487	4	3.009
NCH-55	Ol5C	37.47	26.37	0.36	36.10	0.17	100.47	0.99051	0.58289	0.00814	1.42268	0.00473	4	3.009
NCH-60	Ol18R	38.26	23.22	0.37	38.66	0.23	100.74	0.99261	0.50373	0.00806	1.49527	0.00638	4	3.006
NCH-60	Ol20C1	39.55	16.08	0.22	43.84	0.16	99.85	0.99943	0.33978	0.00480	1.65159	0.00432	4	3.000
NCH-60	Ol20R	38.42	24.00	0.37	37.75	0.14	100.68	0.99889	0.52176	0.00822	1.46319	0.00391	4	2.996
NCH-39	Ol10	38.26	20.55	0.34	39.97	0.19	99.30	0.99460	0.44690	0.00740	1.54880	0.00520	4	3.005

Análisis de plagioclasas en Universidad de Rice

Sample	Crystal	SiO2	Al2O3	FeO	MgO	CaO	Na2O	K2O	Total	Si	Al	Fe	Mg	Ca	Na	K	O	CatTot
NCH-44	Pl1C	55.760	27.680	0.601	0.0747	10.440	5.660	0.212	100.427	2.506	1.467	0.023	0.005	0.503	0.494	0.012	8	5.012
NCH-44	Pl1C1	56.110	27.770	0.598	0.0777	10.360	5.650	0.203	100.769	2.510	1.464	0.022	0.0052	0.497	0.490	0.012	8	5.004
NCH-44	Pl1R	55.840	27.800	0.662	0.0642	10.230	5.670	0.254	100.521	2.508	1.472	0.025	0.0043	0.492	0.494	0.015	8	5.011
NCH-44	Pl1R1	55.880	27.480	0.739	0.0715	9.840	5.780	0.263	100.053	2.519	1.460	0.028	0.0048	0.475	0.505	0.015	8	5.009
NCH-44	Pl2C	55.240	28.370	0.572	0.0707	10.560	5.480	0.231	100.523	2.481	1.502	0.022	0.0047	0.508	0.478	0.013	8	5.011
NCH-44	Pl3C	55.530	28.050	0.656	0.0666	10.580	5.610	0.215	100.707	2.490	1.483	0.025	0.0045	0.509	0.488	0.012	8	5.015
NCH-44	Pl3R	56.860	26.910	0.765	0.0558	9.290	6.300	0.300	100.481	2.549	1.422	0.029	0.0037	0.446	0.547	0.017	8	5.018
NCH-44	Pl3R1	56.870	26.480	0.724	0.0763	8.920	6.180	0.336	99.586	2.567	1.409	0.027	0.0051	0.431	0.541	0.019	8	5.005
NCH-44	Pl4C	55.300	27.980	0.716	0.0723	10.210	5.700	0.270	100.249	2.491	1.485	0.027	0.0037	0.493	0.497	0.016	8	5.019

Sample	Crystal	SiO2	Al2O3	FeO	MgO	CaO	Na2O	K2O	Total	Si	Al	Fe	Mg	Ca	Na	K	O	CatTot
NCH-44	Pl4R	56.960	26.780	0.714	0.0672	8.990	6.370	0.353	100.233	2.557	1.417	0.027	0.004	0.432	0.555	0.020	8	5.017
NCH-44	Pl5C	55.200	28.060	0.679	0.0709	10.530	5.560	0.239	100.339	2.486	1.490	0.026	0.0048	0.508	0.486	0.014	8	5.017
NCH-44	Pl5R	57.620	26.620	0.713	0.0582	8.900	6.460	0.361	100.732	2.573	1.401	0.027	0.0039	0.426	0.559	0.021	8	5.014
NCH-44	Pl6C	55.170	28.320	0.573	0.0595	10.650	5.490	0.221	100.484	2.480	1.500	0.022	0.004	0.513	0.479	0.013	8	5.013
NCH-44	Pl6R	55.110	28.360	0.642	0.0764	10.370	5.570	0.214	100.343	2.481	1.505	0.024	0.0051	0.500	0.486	0.012	8	5.015
NCH-44	Pl7C	55.330	28.010	0.589	0.0727	10.620	5.530	0.199	100.350	2.490	1.486	0.022	0.0049	0.512	0.483	0.011	8	5.013
NCH-44	Pl7R	56.500	26.410	1.400	0.3999	9.280	6.100	0.321	100.411	2.544	1.401	0.053	0.0268	0.448	0.533	0.018	8	5.029
NCH-26	Pl17C	57.320	26.500	0.502	0.0277	8.680	6.340	0.360	99.730	2.581	1.406	0.019	0.0019	0.419	0.553	0.021	8	5.002
NCH-26	Pl17C1	57.020	26.700	0.553	0.0431	8.900	6.370	0.366	99.951	2.566	1.416	0.021	0.0029	0.429	0.556	0.021	8	5.013
NCH-26	Pl17C2	56.800	27.330	0.516	0.0376	9.410	6.100	0.291	100.484	2.543	1.442	0.019	0.0025	0.451	0.530	0.017	8	5.007
NCH-26	Pl17R	60.160	25.010	0.547	0.0191	6.800	7.460	0.512	100.508	2.675	1.311	0.020	0.0013	0.324	0.643	0.029	8	5.005
NCH-26	Pl18C	50.020	31.550	0.627	0.0564	14.420	3.250	0.097	100.021	2.284	1.698	0.024	0.0038	0.705	0.287	0.006	8	5.010
NCH-26	Pl18C1	50.680	31.190	0.605	0.0569	14.120	3.360	0.109	100.121	2.308	1.674	0.023	0.0039	0.689	0.297	0.006	8	5.004
NCH-26	Pl18C2	52.970	29.780	0.554	0.0399	12.420	4.660	0.160	100.583	2.392	1.585	0.021	0.0027	0.601	0.408	0.009	8	5.022
NCH-26	Pl18R	55.160	28.470	0.552	0.054	10.920	5.300	0.224	100.680	2.475	1.506	0.021	0.0036	0.525	0.461	0.013	8	5.006
NCH-26	Pl18R1	56.020	27.610	0.547	0.0486	9.800	5.720	0.309	100.054	2.522	1.465	0.021	0.0033	0.473	0.499	0.018	8	5.003
NCH-26	Pl19C	58.680	25.880	0.396	0.0295	7.930	7.000	0.406	100.321	2.621	1.363	0.015	0.002	0.380	0.607	0.023	8	5.013
NCH-26	Pl19C1	59.230	25.640	0.431	0.0407	7.470	7.060	0.412	100.284	2.642	1.348	0.016	0.0027	0.357	0.611	0.024	8	5.001
NCH-26	Pl19C2	58.370	26.350	0.444	0.0367	8.380	6.650	0.393	100.624	2.602	1.384	0.017	0.0024	0.400	0.575	0.022	8	5.003
NCH-26	Pl19C3	59.040	25.820	0.471	0.0379	7.910	6.780	0.395	100.454	2.630	1.356	0.018	0.0025	0.378	0.585	0.023	8	4.994
NCH-26	Pl19R	58.220	26.210	0.456	0.0372	8.190	6.740	0.371	100.225	2.604	1.382	0.017	0.0025	0.392	0.585	0.021	8	5.006
NCH-45	Pl19C	55.910	27.330	0.568	0.057	10.130	5.570	0.285	99.850	2.524	1.454	0.021	0.0038	0.490	0.487	0.016	8	4.999
NCH-45	Pl19C1	56.520	27.500	0.540	0.0601	9.750	5.890	0.315	100.575	2.531	1.451	0.020	0.004	0.468	0.511	0.018	8	5.006
NCH-45	Pl19R	56.140	27.470	0.565	0.049	10.270	5.550	0.268	100.312	2.522	1.455	0.021	0.0033	0.494	0.484	0.015	8	4.997
NCH-45	Pl20C	59.220	24.950	0.503	0.0495	7.150	7.320	0.489	99.682	2.658	1.320	0.019	0.0033	0.344	0.637	0.028	8	5.011
NCH-45	Pl20C1	59.200	25.450	0.516	0.0573	7.390	6.890	0.504	100.007	2.648	1.342	0.019	0.0038	0.354	0.598	0.029	8	4.995
NCH-45	Pl20R	58.720	25.930	0.634	0.0499	8.170	6.620	0.455	100.579	2.617	1.362	0.024	0.0033	0.390	0.572	0.026	8	4.998

Sample	Crystal	SiO2	Al2O3	FeO	MgO	CaO	Na2O	K2O	Total	Si	Al	Fe	Mg	Ca	Na	K	O	CatTot
NCH-45	Pl21C	56.310	27.440	0.667	0.0855	9.920	5.840	0.340	100.603	2.524	1.450	0.025	0.0057	0.477	0.507	0.020	8	5.012
NCH-45	Pl21C1	56.180	27.370	0.669	0.0884	9.740	5.760	0.294	100.101	2.528	1.451	0.025	0.0059	0.470	0.502	0.017	8	5.003
NCH-45	Pl21R	56.910	26.920	0.571	0.0598	9.430	5.930	0.334	100.155	2.555	1.424	0.021	0.004	0.454	0.516	0.019	8	4.998
NCH-45	Pl21R1	56.990	27.030	0.586	0.0594	9.420	5.980	0.343	100.409	2.554	1.428	0.022	0.004	0.452	0.520	0.020	8	5.001
NCH-45	Pl22C	56.150	27.550	0.406	0.0297	10.190	5.740	0.299	100.364	2.521	1.458	0.015	0.002	0.490	0.499	0.017	8	5.006
NCH-45	Pl22C1	55.730	28.420	0.444	0.0481	10.560	5.520	0.266	100.988	2.491	1.497	0.017	0.0032	0.506	0.478	0.015	8	5.007
NCH-45	Pl22C2	57.470	26.620	0.431	0.0487	9.260	6.310	0.319	100.459	2.572	1.404	0.016	0.0033	0.444	0.548	0.018	8	5.007
NCH-45	Pl22C3	56.300	27.840	0.457	0.055	9.960	5.780	0.298	100.690	2.519	1.468	0.017	0.0037	0.478	0.502	0.017	8	5.006
NCH-45	Pl22R	56.100	27.350	0.590	0.0448	9.870	5.830	0.288	100.073	2.527	1.452	0.022	0.003	0.476	0.509	0.017	8	5.008
NCH-45	Pl23C	56.150	27.140	0.615	0.0703	9.790	5.640	0.307	99.712	2.535	1.444	0.023	0.0047	0.474	0.494	0.018	8	4.996
NCH-45	Pl23C1	56.840	26.790	0.639	0.0682	9.250	5.990	0.352	99.928	2.558	1.421	0.024	0.0046	0.446	0.523	0.020	8	5.000
NCH-45	Pl23R	57.810	26.630	0.557	0.0586	8.950	6.290	0.368	100.663	2.580	1.400	0.021	0.0039	0.428	0.545	0.021	8	5.001
NCH-45	Pl24C	56.330	27.670	0.562	0.0688	10.000	5.630	0.304	100.564	2.523	1.461	0.021	0.0046	0.480	0.489	0.017	8	4.998
NCH-45	Pl24C1	55.940	27.430	0.572	0.0504	10.190	5.640	0.267	100.090	2.520	1.456	0.022	0.0034	0.492	0.493	0.015	8	5.004
NCH-45	Pl24C2	56.270	27.210	0.609	0.0613	9.590	5.760	0.308	99.808	2.538	1.446	0.023	0.0041	0.463	0.504	0.018	8	4.999
NCH-45	Pl24R	56.870	27.100	0.619	0.0532	9.630	5.790	0.347	100.409	2.548	1.431	0.023	0.0036	0.462	0.503	0.020	8	4.994
NCH-45	Pl24R1	56.520	26.940	0.596	0.06	9.270	5.990	0.317	99.694	2.550	1.432	0.023	0.004	0.448	0.524	0.018	8	5.002
NCH-45	Pl25C	59.930	24.950	0.604	0.038	7.010	7.220	0.649	100.401	2.669	1.310	0.023	0.0025	0.335	0.624	0.037	8	5.004
NCH-45	Pl25R	59.990	24.780	0.564	0.0275	6.760	7.330	0.636	100.087	2.678	1.304	0.021	0.0018	0.323	0.635	0.036	8	5.002
NCH-45	Pl26C	56.600	27.170	0.576	0.0639	9.740	5.880	0.331	100.361	2.540	1.438	0.022	0.0043	0.469	0.512	0.019	8	5.005
NCH-45	Pl26C1	57.530	26.370	0.518	0.0708	8.860	6.180	0.346	99.875	2.584	1.396	0.019	0.0047	0.427	0.538	0.020	8	4.993
NCH-45	Pl26R	57.710	26.470	0.594	0.0536	8.640	6.510	0.407	100.384	2.583	1.397	0.022	0.0036	0.414	0.565	0.023	8	5.011
NCH-31	Pl1C	58.080	25.870	0.412	0.0357	8.040	6.580	0.399	99.417	2.617	1.374	0.016	0.0024	0.388	0.575	0.023	8	4.996
NCH-31	Pl1C1	58.390	25.730	0.461	0.0424	8.140	6.640	0.419	99.823	2.621	1.362	0.017	0.0028	0.392	0.578	0.024	8	4.998
NCH-31	Pl1R	59.120	25.330	0.558	0.0535	7.850	6.470	0.632	100.013	2.645	1.336	0.021	0.0036	0.377	0.561	0.036	8	4.983
NCH-31	Pl2C	57.800	26.180	0.419	0.0281	8.560	6.440	0.362	99.790	2.598	1.387	0.016	0.0019	0.412	0.561	0.021	8	4.998
NCH-31	Pl2R	58.460	25.940	0.465	0.0411	8.110	6.900	0.409	100.325	2.613	1.367	0.017	0.0027	0.389	0.598	0.023	8	5.013

Sample	Crystal	SiO2	Al2O3	FeO	MgO	CaO	Na2O	K2O	Total	Si	Al	Fe	Mg	Ca	Na	K	O	CatTot
NCH-31	Pl2R1	58.810	26.140	0.470	0.0386	8.300	6.660	0.425	100.844	2.613	1.369	0.018	0.0026	0.395	0.573	0.024	8	4.998
NCH-31	Pl3C	57.360	26.860	0.499	0.03	9.130	6.180	0.378	100.437	2.567	1.417	0.019	0.002	0.438	0.536	0.022	8	5.002
NCH-31	Pl3R	57.520	26.720	0.513	0.054	8.870	6.290	0.347	100.314	2.574	1.409	0.019	0.0036	0.425	0.546	0.020	8	5.000
NCH-31	Pl4C	57.850	26.370	0.394	0.0333	8.450	6.640	0.392	100.130	2.592	1.393	0.015	0.0022	0.406	0.577	0.022	8	5.010
NCH-31	Pl4C1	57.560	26.380	0.496	0.0275	8.580	6.540	0.360	99.943	2.586	1.397	0.019	0.0018	0.413	0.570	0.021	8	5.009
NCH-31	Pl4R	58.110	26.490	0.444	0.0422	8.620	6.660	0.392	100.759	2.590	1.392	0.017	0.0028	0.412	0.575	0.022	8	5.013
NCH-31	Pl5C	55.360	27.590	0.512	0.0522	10.580	5.580	0.240	99.915	2.502	1.470	0.019	0.0035	0.512	0.489	0.014	8	5.013
NCH-31	Pl5R	58.790	26.000	0.538	0.045	8.310	6.790	0.482	100.956	2.613	1.362	0.020	0.003	0.396	0.585	0.027	8	5.009
NCH-31	Pl5R1	58.540	25.810	0.537	0.0426	8.160	6.860	0.484	100.434	2.616	1.360	0.020	0.0028	0.391	0.595	0.028	8	5.015
NCH-31	Pl6C	58.470	25.990	0.433	0.0348	8.160	6.700	0.308	100.096	2.616	1.371	0.016	0.0023	0.391	0.581	0.018	8	4.996
NCH-31	Pl6R	58.540	26.090	0.405	0.0346	8.200	6.700	0.426	100.396	2.614	1.373	0.015	0.0023	0.393	0.580	0.024	8	5.002
NCH-31	Pl6R1	58.580	26.280	0.432	0.0342	8.060	6.730	0.433	100.550	2.610	1.380	0.016	0.0023	0.385	0.581	0.025	8	5.001
NCH-31	Pl7C	58.370	26.260	0.477	0.0374	8.400	6.590	0.386	100.520	2.603	1.381	0.018	0.0025	0.401	0.570	0.022	8	5.000
NCH-31	Pl7R	58.160	26.100	0.473	0.0244	8.160	6.500	0.364	99.782	2.610	1.381	0.018	0.0016	0.393	0.566	0.021	8	4.992
NCH-31	Pl7R1	58.810	26.000	0.394	0.0303	8.000	6.760	0.416	100.410	2.622	1.367	0.015	0.002	0.382	0.584	0.024	8	4.997
NCH-31	Pl8C	57.810	26.500	0.448	0.0202	8.640	6.360	0.357	100.135	2.589	1.399	0.017	0.0013	0.415	0.552	0.020	8	4.997
NCH-31	Pl8R	58.040	26.560	0.456	0.0463	8.530	6.530	0.374	100.535	2.590	1.397	0.017	0.0031	0.408	0.565	0.021	8	5.003
NCH-37	Pl1C	58.110	26.550	0.427	0.0479	8.670	6.530	0.385	100.720	2.590	1.394	0.016	0.0032	0.414	0.564	0.022	8	5.004
NCH-37	Pl1R	58.100	26.170	0.464	0.0429	8.470	6.660	0.386	100.292	2.599	1.380	0.017	0.0029	0.406	0.578	0.022	8	5.008
NCH-37	Pl1R1	58.260	26.170	0.457	0.0347	8.530	6.680	0.424	100.557	2.601	1.377	0.017	0.0023	0.408	0.578	0.024	8	5.010
NCH-37	Pl1R2	58.670	26.250	0.444	0.0289	8.130	6.760	0.365	100.648	2.611	1.377	0.017	0.0019	0.388	0.584	0.021	8	5.002
NCH-37	Pl2C	55.020	28.420	0.413	0.0387	10.450	5.340	0.248	99.929	2.482	1.512	0.016	0.0026	0.505	0.467	0.014	8	5.001
NCH-37	Pl2R	58.280	26.480	0.420	0.0367	8.390	6.870	0.358	100.834	2.593	1.389	0.016	0.0024	0.400	0.593	0.020	8	5.018
NCH-37	Pl2R1	58.630	26.070	0.446	0.0546	8.200	6.630	0.428	100.459	2.614	1.370	0.017	0.0036	0.392	0.573	0.024	8	4.996
NCH-37	Pl3C	57.750	26.240	0.425	0.03	8.430	6.570	0.400	99.845	2.594	1.390	0.016	0.002	0.406	0.572	0.023	8	5.006
NCH-37	Pl3R	58.170	26.150	0.445	0.0398	8.130	6.960	0.390	100.285	2.603	1.380	0.017	0.0027	0.390	0.604	0.022	8	5.019
NCH-37	Pl3R1	58.000	25.920	0.435	0.0243	8.260	6.840	0.413	99.892	2.605	1.372	0.016	0.0016	0.398	0.596	0.024	8	5.016

Sample	Crystal	SiO2	Al2O3	FeO	MgO	CaO	Na2O	K2O	Total	Si	Al	Fe	Mg	Ca	Na	K	O	CatTot
NCH-37	Pl4R	58.050	26.480	0.430	0.0355	8.350	6.680	0.343	100.368	2.594	1.394	0.016	0.0024	0.400	0.579	0.020	8	5.007
NCH-37	Pl4C1	57.790	26.500	0.420	0.033	8.850	6.370	0.361	100.324	2.586	1.398	0.016	0.0022	0.424	0.552	0.021	8	5.000
NCH-37	Pl4R	58.500	26.100	0.421	0.022	8.500	6.700	0.359	100.603	2.608	1.372	0.016	0.0015	0.406	0.579	0.020	8	5.005
NCH-37	Pl4R1	58.910	25.980	0.426	0.0261	7.920	6.880	0.410	100.552	2.624	1.364	0.016	0.0017	0.378	0.594	0.023	8	5.003
NCH-37	Pl5C	58.620	25.970	0.424	0.0232	8.230	6.810	0.405	100.482	2.616	1.366	0.016	0.0015	0.394	0.589	0.023	8	5.006
NCH-37	Pl5R	58.640	25.660	0.486	0.018	7.900	6.920	0.433	100.057	2.626	1.355	0.018	0.0012	0.379	0.601	0.025	8	5.007
NCH-37	Pl5R1	59.240	25.630	0.479	0.03	7.690	6.860	0.444	100.373	2.639	1.346	0.018	0.002	0.367	0.593	0.025	8	4.995
NCH-37	Pl6C	57.840	26.650	0.433	0.0459	8.780	6.270	0.380	100.399	2.585	1.404	0.016	0.0031	0.420	0.544	0.022	8	4.995
NCH-37	Pl6R	58.970	25.910	0.469	0.0222	7.890	6.850	0.434	100.545	2.626	1.360	0.018	0.0015	0.377	0.592	0.025	8	5.001
NCH-37	Pl6R1	58.690	25.950	0.409	0.0122	7.930	6.730	0.388	100.109	2.623	1.367	0.015	0.0008	0.380	0.583	0.022	8	4.994
NCH-37	Pl6R2	58.940	25.860	0.425	0.0401	7.830	6.690	0.402	100.187	2.632	1.361	0.016	0.0027	0.375	0.579	0.023	8	4.989
Arrau	Pl7	56.02	27.11	0.4854	0.0498	9.77	5.99	0.3135	99.8164	2.532	1.444	0.0183	0.0034	0.473	0.525	0.0181	8	5.0164
Arrau	Pl7	55.93	27.07	0.482	0.0454	9.68	5.85	0.2963	99.491	2.534	1.445	0.0183	0.0031	0.47	0.514	0.0171	8	5.0064
Arrau	Pl7	56.04	27.18	0.4662	0.049	9.57	6	0.317	99.6703	2.534	1.448	0.0176	0.0033	0.464	0.526	0.0183	8	5.0128
Arrau	Pl7	58.09	26.11	0.4435	0.0286	8.07	6.57	0.3677	99.7421	2.609	1.383	0.0167	0.0019	0.388	0.572	0.0211	8	4.9939
Arrau	Pl7	58.35	25.66	0.4396	0.0405	7.81	6.73	0.3778	99.4689	2.626	1.362	0.0166	0.0027	0.377	0.587	0.0217	8	4.9951
Arrau	Pl7	58.35	25.87	0.4152	0.0363	7.94	6.78	0.4075	99.8036	2.62	1.369	0.0156	0.0024	0.382	0.59	0.0233	8	5.0024
Arrau	Pl7	58.65	25.86	0.4149	0.0318	8.01	6.74	0.403	100.1505	2.624	1.363	0.0155	0.0021	0.384	0.584	0.023	8	4.9971
Arrau	Pl7	56.57	27.04	0.4789	0.0383	9.61	5.88	0.3084	99.9686	2.547	1.435	0.018	0.0026	0.464	0.513	0.0177	8	4.9988
Arrau	Pl7	57.06	26.74	0.4906	0.048	9.16	6.17	0.328	100.0448	2.565	1.417	0.0184	0.0032	0.441	0.538	0.0188	8	5.0030
Arrau	Pl7	58.03	25.8	0.4716	0.0372	8.28	6.71	0.3418	99.7442	2.611	1.368	0.0177	0.0025	0.399	0.585	0.0196	8	5.0053
Arrau	Pl8	55.95	27.86	0.4755	0.0488	10.1	5.58	0.2818	100.3861	2.512	1.474	0.0179	0.0033	0.486	0.486	0.0161	8	4.9983
Arrau	Pl8	57.45	26.55	0.4644	0.046	8.57	6.37	0.3588	99.8389	2.583	1.407	0.0175	0.0031	0.413	0.556	0.0206	8	5.0013
Arrau	Pl8	58.21	25.98	0.482	0.0516	8.24	6.78	0.3889	100.2133	2.607	1.372	0.0181	0.0034	0.396	0.589	0.0222	8	5.0106
Arrau	Pl8	58.17	26.04	0.4683	0.0427	8.06	6.74	0.3749	99.9431	2.61	1.377	0.0176	0.0029	0.387	0.587	0.0215	8	5.0047
Arrau	Pl8	57.22	26.88	0.494	0.0335	9.06	6.19	0.3611	100.3278	2.565	1.42	0.0185	0.0022	0.435	0.538	0.0206	8	5.0025
Arrau	Pl8	55.78	27.67	0.4731	0.0437	10.05	5.84	0.3028	100.2046	2.512	1.469	0.0178	0.0029	0.485	0.51	0.0174	8	5.0156

Sample	Crystal	SiO2	Al2O3	FeO	MgO	CaO	Na2O	K2O	Total	Si	Al	Fe	Mg	Ca	Na	K	O	CatTot
Arrau	Pl8	55.97	27.69	0.4793	0.0405	9.99	5.77	0.3155	100.369	2.515	1.467	0.018	0.0027	0.481	0.503	0.0181	8	5.0087
Arrau	Pl8	55.66	27.5	0.4964	0.0443	10.31	5.44	0.227	99.7485	2.516	1.465	0.0188	0.003	0.5	0.477	0.0131	8	4.9953
Arrau	Pl8	55.91	27.33	0.4753	0.0408	10.04	5.69	0.2926	99.817	2.525	1.455	0.018	0.0027	0.486	0.499	0.0169	8	5.0039
Arrau	Pl8	56.61	27.12	0.4789	0.0387	9.62	5.75	0.2918	99.9589	2.548	1.439	0.018	0.0026	0.464	0.502	0.0168	8	4.9922
Arrau	Pl8	57.27	26.53	0.4707	0.0391	8.89	6.43	0.3276	100.004	2.575	1.406	0.0177	0.0026	0.428	0.561	0.0188	8	5.0108
Arrau	Pl8	57.77	26.05	0.4952	0.0448	8.46	6.3	0.3764	99.541	2.603	1.384	0.0187	0.003	0.408	0.55	0.0216	8	4.9899
Arrau	Pl8	56.88	26.61	0.5122	0.0349	9.32	6.19	0.304	99.9139	2.563	1.413	0.0193	0.0023	0.45	0.541	0.0175	8	5.0083
Arrau	Pl9	49.38	31.86	0.5268	0.0396	15.09	2.84	0.0933	99.8831	2.262	1.72	0.0202	0.0027	0.741	0.252	0.0055	8	5.0053
Arrau	Pl9	50.43	31.02	0.5641	0.0482	14.36	3.35	0.1041	99.9312	2.305	1.671	0.0216	0.0033	0.703	0.297	0.0061	8	5.0090
Arrau	Pl9	52.44	29.61	0.5567	0.0365	12.77	4.33	0.1676	99.9747	2.386	1.588	0.0212	0.0025	0.623	0.382	0.0097	8	5.0148
Arrau	Pl9	53.61	29.1	0.5561	0.0492	11.8	4.78	0.1682	100.07	2.429	1.554	0.0211	0.0033	0.573	0.42	0.0097	8	5.0103
Arrau	Pl9	55.64	27.64	0.5552	0.0492	10.23	5.62	0.2549	100.0319	2.51	1.47	0.021	0.0033	0.495	0.492	0.0147	8	5.0074
Arrau	Pl9	56.18	27.46	0.5303	0.0386	9.61	5.99	0.2692	100.1464	2.528	1.457	0.02	0.0026	0.463	0.523	0.0155	8	5.0116
Arrau	Pl9	56.81	26.83	0.4984	0.0411	9.32	6.24	0.2954	100.1219	2.555	1.422	0.0187	0.0028	0.449	0.544	0.017	8	5.0116
Arrau	Pl9	58.13	26.19	0.5071	0.0426	8.32	6.7	0.3533	100.3014	2.601	1.381	0.019	0.0028	0.399	0.581	0.0202	8	5.0060
Arrau	Pl9	58.44	25.96	0.4563	0.0412	8.24	6.68	0.3574	100.1983	2.615	1.369	0.0171	0.0027	0.395	0.58	0.0204	8	5.0000
Arrau	Pl9	59.43	25.11	0.5409	0.0372	7.28	7.13	0.5277	100.0815	2.658	1.324	0.0202	0.0025	0.349	0.618	0.0301	8	5.0027
Arrau	Pl9	57.79	26.22	0.4635	0.0385	8.53	6.48	0.3692	99.9397	2.596	1.388	0.0174	0.0026	0.411	0.565	0.0212	8	5.0028
Nicanor	Pl4	58.52	26.38	0.4903	0.0376	8.25	6.66	0.3659	100.7102	2.605	1.384	0.0183	0.0025	0.393	0.575	0.0208	8	4.9988
Nicanor	Pl4	58.34	26.06	0.4453	0.0335	7.96	6.61	0.408	99.9579	2.615	1.377	0.0167	0.0022	0.382	0.574	0.0233	8	4.9939
Nicanor	Pl4	57.9	26.47	0.4898	0.0318	8.34	6.74	0.3827	100.3957	2.59	1.396	0.0183	0.0021	0.4	0.584	0.0218	8	5.0136
Nicanor	Pl4	57.98	26.43	0.5477	0.0411	8.53	6.47	0.3348	100.4258	2.592	1.393	0.0205	0.0027	0.409	0.561	0.0191	8	5.0005
Nicanor	Pl4	57.84	26.3	0.5724	0.0493	8.46	6.75	0.4127	100.4593	2.589	1.388	0.0214	0.0033	0.406	0.586	0.0236	8	5.0198
Nicanor	Pl4	58.63	26.18	0.4918	0.0471	8.03	6.57	0.3696	100.3678	2.616	1.377	0.0184	0.0031	0.384	0.569	0.021	8	4.9902
Nicanor	Pl4	57.26	26.86	0.5099	0.0506	8.94	6.4	0.332	100.4462	2.564	1.418	0.0191	0.0034	0.429	0.556	0.019	8	5.0117
Nicanor	Pl4	58.11	26.34	0.4623	0.0428	8.3	6.48	0.4152	100.2	2.601	1.389	0.0173	0.0029	0.398	0.563	0.0237	8	4.9966
Nicanor	Pl4	58.37	25.69	0.4173	0.0454	8.01	6.64	0.3798	99.6259	2.624	1.361	0.0157	0.003	0.386	0.579	0.0218	8	4.993

Sample	Crystal	SiO2	Al2O3	FeO	MgO	CaO	Na2O	K2O	Total	Si	Al	Fe	Mg	Ca	Na	K	O	CatTot
Nicanor	Pl4	58.33	26.24	0.4345	0.0338	8.15	6.8	0.3513	100.3973	2.605	1.382	0.0162	0.0022	0.39	0.589	0.02	8	5.0063
Nicanor	Pl4	58.39	26.04	0.4513	0.051	8.3	6.63	0.4032	100.3058	2.611	1.373	0.0169	0.0034	0.398	0.575	0.023	8	5.0018
Nicanor	Pl4	57.84	26.85	0.5002	0.0526	8.71	6.58	0.3643	100.9244	2.576	1.409	0.0186	0.0035	0.416	0.569	0.0207	8	5.0137
Nicanor	Pl4	56.98	27.09	0.5203	0.0487	9.25	6.11	0.3075	100.3562	2.554	1.431	0.0195	0.0033	0.444	0.531	0.0176	8	5.0021
Nicanor	Pl4	58.11	26.17	0.5083	0.0392	8.38	6.44	0.3759	100.1107	2.604	1.382	0.019	0.0026	0.402	0.559	0.0215	8	4.9931
Nicanor	Pl4	57.81	26.47	0.4523	0.0448	8.43	6.6	0.3793	100.2922	2.588	1.397	0.0169	0.003	0.404	0.573	0.0217	8	5.0072
Nicanor	Pl4	58.34	26.05	0.5044	0.0371	7.95	6.85	0.3576	100.1663	2.612	1.375	0.0189	0.0025	0.381	0.595	0.0204	8	5.0075
Nicanor	Pl7	57.88	26.57	0.4671	0.0428	8.79	6.31	0.327	100.4411	2.586	1.4	0.0175	0.0029	0.421	0.547	0.0186	8	4.9949
Nicanor	Pl7	58.35	26.22	0.4711	0.0261	8.07	6.78	0.3855	100.3878	2.607	1.381	0.0176	0.0017	0.386	0.588	0.022	8	5.0061
Nicanor	Pl7	56.11	27.66	0.4539	0.0412	9.86	5.91	0.2718	100.353	2.521	1.464	0.0171	0.0028	0.474	0.515	0.0156	8	5.0111
Nicanor	Pl7	58.74	25.73	0.4662	0.0507	7.72	6.88	0.3899	100.027	2.63	1.358	0.0175	0.0034	0.37	0.598	0.0223	8	5.001
Nicanor	Pl7	57.41	26.85	0.4706	0.0559	8.77	6.4	0.3301	100.3471	2.571	1.417	0.0176	0.0037	0.421	0.556	0.0189	8	5.0073
Nicanor	Pl7	57.64	26.92	0.4555	0.0421	8.73	6.24	0.3481	100.3966	2.577	1.418	0.017	0.0028	0.418	0.541	0.0199	8	4.9945
Nicanor	Pl7	55.82	27.7	0.4787	0.0388	9.97	5.65	0.3022	99.963	2.517	1.472	0.0181	0.0026	0.482	0.494	0.0174	8	5.0032
Nicanor	Pl7	55.93	27.5	0.516	0.0472	9.79	5.87	0.2871	100.0089	2.522	1.461	0.0195	0.0032	0.473	0.513	0.0165	8	5.0106
Nicanor	Pl7	55.84	27.53	0.4826	0.0452	9.8	5.83	0.3028	99.9101	2.52	1.464	0.0182	0.003	0.474	0.51	0.0174	8	5.0094
Nicanor	Pl7	58.36	26.12	0.4542	0.0497	8.29	6.77	0.3567	100.4496	2.607	1.375	0.017	0.0033	0.397	0.586	0.0203	8	5.0072
Nicanor	Pl8	58.46	25.9	0.4065	0.0418	8.05	6.47	0.3882	99.7406	2.623	1.37	0.0153	0.0028	0.387	0.563	0.0222	8	4.9841
Nicanor	Pl8	58.44	26	0.4357	0.0433	8.04	6.67	0.3716	100.0903	2.616	1.372	0.0163	0.0029	0.386	0.579	0.0212	8	4.9965
Nicanor	Pl8	58.91	25.48	0.4018	0.0452	7.49	6.76	0.4549	99.5751	2.645	1.349	0.0151	0.003	0.36	0.589	0.0261	8	4.9883
Nicanor	Pl8	59.41	25.24	0.4041	0.046	7.42	7.13	0.4125	100.1359	2.654	1.329	0.0151	0.0031	0.355	0.617	0.0235	8	4.9992
Nicanor	Pl8	59.01	25.55	0.4201	0.0281	7.56	6.64	0.3886	99.6226	2.646	1.35	0.0158	0.0019	0.363	0.578	0.0222	8	4.9778
Nicanor	Pl8	56.61	27.26	0.4826	0.0549	9.48	6.04	0.3011	100.2756	2.542	1.443	0.0181	0.0037	0.456	0.526	0.0172	8	5.0077
Nicanor	Pl8	58.98	25.61	0.4341	0.0424	7.73	7.12	0.3771	100.3209	2.634	1.348	0.0162	0.0028	0.37	0.616	0.0215	8	5.0095
Nicanor	Pl8	57.68	26.61	0.4232	0.0444	8.62	6.35	0.3468	100.1171	2.585	1.406	0.0159	0.003	0.414	0.552	0.0198	8	4.9971
Nicanor	Pl8	57.02	27.04	0.4409	0.0288	8.96	6.04	0.3161	99.936	2.562	1.432	0.0166	0.0019	0.432	0.526	0.0181	8	4.9917
Nicanor	Pl8	58.13	26.07	0.4643	0.0481	8.22	6.51	0.3558	99.8484	2.609	1.379	0.0174	0.0032	0.395	0.566	0.0204	8	4.9917

Sample	Crystal	SiO2	Al2O3	FeO	MgO	CaO	Na2O	K2O	Total	Si	Al	Fe	Mg	Ca	Na	K	O	CatTot
Nicanor	Pl8	57.52	26.37	0.4123	0.0414	8.66	6.43	0.3274	99.8088	2.587	1.398	0.0155	0.0028	0.417	0.561	0.0188	8	5.0018
Nicanor	Pl8	59.2	25.33	0.4198	0.052	7.52	7.05	0.4151	100.0293	2.648	1.335	0.0157	0.0035	0.36	0.611	0.0237	8	4.9984
Nicanor	Pl8	59.18	25.45	0.4721	0.0392	7.58	6.98	0.4493	100.2208	2.644	1.34	0.0176	0.0026	0.363	0.605	0.0256	8	5.0002
Nicanor	Pl8	57.27	26.77	0.4545	0.0382	8.63	6.21	0.3539	99.8178	2.575	1.419	0.0171	0.0026	0.416	0.541	0.0203	8	4.9942
Nicanor	Pl8	57.45	26.25	0.4679	0.0563	8.5	6.34	0.3814	99.5048	2.591	1.395	0.0177	0.0038	0.411	0.554	0.0219	8	4.9964
Nicanor	Pl8	56.29	27.23	0.5064	0.0272	9.55	6.11	0.2703	100.0353	2.536	1.446	0.0191	0.0018	0.461	0.534	0.0155	8	5.0151
Nicanor	Pl8	56.55	27.22	0.4699	0.0384	9.64	6.03	0.2869	100.3202	2.54	1.441	0.0176	0.0026	0.464	0.525	0.0164	8	5.0096
Nicanor	Pl9	57.47	26.48	0.4391	0.0417	8.64	6.22	0.3735	99.7324	2.586	1.404	0.0165	0.0028	0.416	0.543	0.0214	8	4.9921
Nicanor	Pl9	57.12	26.96	0.4465	0.0385	9.06	6.43	0.3254	100.4123	2.559	1.424	0.0167	0.0026	0.435	0.559	0.0186	8	5.016
Nicanor	Pl9	57.51	26.44	0.4343	0.0434	8.74	6.4	0.3591	99.9899	2.584	1.4	0.0163	0.0029	0.421	0.558	0.0206	8	5.005
Nicanor	Pl9	57.19	26.88	0.4579	0.0463	8.95	6.2	0.3106	100.0901	2.567	1.422	0.0172	0.0031	0.431	0.539	0.0178	8	4.999
Nicanor	Pl9	57.72	26.44	0.4535	0.0436	8.56	6.39	0.3713	100.0702	2.589	1.398	0.017	0.0029	0.412	0.556	0.0212	8	4.9992
Nicanor	Pl9	54.99	28.43	0.5005	0.0462	10.47	5.22	0.2347	99.9934	2.481	1.512	0.0189	0.0031	0.506	0.457	0.0135	8	4.9951
Nicanor	Pl9	54.8	28.22	0.5276	0.046	10.57	5.29	0.2314	99.685	2.482	1.507	0.02	0.0031	0.513	0.464	0.0134	8	5.0025
Nicanor	Pl9	55.9	27.6	0.4997	0.0567	9.83	5.7	0.2671	99.9049	2.521	1.467	0.0188	0.0038	0.475	0.498	0.0154	8	5.0007
Nicanor	Pl9	55.72	27.7	0.4541	0.044	9.94	5.7	0.2695	99.9022	2.514	1.473	0.0171	0.003	0.481	0.498	0.0155	8	5.0042
Nicanor	Pl9	55.78	27.51	0.4784	0.0333	9.88	5.7	0.2567	99.6995	2.521	1.466	0.0181	0.0022	0.479	0.5	0.0148	8	5.0032
Nicanor	Pl9	56.36	27.23	0.4667	0.044	9.53	6.07	0.2858	100.0597	2.537	1.445	0.0176	0.003	0.46	0.53	0.0164	8	5.0116
Nicanor	Pl9	57.64	26.36	0.4376	0.0359	8.71	6.3	0.3416	99.8516	2.591	1.396	0.0165	0.0024	0.42	0.549	0.0196	8	4.9954
Nicanor	Pl9	57.91	26.21	0.4688	0.0461	8.33	6.6	0.377	100.0692	2.597	1.386	0.0176	0.0031	0.4	0.574	0.0216	8	5.0037
Nicanor	Pl9	58.06	26.12	0.4523	0.0383	8.45	6.62	0.3806	100.1223	2.603	1.38	0.017	0.0026	0.406	0.575	0.0218	8	5.0054
Nicanor	Pl9	57.82	26.32	0.4826	0.0415	8.43	6.39	0.3777	99.9294	2.596	1.393	0.0181	0.0028	0.405	0.556	0.0216	8	4.9948
Nicanor	Pl9	58.1	26.37	0.4831	0.0473	8.43	6.59	0.3696	100.4817	2.595	1.388	0.018	0.0031	0.404	0.571	0.0211	8	5.0033
Nicanor	pl10	54.97	28.11	0.5166	0.0457	10.58	5.44	0.2347	99.9608	2.485	1.498	0.0195	0.0031	0.512	0.477	0.0135	8	5.0103
Nicanor	pl10	55.1	28.16	0.5321	0.0466	10.58	5.44	0.2684	100.246	2.484	1.497	0.0201	0.0031	0.511	0.475	0.0154	8	5.0097
Nicanor	pl10	55.63	28.11	0.5256	0.0435	10.43	5.42	0.2556	100.4807	2.498	1.488	0.0197	0.0029	0.502	0.472	0.0146	8	4.9994
Nicanor	pl10	54.95	28.29	0.5174	0.0526	10.64	5.45	0.2695	100.2529	2.478	1.504	0.0195	0.0035	0.514	0.476	0.0155	8	5.0133

Sample	Crystal	SiO2	Al2O3	FeO	MgO	CaO	Na2O	K2O	Total	Si	Al	Fe	Mg	Ca	Na	K	O	CatTot
Nicanor	pl10	55.56	27.8	0.5024	0.0486	10.16	5.55	0.2821	99.9552	2.507	1.479	0.019	0.0033	0.491	0.485	0.0162	8	5.0023
Nicanor	pl10	55.3	27.99	0.5348	0.0513	10.37	5.42	0.2512	99.9937	2.496	1.489	0.0202	0.0035	0.501	0.474	0.0145	8	5.0009
Nicanor	pl10	56.25	27.21	0.5097	0.0399	9.55	5.98	0.3114	99.9149	2.536	1.446	0.0192	0.0027	0.461	0.523	0.0179	8	5.008
Nicanor	pl10	56.77	27.44	0.4837	0.0405	9.34	5.98	0.2928	100.4531	2.542	1.448	0.0181	0.0027	0.448	0.519	0.0167	8	4.9981
Nicanor	pl10	58.18	26.29	0.4961	0.0465	8.33	6.6	0.3718	100.3331	2.601	1.386	0.0186	0.0031	0.399	0.573	0.0212	8	5.0025
Nicanor	pl10	56.5	27.54	0.5196	0.0487	9.61	5.9	0.2683	100.4541	2.533	1.455	0.0195	0.0033	0.461	0.513	0.0153	8	5.0024
Nicanor	pl10	57.32	26.73	0.4895	0.0416	8.88	6.12	0.3323	99.9837	2.574	1.415	0.0184	0.0028	0.427	0.533	0.019	8	4.9916
Nicanor	Pl11	57.26	26.83	0.4668	0.0427	8.92	6.47	0.3554	100.3979	2.566	1.417	0.0175	0.0028	0.428	0.562	0.0203	8	5.0154
Nicanor	Pl11	50.51	31.36	0.5719	0.0505	14.09	3.61	0.1575	100.4592	2.298	1.681	0.0218	0.0034	0.687	0.318	0.0091	8	5.0221
Nicanor	Pl11	50.83	31.13	0.6009	0.0491	13.8	3.64	0.1091	100.2047	2.314	1.67	0.0229	0.0033	0.673	0.321	0.0063	8	5.0121
Nicanor	Pl11	50.56	31.18	0.5425	0.056	14.03	3.57	0.1013	100.1057	2.305	1.676	0.0207	0.0038	0.685	0.315	0.0059	8	5.0137
Nicanor	Pl11	50.34	31.15	0.6074	0.0555	14.07	3.38	0.156	99.8347	2.303	1.679	0.0232	0.0038	0.69	0.299	0.0091	8	5.0098
Nicanor	Pl11	51.09	31.06	0.5879	0.0526	13.8	3.68	0.1383	100.4905	2.319	1.662	0.0223	0.0036	0.671	0.324	0.008	8	5.0128
Nicanor	Pl11	51.47	30.92	0.5741	0.0499	13.65	3.95	0.1221	100.8093	2.329	1.649	0.0217	0.0034	0.662	0.347	0.0071	8	5.0217
Nicanor	Pl11	52.57	29.87	0.5786	0.0446	12.64	4.32	0.1728	100.2674	2.384	1.596	0.0219	0.003	0.614	0.38	0.01	8	5.0115
Nicanor	Pl11	58.42	25.96	0.456	0.0404	8.04	6.63	0.4002	99.9883	2.618	1.371	0.0171	0.0027	0.386	0.576	0.0229	8	4.9951
Nicanor	Pl11	58.14	26.32	0.4714	0.0386	8.45	6.56	0.3598	100.3768	2.599	1.387	0.0176	0.0026	0.405	0.569	0.0205	8	5.0019
Nicanor	Pl12	55.58	28.01	0.5165	0.0408	10.34	5.47	0.2672	100.2679	2.501	1.486	0.0194	0.0027	0.498	0.477	0.0153	8	5.0009
Nicanor	Pl12	55.17	27.87	0.4852	0.0401	10.26	5.53	0.2589	99.6689	2.498	1.487	0.0184	0.0027	0.498	0.485	0.015	8	5.006
Nicanor	Pl12	54.77	28.19	0.4954	0.0394	10.88	5.39	0.2399	100.0766	2.476	1.502	0.0187	0.0027	0.527	0.472	0.0138	8	5.0147
Nicanor	Pl12	53.82	29.34	0.4677	0.0366	11.97	4.83	0.1839	100.6611	2.424	1.558	0.0176	0.0025	0.578	0.422	0.0106	8	5.0132
Nicanor	Pl12	53.1	29.46	0.4486	0.0476	11.69	4.64	0.1779	99.6189	2.415	1.579	0.0171	0.0032	0.57	0.409	0.0103	8	5.0056
Nicanor	Pl12	52.97	29.74	0.5006	0.0345	12.35	4.59	0.1736	100.3925	2.396	1.586	0.0189	0.0023	0.599	0.403	0.01	8	5.0163
Nicanor	Pl12	53.49	29.09	0.5021	0.0405	11.86	4.92	0.2002	100.1643	2.423	1.553	0.019	0.0027	0.576	0.432	0.0116	8	5.0194
Nicanor	Pl12	54.09	29.02	0.5236	0.0423	11.38	5.07	0.2101	100.3874	2.44	1.543	0.0198	0.0028	0.55	0.444	0.0121	8	5.0134
Nicanor	Pl12	56.18	27.46	0.5367	0.0512	9.78	5.82	0.2955	100.19	2.527	1.456	0.0202	0.0034	0.471	0.508	0.017	8	5.0049
Nicanor	Pl12	57.56	26.57	0.5325	0.045	8.43	6.44	0.3607	100.0441	2.583	1.406	0.02	0.003	0.405	0.56	0.0207	8	5.0014

Sample	Crystal	SiO2	Al2O3	FeO	MgO	CaO	Na2O	K2O	Total	Si	Al	Fe	Mg	Ca	Na	K	O	CatTot
Nicanor	Pl13	58.85	25.42	0.4827	0.0523	7.67	7.04	0.3943	100.0021	2.637	1.342	0.0181	0.0035	0.368	0.612	0.0225	8	5.0063
Nicanor	Pl13	59.35	25.78	0.5167	0.0482	7.6	7.23	0.4127	101.0384	2.633	1.348	0.0192	0.0032	0.361	0.622	0.0234	8	5.0132
Nicanor	Pl13	56.03	27.62	0.4993	0.0591	9.92	5.71	0.2678	100.148	2.521	1.465	0.0188	0.004	0.478	0.498	0.0154	8	5.0017
Nicanor	Pl13	56	27.64	0.5294	0.0478	10.09	5.77	0.2509	100.4114	2.516	1.464	0.0199	0.0032	0.486	0.502	0.0144	8	5.0084
Nicanor	Pl13	55.9	27.74	0.5122	0.0526	10.05	5.64	0.25	100.1902	2.515	1.471	0.0193	0.0035	0.484	0.492	0.0143	8	5.0007
Nicanor	Pl13	55.26	28.1	0.5328	0.0473	10.7	5.53	0.2235	100.4081	2.488	1.491	0.0201	0.0032	0.516	0.483	0.0128	8	5.0146
Nicanor	Pl13	55.9	27.81	0.4915	0.0442	10.27	5.66	0.2704	100.5184	2.509	1.471	0.0185	0.003	0.494	0.493	0.0155	8	5.0064
Nicanor	Pl13	56.12	27.38	0.5044	0.0462	9.82	5.81	0.2742	100.0306	2.528	1.454	0.019	0.0031	0.474	0.508	0.0158	8	5.0045
Nicanor	Pl13	56.12	27.49	0.4853	0.0513	9.73	5.75	0.2774	99.9546	2.529	1.46	0.0183	0.0034	0.47	0.502	0.0159	8	5.0004
Nicanor	Pl13	57.12	26.65	0.4945	0.0337	9.06	6.35	0.3592	100.1332	2.567	1.412	0.0186	0.0023	0.436	0.553	0.0206	8	5.0117
Nicanor	Pl14	55.11	28.04	0.4737	0.0472	10.59	5.46	0.2453	100.1	2.487	1.492	0.0179	0.0032	0.512	0.478	0.0141	8	5.0089
Nicanor	Pl14	55.13	28.27	0.4966	0.0517	10.71	5.43	0.2486	100.3944	2.482	1.5	0.0187	0.0035	0.517	0.474	0.0143	8	5.0116
Nicanor	Pl14	57.26	26.87	0.4854	0.0481	9.07	6.48	0.3467	100.5924	2.563	1.417	0.0182	0.0032	0.435	0.562	0.0198	8	5.0193
Nicanor	Pl14	56.47	27.08	0.5068	0.0537	9.68	6.08	0.276	100.2107	2.54	1.436	0.0191	0.0036	0.467	0.53	0.0158	8	5.0137
Nicanor	Pl14	55.66	27.39	0.4735	0.053	9.94	5.83	0.2738	99.6879	2.519	1.461	0.0179	0.0036	0.482	0.512	0.0158	8	5.0137
Nicanor	Pl14	55.44	27.84	0.4898	0.0615	10.32	5.73	0.2508	100.2266	2.499	1.479	0.0185	0.0041	0.499	0.501	0.0144	8	5.0183
Nicanor	Pl14	55.34	28.01	0.5085	0.0451	10.45	5.57	0.2247	100.2226	2.493	1.488	0.0192	0.003	0.505	0.487	0.0129	8	5.0106
Nicanor	Pl14	55.57	28.05	0.489	0.0484	10.47	5.62	0.2368	100.5034	2.497	1.485	0.0184	0.0032	0.504	0.49	0.0136	8	5.0118
Nicanor	Pl14	55.99	27.53	0.4732	0.0434	9.92	5.84	0.2912	100.1861	2.521	1.461	0.0178	0.0029	0.478	0.51	0.0167	8	5.0109
Nicanor	Pl14	55.58	27.64	0.4739	0.0491	10.05	5.61	0.28	99.7579	2.512	1.472	0.0179	0.0033	0.487	0.492	0.0161	8	5.0029
Nicanor	Pl14	55.28	27.79	0.4689	0.0519	10.44	5.46	0.2649	99.7621	2.501	1.482	0.0177	0.0035	0.506	0.479	0.0153	8	5.0047
Nicanor	Pl14	54.47	28.58	0.479	0.0377	11.13	5.16	0.2173	100.1984	2.46	1.521	0.0181	0.0025	0.538	0.451	0.0125	8	5.0074
Nicanor	Pl14	54.48	28.41	0.4408	0.046	10.98	5.21	0.2176	99.8358	2.467	1.517	0.0167	0.0031	0.533	0.457	0.0126	8	5.0082
Nicanor	Pl14	55.93	27.64	0.5377	0.0527	10.12	5.7	0.2343	100.2773	2.516	1.465	0.0202	0.0035	0.488	0.497	0.0134	8	5.0052
Nicanor	Pl14	56.97	26.26	0.4975	0.0403	8.89	6.48	0.3132	99.511	2.576	1.4	0.0188	0.0027	0.43	0.568	0.0181	8	5.0156
Nicanor	Pl15	57.27	26.65	0.4306	0.0393	8.96	6.1	0.3339	99.8342	2.576	1.413	0.0162	0.0026	0.432	0.532	0.0192	8	4.9927
Nicanor	Pl15	57.29	26.68	0.443	0.0364	8.87	6.27	0.3293	99.9616	2.574	1.413	0.0166	0.0024	0.427	0.546	0.0189	8	4.9994

Sample	Crystal	SiO2	Al2O3	FeO	MgO	CaO	Na2O	K2O	Total	Si	Al	Fe	Mg	Ca	Na	K	O	CatTot
Nicanor	PI15	57.51	26.18	0.4394	0.0386	8.68	6.44	0.3571	99.7157	2.59	1.39	0.0165	0.0026	0.419	0.562	0.0205	8	5.003
Nicanor	PI15	58.22	25.99	0.4298	0.0336	8.19	6.65	0.3875	99.925	2.612	1.374	0.0161	0.0022	0.394	0.578	0.0222	8	4.9993
Nicanor	PI15	58.59	25.92	0.4343	0.0407	7.93	6.75	0.4163	100.1011	2.622	1.367	0.0163	0.0027	0.38	0.586	0.0238	8	4.9985
Nicanor	PI15	57.86	26.1	0.3944	0.0416	8.36	6.36	0.3455	99.5625	2.604	1.385	0.0148	0.0028	0.403	0.555	0.0198	8	4.9878
Nicanor	PI15	58.34	25.99	0.4004	0.0414	8.28	6.5	0.3963	99.9853	2.615	1.373	0.015	0.0028	0.398	0.565	0.0227	8	4.9927
Nicanor	PI15	58.46	25.59	0.3957	0.0328	7.64	6.69	0.4642	99.2995	2.634	1.359	0.0149	0.0022	0.369	0.584	0.0267	8	4.9907
Nicanor	PI15	57.85	26.35	0.4195	0.0376	8.63	6.41	0.3368	100.0916	2.593	1.392	0.0157	0.0025	0.415	0.557	0.0193	8	4.9964
Nicanor	PI15	57.34	26.49	0.4417	0.0415	8.97	6.04	0.3248	99.7418	2.581	1.405	0.0166	0.0028	0.433	0.527	0.0187	8	4.9874
Nicanor	PI15	58.24	25.95	0.4511	0.0409	8.03	6.45	0.3717	99.5796	2.618	1.375	0.017	0.0027	0.387	0.562	0.0213	8	4.9846
Nicanor	PI15	57.71	25.91	0.4638	0.0454	8.39	6.61	0.3876	99.5624	2.603	1.377	0.0175	0.003	0.405	0.578	0.0223	8	5.0074

Análisis de clinopiroxenos en Universidad de Rice

Sample	Crystal	SiO2	Al2O3	FeOt	MnO	MgO	CaO	Na2O	Total	Si	Al	Fe	Mn	Mg	Ca	Na	O	CatTot
NCH-44	CPX15C	52.387	1.934	10.106	0.331	14.973	19.719	0.324	99.774	1.956	0.085	0.316	0.010	0.833	0.789	0.023	6	4.013
NCH-44	CPX15R	52.252	1.825	10.247	0.312	15.167	19.873	0.319	99.995	1.950	0.080	0.320	0.010	0.844	0.795	0.023	6	4.022
NCH-63	CPX8C	53.179	1.747	8.578	0.277	15.999	20.359	0.280	100.419	1.960	0.076	0.264	0.009	0.879	0.804	0.020	6	4.012
NCH-63	CPX8R	52.266	2.580	8.578	0.210	15.015	20.714	0.311	99.674	1.944	0.113	0.267	0.007	0.832	0.825	0.022	6	4.011
NCH-63	CPX8R1	52.209	2.447	9.057	0.208	15.155	20.057	0.297	99.430	1.947	0.108	0.283	0.007	0.843	0.802	0.021	6	4.010
NCH-63	CPX9C	52.601	2.051	8.656	0.236	15.331	20.654	0.316	99.845	1.953	0.090	0.269	0.007	0.849	0.822	0.023	6	4.013
NCH-63	CPX9R	51.801	2.914	8.493	0.210	14.935	21.205	0.324	99.882	1.926	0.128	0.264	0.007	0.828	0.845	0.023	6	4.022
NCH-63	CPX9R1	52.122	1.881	11.959	0.280	14.121	18.965	0.341	99.669	1.961	0.083	0.376	0.009	0.792	0.764	0.025	6	4.010
NCH-63	CPX10C	52.666	2.039	8.325	0.235	15.472	20.802	0.311	99.850	1.953	0.089	0.258	0.007	0.855	0.827	0.022	6	4.013
NCH-63	CPX10C1	52.677	2.055	8.252	0.215	15.792	20.569	0.311	99.871	1.952	0.090	0.256	0.007	0.872	0.817	0.022	6	4.015
NCH-63	CPX10R	51.657	3.090	9.626	0.278	15.348	19.472	0.246	99.717	1.923	0.136	0.300	0.009	0.852	0.777	0.018	6	4.017
NCH-63	CPX10R1	51.855	2.701	8.777	0.232	15.203	20.431	0.361	99.560	1.933	0.119	0.274	0.007	0.845	0.816	0.026	6	4.020
NCH-63	CPX11C	50.931	3.632	8.944	0.202	14.407	20.571	0.348	99.035	1.912	0.161	0.281	0.006	0.806	0.827	0.025	6	4.020
NCH-63	CPX11C1	50.577	3.620	8.708	0.180	14.418	20.751	0.351	98.605	1.908	0.161	0.275	0.006	0.811	0.839	0.026	6	4.025

Sample	Crystal	SiO2	Al2O3	FeOt	MnO	MgO	CaO	Na2O	Total	Si	Al	Fe	Mn	Mg	Ca	Na	O	CatTot
NCH-63	CPX11R	50.992	3.424	8.925	0.206	14.703	20.527	0.308	99.085	1.914	0.151	0.280	0.007	0.823	0.825	0.022	6	4.022
NCH-63	CPX11R1	50.984	3.657	8.971	0.216	14.519	21.019	0.346	99.712	1.904	0.161	0.280	0.007	0.808	0.841	0.025	6	4.028
NCH-63	CPX12C	52.671	2.194	8.519	0.229	15.548	20.641	0.303	100.105	1.949	0.096	0.264	0.007	0.858	0.818	0.022	6	4.014
NCH-63	CPX12R	52.407	2.344	8.485	0.233	15.168	20.682	0.354	99.673	1.948	0.103	0.264	0.007	0.841	0.824	0.026	6	4.013
NCH-63	CPX12R1	52.618	2.124	8.703	0.254	15.357	20.576	0.328	99.960	1.951	0.093	0.270	0.008	0.849	0.818	0.024	6	4.014
NCH-27	CPX12C	52.525	1.491	10.945	0.326	14.508	19.591	0.323	99.709	1.969	0.066	0.343	0.010	0.811	0.787	0.024	6	4.010
NCH-27	CPX12C1	52.209	1.357	11.060	0.303	14.485	19.550	0.384	99.348	1.967	0.060	0.349	0.010	0.814	0.789	0.028	6	4.017
NCH-27	CPX12R	51.994	1.619	11.725	0.325	14.938	18.042	0.339	98.982	1.963	0.072	0.370	0.010	0.841	0.730	0.025	6	4.013
NCH-27	CPX12R1	51.920	2.269	10.843	0.309	15.076	18.747	0.310	99.474	1.945	0.100	0.340	0.010	0.842	0.753	0.023	6	4.015
NCH-27	CPX13C	52.183	2.081	8.961	0.232	15.554	20.317	0.316	99.644	1.944	0.091	0.279	0.007	0.864	0.811	0.023	6	4.021
NCH-27	CPX131	52.374	2.272	8.658	0.179	15.681	20.627	0.301	100.092	1.940	0.099	0.268	0.006	0.866	0.819	0.022	6	4.021
NCH-27	CPX13R	52.444	1.392	12.022	0.319	15.588	17.346	0.319	99.430	1.969	0.062	0.377	0.010	0.872	0.698	0.023	6	4.012
NCH-27	CPX13R1	52.153	1.628	11.644	0.288	15.099	18.142	0.347	99.301	1.962	0.072	0.366	0.009	0.847	0.731	0.025	6	4.015
NCH-45	CPX12C	52.610	1.794	11.319	0.376	14.358	19.643	0.361	100.461	1.961	0.079	0.353	0.012	0.798	0.784	0.026	6	4.013
NCH-45	CPX12C1	52.554	1.428	11.377	0.342	14.449	19.234	0.337	99.721	1.971	0.063	0.357	0.011	0.808	0.773	0.025	6	4.009
NCH-45	CPX12R	52.572	1.497	11.146	0.440	14.440	19.679	0.349	100.123	1.966	0.066	0.349	0.014	0.805	0.789	0.025	6	4.014
NCH-45	CPX13C	50.981	2.655	11.984	0.344	14.325	18.593	0.300	99.182	1.929	0.118	0.379	0.011	0.808	0.754	0.022	6	4.023
NCH-45	CPX13C1	52.446	1.563	11.086	0.347	14.430	19.483	0.307	99.662	1.968	0.069	0.348	0.011	0.807	0.783	0.022	6	4.009
NCH-45	CPX13R	52.982	1.371	11.494	0.393	14.560	18.992	0.348	100.140	1.978	0.060	0.359	0.012	0.810	0.760	0.025	6	4.005
NCH-31	CPX1C	52.306	1.057	12.474	0.467	13.373	19.343	0.287	99.307	1.983	0.047	0.396	0.015	0.756	0.786	0.021	6	4.004
NCH-31	CPX1R	51.902	1.167	12.811	0.517	13.084	19.549	0.313	99.343	1.974	0.052	0.407	0.017	0.742	0.797	0.023	6	4.012
NCH-31	CPX1R1	51.930	1.103	12.862	0.549	13.201	19.451	0.239	99.335	1.975	0.049	0.409	0.018	0.748	0.793	0.018	6	4.010
NCH-31	CPX2C	52.518	0.996	12.406	0.527	13.683	18.872	0.241	99.243	1.988	0.044	0.393	0.017	0.772	0.766	0.018	6	3.998
NCH-31	CPX2R	52.600	1.091	12.775	0.534	13.242	19.356	0.329	99.927	1.984	0.048	0.403	0.017	0.745	0.782	0.024	6	4.004
NCH-31	CPX2R1	52.766	1.093	12.556	0.513	13.596	19.432	0.248	100.204	1.982	0.048	0.394	0.016	0.761	0.782	0.018	6	4.003
NCH-37	CPX1C	52.682	1.039	12.314	0.467	13.317	19.861	0.304	99.984	1.984	0.046	0.388	0.015	0.748	0.801	0.022	6	4.004
NCH-37	CPX1C1	52.741	1.186	11.925	0.409	13.610	20.023	0.341	100.235	1.978	0.052	0.374	0.013	0.761	0.805	0.025	6	4.008
NCH-37	CPX1R	52.896	1.046	12.619	0.501	13.441	19.865	0.327	100.695	1.980	0.046	0.395	0.016	0.750	0.797	0.024	6	4.009
Arrau	CPX12R	51.884	1.505	12.536	0.432	14.007	18.948	0.357	100.321	1.9483	0.0666	0.3937	0.0137	0.7841	0.7624	0.026	6	4.0133
Arrau	CPX12R1	51.516	1.858	12.214	0.426	13.558	19.43	0.335	100.152	1.9382	0.0824	0.3843	0.0136	0.7604	0.7833	0.0244	6	4.0097

Sample	Crystal	SiO2	Al2O3	FeOt	MnO	MgO	CaO	Na2O	Total	Si	Al	Fe	Mn	Mg	Ca	Na	O	CatTot
Arrau	CPX12R	52.018	1.191	12.259	0.441	13.695	19.288	0.31	99.863	1.9615	0.053	0.3866	0.0141	0.7698	0.7793	0.0227	6	4.0064
Arrau	CPX12R2	52.601	1.099	12.265	0.468	13.707	19.591	0.27	100.47	1.9704	0.0485	0.3842	0.0148	0.7654	0.7863	0.0196	6	4.0028
Arrau	CPX13C	52.512	1.032	11.85	0.404	13.666	20.096	0.328	100.378	1.9686	0.0456	0.3715	0.0128	0.7637	0.8073	0.0239	6	4.0076
Arrau	CPX13R	52.688	1.018	11.846	0.376	13.866	20.271	0.334	100.86	1.9658	0.0448	0.3696	0.0119	0.7712	0.8104	0.0242	6	4.0108
Arrau	CPX13R1	52.413	1.218	11.52	0.435	13.886	20.23	0.313	100.554	1.9598	0.0537	0.3603	0.0138	0.774	0.8105	0.0227	6	4.0102
Arrau	CPX13R2	52.51	1.325	11.412	0.397	14.052	19.994	0.343	100.51	1.9611	0.0583	0.3564	0.0126	0.7823	0.8001	0.0249	6	4.0093
Arrau	CPX14C	52.622	0.999	11.606	0.366	13.89	20.542	0.344	100.774	1.9649	0.044	0.3625	0.0116	0.7732	0.8219	0.0249	6	4.0145
Arrau	CPX14R	52.702	0.997	11.353	0.443	14.092	20.389	0.34	100.707	1.9664	0.0438	0.3543	0.014	0.7838	0.8151	0.0246	6	4.013
Arrau	CPX14R1	52.401	1.096	11.802	0.396	13.847	20.28	0.325	100.634	1.9607	0.0483	0.3693	0.0125	0.7724	0.8131	0.0236	6	4.0137
Arrau	CPX15R	52.124	1.559	12.083	0.379	13.596	19.869	0.34	100.548	1.952	0.0688	0.3784	0.012	0.759	0.7973	0.0247	6	4.009
Arrau	CPX15R1	52.653	0.989	12.269	0.473	13.641	19.69	0.311	100.465	1.9732	0.0437	0.3845	0.015	0.762	0.7906	0.0226	6	4.004
Arrau	CPX16C	52.798	1.473	9.562	0.271	15.258	20.067	0.283	100.295	1.9578	0.0644	0.2965	0.0085	0.8435	0.7973	0.0203	6	4.0049
Arrau	CPX16C1	52.603	1.594	9.724	0.294	15.013	20.136	0.291	100.23	1.9542	0.0698	0.3021	0.0093	0.8314	0.8015	0.021	6	4.0054
Arrau	CPX16R	52.772	1.558	10.046	0.367	15.243	19.818	0.342	100.764	1.952	0.0679	0.3108	0.0115	0.8405	0.7855	0.0245	6	4.0103
Arrau	CPX16R1	52.477	1.719	9.721	0.285	15.013	20.017	0.294	100.073	1.9521	0.0754	0.3024	0.009	0.8325	0.7979	0.0212	6	4.0059
Arrau	CPX17C	52.429	1.256	10.726	0.358	14.378	19.927	0.298	99.861	1.9642	0.0555	0.3361	0.0113	0.803	0.7999	0.0216	6	4.0056
Arrau	CPX17C1	52.536	1.331	10.765	0.328	14.416	20.492	0.318	100.751	1.9541	0.0583	0.3349	0.0103	0.7994	0.8167	0.0229	6	4.0124
Arrau	CPX17R	52.511	1.364	11.193	0.418	14.095	20.19	0.323	100.594	1.9588	0.06	0.3492	0.0132	0.7838	0.807	0.0234	6	4.0098
Arrau	CPX17R1	52.471	0.979	12.568	0.471	13.598	19.293	0.297	100.138	1.9738	0.0434	0.3954	0.015	0.7625	0.7776	0.0217	6	4.0025
Arrau	CPX18C	51.973	1.151	11.859	0.455	13.784	19.407	0.271	99.442	1.9649	0.0513	0.375	0.0146	0.7768	0.7862	0.0199	6	4.0041
Arrau	CPX18C1	52.276	1.224	11.711	0.434	13.927	19.789	0.348	100.137	1.9626	0.0542	0.3677	0.0138	0.7794	0.7961	0.0253	6	4.0114
Arrau	CPX18R	52.299	1.056	12.19	0.434	14.117	19.59	0.296	100.453	1.9607	0.0467	0.3822	0.0138	0.789	0.7869	0.0215	6	4.0143
Arrau	CPX18R1	52.201	1.157	11.546	0.414	14.225	19.777	0.371	100.15	1.959	0.0512	0.3624	0.0132	0.7958	0.7953	0.027	6	4.0173
Nicanor	CPX12C	52.504	1.27	10.881	0.358	14.331	19.962	0.256	100.035	1.9644	0.056	0.3405	0.0113	0.7993	0.8003	0.0186	6	4.0037
Nicanor	CPX12C1	52.294	1.421	10.748	0.366	14.417	20.144	0.268	100.158	1.9553	0.0626	0.3361	0.0116	0.8036	0.8071	0.0194	6	4.01
Nicanor	CPX12R	52.266	1.255	11.681	0.379	14.176	19.987	0.289	100.561	1.9544	0.0553	0.3653	0.012	0.7902	0.8008	0.021	6	4.0139
Nicanor	CPX12R1	52.37	1.262	10.788	0.396	14.173	20.195	0.272	99.972	1.9623	0.0557	0.3381	0.0126	0.7917	0.8108	0.0197	6	4.0057
Nicanor	CPX13C	52.082	1.363	11.32	0.367	14.418	20.066	0.268	100.489	1.9468	0.0601	0.3539	0.0116	0.8034	0.8037	0.0195	6	4.016
Nicanor	CPX13C1	51.873	1.457	11.812	0.449	13.915	19.289	0.325	99.722	1.9551	0.0647	0.3723	0.0143	0.7818	0.779	0.0238	6	4.0084
Nicanor	CPX13R	52.334	1.325	11.676	0.349	14.022	19.754	0.343	100.36	1.9587	0.0584	0.3655	0.0111	0.7823	0.7922	0.0249	6	4.0088
Nicanor	CPX13R1	51.937	1.718	11.694	0.377	13.788	19.781	0.317	100.301	1.9464	0.0759	0.3665	0.012	0.7703	0.7943	0.023	6	4.0078
Nicanor	CPX14C	51.889	1.415	11.359	0.442	14.082	19.799	0.347	99.828	1.9527	0.0628	0.3575	0.0141	0.79	0.7984	0.0253	6	4.0148

Sample	Crystal	SiO2	Al2O3	FeOt	MnO	MgO	CaO	Na2O	Total	Si	Al	Fe	Mn	Mg	Ca	Na	O	CatTot
Nicanor	CPX14C1	52.437	1.422	11.079	0.378	13.843	19.883	0.314	99.867	1.9666	0.0629	0.3475	0.012	0.7739	0.799	0.0228	6	3.9992
Nicanor	CPX14R	52.131	1.28	12.075	0.397	13.797	19.766	0.362	100.406	1.9556	0.0566	0.3788	0.0126	0.7715	0.7945	0.0263	6	4.0131
Nicanor	CPX15C	51.767	1.272	12.086	0.433	13.492	19.986	0.325	99.834	1.9558	0.0566	0.3819	0.0139	0.7599	0.8091	0.0238	6	4.0145
Nicanor	CPX15C1	52.394	1.135	12.253	0.435	13.552	19.596	0.345	100.222	1.9685	0.0503	0.385	0.0139	0.759	0.7889	0.0251	6	4.0055
Nicanor	CPX15R	52.162	1.201	12.141	0.439	13.585	19.576	0.359	99.972	1.9646	0.0533	0.3824	0.014	0.7627	0.79	0.0262	6	4.0077
Nicanor	CPX15R1	51.943	1.105	12.223	0.455	13.764	19.695	0.298	99.892	1.9606	0.0492	0.3858	0.0146	0.7744	0.7965	0.0218	6	4.0145
Nicanor	CPX16C	51.968	1.285	11.043	0.339	14.092	20.042	0.247	99.518	1.9586	0.0571	0.3481	0.0108	0.7917	0.8094	0.018	6	4.0081
Nicanor	CPX16C1	52.395	1.082	11.565	0.387	13.91	20.197	0.292	100.214	1.9655	0.0478	0.3628	0.0123	0.7778	0.8118	0.0213	6	4.0102
Nicanor	CPX16R	52.39	1.087	11.427	0.387	14.371	20.248	0.28	100.672	1.9561	0.0478	0.3568	0.0122	0.7999	0.8101	0.0202	6	4.0166
Nicanor	CPX16R1	52.115	1.458	11.357	0.419	14.174	20.091	0.348	100.539	1.948	0.0642	0.355	0.0133	0.7898	0.8047	0.0252	6	4.0165
Nicanor	CPX17R	51.53	2.083	11.691	0.416	13.791	19.881	0.4	100.615	1.9281	0.0919	0.3658	0.0132	0.7692	0.7971	0.029	6	4.0175
Nicanor	CPX17R1	52.185	1.527	11.701	0.374	13.884	19.698	0.297	100.215	1.9559	0.0675	0.3668	0.0119	0.7757	0.7911	0.0216	6	4.006
Nicanor	CPX18C	52.49	1.165	12.569	0.449	13.076	19.683	0.259	100.108	1.9761	0.0517	0.3957	0.0143	0.7338	0.794	0.0189	6	3.9967
Nicanor	CPX18C1	52.309	1.069	12.012	0.424	13.927	19.811	0.289	100.211	1.9649	0.0473	0.3773	0.0135	0.7799	0.7974	0.0211	6	4.0119
Nicanor	CPX18R	52.704	1.036	11.673	0.412	13.817	20.068	0.314	100.45	1.9717	0.0457	0.3652	0.013	0.7705	0.8044	0.0228	6	4.0056
Nicanor	CPX19C	51.738	1.336	12.885	0.445	13.265	19.568	0.302	100.195	1.9522	0.0594	0.4066	0.0142	0.7462	0.7911	0.0221	6	4.0104
Nicanor	CPX19R	51.609	1.34	13.145	0.512	13.206	19.471	0.312	100.265	1.949	0.0596	0.4152	0.0164	0.7435	0.7879	0.0229	6	4.0135
Nicanor	CPX19R1	52.374	0.931	14.178	0.525	13.941	17.647	0.314	100.328	1.9724	0.0413	0.4465	0.0168	0.7826	0.7121	0.023	6	4.0065
Nicanor	CPX20C	52.063	1.281	11.511	0.376	14.071	20.055	0.299	100.197	1.9535	0.0566	0.3612	0.012	0.7871	0.8063	0.0218	6	4.0138
Nicanor	CPX20C1	51.764	1.639	11.741	0.413	13.38	20.074	0.312	99.979	1.9493	0.0727	0.3698	0.0132	0.7511	0.81	0.0228	6	4.0076
Nicanor	CPX20R	52.282	1.287	11.498	0.46	13.886	20.058	0.311	100.382	1.9577	0.0568	0.3601	0.0146	0.7751	0.8047	0.0226	6	4.0085
Nicanor	CPX20R1	52.043	1.331	11.665	0.436	13.962	19.879	0.328	100.163	1.9545	0.0589	0.3664	0.0139	0.7817	0.7999	0.0239	6	4.0142
Nicanor	CPX21C	52.365	1.225	11.826	0.412	14.101	19.687	0.35	100.493	1.9592	0.054	0.37	0.0131	0.7864	0.7892	0.0254	6	4.0124
Nicanor	CPX21R	52.002	1.554	11.587	0.424	14.031	19.551	0.284	99.928	1.9539	0.0688	0.3641	0.0135	0.7859	0.7871	0.0207	6	4.0079
Nicanor	CPX21R1	52.399	1.415	11.974	0.438	14.253	19.148	0.303	100.469	1.9584	0.0623	0.3743	0.0139	0.7941	0.7669	0.022	6	4.0074
Nicanor	CPX22C	51.714	1.463	10.667	0.311	14.569	20.064	0.292	99.645	1.9448	0.0648	0.3355	0.0099	0.8167	0.8085	0.0213	6	4.0175
Nicanor	CPX22R	52.312	1.299	11.455	0.383	14.113	19.832	0.293	100.181	1.9601	0.0574	0.359	0.0122	0.7883	0.7962	0.0213	6	4.0085
Nicanor	CPX22R1	51.473	1.645	11.581	0.381	13.931	19.936	0.32	99.896	1.9394	0.0731	0.3649	0.0122	0.7824	0.8049	0.0233	6	4.0181

Análisis de ortopiroxenos en Universidad de Rice

Sample	Crystal	SiO2	Al2O3	FeOt	MnO	MgO	CaO	Na2O	Total	Si	Al	Fe	Mn	Mg	Ca	Na	O	CatTot
NCH-44	OPX16C	54.206	0.769	18.654	0.539	24.338	1.613	0.005	100.119	1.985	0.033	0.571	0.017	1.329	0.063	0.000	6	3.999
NCH-44	OPX16R	54.003	0.789	18.855	0.567	24.115	1.656	0.035	99.985	1.983	0.034	0.579	0.018	1.320	0.065	0.003	6	4.001
NCH-44	OPX18C	53.788	0.935	18.764	0.527	24.147	1.785	0.051	99.946	1.976	0.041	0.576	0.016	1.322	0.070	0.004	6	4.006
NCH-26	OPX13C	52.716	0.375	24.656	0.866	19.636	1.617	0.016	99.866	1.996	0.017	0.781	0.028	1.108	0.066	0.001	6	3.997
NCH-26	OPX13R	52.884	0.483	23.977	0.806	19.958	1.674	0.006	99.782	1.997	0.022	0.757	0.026	1.123	0.068	0.000	6	3.993
NCH-26	OPX14C	52.849	0.908	21.577	0.661	22.135	1.613	0.008	99.743	1.974	0.040	0.674	0.021	1.232	0.065	0.001	6	4.007
NCH-26	OPX14R	52.131	0.539	25.323	0.775	19.454	1.582	0.026	99.804	1.983	0.024	0.805	0.025	1.103	0.064	0.002	6	4.006
NCH-26	OPX15C	52.949	0.666	22.993	0.622	20.818	1.724	0.055	99.772	1.988	0.029	0.722	0.020	1.165	0.069	0.004	6	3.999
NCH-26	OPX15R	51.419	0.397	29.466	1.120	15.811	1.746	0.05	99.959	1.995	0.018	0.956	0.037	0.915	0.073	0.004	6	3.998
NCH-26	OPX15R1	51.974	0.555	25.345	0.809	18.590	1.766	0.057	99.039	1.993	0.025	0.813	0.026	1.063	0.073	0.004	6	3.998
NCH-27	OPX13C	53.699	0.769	19.932	0.432	23.237	1.931	0.027	100.000	1.982	0.033	0.615	0.014	1.279	0.076	0.002	6	4.002
NCH-27	OPX13C1	53.506	0.736	19.796	0.523	23.033	1.848	0.018	99.442	1.986	0.032	0.615	0.016	1.274	0.074	0.001	6	3.999
NCH-27	OPX13R	53.939	0.657	19.663	0.430	22.935	2.118	0.074	99.742	1.993	0.029	0.608	0.013	1.263	0.084	0.005	6	3.995
NCH-27	OPX13R1	52.713	1.510	19.077	0.435	23.817	2.101	0.053	99.653	1.949	0.066	0.590	0.014	1.313	0.083	0.004	6	4.020
NCH-27	OPX14C	53.895	1.041	17.902	0.365	24.543	1.885	0.022	99.631	1.977	0.045	0.549	0.011	1.342	0.074	0.002	6	4.001
NCH-27	OPX14C1	53.288	1.452	18.171	0.419	24.083	1.901	0.05	99.314	1.964	0.063	0.560	0.013	1.323	0.075	0.004	6	4.005
NCH-27	OPX14R	53.414	0.841	19.384	0.438	22.930	2.132	0.034	99.139	1.985	0.037	0.603	0.014	1.271	0.085	0.002	6	3.997
NCH-27	OPX14R1	53.431	1.781	19.446	0.403	21.747	2.232	0.238	99.040	1.982	0.078	0.603	0.013	1.203	0.089	0.017	6	3.989
NCH-27	OPX15C	53.694	0.819	19.088	0.441	23.175	1.873	0.031	99.090	1.991	0.036	0.592	0.014	1.281	0.074	0.002	6	3.992
NCH-27	OPX15C1	53.564	0.764	19.209	0.445	23.759	1.949	0.065	99.690	1.978	0.033	0.593	0.014	1.308	0.077	0.005	6	4.008
NCH-27	OPX15R	53.319	0.856	20.709	0.469	21.845	2.176	0.046	99.374	1.989	0.038	0.646	0.015	1.215	0.087	0.003	6	3.993
NCH-27	OPX16C	53.713	0.870	18.492	0.443	24.227	1.938	0	99.683	1.977	0.038	0.569	0.014	1.329	0.076	0.000	6	4.004
NCH-27	OPX16C1	53.984	0.787	18.063	0.421	24.087	1.984	0.038	99.326	1.988	0.034	0.556	0.013	1.322	0.078	0.003	6	3.996
NCH-27	OPX16R	53.805	0.899	19.673	0.465	23.117	2.127	0.061	100.086	1.982	0.039	0.606	0.015	1.269	0.084	0.004	6	4.000
NCH-27	OPX16R1	53.025	1.063	19.051	0.430	22.925	2.183	0.057	98.677	1.978	0.047	0.594	0.014	1.275	0.087	0.004	6	4.000
NCH-34	OPX1C	53.096	0.764	21.301	0.985	21.867	1.674	0.05	99.687	1.983	0.034	0.665	0.031	1.217	0.067	0.004	6	4.002
NCH-34	OPX1C1	52.856	0.940	21.458	0.862	21.749	1.536	0.018	99.401	1.980	0.042	0.672	0.027	1.215	0.062	0.001	6	4.000
NCH-34	OPX1R	53.427	0.639	20.330	0.890	22.264	1.496	0	99.046	1.997	0.028	0.635	0.028	1.240	0.060	0.000	6	3.989
NCH-34	OPX1R1	53.681	0.640	20.579	0.869	22.428	1.415	0.01	99.612	1.996	0.028	0.640	0.027	1.243	0.056	0.001	6	3.991
NCH-34	OPX2C	53.107	0.628	21.463	0.965	22.080	1.463	0.012	99.706	1.984	0.028	0.671	0.031	1.230	0.059	0.001	6	4.002
NCH-34	OPX2C1	53.370	0.633	21.409	0.983	22.079	1.461	0.014	99.935	1.987	0.028	0.667	0.031	1.226	0.058	0.001	6	3.999
NCH-34	OPX2R	53.734	0.820	19.495	0.731	23.075	1.512	0.048	99.367	1.991	0.036	0.604	0.023	1.275	0.060	0.003	6	3.993
NCH-34	OPX2R1	53.583	0.936	19.350	0.727	23.037	1.544	0.045	99.177	1.989	0.041	0.601	0.023	1.275	0.061	0.003	6	3.993

Sample	Crystal	SiO2	Al2O3	FeOt	MnO	MgO	CaO	Na2O	Total	Si	Al	Fe	Mn	Mg	Ca	Na	O	CatTot
NCH-34	OPX3C	53.604	0.421	20.635	0.851	22.757	1.478	0.019	99.746	1.992	0.018	0.641	0.027	1.261	0.059	0.001	6	4.000
NCH-34	OPX3C1	53.419	0.653	20.517	0.980	22.728	1.449	0.028	99.746	1.985	0.029	0.638	0.031	1.259	0.058	0.002	6	4.001
NCH-34	OPX3R	53.352	0.501	20.569	0.805	22.789	1.542	0.006	99.558	1.987	0.022	0.641	0.025	1.265	0.062	0.000	6	4.003
NCH-34	OPX3R1	53.248	0.619	20.355	0.847	22.808	1.470	0.054	99.347	1.985	0.027	0.635	0.027	1.267	0.059	0.004	6	4.003
NCH-34	OPX4C	52.771	1.270	20.099	0.780	23.239	1.409	0.016	99.568	1.961	0.056	0.625	0.025	1.288	0.056	0.001	6	4.012
NCH-34	OPX4C1	53.353	1.062	20.002	0.801	23.211	1.459	0.052	99.888	1.974	0.046	0.619	0.025	1.280	0.058	0.004	6	4.005
NCH-34	OPX4R	53.230	0.874	20.577	0.884	22.524	1.561	0.055	99.650	1.980	0.038	0.640	0.028	1.249	0.062	0.004	6	4.002
NCH-34	OPX4R1	53.573	0.673	20.115	0.809	23.063	1.450	0.023	99.683	1.987	0.029	0.624	0.025	1.275	0.058	0.002	6	4.000
NCH-34	OPX5C	53.541	0.731	21.253	0.841	22.087	1.558	0.051	100.011	1.989	0.032	0.660	0.026	1.223	0.062	0.004	6	3.997
NCH-34	OPX5C1	52.971	0.920	21.382	0.812	21.912	1.864	0.099	99.861	1.975	0.040	0.667	0.026	1.218	0.074	0.007	6	4.008
NCH-34	OPX5R	53.468	0.703	20.748	0.844	23.203	1.404	0.021	100.370	1.976	0.031	0.641	0.026	1.278	0.056	0.001	6	4.010
NCH-34	OPX5R1	53.629	0.732	19.750	0.811	22.729	1.475	0.011	99.126	1.996	0.032	0.615	0.026	1.261	0.059	0.001	6	3.989
NCH-34	OPX6C	52.545	1.073	21.775	0.912	21.954	1.570	0.025	99.829	1.965	0.047	0.681	0.029	1.224	0.063	0.002	6	4.012
NCH-34	OPX6C1	53.254	0.799	21.679	0.968	21.712	1.665	0.026	100.077	1.984	0.035	0.675	0.031	1.206	0.066	0.002	6	3.999
NCH-34	OPX6R	53.605	0.721	20.346	0.808	23.065	1.427	0.055	99.972	1.984	0.031	0.630	0.025	1.272	0.057	0.004	6	4.003
NCH-34	OPX6R1	53.700	0.724	19.776	0.820	23.114	1.551	0.026	99.685	1.988	0.032	0.612	0.026	1.276	0.062	0.002	6	3.997
NCH-34	OPX7C	53.346	0.774	20.712	0.793	23.000	1.489	0.051	100.114	1.975	0.034	0.641	0.025	1.270	0.059	0.004	6	4.009
NCH-34	OPX7C1	53.619	0.763	20.294	0.820	22.798	1.417	0.025	99.711	1.988	0.033	0.629	0.026	1.260	0.056	0.002	6	3.996
NCH-34	OPX7R	53.525	0.726	20.316	0.823	22.831	1.542	0.063	99.763	1.985	0.032	0.630	0.026	1.262	0.061	0.005	6	4.001
NCH-34	OPX7R1	53.749	0.668	20.246	0.775	22.795	1.493	0	99.726	1.992	0.029	0.628	0.024	1.260	0.059	0.000	6	3.993
NCH-45	OPX16C	53.690	0.754	21.115	0.659	21.822	1.632	0.04	99.672	1.997	0.033	0.657	0.021	1.210	0.065	0.003	6	3.988
NCH-45	OPX16C1	53.238	0.859	21.747	0.615	21.791	1.579	0.018	99.829	1.985	0.038	0.678	0.019	1.211	0.063	0.001	6	3.997
NCH-45	OPX16R	52.865	0.904	21.835	0.681	21.278	1.597	0.046	99.160	1.987	0.040	0.686	0.022	1.192	0.064	0.003	6	3.995
NCH-45	OPX17C	53.523	0.754	20.910	0.642	22.173	1.757	0.048	99.759	1.990	0.033	0.650	0.020	1.229	0.070	0.003	6	3.995
NCH-45	OPX17C1	53.554	0.659	20.443	0.611	22.371	1.776	0.044	99.414	1.994	0.029	0.636	0.019	1.241	0.071	0.003	6	3.994
NCH-45	OPX17C2	53.437	1.359	19.793	0.507	23.099	1.746	0.045	99.941	1.972	0.059	0.611	0.016	1.271	0.069	0.003	6	4.000
NCH-45	OPX18C	53.231	0.492	22.158	0.687	21.207	1.598	0.021	99.373	1.999	0.022	0.696	0.022	1.187	0.064	0.002	6	3.991
NCH-45	OPX18C1	53.842	0.620	20.739	0.522	22.675	1.705	0.063	100.103	1.991	0.027	0.641	0.016	1.250	0.068	0.005	6	3.998
NCH-55	OPX12C	53.614	1.105	18.296	0.311	24.283	1.808	0.044	99.417	1.974	0.048	0.563	0.010	1.333	0.071	0.003	6	4.003
NCH-55	OPX12C1	53.953	1.161	18.276	0.347	24.585	1.891	0.012	100.213	1.971	0.050	0.558	0.011	1.339	0.074	0.001	6	4.004
NCH-55	OPX12C2	53.909	1.070	18.562	0.358	24.315	1.860	0.039	100.074	1.974	0.046	0.569	0.011	1.328	0.073	0.003	6	4.004
NCH-55	OPX13C	53.216	0.681	19.634	0.499	23.179	1.630	0.042	98.839	1.985	0.030	0.613	0.016	1.289	0.065	0.003	6	4.001
NCH-55	OPX13C1	53.336	0.705	19.910	0.596	23.199	1.728	0.027	99.474	1.981	0.031	0.618	0.019	1.285	0.069	0.002	6	4.005
NCH-55	OPX13C2	53.349	0.770	20.257	0.588	23.049	1.695	0.038	99.708	1.979	0.034	0.629	0.018	1.275	0.067	0.003	6	4.005
NCH-55	OPX13R	54.027	0.553	19.336	0.511	23.267	1.680	0.059	99.374	1.999	0.024	0.598	0.016	1.283	0.067	0.004	6	3.992

Sample	Crystal	SiO2	Al2O3	FeOt	MnO	MgO	CaO	Na2O	Total	Si	Al	Fe	Mn	Mg	Ca	Na	O	CatTot
NCH-55	OPX13R1	53.242	0.465	21.045	0.583	22.509	1.677	0.076	99.521	1.986	0.020	0.657	0.018	1.252	0.067	0.006	6	4.006
NCH-55	OPX14C	52.598	0.603	24.134	0.699	19.826	1.603	0.017	99.463	1.993	0.027	0.765	0.022	1.120	0.065	0.001	6	3.994
NCH-55	OPX14C1	52.452	0.591	24.176	0.759	20.016	1.559	0.051	99.553	1.987	0.026	0.766	0.024	1.130	0.063	0.004	6	4.002
NCH-55	OPX14C2	52.806	0.528	23.516	0.694	20.780	1.663	0.06	99.987	1.985	0.023	0.739	0.022	1.164	0.067	0.004	6	4.006
NCH-55	OPX14R	52.987	0.573	22.651	0.638	20.814	1.653	0.088	99.316	1.995	0.025	0.713	0.020	1.168	0.067	0.006	6	3.996
NCH-55	OPX14R1	53.314	0.589	22.655	0.607	20.801	1.711	0.045	99.677	1.999	0.026	0.710	0.019	1.163	0.069	0.003	6	3.990
NCH-55	OPX14R2	52.858	0.588	22.867	0.747	20.813	1.709	0.022	99.582	1.990	0.026	0.720	0.024	1.168	0.069	0.002	6	3.999
NCH-55	OPX15C	52.700	0.545	23.217	0.784	20.604	1.718	0.065	99.568	1.988	0.024	0.732	0.025	1.159	0.069	0.005	6	4.003
NCH-55	OPX15C1	52.613	0.573	23.388	0.715	20.223	1.714	0.021	99.226	1.993	0.026	0.741	0.023	1.142	0.070	0.002	6	3.995
NCH-55	OPX15R	52.659	0.563	23.172	0.629	20.818	1.664	0.044	99.505	1.986	0.025	0.731	0.020	1.170	0.067	0.003	6	4.003
NCH-55	OPX15R1	52.929	0.622	22.345	0.687	20.897	1.603	0.031	99.083	1.996	0.028	0.705	0.022	1.175	0.065	0.002	6	3.992
NCH-55	OPX16C	53.023	0.571	22.932	0.686	20.579	1.608	0.017	99.399	1.998	0.025	0.723	0.022	1.156	0.065	0.001	6	3.990
NCH-55	OPX16C1	52.668	0.559	23.223	0.695	20.615	1.605	0.046	99.365	1.990	0.025	0.734	0.022	1.161	0.065	0.003	6	4.000
NCH-55	OPX16R	52.637	0.668	22.566	0.702	20.554	1.685	0.049	98.812	1.993	0.030	0.715	0.023	1.160	0.068	0.004	6	3.994
NCH-55	OPX16R1	52.909	0.601	23.103	0.740	20.579	1.785	0.02	99.717	1.991	0.027	0.727	0.024	1.154	0.072	0.001	6	3.996
NCH-55	OPX17C	53.862	0.887	18.393	0.517	23.237	2.351	0	99.247	1.991	0.039	0.569	0.016	1.280	0.093	0.000	6	3.990
NCH-55	OPX17C1	53.119	1.041	18.718	0.524	22.688	2.126	0.046	98.216	1.988	0.046	0.586	0.017	1.266	0.085	0.003	6	3.991
NCH-55	OPX17R	52.776	0.911	19.892	0.568	21.882	2.003	0.063	98.032	1.990	0.040	0.627	0.018	1.230	0.081	0.005	6	3.994
NCH-31	OPX1C	53.645	0.756	20.992	0.667	22.228	1.710	0.008	99.998	1.990	0.033	0.651	0.021	1.229	0.068	0.001	6	3.994
NCH-31	OPX1C1	53.124	0.897	20.926	0.685	21.966	1.724	0.028	99.322	1.985	0.039	0.654	0.022	1.224	0.069	0.002	6	3.996
NCH-31	OPX1C2	53.503	0.839	21.153	0.664	21.974	1.846	0.004	99.979	1.988	0.037	0.657	0.021	1.217	0.073	0.000	6	3.994
NCH-31	OPX1R	53.251	0.655	23.008	0.831	20.489	1.599	0.063	99.833	1.998	0.029	0.722	0.026	1.146	0.064	0.005	6	3.990
NCH-31	OPX1R1	53.080	0.657	23.305	0.786	20.537	1.602	0.06	99.967	1.992	0.029	0.731	0.025	1.149	0.064	0.004	6	3.996
NCH-31	OPX2C	52.843	0.348	23.417	0.824	20.264	1.682	0.027	99.378	1.998	0.016	0.741	0.026	1.142	0.068	0.002	6	3.994
NCH-31	OPX2R	52.893	0.446	23.458	0.851	20.091	1.655	0.001	99.394	2.000	0.020	0.742	0.027	1.133	0.067	0.000	6	3.990
NCH-31	OPX2R1	53.119	0.519	23.428	0.815	20.254	1.569	0.038	99.704	2.000	0.023	0.738	0.026	1.137	0.063	0.003	6	3.990
NCH-31	OPX3C	53.336	0.509	23.476	0.837	20.444	1.646	0	100.248	1.998	0.022	0.735	0.027	1.142	0.066	0.000	6	3.991
NCH-31	OPX3R	52.751	0.473	23.421	0.819	20.476	1.629	0.08	99.569	1.991	0.021	0.739	0.026	1.152	0.066	0.006	6	4.002
NCH-31	OPX3R1	52.784	0.505	23.231	0.862	20.126	1.662	0.034	99.170	1.999	0.023	0.736	0.028	1.136	0.067	0.002	6	3.991
NCH-31	OPX4C	52.948	0.550	22.711	0.853	20.523	1.567	0.048	99.152	1.999	0.024	0.717	0.027	1.155	0.063	0.004	6	3.991
NCH-31	OPX4C1	53.326	0.671	21.391	0.734	21.705	1.722	0.053	99.549	1.992	0.030	0.668	0.023	1.209	0.069	0.004	6	3.996
NCH-31	OPX4R	52.701	0.573	22.902	0.750	20.509	1.685	0	99.120	1.994	0.026	0.725	0.024	1.157	0.068	0.000	6	3.994
NCH-31	OPX4R1	53.213	0.601	22.750	0.776	20.813	1.601	0.039	99.754	1.996	0.027	0.714	0.025	1.164	0.064	0.003	6	3.993
NCH-31	OPX5C	54.016	1.361	18.501	0.447	24.162	1.641	0.008	100.128	1.975	0.059	0.566	0.014	1.317	0.064	0.001	6	3.996
NCH-31	OPX5R	53.079	1.184	23.730	0.884	18.904	2.039	0.095	99.820	1.998	0.053	0.747	0.028	1.061	0.082	0.007	6	3.983

Sample	Crystal	SiO2	Al2O3	FeOt	MnO	MgO	CaO	Na2O	Total	Si	Al	Fe	Mn	Mg	Ca	Na	O	CatTot
NCH-31	OPX5R1	53.015	0.513	22.381	0.777	20.721	1.680	0.029	99.087	2.000	0.023	0.706	0.025	1.165	0.068	0.002	6	3.989
NCH-31	OPX6C	53.157	0.464	23.367	0.842	20.185	1.625	0.018	99.640	2.003	0.021	0.736	0.027	1.134	0.066	0.001	6	3.987
NCH-31	OPX6R	52.670	0.413	24.565	1.026	19.743	1.703	0.033	100.120	1.990	0.018	0.776	0.033	1.112	0.069	0.002	6	4.002
NCH-31	OPX6R1	52.621	0.473	23.580	0.894	20.098	1.724	0.063	99.390	1.992	0.021	0.747	0.029	1.134	0.070	0.005	6	3.999
NCH-31	OPX7C	52.762	0.542	23.438	0.834	20.098	1.686	0.027	99.360	1.996	0.024	0.742	0.027	1.134	0.068	0.002	6	3.993
NCH-31	OPX7R	52.812	0.470	23.642	0.833	19.544	1.644	0.048	98.945	2.007	0.021	0.751	0.027	1.107	0.067	0.004	6	3.984
NCH-31	OPX7R1	52.389	0.648	24.621	0.809	19.544	1.653	0.017	99.664	1.988	0.029	0.781	0.026	1.105	0.067	0.001	6	3.998
NCH-31	OPX8C	52.574	0.538	23.739	0.868	19.787	1.643	0.078	99.149	1.996	0.024	0.754	0.028	1.120	0.067	0.006	6	3.995
NCH-31	OPX8R1	52.682	0.460	25.169	0.955	19.216	1.636	0	100.118	1.995	0.021	0.797	0.031	1.085	0.066	0.000	6	3.995
NCH-31	OPX8R1	52.570	0.501	24.492	0.896	19.406	1.750	0	99.615	1.995	0.022	0.777	0.029	1.098	0.071	0.000	6	3.994
NCH-31	OPX9C	53.112	0.553	23.524	0.889	20.266	1.667	0.041	100.011	1.996	0.025	0.739	0.028	1.135	0.067	0.003	6	3.994
NCH-31	OPX9R	52.778	0.463	23.667	0.874	20.057	1.684	0	99.523	1.996	0.021	0.749	0.028	1.131	0.068	0.000	6	3.994
NCH-37	OPX1C	53.289	0.555	23.389	0.763	20.436	1.561	0.03	99.993	1.999	0.025	0.734	0.024	1.143	0.063	0.002	6	3.990
NCH-37	OPX1R	53.186	0.636	23.496	0.719	20.241	1.529	0.025	99.807	2.000	0.028	0.739	0.023	1.134	0.062	0.002	6	3.987
NCH-37	OPX1R1	53.241	0.485	23.601	0.854	20.010	1.537	0.016	99.728	2.005	0.022	0.743	0.027	1.124	0.062	0.001	6	3.984
NCH-37	OPX2C	53.300	0.555	24.289	0.839	19.842	1.709	0.025	100.534	1.998	0.025	0.762	0.027	1.109	0.069	0.002	6	3.990
NCH-37	OPX2R	52.655	0.412	24.993	1.020	18.973	1.824	0.044	99.877	1.998	0.018	0.793	0.033	1.073	0.074	0.003	6	3.994
NCH-37	OPX2R1	52.577	0.543	24.784	0.841	19.379	1.630	0.031	99.754	1.994	0.024	0.786	0.027	1.095	0.066	0.002	6	3.996
NCH-37	OPX3C	52.555	0.564	24.748	0.917	18.994	1.700	0.009	99.478	1.999	0.025	0.787	0.030	1.077	0.069	0.001	6	3.988
NCH-37	OPX3R	52.265	0.477	24.974	0.933	18.963	1.734	0.071	99.346	1.994	0.021	0.797	0.030	1.079	0.071	0.005	6	3.999
NCH-37	OPX3R1	52.539	0.509	25.093	0.912	18.796	1.654	0.003	99.503	2.001	0.023	0.799	0.029	1.067	0.068	0.000	6	3.988
NCH-37	OPX4C	52.767	0.560	25.031	0.859	19.098	1.718	0.036	100.033	1.997	0.025	0.792	0.028	1.077	0.070	0.003	6	3.992
NCH-37	OPX4R	52.984	0.489	25.083	0.878	18.963	1.708	0.036	100.105	2.003	0.022	0.793	0.028	1.069	0.069	0.003	6	3.988
NCH-37	OPX4R1	52.435	0.662	24.877	0.969	18.562	1.653	0.073	99.158	2.002	0.030	0.794	0.031	1.056	0.068	0.005	6	3.987
NCH-37	OPX5C	52.783	0.487	24.735	0.985	19.267	1.735	0.037	99.992	1.997	0.022	0.783	0.032	1.087	0.070	0.003	6	3.993
NCH-37	OPX5R	52.609	0.549	24.971	0.889	19.215	1.620	0.024	99.853	1.995	0.025	0.792	0.029	1.086	0.066	0.002	6	3.994
NCH-37	OPX5R1	52.065	0.427	25.730	0.977	18.258	1.698	0.043	99.155	1.998	0.019	0.826	0.032	1.044	0.070	0.003	6	3.994
NCH-37	OPX6C	52.847	0.513	24.757	0.937	19.662	1.519	0.02	100.235	1.993	0.023	0.781	0.030	1.106	0.061	0.001	6	3.996
NCH-37	OPX6R	52.828	0.574	24.621	0.931	19.291	1.646	0.033	99.891	1.998	0.026	0.779	0.030	1.088	0.067	0.002	6	3.990
NCH-37	OPX6R1	52.476	0.560	24.917	0.894	19.231	1.672	0.017	99.750	1.992	0.025	0.791	0.029	1.088	0.068	0.001	6	3.996
Arrau	OPX16C	52.858	0.598	22.09	0.652	21.196	1.73	0.01	99.438	1.9858	0.0265	0.694	0.0208	1.187	0.0696	0.0007	6	3.993
Arrau	OPX16R	52.666	0.613	23.307	0.695	20.649	1.658	0.021	99.954	1.9801	0.0272	0.7329	0.0221	1.1573	0.0668	0.0015	6	3.9978
Arrau	OPX16R1	53.107	0.665	21.311	0.605	22.01	1.753	0.019	99.772	1.9806	0.0292	0.6647	0.0191	1.2236	0.0701	0.0014	6	3.9973
Arrau	OPX16R2	53.229	0.707	21.001	0.596	21.906	1.944	0.021	99.745	1.9834	0.0311	0.6545	0.0188	1.2168	0.0776	0.0015	6	3.9938
Arrau	OPX16R3	52.973	0.611	23.117	0.798	20.647	1.603	0.014	100.041	1.987	0.027	0.7252	0.0254	1.1545	0.0644	0.001	6	3.9924

Sample	Crystal	SiO2	Al2O3	FeOt	MnO	MgO	CaO	Na2O	Total	Si	Al	Fe	Mn	Mg	Ca	Na	O	CatTot
Arrau	OPX17R	52.96	0.632	22.923	0.651	20.898	1.713	0	100.091	1.9833	0.0279	0.7179	0.0206	1.1666	0.0688	0	6	3.9939
Arrau	OPX17R1	52.767	0.524	22.892	0.701	21.039	1.685	0	99.888	1.9814	0.0232	0.7189	0.0223	1.1777	0.0678	0	6	3.9993
Arrau	OPX17R2	53.213	0.554	23.238	0.704	21.143	1.647	0.027	100.823	1.9809	0.0243	0.7235	0.0222	1.1733	0.0657	0.0019	6	4.0001
Arrau	OPX19C	52.466	0.53	23.788	0.825	20.105	1.726	0.051	99.779	1.9829	0.0236	0.7519	0.0264	1.1327	0.0699	0.0037	6	3.9994
Arrau	OPX19R	52.679	0.495	23.187	0.746	20.782	1.748	0.032	99.976	1.9804	0.0219	0.729	0.0238	1.1646	0.0704	0.0024	6	4.0012
Arrau	OPX19R1	52.877	0.497	23.292	0.745	20.251	1.668	0.052	99.633	1.9935	0.0221	0.7344	0.0238	1.1381	0.0674	0.0038	6	3.9902
Arrau	OPX19R	52.963	0.579	23.517	0.694	20.611	1.605	0.044	100.337	1.9839	0.0256	0.7367	0.022	1.1509	0.0644	0.0032	6	3.9958
Arrau	OPX19R1	53.007	0.616	23.347	0.715	20.63	1.6	0.034	100.242	1.9856	0.0272	0.7314	0.0227	1.152	0.0642	0.0025	6	3.9939
Arrau	OPX19R2	52.652	0.579	23.529	0.748	20.531	1.644	0.038	100.074	1.9798	0.0257	0.7399	0.0238	1.1509	0.0662	0.0028	6	3.9992
Arrau	OPX19R3	52.696	0.644	23.591	0.727	20.353	1.774	0.037	100.131	1.9808	0.0285	0.7416	0.0231	1.1405	0.0714	0.0027	6	3.9973
Arrau	OPX20R	53.503	0.638	20.877	0.556	22.224	1.706	0.04	99.792	1.9885	0.028	0.6489	0.0175	1.2313	0.0679	0.0029	6	3.9919
Arrau	OPX20R1	53.166	0.678	21.072	0.535	22.402	1.65	0.021	99.785	1.9791	0.0298	0.656	0.0169	1.2431	0.0658	0.0015	6	3.9995
Arrau	OPX20R2	52.623	0.774	21.672	0.665	21.75	1.715	0	99.497	1.9734	0.0342	0.6797	0.0211	1.2159	0.0689	0	6	4.0018
Arrau	OPX21R	52.503	0.517	23.443	0.755	20.317	1.614	0	99.419	1.9865	0.023	0.7418	0.0242	1.1459	0.0654	0	6	3.9945
Arrau	OPX21R1	52.906	0.467	23.555	0.788	20.458	1.692	0.018	100.197	1.9866	0.0207	0.7397	0.025	1.1451	0.0681	0.0013	6	3.9957
Arrau	OPX21C	52.852	0.56	23.166	0.7	20.658	1.762	0.02	100.046	1.9838	0.0248	0.7272	0.0222	1.1559	0.0709	0.0014	6	3.9955
Arrau	OPX21R	52.803	0.517	22.937	0.7	20.832	1.88	0.018	100.022	1.9816	0.0229	0.7199	0.0223	1.1654	0.0756	0.0013	6	3.9985
Nicanor	OPX18C	52.819	0.515	23.119	0.752	20.966	1.649	0.037	100.229	1.9792	0.0227	0.7245	0.0239	1.1711	0.0662	0.0027	6	4.001
Nicanor	OPX18C1	52.034	0.976	24.07	0.674	19.73	2.127	0.038	100.042	1.9659	0.0435	0.7605	0.0216	1.1112	0.0861	0.0028	6	4.0028
Nicanor	OPX18R	52.58	0.57	23.273	0.708	20.674	1.641	0.017	99.718	1.9816	0.0253	0.7335	0.0226	1.1614	0.0663	0.0012	6	3.9991
Nicanor	OPX18R1	52.802	0.673	21.982	0.679	21.462	1.481	0.049	99.432	1.9822	0.0298	0.6902	0.0216	1.2011	0.0596	0.0035	6	3.9969
Nicanor	OPX19C	52.28	0.699	23.525	0.726	20.381	1.592	0.024	99.585	1.9762	0.0311	0.7437	0.0233	1.1485	0.0645	0.0018	6	3.9995
Nicanor	OPX19C1	52.551	0.682	23.78	0.725	20.27	1.613	0.048	100.122	1.9775	0.0302	0.7484	0.0231	1.137	0.065	0.0035	6	3.998
Nicanor	OPX19R	52.23	0.694	23.334	0.794	20.427	1.719	0.07	99.557	1.975	0.0309	0.738	0.0254	1.1515	0.0697	0.0052	6	4.0039
Nicanor	OPX19R1	52.838	0.508	23.359	0.796	20.873	1.715	0.048	100.428	1.9788	0.0224	0.7316	0.0253	1.1653	0.0688	0.0035	6	4.0041
Nicanor	OPX20C	52.378	0.672	24.225	0.728	20.334	1.551	0	100.214	1.973	0.0298	0.7632	0.0232	1.1418	0.0626	0	6	4.0028
Nicanor	OPX20C1	52.818	0.577	23.733	0.751	20.373	1.685	0.084	100.369	1.9817	0.0255	0.7447	0.0239	1.1395	0.0678	0.0061	6	3.999
Nicanor	OPX20R	52.711	0.676	23.717	0.657	20.58	1.597	0.044	100.329	1.9771	0.0299	0.744	0.0209	1.1507	0.0642	0.0032	6	3.9997
Nicanor	OPX21C	52.213	0.585	23.925	0.709	20.19	1.654	0.018	99.582	1.978	0.0261	0.758	0.0228	1.1401	0.0671	0.0013	6	4.0016
Nicanor	OPX21C1	52.984	0.532	23.564	0.831	20.6	1.57	0.014	100.363	1.9855	0.0235	0.7385	0.0264	1.1508	0.0631	0.001	6	3.9967
Nicanor	OPX21R	53.038	0.459	23.257	0.767	20.922	1.773	0.063	100.515	1.9828	0.0202	0.7272	0.0243	1.166	0.071	0.0046	6	4.0028
Nicanor	OPX21R1	52.58	0.473	23.651	0.776	20.244	1.747	0.037	99.735	1.9859	0.0211	0.7471	0.0248	1.1398	0.0707	0.0027	6	3.9985
Nicanor	OPX22C	52.77	0.837	22.409	0.631	21.673	1.575	0.039	100.295	1.9682	0.0368	0.699	0.0199	1.205	0.0629	0.0028	6	4.0047
Nicanor	OPX22C1	52.373	1.019	22.176	0.722	21.42	1.54	0.028	99.701	1.9647	0.0451	0.6957	0.023	1.1978	0.0619	0.002	6	4.0023
Nicanor	OPX22R	52.947	0.812	22.253	0.593	21.396	1.626	0.035	100.047	1.9771	0.0357	0.6949	0.0187	1.191	0.0651	0.0025	6	3.996
Nicanor	OPX22R1	52.381	1.151	22.701	0.681	21.048	1.648	0.06	100.071	1.9624	0.0508	0.7112	0.0216	1.1755	0.0662	0.0044	6	4.0035
Nicanor	OPX23C	52.157	1.036	22.195	0.648	21.519	1.818	0.028	99.792	1.9571	0.0458	0.6965	0.0206	1.2037	0.0731	0.002	6	4.0098

Sample	Crystal	SiO2	Al2O3	FeOt	MnO	MgO	CaO	Na2O	Total	Si	Al	Fe	Mn	Mg	Ca	Na	O	CatTot
Nicanor	OPX23C1	53.018	0.577	22.278	0.718	21.365	1.607	0	99.872	1.9843	0.0255	0.6973	0.0228	1.192	0.0645	0	6	3.9952
Nicanor	OPX23R	52.908	0.511	22.835	0.671	20.848	1.695	0.02	99.736	1.9881	0.0226	0.7176	0.0214	1.1678	0.0682	0.0014	6	3.9941
Nicanor	OPX23R1	53.467	0.503	22.804	0.72	20.829	1.726	0.015	100.313	1.9952	0.0221	0.7117	0.0228	1.1587	0.069	0.0011	6	3.9877
Nicanor	OPX24C	52.968	0.566	22.183	0.732	21.672	1.629	0.022	100.081	1.9784	0.0249	0.6929	0.0232	1.2066	0.0652	0.0016	6	4.0016
Nicanor	OPX24C1	53.179	0.525	22.11	0.695	21.792	1.626	0.022	100.228	1.9814	0.0231	0.689	0.0219	1.2104	0.0649	0.0016	6	4.0002
Nicanor	OPX24R1	53.435	0.404	22.462	0.687	21.452	1.578	0.01	100.201	1.9927	0.0178	0.7006	0.0217	1.1926	0.063	0.0007	6	3.9939
Nicanor	OPX24R2	53.507	0.471	21.699	0.666	21.73	1.66	0.025	99.999	1.9928	0.0207	0.6759	0.021	1.2065	0.0662	0.0018	6	3.9921
Nicanor	OPX25C	51.981	0.573	25.007	0.802	19.243	1.816	0.041	99.738	1.9783	0.0257	0.796	0.0259	1.0917	0.074	0.003	6	4.0025
Nicanor	OPX25C1	52.146	0.607	25.064	0.772	19.105	1.769	0.04	99.858	1.9811	0.0272	0.7964	0.0248	1.082	0.072	0.0029	6	3.9965
Nicanor	OPX25R	52.109	0.577	25.184	0.946	19.068	1.788	0.003	100.023	1.9794	0.0258	0.8001	0.0304	1.0797	0.0728	0.0002	6	3.9986
Nicanor	OPX25R1	52.211	0.577	24.588	0.813	18.907	1.92	0.028	99.439	1.9883	0.0259	0.7831	0.0262	1.0733	0.0784	0.0021	6	3.9887
Nicanor	OPX26C	52.492	0.756	23.092	0.742	20.525	1.592	0.037	99.57	1.9796	0.0336	0.7283	0.0237	1.1538	0.0643	0.0027	6	3.9955
Nicanor	OPX26R	52.516	0.431	22.442	0.67	21.061	1.685	0.021	99.142	1.984	0.0192	0.7091	0.0214	1.186	0.0682	0.0015	6	3.9986
Nicanor	OPX26R1	52.785	0.443	22.571	0.71	20.762	1.691	0.055	99.34	1.9903	0.0197	0.7118	0.0227	1.167	0.0683	0.004	6	3.9931
Nicanor	OPX26R2	52.819	0.59	22.574	0.745	20.437	1.741	0.041	99.274	1.9926	0.0262	0.7122	0.0238	1.1493	0.0704	0.003	6	3.9868
Nicanor	OPX27C	52.742	0.672	22.004	0.68	21.346	1.593	0.001	99.421	1.9811	0.0297	0.6912	0.0216	1.1952	0.0641	0.0001	6	3.9942
Nicanor	OPX27R	52.894	0.798	21.436	0.687	21.446	1.623	0.044	99.279	1.9839	0.0353	0.6724	0.0218	1.1991	0.0652	0.0032	6	3.9911
Nicanor	OPX27R1	52.729	0.832	22.047	0.605	21.47	1.558	0.04	99.653	1.9754	0.0368	0.6908	0.0192	1.1991	0.0625	0.0029	6	3.9972

Análisis de óxidos de Fe-Ti en Universidad de Rice

Samples	Crystal	SiO2	FeO	TiO2	V2O3	Al2O3	MgO	MnO	ZnO	Total	Si	Fe	Ti	V	Al	Mg	Mn	Zn	Total
NCH-31	Mg1	0.068	76.21	18.236	0.361	1.98	1.614	0.616	0.052	99.161	0.0165	15.572	3.3508	0.0708	0.5701	0.5879	0.1275	0.0094	20.3097
NCH-31	Mg2	0.054	78.142	18.083	0.33	1.96	1.421	0.586	0.023	100.652	0.0132	15.8089	3.2899	0.0641	0.5588	0.5123	0.1202	0.0042	20.3842
NCH-31	Mg3	0.058	75.692	18.95	0.354	1.819	1.556	0.568	0.16	99.292	0.0142	15.405	3.4682	0.0692	0.5217	0.5645	0.1171	0.0288	20.2178
NCH-31	Ilm1	0	48.008	48.933	0.185	0.231	2.483	0.701	0	100.606	0	8.1152	7.4382	0.0301	0.0549	0.7481	0.12	0	16.5192
NCH-31	Ilm2	0.056	49.051	48.3	0.165	0.23	2.411	0.689	0	100.976	0.0114	8.298	7.3476	0.0267	0.0548	0.7269	0.1181	0	16.598
NCH-31	Ilm3	0	48.831	48.6	0.207	0.235	2.472	0.687	0.017	101.083	0	8.2416	7.3761	0.0335	0.056	0.7438	0.1175	0.0026	16.5774